Konstantinos Spiliopoulos
Dieter Weichert *Editors*

Direct Methods for Limit States in Structures and Materials

Springer

Direct Methods for Limit States in Structures and Materials

Konstantinos Spiliopoulos • Dieter Weichert
Editors

Direct Methods for Limit States in Structures and Materials

Springer

Editors
Konstantinos Spiliopoulos
School of Civil Engineering,
Department of Structural Engineering
National Technical University of Athens
Athens, Greece

Dieter Weichert
Institute of General Mechanics
RWTH-Aachen University
Aachen, Germany

ISBN 978-94-007-6826-0 ISBN 978-94-007-6827-7 (eBook)
DOI 10.1007/978-94-007-6827-7
Springer Dordrecht Heidelberg New York London

Library of Congress Control Number: 2013947157

Printed on acid-free paper

Springer is part of Springer Science+Business Media (www.springer.com)

Foreword

In the history of structural engineering, safety with respect to collapse, rather than stress admissibility, turns out to be the main worry of several pioneers. In the eighteenth century the Saint Peter dome in Rome and the highest spire of the Milan cathedral (with the "Madonnina" on its top) have been structures investigated for restoration (by Poleni and Boscovich, respectively, both primarily mathematicians) from a standpoint and by a graphical-computational procedure which can be regarded as anticipations of limit analysis methods.

Another memorable event might be regarded as a contribution of limit structural analysis to the solution of crucial social problems: the design of the Morison shelters for protection of British families against V2 bombs during one of the most tragic periods of the Second World War; such design was due to the research team of Sir John Baker in Cambridge. In those years, early forties, two other circumstances occurred in the United States with consequences fruitful also for the development of the direct methods: at Brown University, Providence RI, the successful research stream on structural mechanics centered on plasticity was starting under the guidance of Prager; almost simultaneously, linear (and later nonlinear) mathematical programming was developed in Stanford, by George Dantzing and his team, initially in terms of algorithms for optimization of American navy strategies. Later a productive convergence occurred between mathematical programming and elastoplastic structural mechanics, particularly as for direct methods and their practical applications.

Limit analysis and its generalization to shakedown analysis after the mid of the last century have been one of the most fruitful developments of structural mechanics, simultaneously and interactively with another fast growth in applied science, namely finite element and other methods for computer simulations of physical phenomena, particularly of inelastic responses of structures to external actions.

Each important scientific research area exhibits a flourishing era, characterized by intensive activities and fast growth. Such era for direct methods of limit and shakedown analyses grew with contributions provided by several internationally acknowledged research leaders; obviously they are well known to all research workers in applied mechanics and, therefore, they are not considered in this brief foreword. Here I take the liberty to mention with gratitude only some of them, with whom

I had opportunities of personal meetings and pleasant interactions before our international scientific community lost them: Drucker, Symonds, Koiter, Massonnet, Sawczuk, König, Martin; in my country Capurso, Ceradini, Gavarini.

But direct methods still represent a fertile research field, still attractive and fashionable, with challenges still open to fruitful and synergistic convergence of structural mechanics, mathematical developments, computational techniques and not only structural engineering, but also diverse technologies. Evidence of such closing remark is provided by this book and by the Athens conference which originated it, and by the sequence of recent meetings and papers collections on direct methods. Colleagues from various research institutions, who promote such initiatives on direct methods and successfully contribute to them, do deserve, in my opinion, the appreciation of the international community of theoretical and applied mechanics.

Technical University (Politecnico), Milan, Italy Giulio Maier

Preface

Civil and mechanical engineers are to a large extent concerned with safety- and life assessment of structures under thermo-mechanical loading which may cause severe inelastic straining. This task is virtually impossible to perform following cumbersome and time consuming evolutionary methods which, additionally, require the complete knowledge of the loading history. Mostly, however, only variation intervals of the loads are known. Thus, it is important to be able to produce margins of safe service conditions for structures, as well as for structural material, against excessive inelastic deformations.

Methods that aim towards this end, avoiding step-by-step analysis, are called Direct Methods. They are non-evolutionary, and although such methods have existed for some time, they are attracting an increasing interest from scientists and researchers, based on new mathematical formulations and new developments on numerical analysis.

The present volume contains the most recent advances on these methods. It is the outcome of the third international workshop that was held in Athens on February 2012, following the successful first and second workshops in Aachen in 2007 and Lille in 2009. The event, which attracted more than 30 scientists from 6 countries, was organized by the National Technical University of Athens and was hosted by the Onassis Cultural Center.

The papers in the book are arranged in the order of their appearance in the workshop and their contributions are in the fields of Structural and Soil Mechanics as well as Material Science. All the contributed papers have undergone a rigorous review process before acceptance for publication.

We would like to thank all the scientists that have participated in this book for the high quality level of their work.

We would also like to express our thanks to Professor Giulio Maier, of the Technical University of Milan, for his kindness to foreword this book.

Athens, Greece — Konstantinos Spiliopoulos
Aachen, Germany — Dieter Weichert

Contents

Finite Element Limit Analysis and Porous Mises-Schleicher Material

Franck Pastor, Joseph Pastor, and Djimedo Kondo

Abstract By using the kinematic approach of limit analysis (LA) for a hollow sphere whose solid matrix obeys the von Mises criterion, Gurson (J. Eng. Mater. Technol. 99:2–15, 1977) derived a macroscopic criterion of ductile porous medium. The relevance of such criterion has been widely confirmed in several studies and in particular in Trillat and Pastor (Eur. J. Mech. A, Solids 24:800–819, 2005) through numerical lower and upper bound formulations of LA. In the present paper, these formulations are extended to the case of a pressure dependent matrix obeying the parabolic Mises-Schleicher criterion. This extension has been made possible by the use of a specific component of the conic optimization. We first provide the basics of LA for this class of materials and of the required conic optimization; then, the LA hollow sphere model and the resulting static and mixed kinematic codes are briefly presented. The obtained numerical bounds prove to be very accurate when compared to available exact solutions in the particular case of isotropic loadings. A second series of tests is devoted to assess the upper bound and approximate criterion established by Lee and Oung (J. Appl. Mech. 67:288–297, 2000), and also the criterion proposed by Durban et al. (Mech. Res. Commun. 37:636–641, 2010). As a matter of conclusion, these criteria can be considered as admissible only for a slight tension/compression asymmetry ratio for the matrix; in other words, our results show that the determination of the macroscopic criterion of the "porous Mises-Schleicher" material still remains an open problem.

F. Pastor
Laboratoire de Mécanique de Lille (LML), UMR-CNRS 8107, Villeneuve d'Ascq, France
e-mail: franck.pastor@skynet.be

J. Pastor (✉)
Laboratoire LOCIE, UMR-CNRS 5271, Université de Savoie, Chambéry, France
e-mail: joseph.pastor@univ-savoie.fr

D. Kondo
Institut D'Alembert, UMR-CNRS 7190, Université Pierre et Marie Curie, Paris, France
e-mail: djimedo.kondo@upmc.fr

K. Spiliopoulos, D. Weichert (eds.), *Direct Methods for Limit States in Structures and Materials*, DOI 10.1007/978-94-007-6827-7_1,

1 Introduction

The criteria for yielding of ductile porous materials, proposed by Gurson [8], are based on limit analysis (LA) of a hollow sphere or cylinder obeying the von Mises criterion and subjected to uniform strain rate boundary conditions. In his analysis, Gurson used a LA kinematical approach to obtain an upper bound to the exact solution of the hollow sphere model and to the strength of isotropic porous materials which is shown later to correspond to microstructures of the type Hashin Composite Spheres Assemblages (see for instance [12]). In the context of isotropy, the Gurson approach has been extended in several directions among which that allowing to investigate analytically porous materials with matrix exhibiting pressure sensitive behavior (see among others, [5, 7, 9, 13, 15]).

On the other hand, using a finite element discretization of a unit cell, both static and kinematical methods of LA have been developed to obtain rigorous lower and upper bounds and assess Gurson's criteria for cylindrical as well as spherical cavities in [6] and [21]. Using these numerical approaches, the yield function of a porous material with cylindrical voids was studied first; it was shown that Gurson criterion is approximate and does not exhibit the corner that the exact criterion displays in the plane strain case. However, the Gurson criterion for materials containing spherical cavities appears to be satisfactory [32], although it does not account for possible dissymmetry (with respect to the hydrostatic axis) associated with third stress invariant effects [31].

It is worth noticing that the above mentioned LA based numerical approaches lead to rigorous lower and upper bounds of the macroscopic criterion and allow *a posteriori* verification of these bounds from the final optimal solution. Consequently, their use to assess existing theoretical yield functions of porous media is intrinsically relevant. Obviously, such assessment is crucial for confidence in the formulation of constitutive relations based on these yield functions, in the perspective of structural computations.

This paper is focused on a class of materials for which the pressure-sensitive parabolic criterion of Mises-Schleicher [27] is used, see for example [14, 30], and [3] for a detailed comparison with experimental data. Following [4], this criterion well represents the strength differential between uniaxial compression (σ_C) and uniaxial tension (σ_T) which has been observed for many polycristalline materials and geomaterials. Moreover the absence of an apex (as in the Drucker-Prager and Coulomb case) around the minimum value of I_1 ($= \mathrm{tr}\sigma$), which agrees with experimental observations [28], constitutes an advantage from a physical and numerical point of view. This explains that recent papers have investigated the influence of the porosity for such materials. Therefore, in the present paper, analytical Gurson-like macroscopic criteria for spherically porous media with Mises-Schleicher matrix will be assessed by using original LA techniques.

The paper is organized as follows. Section 2 presents the main features of the LA theory and completes the expressions needed by the LA methods; a brief description of these methods is given afterwards, ending with a summary of the mixed kinematic approach and of the specific conic optimization which has allowed to solve

the final optimization problem. In Sect. 3, the micro-macro hollow sphere model is detailed with its 3D finite element discretizations of stress and velocity fields to obtain the macroscopic criterion in terms of average macroscopic stresses. In Sect. 3.3 is presented the implementation of the static approach, which leads to an original *rotated quadratic cone* formulation. Section 3.4 briefly presents the also original mixed kinematic formulation, with discontinuous velocity fields, which leads also to a rotated cone formulation that bypasses the singularity problem when d_m becomes null in an element, or *a fortiori* when the special case of von Mises criterion is considered.

Section 4 recalls the criteria given in the above mentioned papers of the literature that will be assessed in the present work. In Sect. 5, the obtained numerical bounds in the case of hydrostatic loadings are validated first by comparison to available analytical solution (see for instance [15]). Finally, for general loadings, the available criteria of Lee and Oung [13] and of Durban et al. [5] are assessed by comparing them to the numerical bounds; to this end we consider two porosities and two representative tensile and compressive strengths (σ_T, σ_C) ratios which characterize the Mises-Schleicher material.

2 Summary of Limit Analysis for Mises-Schleicher Material

In this section, the basic principles of Limit Analysis (LA) for the Mises-Schleicher material and the resulting methods are recalled, ending with the specific formulation of the conic algorithm used to solve the resulting optimization problems.

2.1 General Limit Analysis and Mises-Schleicher Material

According to [25], a stress tensor field, σ, is said to be admissible if it is both statically admissible (SA), i.e., satisfies equilibrium equations, stress vector continuity, and stress boundary conditions and plastically admissible (PA), i.e., $f(\sigma) \leq 0$, where $f(\sigma)$ is the convex plasticity criterion. In the present problem we consider the yield condition given by F. Schleicher [27] (see also [14, 33] for an application to composite materials, or [10] for a plane stress study):

$$f(\sigma) = \sigma_{eq}^2 + 3\alpha\sigma_0\sigma_m - \sigma_0^2 \leq 0; \quad \sigma_{eq} = \sqrt{\frac{3}{2}\sigma_d : \sigma_d} \tag{1}$$

where σ_d is the deviatoric part of σ and σ_m the main (also called hydrostatic) stress; α and σ_0 are related to the tensile yield stress σ_T and to the absolute yield stress in compression σ_C (with $\sigma_C \geq \sigma_T$) by

$$\alpha = (\sigma_C - \sigma_T)/\sigma_0; \quad \sigma_0 = \sqrt{\sigma_C \sigma_T}. \tag{2}$$

Similarly, a strain rate tensor field, d, is admissible if it is both kinematically admissible (KA, i.e., it is derived from a piecewise continuous velocity vector field u, with bounded discontinuities $[u]$, such that the velocity boundary conditions are fulfilled) and plastically admissible (PA), i.e., the following associated flow rules (3a), (3b) are satisfied

$$d = \lambda \frac{\partial f}{\partial \sigma}, \quad \lambda f(\sigma) = 0,\ \lambda \geq 0,\ f(\sigma) \leq 0; \tag{3a}$$

$$[u] = \xi \frac{\partial f_{disc}}{\partial T}, \quad \xi f_{disc}(T) = 0,\ \xi \geq 0,\ f_{disc}(T) \leq 0, \tag{3b}$$

where d is the strain rate tensor, $[u]$ the velocity jump across the discontinuity surfaces, and $T = (\sigma_n, \sigma_{nt})$ the corresponding stress vector acting on them. The definitions (3a), (3b) lead to the so-called plastic admissibility condition (PA condition) that d and $[u]$ must verify to be plastically admissible, i.e. at least one stress tensor σ or stress vector T (such that $f(\sigma) = 0$ and $f_{disc}(T) = 0$, respectively) can be associated to them. Let us recall that the criterion $f_{disc}(T)$ results from the projection of the plasticity criterion $f(\sigma)$ on the (n, t) Mohr plane associated to the velocity discontinuity surface of normal n, which results for the present material:

$$f_{disc}(T) = \sigma_{nt}^2 + \alpha\sigma_0\sigma_n - \sigma_0^2 \frac{1+\alpha^2}{3} \leq 0. \tag{4}$$

If (3a) and (3b) are fulfilled, the quantities $\sigma : d$ and $T \cdot [u]$ become, respectively, the *convex* unit dissipated powers $\pi_{vol}(d)$ and $\pi_{disc}([u])$, i.e.:

$$\pi_{vol}(d) = \sigma : d; \qquad \pi_{disc}\big([u]\big) = T \cdot [u]. \tag{5}$$

Finally, denoting d_m the average value of the strain rate tensor d, for the Mises-Schleicher material the PA conditions resulting from (3a), (3b) read:

$$d_m \geq 0; \qquad [u_n] \geq 0, \tag{6}$$

and the unit dissipated powers become:

$$\pi_{vol}(d) = \frac{\sigma_0 d_m}{\alpha} + \frac{\alpha\sigma_0}{4}\frac{d_{eq}^2}{d_m}, \tag{7}$$

$$\pi_{disc}\big([u]\big) = \frac{\sigma_0(1+\alpha^2)}{3\alpha}[u_n] + \frac{\alpha\sigma_0}{4}\frac{[u_t]^2}{[u_n]}, \tag{8}$$

where $d_{eq} = \sqrt{\frac{2}{3} d_d : d_d}$ and d_d the deviatoric part of d.

Let us point out that relation (4) and its consequences in (6) and (8) are original; they will allow to check *a posteriori* the admissibility of the optimal velocity field and the corresponding dissipated power along the discontinuities of the mixed

numerical problem described in Sect. 2.3. It is also worth noting that the use of relations (7) and (8) in a classic kinematic method may lead to singularities during the optimization process.

Let us assume now that the virtual power of the external loads P_{ext} can be written as the scalar product of a loading p-vector $Q = Q(\sigma)$ (linear in σ, with σ SA), and a generalized velocity p-vector $q = q(u)$ (linear in u, with u KA) the components of which are called kinematic parameters. The vectors Q and q are also assumed to be linear in their respective arguments, such assumption being always verified in usual cases and in the present problem. The virtual power theorem then reads:

$$P_{ext} = Q \cdot q = \int_V \sigma : d\,dV + \int_{S_{disc}} T \cdot [u] dS = P, \tag{9}$$

where V is the volume of the mechanical system, S_{disc} the union of the velocity discontinuity surfaces; let us note that P becomes the so-called dissipated power P_{diss} when the fields (σ, T) and $(d, [u])$ are also PA and associated, respectively.

Basically, a solution of the LA problem is a pair (σ, u) where the fields σ and u are both admissible and associated by the normality rule. In this case, the loading vector corresponding to the field σ is a limit load Q_{lim} of the mechanical system. It can be proved that the admissible loading vectors Q, i.e., corresponding to an admissible field σ, belongs to a convex set K whose boundary ∂K is the locus of the limit loads Q_{lim}. The vector q complies with normality to ∂K, i.e. the maximum dissipation principle is verified in terms of Q and q. However, solving the LA problem by the determination of the above mentioned pair (σ, u) is rarely possible; fortunately, the solution can be bracketed by using the so-called lower and upper bound methods of LA, more precisely the following static and kinematic approaches.

2.2 The Classic Static and Kinematic Approach of LA

The main goal of limit analysis is thus the determination of ∂K which corresponds to the searched plasticity criterion in the present study. Classically, the limit loads can be found or approached using two dual optimization methods.

The first one is the static method which is in terms of stresses and leads to a lower bound of the admissible loads. The final problem to be solved reads:

$$Q_{lim} = \left(Q_1^d, \ldots, \lambda_0 Q_i^d, \ldots, Q_n^d\right); \tag{10a}$$

$$\lambda_0 = \max\left\{\lambda,\, Q(\sigma) = \left(Q_1^d, \ldots, \lambda Q_i^d, \ldots, Q_n^d\right)\right\} \tag{10b}$$

where the stress tensors σ are admissible, and Q_d is a fixed admissible loading vector. Relations (10a), (10b) hold when all admissible fields σ can be taken into account, which is not the case in general. Then, by varying the direction of Q_d, a set of admissible Q, located near or on ∂K, are obtained: the smallest convex envelope of the corresponding points in K is an inner approach of the boundary ∂K, i.e. a lower bound to the exact macroscopic criterion investigated in the following.

The second method, involving only the displacement velocities as variables, is the classic kinematic (or upper bound) method. Let us assume that the velocity field u is q^d-admissible, i.e., u is admissible and verify $q(u) = q^d$, where q^d is a fixed value of q. This kinematic approach of LA consists in obtaining the planes orthogonal to the vectors q_d and tangent to ∂K by solving the following minimization problem:

$$Q \cdot q^d = \min_{u \ q^d\text{-admissible}} \left(\int_V \pi_{vol}\big(d(u)\big) dV + \int_{S_{disc}} \pi_{disc}\big([u]\big) dS = P_{diss}(u) \right), \quad (11)$$

for various values of q^d. Therefore, the classic method needs the analytical expressions of the unit dissipated powers $\pi_{vol}(d)$ and $\pi_{disc}([u])$. As it can be seen in (7), (8), some difficulties may arise when a non-linear optimization algorithm is used which needs Jacobian and Hessian matrices.

In fact, here also, relation (11) holds when all admissible fields u can be considered, which is rarely possible. In practice, a set of planes exterior or tangent to ∂K is obtained: the domain defined by the intersection of the corresponding half spaces constitutes an outer approach of the boundary ∂K, i.e. an upper bound to the exact macroscopic criterion.

2.3 The Mixed Kinematic Approach of LA

On the other hand, a so-called mixed kinematic formulation was pioneered by Anderheggen and Knopfel [2] in the continuous case and materials with linearized yield criteria. This formulation needs only the plasticity criterion as characteristic data of the material, here the analytic yield functions (1) and (4), and the above mentioned singularities of the dissipated powers (7) and (8) are then bypassed. Various extensions of the existing mixed algorithms to the discontinuous velocity case (see also [11]) were successfully experienced in the references [18, 22] for structural plane strain problems with von Mises and Gurson homogeneous materials and in [24] for the hollow spheroid problem with an anisotropic Hill matrix.

These formulations are here extended to the 3D-case and for a pressure-dependent matrix obeying the Mises-Schleicher yield condition; up to our knowledge, it is the first time that the LA numerical techniques are applied to such problems. This lack in the literature is probably due to the need of a specific large scale non linear optimization code if the problem is not cast into a rotated quadratic cone programming one as here.

Let us now consider a KA virtual velocity field u. The virtual power principle (VPP) states that the stress tensor fields σ and the load vector Q are in equilibrium if, *for any KA* u, Eq. (9) is verified. The mixed formulation of [18] and [23] can be modified as:

$$\max_{Q,\sigma,\sigma'} F = Q \cdot q_d \tag{12a}$$

$$\text{s.t.} \int_V \sigma : d\,dV + \int_{S_d} \left(\sigma' \cdot n\right) \cdot [u] dS = Q \cdot q(u) \quad \forall K\,Au, \tag{12b}$$

$$f(\sigma) \leq 0, \quad f\left(\sigma'\right) \leq 0, \tag{12c}$$

where σ is the stress tensor inside the 3D finite elements, and σ' the stress tensor specific to the discontinuity surfaces whose set is denoted S_d.

The previous formulation gives the exact solution if any velocity and stress fields could be taken into account. This is not always the case when a discretization of the mechanical system in finite elements is considered, giving in fact only estimates of the limit loads. Then, to preserve the rigorous kinematic (or upper bound) character of the final result, we will need to modify the numerical implementation of the virtual power principle (12b) on the basis of convexity properties when taking into account the contribution of the discontinuities. In this study, the finite element formulations of both problems (10a), (10b) and (12a)–(12c) are solved using the specific method briefly presented in the following section.

2.4 Summary of the Second Order Conic Programming Method (SOCP)

Let us first indicate that conic programming is a recent and very active research subdomain of convex optimization. For more details the reader is, for example, referred to [29]. Let us consider now the convex programming problems with linear objective function whose convex constraints can be written as $x \in \mathscr{C}$, where x is the variable vector and $\mathscr{C}$ a non empty convex *cone*. Since conic programming is a subset of nonlinear convex programming and a generalization of linear programming, the optimization problem to be solved reads:

$$\begin{aligned} &\min\ c^T x \\ &\text{s.t.}\quad Ax = b, \\ &\qquad x \in \mathscr{C} \end{aligned} \tag{13}$$

with $A \in \mathbb{R}^{m \times n}$, $c, x \in \mathbb{R}^n$, $b \in \mathbb{R}^m$. One of the specific features of the conic programming codes is to solve the problems where $\mathscr{C}$ is defined by a product of the following cones $\mathscr{C}^{n+2}$:

$$\mathscr{C}^{n+2} = \left\{ x \in \mathbb{R}^{n+2} \;\middle|\; \sum_{j=1}^{n} x_j^2 \leq 2x_{n+1}x_{n+2} \right\}, \quad x_{n+1} \geq 0,\ x_{n+2} \geq 0. \tag{14}$$

With the cone (14) the resulting optimization problem is called *rotated quadratic cone programming problem*. Among the existing commercial codes, the most efficient is the code MOSEK, developed by E. Andersen [16], which allows to solve very

large scale optimization problems. Its applications in mechanics began about ten years ago, but always for solving classic limit analysis problems which involves von Mises or Drucker-Prager criterion where $\mathscr{C}$ is defined by a product of the Lorentz cones $\mathscr{L}^{n+1}$:

$$\mathscr{L}^{n+1} = \left\{ x \in \mathbb{R}^{n+1} \;\middle|\; \left(\sum_{j=1}^{n} x_j^2 \right)^{\frac{1}{2}} \leq x_{n+1} \right\}. \tag{15}$$

3 The Mises-Schleicher Hollow Sphere Model

3.1 Statement of the Mechanical Problem

Let us consider as elementary cell a sphere cavity of radius a embedded in a concentric sphere cell of radius b (see Fig. 1). The solid matrix is assumed to be isotropic, homogeneous, and obeys the Mises-Schleicher yield condition. We consider now the mechanical micro-macro problem and denote by Σ and E the macroscopic stress and strain rate symmetric tensors, respectively. These quantities are defined by averaging their microscopic counterparts over the cell of volume V. Under the uniform strain rate boundary conditions allowing the macro-homogeneity Hill-Mandel lemma to be verified (i.e. $u_i = E_{ij} x_j$ on the external boundary) the power $P_{ext} = \int_{\partial V} \sigma_{ij} n_j u_i dS$ of the external loads leads to:

$$P_{ext} = V \Sigma_{ij} E_{ij}. \tag{16}$$

From (16), the p components Q_i of the loading vector Q (see Sect. 2.1) can be defined as the six components of the tensor Σ, and the q_i as the corresponding components of E. In fact, depending on the results we are searching for, more relevant definitions of the Q and q vectors can be chosen. Here, the LA loading parameters and their associated generalized velocities, such that (16) remains verified, are chosen as follows:

$$Q_1 = \Sigma_m = \frac{\mathrm{tr}(\Sigma)}{3}; \qquad Q_2 = \frac{\Sigma_{xx} + \Sigma_{yy}}{2} - \Sigma_{zz}; \tag{17}$$

$$Q_3 = \frac{\sqrt{3}}{2}(\Sigma_{xx} - \Sigma_{yy}); \qquad Q_4 = \Sigma_{yz}; \qquad Q_5 = \Sigma_{zx}; \qquad Q_6 = \Sigma_{xy}; \tag{18}$$

$$q_1 = \mathrm{tr}(E); \qquad q_2 = \frac{2}{3}\left(\frac{E_{xx} + E_{yy}}{2} - E_{zz} \right); \tag{19}$$

$$q_3 = \frac{1}{\sqrt{3}}(E_{xx} - E_{yy}); \qquad q_4 = 2E_{yz}; \qquad q_5 = 2E_{zx}; \qquad q_6 = 2E_{xy}. \tag{20}$$

From these definitions, the external power P_{ext} here reads:

$$P_{ext} = V Q \cdot q. \tag{21}$$

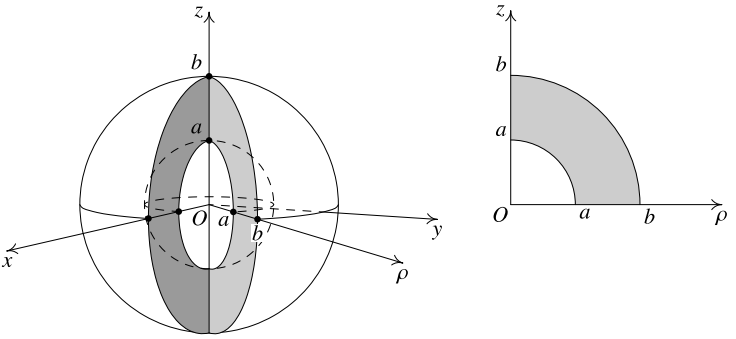

Fig. 1 The hollow sphere model

The stress components represent the loading vector Q in terms of LA and the corresponding macroscopic strain rates define the associated generalized velocity vector q of Sect. 2, with $p = 6$. The locus ∂K corresponds then to the investigated macroscopic criterion, further denoted $g^*(Q)$, of the porous material.

To compare with available analytical results, we search for the projection of $g^*(Q)$ on the (Σ_m, Q_2) plane by optimizing Q_2 for fixed average stresses Σ_m, the other stress components defined in (18) being free. Then $\frac{\partial g^*}{\partial Q_i} = 0 = q_i$ for $i \geq 4$, and $\frac{\partial g^*}{\partial Q_3} = 0 = q_3$ since the macroscopic material complies with the normality rule in terms of q and Q relatively to g^*. As a final result, loadings can be restricted to the principal macroscopic strain rates E (as well as Σ from the macroscopic isotropy) with $q_3 = 0 = E_{xx} - E_{yy}$. Moreover, from the isotropy of the macroscopic material, we also impose, although this is not mandatory, $\Sigma_{xx} - \Sigma_{yy} = 0 = Q_3$. Indeed, as expected, when non imposed *a priori*, the axisymmetry of loading is always verified in the optimal solutions, giving by the way a good control of the mesh quality. Note that the macroscopic equivalent stress Σ_{eq} is, in the present case, linked to Q_2 by:

$$\Sigma_{eq}^2 = \frac{3}{2}\Sigma_d : \Sigma_d = Q_2^2 + Q_3^2 = Q_2^2 = (\Sigma_{xx} - \Sigma_{zz})^2, \tag{22}$$

where Σ_d is the deviatoric part of Σ.

Let us remark that Σ_{eq}, even for axisymmetric loadings, has not the status of a loading parameter $Q_i(\sigma)$ as they are defined in Sect. 2; hence it cannot be used as it is when using the LA methods. Moreover, it is worth noting that, in the present problem, the optimal lower and upper bounds presented in terms of (Q_1, Q_2) are also bounds for the fully 3D loading case, since the resulting axisymmetric loading is also a 3D loading. This is not always the case when the results are presented in terms of (Σ_{eq}, Σ_m), using $\Sigma_{eq} = |Q_2|$ from (22) since Q_3 is zero. For example, the optimal positive and negative Q_2 of the real macroscopic criterion, for the same fixed $Q_1 = \Sigma_m$, are slightly different in absolute value (except on the axis as expected), with a maximum of 2 % in the present tests, as shown in [31] for the porous von Mises material.

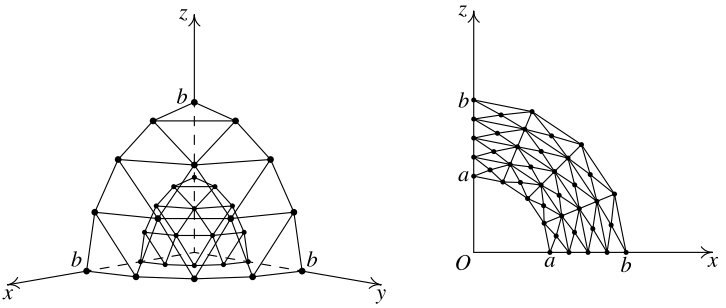

Fig. 2 General view and Oxz plane of a 896-tetrahedron mesh ($f = 0.1$)

3.2 The Finite Element Discretization

First is summarized the meshing technique adapted from the one presented in [32], resulting in a common discretization for the static and kinematic codes. From the above mentioned discussion, one eighth of the hollow spheroid is meshed into tetrahedral elements as shown in Fig. 2. This mesh respects the symmetries of the problem since the coordinate planes are equivalent concerning the distribution of elements, giving rise to a well-posed numerical problem. Each triangle of a polyhedral surface n is the top basis of a prism whose the bottom basis is the corresponding triangle of the surface $n - 1$, and so on until the cavity boundary. Each prism is divided into two tetrahedrons and three pyramids and each pyramid is divided into four tetrahedrons. Hence, each prism is meshed using 14 tetrahedral elements. For example the mesh of Fig. 2 involves 4 concentric layers of 4×4 prisms each, resulting finally in 896 tetrahedrons.

Since the FEM "nodal" stress or velocity variables are located at each *apex* of the tetrahedrons (and not at the *nodes* of usual FEM meshes), discontinuities in terms of stress or velocity are allowed across any element side; this feature has been proved to be crucial in the static approach (see [17, 20] and for the kinematic one [1]). For example, in the von Mises matrix case, if we consider continuous FEM fields (i.e. without any inter-element discontinuity) in the present 3D-model, no feasible solution is found under a isotropic (or hydrostatic) loading. These discontinuity sides are automatically detected by searching for the tetrahedron sides having their apices located at the same points; a special care is paid to verify the coherence of the normal n (defined from the description of the side apices) with the description of the discontinuities, taking into account that tensile normal stresses are positively counted (see Fig. 3). This point is important in the kinematic case since the velocity discontinuity must have the same direction as the outer normal to the plasticity criterion in the Mohr plane.

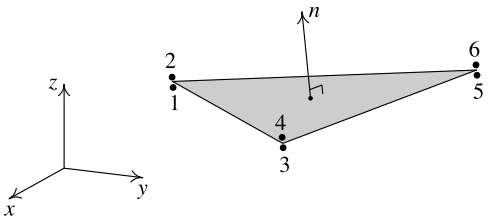

Fig. 3 A typical kinematic discontinuity side: $[u_i] = u_2 - u_1$, $[u_j] = u_4 - u_3$, $[u_m] = u_6 - u_5$

3.3 Implementation of the Static Method

In this subsection we first explicit the Mises-Schleicher criterion; then, we present the static approach implementation. In a (x, y, z) reference frame, the Mises-Schleicher criterion (1) reads:

$$\left(\frac{\sigma_{xx}+\sigma_{yy}}{2}-\sigma_{zz}\right)^2+\frac{3}{4}(\sigma_{xx}-\sigma_{yy})^2+3\left(\sigma_{yz}^2+\sigma_{zx}^2+\sigma_{xy}^2\right)$$
$$\leq \sigma_0\left(\sigma_0-\alpha(\sigma_{xx}+\sigma_{yy}+\sigma_{zz})\right). \tag{23}$$

After an obvious change of variables, criterion (23) can be written as a rotated quadratic cone constraint (14) in the form required by the optimizer MOSEK, i.e.:

$$\sum_{j=1}^{5} x_j^2 \leq 2x_6x_7. \tag{24}$$

Concerning the numerical implementation of the static approach, the local stress field is chosen as linearly varying with x, y, z in each tetrahedral element, and represented by a 6-component tensor σ for *each vertex* of this tetrahedral element. Consequently, this stress field can be discontinuous across any element boundary. Finally, to reduce the size of the constraint matrix of the numerical problem, a change of variables $\sigma \rightarrow (x_0, x_1, \ldots, x_5)$ is performed, where $x_0 = \mathrm{tr}\sigma$ and x_1 to x_5 defined from (24), so that only the definitions of $x_6 = \sigma_0/2$ and $x_7 = \sigma_0 - \alpha\mathrm{tr}(\sigma)$ are needed as new constraints (and new auxiliary variables) for each tetrahedron vertex.

To get a statically and plastically admissible microscopic stress field, the following conditions are implemented in the final form of a matrix of linear equality constraints:

- Definition of the macroscopic stress components Σ_{xx}, Σ_{yy}, Σ_{zz} as averages of the corresponding microscopic ones i.e., three linear conditions.
- Definition of $Q_1 = \Sigma_m$, Q_2, Q_3 as functions of the previous ones, i.e., three linear conditions.
- In each element, from the linearity of the stress variation, the equilibrium equations, $\sigma_{ij,j} = 0$, generate three linear conditions.
- Continuity conditions: the stress vector is continuous across every discontinuity surface; each discontinuity triangle generates nine linear conditions.

- Boundary conditions: on the triangles belonging to the cavity boundary, the components of the stress vector $T_i = \sigma_{ij} n_j$ are null at each apex of each triangle (whose normal is n), here also generating nine linear conditions per triangle.
- Symmetry conditions: the microscopic tangential stresses are null at the triangle apices of the coordinate planes, i.e., six linear conditions for each triangle of these planes.

To enforce the stress field to be plastically admissible, the criterion (23) is imposed at each apex of the tetrahedron; hence, due to its convexity, the criterion is fulfilled anywhere in the element. For each tetrahedron the four conic inequalities are directly handled by MOSEK by indicating the names of the variables x_j involved in (24).

Concerning the functional to be optimized, Σ_m is given successive desired values and Q_2 is minimized; when Σ_m is close to its maximum value, Q_2 is fixed and Σ_m is optimized for better convergence of the optimization process. The final result is a rotated quadratic cone programming problem, which is one of the features of MOSEK; the optimal solution gives a rigorous lower bound to the exact solution of the FEM model; this lower bound character is systematically verified by a post-analysis of the optimal stress field given by the optimizer. It is worth noting that, in all tests, the best values of Σ_{eq}, for fixed Σ_m, are obtained for negative Q_2, i.e. by minimizing Q_2 in fact. This point proves here also a slight influence of the third stress invariant of the macroscopic stress tensor, as in [31].

3.4 Implementation of the Mixed Kinematic Method

As said yet, the mesh is elaborated as in the static case. First, we examine the contribution of the continuous velocity fields to the VPP expression (9); the role of inter-element discontinuities will be discussed in the next subsection.

3.4.1 Contribution of the Element Velocity Fields

A three-component nodal vector $\{u\}$ is located at each apex of the tetrahedron, and the velocity u is assumed to vary linearly, giving rise to a constant strain rate $\{d\}$ in the element. To the global vector of these velocities are added q_1, q_2, q_3 in order to form the final virtual vector $\{u\}$. Then, a single stress tensor $\{\sigma\}$ is assigned at each tetrahedron. Thus, from its definition, the external power reads:

$$P_{ext} = Vq \cdot Q = V\{q\}^T\{Q\} = \{u\}^T V[\beta]\{Q\} \tag{25}$$

where $\{q\} = [\beta]^T\{u\}$.

Inside the element k, the strain rate $\{d\}$ is defined by the classic equation:

$$\{d\}_k = [B]_k\left\{u^n\right\}, \tag{26}$$

where the vector $\{u^n\}$ collects the twelve degrees of freedom of the element. Then the VPP reads:

$$\{u\}^T V[\beta]\{Q\} = \sum_k V_k \{d\}_k^T \{\sigma\} \quad \forall \{u\}\ KA, \tag{27}$$

where V_k denotes the volume of the tetrahedron k. Using Eq. (26), and after the assembly of the elements, the relationship (27) gives rise to the following variational system:

$$\{u\}^T \big[-[\alpha]\{\sigma\} + V[\beta]\{Q\}\big] = 0 \quad \forall \{u\}\ KA, \tag{28}$$

where the matrix $[\alpha]$ results from the assembly of the submatrices $[\alpha] = V_k[B^T]$ calculated for each element k in (27).

3.4.2 Contribution of the Velocity Discontinuities

According to [26], a discontinuity surface element (of normal n) can be assimilated to a thin zone where the appropriate static and kinematic variables are respectively the stress vector $T' = \sigma' \cdot n$ and the velocity jump vector $[u]$ which are associated by the normality law relatively to the $f_{nt}(T')$ criterion, or, equivalently (see [26]), where the corresponding σ' and $d' = [u_n]n \otimes n + \frac{1}{2}[u_t](n \otimes t + t \otimes n)$ can be associated relatively to $f(\sigma')$.

The second left hand side term of (12b) becomes the dissipated power $\pi_{disc}([u])$ when the optimal solution is reached (see [18, 23]), so we can use the convexity of π_{disc} since the velocity jump $[u]$ varies linearly along the discontinuity side. Hence an auxiliary stress tensor σ' is assigned at each apex i, j, m of the triangular discontinuity side S_{ijm}, and the integral on this side can be upper bounded by writing:

$$\begin{aligned} &\int_{S_{ijm}} \big(\sigma' \cdot n\big) \cdot [u] dS \\ &\quad \le A_{ijm}\Big(\big\{[u]\big\}_i^T \big[\sigma_i'\big]\{n\} + \big\{[u]\big\}_j^T \big[\sigma_j'\big]\{n\} + \big\{[u]\big\}_m^T \big[\sigma_m'\big]\{n\}\Big)/3, \end{aligned} \tag{29}$$

where A_{ijm} is the area of S_{ijm} whose the normal is n. Using these bounds gives rise to a matrix $[\alpha']$ in an analogous manner than in the previous subsection.

Finally the resulting numerical form of the mixed problem (12a)–(12c) is the following:

$$\text{Max } \{q_d\}^T \{Q\} \tag{30a}$$

$$\text{s.t.} \quad -[\alpha]\{\sigma\} - \big[\alpha'\big]\big\{\sigma'\big\} + V[\beta]\{Q\} = 0, \tag{30b}$$

$$f(\sigma) \le 0; \qquad f\big(\sigma'\big) \le 0 \tag{30c}$$

$$+\text{KA conditions.} \tag{30d}$$

At this stage, it is worth recalling that the optimal velocities components are the values of the dual variables associated to the rows of the final matrix $[-\alpha, -\alpha']$, which are available in the optimal solution given by the code MOSEK, or the interior point optimizer of [19]. Note also that there is no restriction to the allocated stress tensors, except the verification of the criterion; then, for any non-zero velocity field (and the corresponding strain rates and velocity jumps) an associated PA stress tensor can be found. Consequently, from Hill's maximum work principle, the upper bound character is preserved with the above selected formulation. Here also, the optimal solutions are post-analyzed by using the Mises-Schleicher results of Sect. 2.1.

3.4.3 Formulation of the KA Conditions

From the variational formulation (28) leading to the final problem (30a)–(30d), let us define three supplementary lines (constraints) whose associated virtual variables are E_{xx}, E_{yy}, E_{zz} (and three columns for the associated macroscopic stresses), so that the $u_i = E_{ij}x_j$ conditions on the boundary here reads $u_x = E_{xx}x$, $u_y = E_{yy}y$, $u_z = E_{zz}z$. Hence, for example for the first relation, in an additional column (located after the real variables) we initialize to 1 and $-x$ the components of the column corresponding to the virtual variable u_x and to the virtual variable E_{xx}, respectively. Since this additional column does not appear in the functional, the desired relation will be verified in the optimal solution, as it can be verified from the Karush-Kuhn-Tucker optimality conditions. When, as here, the chosen kinematic parameters q_i are an invertible combination of E_{xx}, E_{yy}, E_{zz} (represented by a non-singular square matrix A, for example), the above coefficients x, y, z are dispatched on the three additional lines (associated now to the q_i), according to the inverse of A. A similar technique is used to impose the null symmetry values to the required velocity components of the planes $x = 0$, $y = 0$ and $z = 0$.

This original technique gives rise to a better conditioning of the final matrix and avoids to have to renumber the rows when using the condensation technique of [23].

4 Analytical Yield Criteria of Porous Materials with Mises-Schleicher Matrix

As previously mentioned, Lee and Oung [13] studied ductile porous media with a Mises-Schleicher matrix by performing limit-analysis of a hollow sphere. Durban et al. [5] investigated the same problem by means of a simple statically determined procedure. More recently, Monchiet and Kondo [15] derived exact solutions for isotropic loadings. In this section, we briefly recall the analytical yield criteria of [13] and [5] that will be assessed; the porosity is denoted f.

Indeed, by studying the hollow sphere problem in a manner analogous to that of Gurson (for the von Mises matrix case), Lee and Oung found the following upper

bound to the real criterion:

$$\Sigma_{eq}^2 + \frac{f}{4}(3\Sigma_m)^2 + 3\alpha\sigma_0(1-f)\Sigma_m - (1-f)^2\sigma_0^2 = 0. \tag{31}$$

Then, they proposed the following approximate criterion:

$$\left(\frac{\Sigma_{eq}}{\sigma_0}\right)^2 + 2f\cosh\left(\frac{3\Sigma_m}{2\sigma_0}\right) + 3\alpha(1-f)\frac{\sigma_m}{\sigma_0} - \left(1+f^2\right) = 0. \tag{32}$$

By following a practical procedure consisting in expanding yield function in powers of porosity ratio f, Durban et al. obtained a macroscopic porous Mises-Schleicher criterion whose parameters are determined by taking advantage of the static solutions of the hollow sphere model under hydrostatic loading; the resulting approximate expression reads:

$$\left(\frac{\Sigma_{eq}}{\sigma_0}\right)^2 + 2f\left(1 + G\sqrt{1+\alpha^2}\cosh\frac{G}{\alpha}\right) - 2\alpha f G\sinh\frac{G}{\alpha} + 3\alpha\frac{\Sigma_m}{\sigma_0} - \left(1+f^2\right) = 0, \tag{33a}$$

where

$$G = \sqrt{1 - 3\alpha\frac{\Sigma_m}{\sigma_0} + \alpha^2} - \sqrt{1+\alpha^2}. \tag{33b}$$

As already noted by the authors, (32) and (33a), (33b) reduce to the Gurson expression when α tends to zero, while (31) does not meet this expected property.

5 Numerical Tests

5.1 Comparison with Exact Results for Isotropic Loadings

Monchiet and Kondo [15] have confirmed that the Σ_m solutions of Lee and Oung [13] (obtained by limit equilibrium considerations) are exact LA solutions by exhibiting associated admissible stress and velocity fields, following an approach already used by Thoré et al. [31] for Drucker-Prager and Coulomb matrices. These exact solutions are considered here for a first validation of the numerical bounds that we derived by means of the above mentioned static and (mixed) kinematic codes. Tables 1 and 2 give the corresponding values for isotropic tensile and compressive loadings, respectively; six decimal are reported.

The analytical values were obtained by solving with MATLAB the following equations given in [13, 15] for $\Sigma_m \geq 0$:

$$\ln\left[\frac{-\alpha + \sqrt{1+\alpha^2 - 3\alpha\Sigma_m/\sigma_0}}{-\alpha + \sqrt{1+\alpha^2}]}\right] + \frac{1}{\alpha}\sqrt{1+\alpha^2 - 3\alpha\Sigma_m/\sigma_0} - \frac{1}{\alpha}\sqrt{1+\alpha^2} = \ln f, \tag{34}$$

Table 1 Comparison of the present bounds to exact solution Σ_m/σ_0 for isotropic *tensile* loadings

α	0	0.2	0.4	0.6	0.8	1.0
3D-kine	1.537747	0.985438	0.651860	0.468268	0.361183	0.292810
[15]	1.535057	0.984299	0.651539	0.468153	0.361131	0.292782
3D-stat	1.526208	0.981093	0.650016	0.467134	0.360237	0.292016

Table 2 Comparison of the present bounds to exact solution Σ_m/σ_0 for isotropic *compressive* loadings

α	0	0.2	0.4	0.6	0.8	1.0
3D-kine	−1.537747	−2.291437	−3.182374	−4.159597	−5.190714	−6.256271
[15]	−1.535057	−2.285464	−3.172361	−4.144888	−5.170962	−6.231292
3D-stat	−1.525985	−2.269164	−3.142363	−4.101975	−5.113655	−6.109577

and for $\Sigma_m \leq 0$:

$$\ln\left[\frac{\alpha+\sqrt{1+\alpha^2-3\alpha\,\Sigma_m/\sigma_0}}{\alpha+\sqrt{1+\alpha^2]}}\right]-\frac{1}{\alpha}\sqrt{1+\alpha^2-3\alpha\,\Sigma_m/\sigma_0}+\frac{1}{\alpha}\sqrt{1+\alpha^2}=\ln f. \tag{35}$$

The numerical bounds are mainly obtained with a $14\times14\times14$ prism mesh resulting in 990, 587 linear constraints, 264, 796 conic constraints, and 2, 127, 191 variables for the mixed kinematic code; the problem is solved in about 700 seconds of CPU time (with one thread) on an Apple iMac-i7 with 16 gigabytes of RAM. The static problem with that mesh (1, 117, 600 linear and 153, 664 conic constraints with 1, 229, 319 variables) needs about 1100 seconds of CPU time.

From these tests, it can be firstly noted that the exact solution is always located between the numerical bounds, even when these bounds are very close to each other. Secondly, due to the remarkable efficiency of MOSEK, the solving CPU times are very low, given the large scale of the generated optimization problems. Finally, regarding the high performance in terms of bounds, and these first validations of the proposed numerical procedure, it should be noted that the presence of discontinuities everywhere plays a crucial role in both static and kinematic results.

In the following tests, owing to the very small difference between positive and negative optimal values of Q_2, for the same fixed $Q_1=\Sigma_m$, we will present for conciseness only the results for the negative Q_2, which are here a bit larger than the positive ones in absolute value. As it will be seen, this has no consequence about assessing the available criteria.

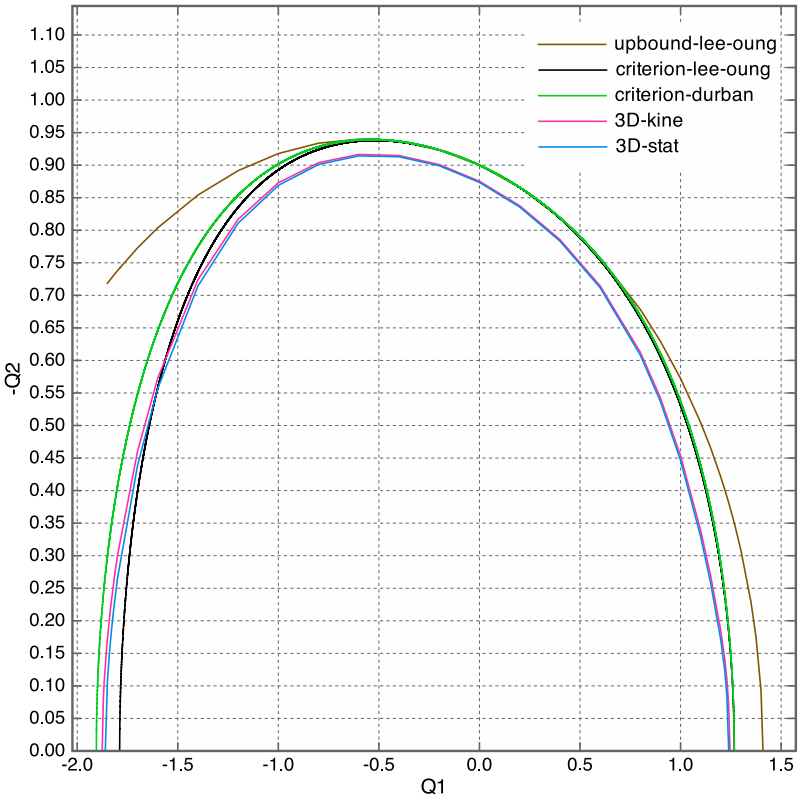

Fig. 4 Present bounds versus [13] and [5] results for $\sigma_C/\sigma_T = 1.1$, $f = 0.1$ ($\sigma_0 = 1$)

5.2 Comparison with Lee-Oung [13] and Durban [5] Results

In [13] the authors have considered several cases of σ_C/σ_T, with more details for $\sigma_C/\sigma_T = 1.1$ corresponding to $\alpha = 0.1/\sqrt{1.1}$. Therefore we have investigated this case, and $\sigma_C/\sigma_T = 2$ which corresponds to $\alpha = 1/\sqrt{2}$; the porosity is set to 0.1 and 0.01.

5.2.1 Case $\sigma_C/\sigma_T = 1.1$

In Fig. 4 are represented the present static and kinematic bounds together with the results of Lee and Oung, and Durban et al., for $\sigma_c/\sigma_T = 1.1$. It can be seen, first, that the numerical bounds are very close each other. As indicated by the authors themselves, the upper bound of Lee and Oung is clearly not efficient, particularly for high triaxiality loadings. The criterion of Lee and Oung and of Durban are close on a large part of the loading domain, but the Lee and Oung criterion violates the static bound for high compressive loadings. This confirmed the observation made

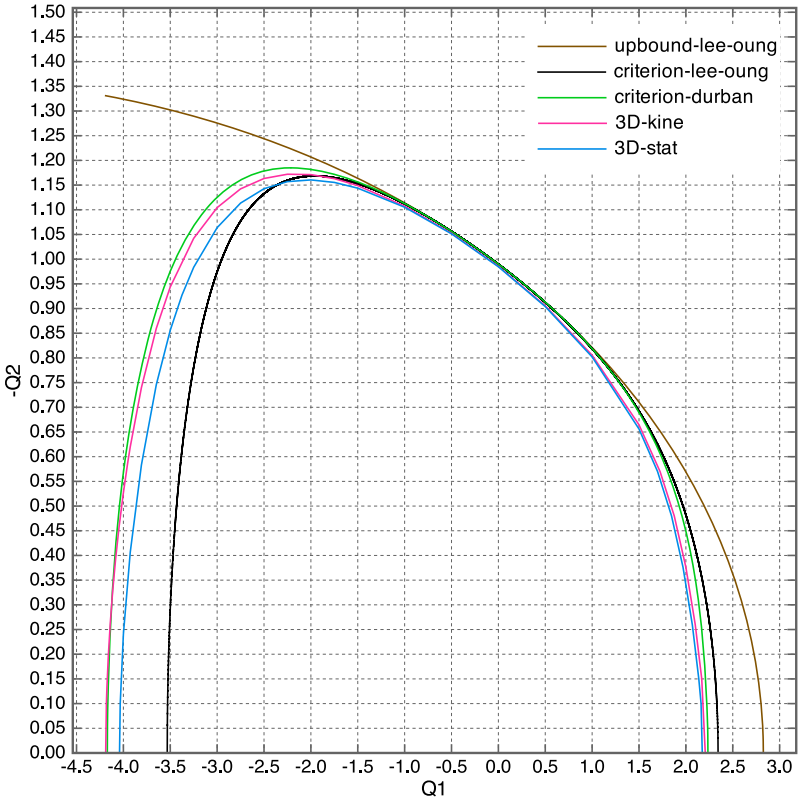

Fig. 5 Present bounds vs. [13] and [5] results for $\sigma_C/\sigma_T = 1.1$, $f = 0.01$ ($\sigma_0 = 1$)

by [15] on the poor performance of the Lee and Oung criterion when compressive hydrostatic loadings are considered.

For $f = 0.01$, from Fig. 5 the same remarks can be made, but the differences between both criteria are amplified as well as the violation of the static bound for the Lee and Oung criterion. At this stage, we could conclude that the Durban criterion can be selected.

5.2.2 Case $\sigma_C/\sigma_T = 2$

The results for $\sigma_c/\sigma_T = 2$ (strong asymmetry) are plotted in Figs. 6 and 7; it can be seen that the numerical static and kinematic bounds still remain close with a better performance for $f = 0.1$, more or less expected since the mesh is the same for both porosity cases. Curiously, the results present an inversion between the Lee and Oung upper bound and the Durban et al. criterion. This proves that, for high asymmetry ratio, the Lee and Oung criterion, as well as that proposed by Durban (even if this one does not violate the static bounds) cannot be considered relevant.

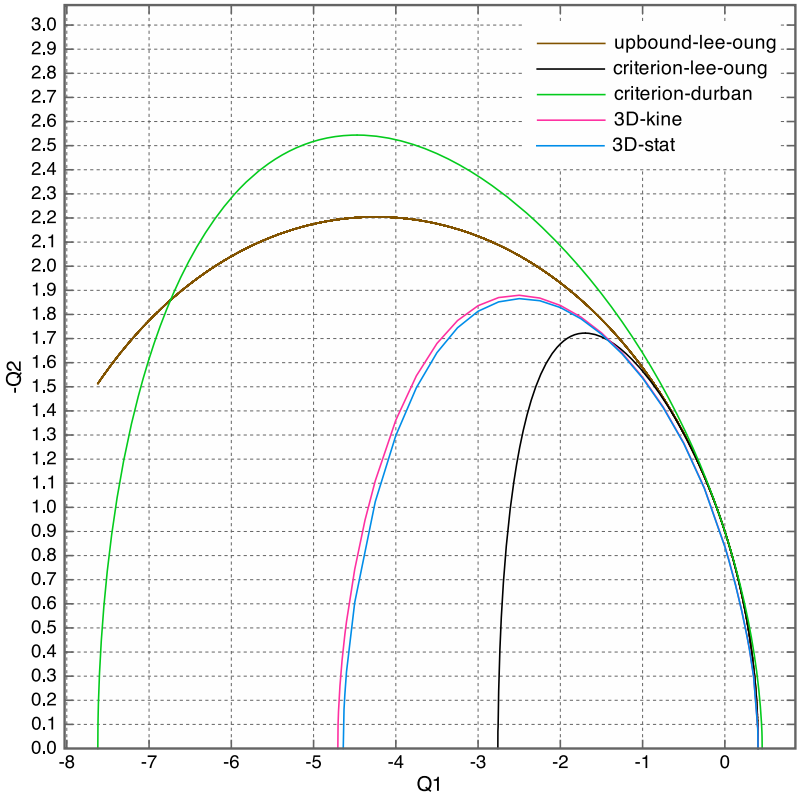

Fig. 6 Present bounds vs. [13] and [5] results for $\sigma_C/\sigma_T = 2$, $f = 0.1$ ($\sigma_0 = 1$)

6 Conclusion

In the present paper, we present original finite element formulations of the static and kinematic methods of Limit Analysis of a hollow sphere with a Mises-Schleicher matrix, both in the three-dimensional case. The resulting optimization problems are cast into the so-called rotated quadratic cone optimization, which are solved using the excellent commercial code MOSEK. The static and kinematic mixed codes appear very efficient in all tests, both in terms of computational speed and of accuracy of the solutions which were systematically verified by post-analysis. First, for isotropic loadings, the corresponding closed form solutions of Lee and Oung, confirmed as exact LA solutions by [15], allow to validate the present numerical bounds in this particular case. Then, the comparison with the upper bound and the criterion of Lee and Oung [13] confirms that both expressions are relevant for tensile and low compressive loadings, but not in highly compressive loading cases. Moreover, the Lee and Oung criterion noticeably violates the numerical static bounds when the tensile/compressive strength asymmetry is not small and for compressive loadings. This is not the case with the Durban [5] closed-form expression, but this criterion

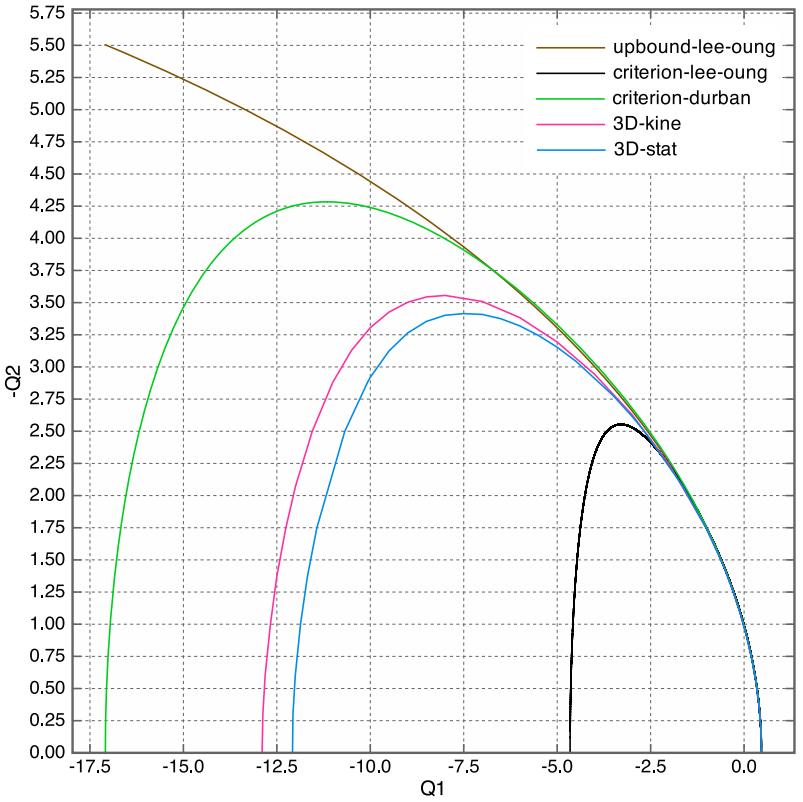

Fig. 7 Present bounds vs. [13] and [5] results for $\sigma_C/\sigma_T = 2$, $f = 0.01$ ($\sigma_0 = 1$)

strongly overestimates the real solution for compressive loadings when the above mentioned asymmetry is high. Finally, it can be concluded that the question of the determination of a satisfactory analytical criterion for a ductile porous medium with a Mises-Schleicher matrix still remains open.

References

1. Abdi R, Buhan PD, Pastor J (1994) Calculation of the critical height of a homogenized reinforced soil wall: a numerical approach. Int J Numer Anal Methods Geomech 18:485–505
2. Anderheggen E, Knopfel H (1972) Finite element limit analysis using linear programming. Int J Solids Struct 8:1413–1431
3. Aubertin M, Li L (1974) Yield locus studies of oriented polycarbonate: an anisotropic and pressure-dependent solid. Int J Mech Sci 16:789–799
4. Aubertin M, Li L (2004) A porosity-dependent inelastic criterion for engineering materials. Int J Plast 20:2179–2208
5. Durban D, Cohen T, Hollander Y (2010) Plastic response of porous solids with pressure sensitive matrix. Mech Res Commun 37:636–641

6. Francescato P, Pastor J, Riveill-Reydet B (2004) Ductile failure of cylindrically porous materials, part I: plane stress problem and experimental results. Eur J Mech A, Solids 23:181–190
7. Guo TF, Faleskog J, Shih CF (2008) Continuum modeling of a porous solid with pressure sensitive dilatant matrix. J Mech Phys Solids 56:2188–2212
8. Gurson AL (1977) Continuum theory of ductile rupture by void nucleation and growth, part I: yield criteria and flow rules for porous ductile media. J Eng Mater Technol 99:2–15
9. Jeong HY (2002) A new yield function and a hydrostatic stress-controlled model for porous solids with pressure-sensitive matrices. Int J Solids Struct 39:1385–1403
10. Kovrizhnykh AM (2004) Plane stress equations for the von Mises-Schleicher yield criterion. J Appl Mech Tech Phys 45:894–901
11. Krabbenhoft K, Lyamin A, Hijaj M, Sloan S (2005) A new discontinuous upper bound limit analysis formulation. Int J Numer Methods Eng 63:1069–1088
12. Leblond JB, Perrin G, Suquet P (1994) Exact results and approximate models for porous viscoplastic solids. Int J Plast 10:213–235
13. Lee JH, Oung J (2000) Yield functions and flow rules for porous pressure-dependent strain-hardening polymeric materials. J Appl Mech 67:288–297
14. Lubliner J (1990) Plasticity theory. McMillan, New York
15. Monchiet V, Kondo D (2012) Exact solution of a plastic hollow sphere with a Mises-Schleicher matrix. Int J Eng Sci 51:168–178
16. MOSEK ApS (2002) C/O Symbion Science Park, Fruebjergvej 3, Box 16, 2100 Copenhagen ϕ, Denmark
17. Pastor J (1978) Analyse limite : détermination numérique de solutions statiques complètes. Application au talus vertical. J Méc Appl 2:167–196
18. Pastor F (2007) Résolution par des méthodes de point intérieur de problèmes de programmation convexe posés par l'analyse limite. Thèse de doctorat, Facultés universitaires Notre-Dame de la Paix, Namur
19. Pastor F, Loute E (2005) Solving limit analysis problems: an interior-point method. Commun Numer Methods Eng 21(11):631–642
20. Pastor J, Turgeman S (1976) Mise en œuvre numérique des méthodes de l'analyse limite pour les matériaux de von Mises et de Coulomb standards en déformation plane. Mech Res Commun 3:469–474
21. Pastor J, Francescato P, Trillat M, Loute E, Rousselier G (2004) Ductile failure of cylindrically porous materials, part II: other cases of symmetry. Eur J Mech A, Solids 23:191–201
22. Pastor F, Loute E, Pastor J (2009) Limit analysis and convex programming: a decomposition approach of the kinematical mixed method. Int J Numer Methods Eng 78:254–274
23. Pastor F, Loute E, Pastor J, Trillat M (2009) Mixed method and convex optimization for limit analysis of homogeneous Gurson materials: a kinematical approach. Eur J Mech A, Solids 28:25–35
24. Pastor F, Pastor J, Kondo D (2012) Limit analysis of hollow sphere or spheroid with Hill orthotropic matrix. C R, Méc 340:120–129
25. Salençon J (1974) Théorie de la plasticité pour les applications à la mécanique des sols. Eyrolles, Paris
26. Salençon J (1983) Calcul à la rupture et analyse limite. Presses des Ponts et Chaussées, Paris
27. Schleicher F (1926) Der Spannungszustand an der Fließgrenze (Plastizitätsbedingung). Z Angew Math Mech 6:199–216
28. Stassi-d'Alia F (1961) Une fonction quadratique des tensions principales comme conditions de plasticité des corps solides. Bull RILEM 13:44–45
29. Tal AB, Nemirovsky A (2001) Lectures on modern convex optimization. SIAM, Philadelphia
30. Theocaris PS (1995) Failure criteria for isotropic bodies revisited. Eng Fract Mech 51:239–264

31. Thoré P, Pastor F, Pastor J (2011) Hollow sphere models, conic programming and third stress invariant. Eur J Mech A, Solids 30:63–71
32. Trillat M, Pastor J (2005) Limit analysis and Gurson's model. Eur J Mech A, Solids 24:800–819
33. Zhang H, Ramesh KT, Chin E (2008) A multiaxial constitutive model for metal matrix composites. J Mech Phys Solids 56:2972–2983

Limit Analysis: A Layered Approach for Composite Laminates

Aurora Angela Pisano, Paolo Fuschi, and Dario De Domenico

Abstract The present contribution summarizes the results of recent studies carried on by the authors in the last few years concerning the evaluation of the load bearing capacity of single- and multi-pin joints in composite orthotropic plates. The problem, tackled via limit analysis, employs a Tsai-Wu-type yield surface and a non standard treatment of limit analysis approach. Upper and lower bounds to the real peak load value are evaluated by two FE based numerical procedures predicting also the joint failure mode. The whole procedure is implemented at lamina level so taking into account some of the through thickness effects on the joint strength capabilities. A wide number of experimental findings, coming from laboratory tests on real prototypes and available in the relevant literature, is considered to validate, by comparison, the expounded methodology.

1 Premises and Main Assumptions

Limit analysis plays an eminent role among the theoretical and numerical methods aimed at predicting the load bearing capacity of structures or structural elements. It also becomes very effective and attractive for the design of many modern industrial prototypes often manufactured with materials whose constitutive behaviour does not have a well defined mathematical description. In composite laminates, for example, the available constitutive models are often affected by values of material parameters hardly identifiable via experimental tests so that, in such a context, results obtained via a step-by-step post-elastic analysis may be useless for applications of engineering interest. Nevertheless, even in those cases where the constitutive behavior is well

A.A. Pisano (✉) · P. Fuschi · D. De Domenico
Dept. PAU, University Mediterranea of Reggio Calabria, Via Melissari, 89124 Reggio Calabria, Italy
e-mail: aurora.pisano@unirc.it

P. Fuschi
e-mail: paolo.fuschi@unirc.it

D. De Domenico
e-mail: dario.dedomenico@unirc.it

K. Spiliopoulos, D. Weichert (eds.), *Direct Methods for Limit States in Structures and Materials*, DOI 10.1007/978-94-007-6827-7_2,

settled, limit analysis can be used as a preliminary/first design tool: once a good prototype is individuated for a specific problem, sophisticated post elastic FE analysis or experimental laboratory tests can be performed for a deeper and exhaustive understanding of its mechanical behaviour with a considerable saving of efforts either economic or time consuming.

The classical approaches of limit analysis rely upon mathematical programming procedures which have progressed significantly in recent years (see e.g. [15, 16, 19, 20, 35, 36, 40]). A number of contributions in this field (see e.g. [41] and references therein) adopt however a different approach whose basic assumption is that limit state solutions may be developed from sequences of elastic (linear) analyses easy to handle via any commercial finite element code. In this context a numerical FE-based approach has been recently proposed by the authors to a peculiar problem of orthotropic composite laminates, namely the evaluation of the load bearing capacity of pinned-joint composite plates with single- or multi-pin fastenings [24–27]. This is a topical problem in the composite realm as witnessed by the number of recent paper on the subject, more than 700 papers are listed in the work of Mackerle [21] which provides an interesting review of finite elements methods applied for the analysis of joints; remarkable reviews are also the ones given in [6, 10, 31, 37]. For design purposes, Researchers are mainly interested in determining the effects on joints failure strength and failure modes of some peculiar geometrical parameters such as: the ratios between hole-distance from the free plate edge to hole-diameter, or the one between the plate-width to hole-diameter or, also, the relative distances between fastener holes as well as their spatial distribution within the plate [2–4, 9, 12–14, 22].

The results of a research carried on in the last few years and concerning the analysis of mechanically fastened joints in multi layers composite plates are expounded in the following. Details, and deeper explanations are given in the papers [24–27] to which the Reader could refer for more information. In particular, two well known FE procedures have been rephrased: (i) the Linear Matching Method, conceived by Ponter and Carter [28], (see also [8]), has been used to compute an upper bound to the peak load multiplier; (ii) the Elastic Compensation Method, due to Mackenzie and Boyle [18], has been employed to evaluate a lower bound to the peak load multiplier. The former, considering a structure made by a fictitious linear viscous material with elastic parameters spatially varying, allows to construct a collapse mechanism and eventually to evaluate an upper bound to the peak load. The latter, grounding on a stress redistribution procedure pursued by a sequence of elastic analyses in which highly loaded regions are systematically weakened, produces an admissible stress field suitable for a lower bound evaluation.

The assumption of a Tsai-Wu-type yield surface for composite laminates [7, 34, 38, 39] allows one to locate stress states at which the material has exhausted its strength capabilities. The further assumption of a non-associate flow rule makes the whole methodology of general applicability following a nonstandard approach [17, 30]. Limit analysis is used indeed to evaluate the strength capability of the joint by evaluating upper and lower bounds bracketing the real peak load value.

The main novelty of the authors' recent studies hereafter summarized, is related either to the extension of the mentioned FE procedures in the realm of anisotropic

composites and, in general, non associative materials or, also, to their non trivial implementation at layer laminate level. The latter peculiarity reveals undoubtedly more burdensome computations but, as witnessed by the obtained results, allows to take into account the stacking sequence of the laminate. Some of the through-thickness effects depending on the number of the laminae the laminate is made with as well as the effects of fiber orientations within each lamina can indeed be handled with good accuracy. To this aim higher order shell-type multilayered finite elements have been used, performing all the relevant operations at the Gauss points of each element layer (lamina).

In order to verify the reliability of the proposed procedure, checking its ability of bracketing the real (experimentally detected) peak load, a considerable number of experimental tests at rupture, available in the literature [2, 12–14, 22], have been numerically reproduced. The possibility of localizing the collapse zone so predicting the related failure mode has been also investigated highlighting the potentialities of the layer by layer implementation. In conclusion, the proposed procedure seems to guarantee, at least for the studied problem, a great accuracy for different laminate lay-ups and different joint geometries establishing an effective design tool useful to avoid expensive trials on real prototypes.

2 Limit Analysis and Constitutive Assumptions

2.1 The Limit Analysis Problem

Following the kinematic theorem of the limit analysis, considering a body of volume V, for a given distribution of compatible strain rates $\dot{\varepsilon}_j$, say $\dot{\varepsilon}_j^c$, an upper bound to the (collapse) peak load multiplier is given by:

$$P_{UB} = \frac{\int_V \sigma_j^y \dot{\varepsilon}_j^c \mathrm{d}V}{\int_{\partial V_t} \bar{p}_i \dot{u}_i^c \mathrm{d}(\partial V)} \tag{1}$$

where: $\dot{\varepsilon}_j^c = \dot{\lambda}\partial f/\partial\sigma_j$ are the components of the outward normal to the yield surface $f(\sigma_j) = 0$ (with $\dot{\lambda} > 0$ scalar multiplier); P_{UB} denotes the upper bound load multiplier (for simplicity only surface forces, $\bar{p}_i$, acting on the external portion of the body ∂V_t, are considered); σ_j^y are the stresses at yield associated to the compatible strain rates $\dot{\varepsilon}_j^c$; $\dot{u}_i^c$ are the related displacement rates. The set $(\dot{\varepsilon}_j^c, \dot{u}_i^c)$ indeed defines a collapse mechanism.

On the other hand, the static theorem of limit analysis states that if at every point within V exists a stress field $\tilde{\sigma_j}$ which satisfies the condition $f(\tilde{\sigma_j}) \leq 0$ and in equilibrium with the applied load $P\bar{\mathbf{p}}$ for a certain value of P, say P_{LB}, then P_{LB} is a lower bound to the limit load multiplier.

Two remarks appear necessary to focus what will be expounded in the next sections.

Remark 1 For nonstandard materials, see e.g.: [17, 30, 32, 33], the Radenkovic's first and second theorems state that (after [17]): every value of the limit load for a body made of a nonstandard material is located between two fixed boundaries defined by the values of the limit loads for two corresponding standard materials. The hypothesis of a nonstandard constitutive behavior assumed next will then imply to search for an upper and a lower bound to the (collapse) peak load of the joint.

Remark 2 The two numerical procedures, expounded in Sects. 3 and 4, play two distinct roles as specified in the following. The Linear Matching Method (LMM) is naturally related to the kinematic approach of limit analysis being able to construct a compatible collapse mechanism. It then gives an upper bound, P_{UB}, to the peak load multiplier. The Elastic Compensation Method (ECM) is indeed strictly related to the concept of stress redistribution aimed at producing an admissible stress field. It is then related to the static approach of limit analysis furnishing a lower bound, P_{LB}, to the peak load multiplier.

2.2 Constitutive Assumptions

By hypothesis, the constitutive behaviour of the composite laminate obeys to a second-order tensor polynomial form of the Tsai-Wu failure criterion [39] having the following analytical form:

$$F_{11}\sigma_1^2 + F_{22}\sigma_2^2 + F_{66}\sigma_6^2 + 2F_{12}\sigma_1\sigma_2 + F_1\sigma_1 + F_2\sigma_2 = 1, \tag{2}$$

where:

$$\begin{aligned} F_1 &:= \frac{1}{X_t} + \frac{1}{X_c}; \qquad F_2 := \frac{1}{Y_t} + \frac{1}{Y_c}; \qquad F_{11} := -\frac{1}{X_t X_c}; \\ F_{22} &:= -\frac{1}{Y_t Y_c}; \qquad F_{66} := -\frac{1}{S^2}; \qquad F_{12} := -\frac{1}{2}\sqrt{F_{11}F_{22}}; \end{aligned} \tag{3}$$

with X_t, X_c the longitudinal tensile and compressive strengths respectively; Y_t, Y_c the transverse tensile and compressive strengths respectively and S the longitudinal shear strength; moreover, as usual for composite structures, 1 and 2 denote the principal directions of orthotropy in plane stress case while $\sigma_6 \equiv \tau_{12}$. In Eqs. (3) the compressive strengths X_c and Y_c have to be considered intrinsically negative. The quadratic form given by Eq. (2) defines an admissible stress states domain: points within the domain locate stress states pertaining to an orthotropic linear elastic behaviour of the material; points lying on the domain boundary locate stress states at which the material has exhausted its strength capabilities. The Tsai-Wu-type surface, in the quadratic form adopted allows one to apply the standard rules of transformation, invariance and symmetry, and locates an ellipsoid in the stress space which is assumed as yield surface for the orthotropic material considered. Moreover, the orthotropy of the composite laminates infers the general assumption of non associativity so, as noted above, the peak load values of the analyzed specimens will be located by the determination of upper and lower bounds.

Remark 3 On taking into account the previous Remark 1 and the strict convexity of the Tsai-Wu-type yield surface the postulated non associativity can be treated following the Radenkovic approach and, in this case, the assumed yield surface can itself play the double role of inner and outer surface.

3 The Linear Matching Method (LMM)

3.1 Fundamentals

An upper bound to the (collapse) peak load multiplier can be evaluated by the LMM which furnishes all the ingredients entering Eq. (1) namely: the kinematic fields $\dot{\varepsilon}_j^c, \dot{u}_i^c$, and the associated stresses at yield (with respect to the yield surface (2)), i.e. σ_j^y. To this aim an iterative procedure, involving a sequence of linear FE-based analyses, is performed on the structural element assumed as made of an orthotropic linear viscous *fictitious* material *with spatially varying moduli* and subjected to a distribution of *imposed initial stresses*. At each iteration, the fictitious moduli are then adjusted and the initial stresses are varied so that the computed fictitious linear stresses are brought on the yield surface at a fixed strain rate distribution. This allows one to define a collapse mechanism (strain and displacement rates $(\dot{\varepsilon}_j^c, \dot{u}_i^c)$), the related stresses at yield σ_j^y and eventually, by Eq. (1), allows to evaluate a P_{UB}. All the above can be geometrically interpreted as given in next subsection for a quick understanding.

3.2 Linear Matching Method and FE Procedure

The fundamental steps of the LMM are schematically shown in Fig. 1 where a *fictitious linear viscous solution*, computed at a generic Gauss point (GP) inside a generic layer of a generic finite element, is represented in the stress space $(\sigma_1, \sigma_2, \sigma_6)$. In particular, denoting with apex $^{(0)}$ the values of fictitious material parameters and initial stresses at iteration k, and with apex $^{(*)}$ those at iteration $k+1$, the fictitious solution computed at k is displayed by a stress point, located by the stress vector $\boldsymbol{\sigma}^e$, lying on the complementary dissipation rate equipotential surface $W[E_j^{(0)}, \nu_{12}^{(0)}, \bar{\sigma}_j^{(0)}] = \text{const}$ pertaining to the fictitious material. Such solution is also displayed, in terms of linear viscous strain rates, i.e. by the outward normal, $\dot{\varepsilon}_j^e$, to $W = \text{const}$ at σ_j^e. The related $\dot{u}_i^e$ being the compatible displacement rates. At iteration $k+1$, the material moduli and the initial stresses are varied (assigning them the starred values), in such a way that $\dot{\varepsilon}_j^e$ can be interpreted as $\dot{\varepsilon}_j^c$, the latter being the strain rate at collapse at the current GP. The above operation simply implies to find a (stress) point of assigned normal $(\dot{\varepsilon}_j^e = \dot{\varepsilon}_j^c)$ belonging either to the yield surface or to a "modified" complementary dissipation rate equipotential surface, say

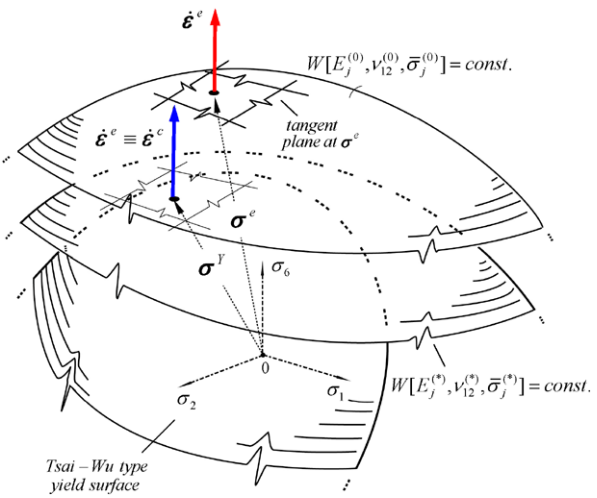

Fig. 1 Matching procedure at a GP in the FE mesh: $(\cdot)^{(0)}$ = values at iteration k; $(\cdot)^{(*)}$ = values at iteration $k+1$

$W[E_j^{(*)}, \nu_{12}^{(*)}, \bar{\sigma}_j^{(*)}] = \text{const}$, where the starred quantities define indeed the modified $W = \text{const}$ at $k+1$. The corresponding stresses, $\boldsymbol{\sigma}^Y$, are then "stresses at yield", the related displacement rates the "incipient displacements at collapse". This operation, which also explains the name of the method, the surface W matches the yield surface at a point of given normal, is performed at each GP of the FE mesh and obviously violates the global equilibrium conditions. The stresses at yield, evaluated by matching, do not satisfy equilibrium with the loads acting at iteration k; this essential condition is indeed assured at the end of an iterative process. To this concern, a sufficient condition for convergence is given in [29] and is not reported for brevity.

Moreover, grounding on the formal analogy between the linear viscous problem and the linear elastic problem (see e.g. [23]), the fictitious *linear viscous* solution (in rate form) can, in practice, be computed as a fictitious *linear elastic* solution (in finite form), W playing the role of complementary energy potential of the fictitious material. The FE analysis is then achievable as a linear elastic analysis by any commercial FE code.

4 The Elastic Compensation Method (ECM)

4.1 Fundamentals

A lower bound to the peak load multiplier can be evaluated via the ECM aimed at constructing an admissible stress field suitable for the evaluation of a P_{LB}. As the previous procedure, the ECM is also an iterative procedure involving sequences of linear elastic FE-based analyses in which *highly loaded regions* of the structure *are systematically weakened by reduction of the local modulus of elasticity*. Precisely,

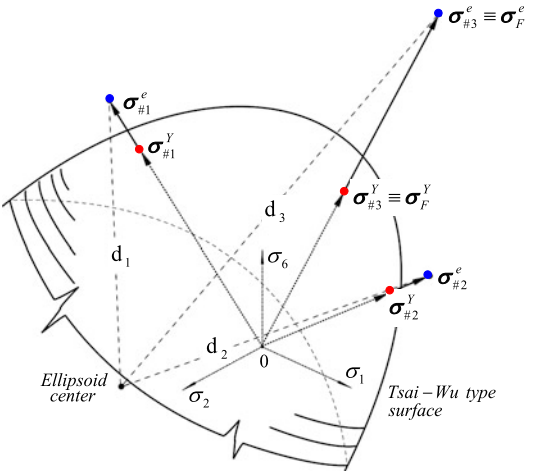

Fig. 2 ECM procedure at three generic layers belonging to elements # 1, #2 and #3 in the FE mesh

a sequence of linear elastic FE analyses is carried out in which, for a given load value, the elastic moduli are reduced within "critical regions" of the structure identified by the elements where the stresses attain values greater than the yield one. This allows one to define a *maximum admissible* stress value in the whole structure and for the given load. Increased values of loads are then considered in the subsequent sequences of analyses till further load increase do not allow the maximum stresses to be brought below yield by the reduction (or redistribution) procedure. A P_{LB} load multiplier can be easily evaluated at last admissible stress values attained for a maximum acting load in the spirit of the static approach of limit analysis.

4.2 Elastic Compensation Method and FE Procedure

Also in this case, the fundamental steps of the ECM are schematically shown. In Fig. 2 the solution pertaining to an elastic analysis carried on the structure for a given (arbitrary) fixed load level P_D is displayed in terms of elastic stress vectors evaluated at three generic layers of three generic FEs in the mesh. The latter, for simplicity, are denoted by elements #1, #2 and #3. In particular, with reference to the stress space $(\sigma_1, \sigma_2, \sigma_6)$, the value $\boldsymbol{\sigma}^e_{\#e}$ denotes the stress vector representing the average elastic stress computed within a layer of element #e (its components are simply the averaged values of the stress components measured at the GPs of the layer); $\boldsymbol{\sigma}^Y_{\#e}$ denotes the corresponding stress at yield (on the Tsai-Wu-type surface) measured on the direction $\boldsymbol{\sigma}^e_{\#e}/|\boldsymbol{\sigma}^e_{\#e}|$.

For the fixed load P_D a sequence of FE elastic analyses is carried out on the structure such that, at the i-th iteration (analysis) of the sequence, within the FEs layers where $|\boldsymbol{\sigma}^e_{\#e}| > |\boldsymbol{\sigma}^Y_{\#e}|$ the elastic moduli of the layer are reduced according to:

$$E^{(i)}_{\#ej} := E^{(i-1)}_{\#ej} \left[\frac{|\boldsymbol{\sigma}^Y_{\#e}|^{(i-1)}}{|\boldsymbol{\sigma}^e_{\#e}|^{(i-1)}} \right]^2 . \tag{4}$$

Among all the $\boldsymbol{\sigma}^{e}_{\#e}$ in the mesh, the "maximum stress", i.e. the stress point farthest away from the Tsai-Wu type surface, say $\boldsymbol{\sigma}_R$ (coincident with $\boldsymbol{\sigma}^{e}_{\#3}$ in Fig. 2), is detected, $\boldsymbol{\sigma}^{Y}_{R}$ being the corresponding stress at yield (measured on the direction $\boldsymbol{\sigma}_R/|\boldsymbol{\sigma}^{Y}_{R}|$). The iterations (analyses) are carried out inside the given sequence until this maximum stress in the whole mesh $\boldsymbol{\sigma}_R$ just reaches (is below) its yield value $\boldsymbol{\sigma}^{Y}_{R}$, and this by the above reduction or redistribution procedure. Further sequences of elastic analyses are then carried on, each one with an increased value of P_D, and the reduction procedure repeated till further load increases do not allow the $\boldsymbol{\sigma}_R$ stress to be brought below yield. A lower bound to the collapse load multiplier can then be computed as:

$$P_L := \left|\boldsymbol{\sigma}^{Y}_{R}\right| \frac{P_D}{|\boldsymbol{\sigma}_R|}. \tag{5}$$

Concerning the evaluation of a lower bound via the ECM, it is worth to mention the remarkable works of Staat and Co-workers (see e.g. [35, 36]), where the effectiveness of the ECM is analyzed through a comparative study with respect to other optimization procedures. In [40] a better performance of the so called primal-dual procedure with respect to the ECM is also shown. The results obtained in the above quoted papers, all concerning von Mises type materials, show, at least for the cases there addressed, that the ECM is too conservative. Such assertion deserves surely further investigations also in the present context even if, for the mechanical problem herein tackled and the material utilized, at least for the analyzed cases, such drawbacks seem do not appear.

5 Layer-by-Layer Formulation

5.1 FE Modeling and Assumptions

From a numerical point of view, both iterative procedures are driven by a Fortran main program which utilizes the results of elastic analyses of the examined structural element carried out using the commercial FE code ADINA [1]. In the discrete model, the number of FEs is chosen taking into account the geometry of the modeled test and with the aim to obtain an enough accurate elastic FE solution. To this end, as general rule, a finer mesh is always employed around the fastener holes and a preliminary sensitive study on the elastic solution is performed for each different considered geometry. Moreover, when the analyzed specimens are made by quasi-isotropic laminates, isoparametric shell elements with 16 nodes and 16 GPs per element are utilized in the mesh, while, when dealing with laminates with a general stacking sequence, higher order isoparametric *multilayered* shell elements with 16 nodes per element, referred as DISP 16 in the quoted code, are employed. In particular, the employed multilayered shell elements are an extension to the case of composite laminates of mixed interpolated tensorial components (MITC) fam-

ily of plates and shell elements (see e.g. [11]). The modelling of the sublaminate is so entrusted to the element's layers endowed with 16 (on the top) plus 16 (on the bottom) Gauss points. For each element layer a proper material axes system is fixed and an order 2 Gauss integration is performed in the layer thickness. The number of layers per element is, obviously, chosen equal to the numbers of the laminae the analyzed laminate is made with. In Fig. 3(a) the modeling assumptions, namely the transition from the real stacking sequence of the laminate to the layers' element with the proper definition of the layer material axes system, are sketched. For both procedures, as shown in Fig. 3(b), the updating and/or reduction of the elastic moduli is carried into effect at each GP of the element (or of the layer for the multilayer shells) but, on taking into account that a unique set of E_j—i.e. a unique (orthotropic) material—has to be assigned to each single element layer, the modified moduli are averaged within the single element layer at the beginning of each FE analysis.

Finally, to simulate the presence of the rigid pins, two different schemes have been adopted. The first, used for single-pin fastenings, assumes a cosine load normal distribution to approximate the pressure exerted by the pin on the inner hole surface. The second, used for multi-pin fastenings, assumes boundary conditions of contact type between the pins and the fastener holes. In particular, the constrain function method (see e.g. [5] and references therein), available in the ADINA code, is used. The method requires the definition of a target line (the pin contour) and the definition of a contactor line (the fastener hole contour in the laminate) such that no material overlap between them can occur during the deformation process, while the contactor line can scroll or leave the target line.

5.2 Iterative Schemes for Upper and Lower Bounds Evaluation

5.2.1 Flow-Chart of the LMM Iterative Procedure

- *Initialization*
  Knowing the strength values of the orthotropic material (X_c; X_t; Y_c; Y_t; S); assign to all FEs layers an initial set of fictitious elastic parameters and initial stresses such that the complementary energy equipotential surface is homothetic to the Tsai-Wu type surface, i.e.:

$$E_1^{(0)} = 1/(2F_{11}); \qquad E_2^{(0)} = 1/(2F_{22}); \qquad E_6^{(0)} = 1/(2F_{66});$$

$$\nu_{12}^{(0)} = -f_{12}\sqrt{F_{11}}/\sqrt{F_{22}};$$

$$\bar{\sigma}_1^{(0)} = \alpha_{TW}/\sqrt{F_{11}}; \qquad \bar{\sigma}_2^{(0)} = \beta_{TW}/\sqrt{F_{22}}; \qquad \bar{\sigma}_6^{(0)} = 0;$$

  α_{TW} and β_{TW} being the X, Y coordinates of the Tsai-Wu type ellipsoid centre, while F_{11}, F_{22} and F_{66} are functions of the strength values. Set also: $k = 1$,

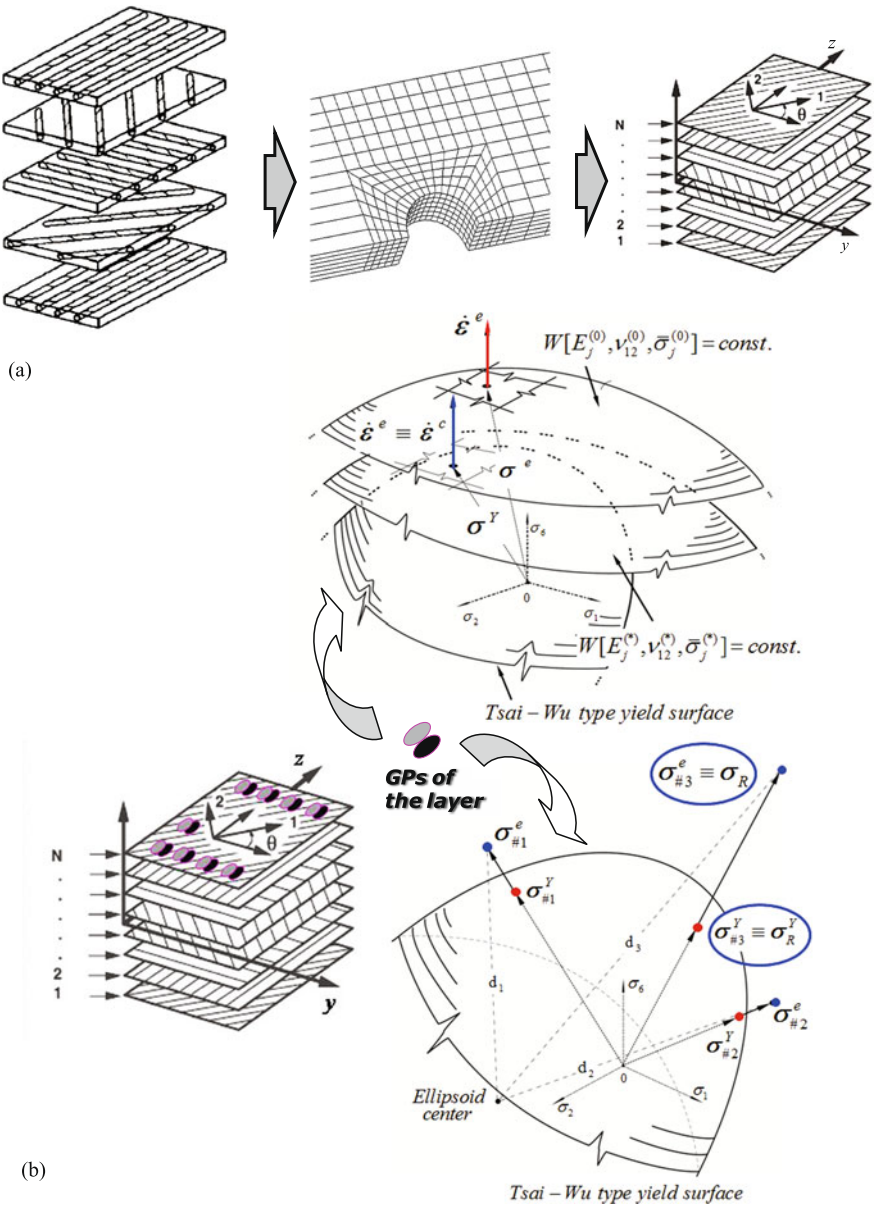

Fig. 3 Modeling assumptions: (**a**) definition of material axes at element layer following the stacking sequence; (**b**) sketch of the LMM and the ECM carried into effect at element layer

$P_{UB}^{(k-1)} = P_{UB}^{(0)} = 1$ (for $k = 1$, $P_{UB}^{(0)}$ can be any arbitrary value) and compute the constant $\Omega = 1 + \alpha_{TW}^2 + 2 f_{12} \alpha_{TW} \beta_{TW} + \beta_{TW}^2$ for later use.

- *Start iterative procedure*

- *Start elements loop*
- *Start layers loop*

  step # **1**: perform a fictitious elastic analysis with elastic parameters $E_j^{(k-1)}$, $\nu_{12} = \nu_{12}^{(0)}$, initial stresses $\bar{\sigma}_j = \bar{\sigma}_j^{(0)}$ and with loads $P_{UB}^{(k-1)}\bar{p}_i$ ($\bar{p}_i :=$ reference loads), computing a fictitious elastic solution at Gauss points of each layer, namely: $\dot{\varepsilon}_j^{e(k-1)}$, $\dot{u}_i^{(k-1)}$, $\sigma_j^{e(k-1)}$.

  step # **2**: compute the constant value of the complementary potential energy:

$$\bar{W}^{(k-1)} = \frac{1}{2}\sigma_j^{e(k-1)}\varepsilon_j^{e(k-1)}$$

  step # **3**: compute the homothety ratio, namely

$$\Gamma^{(k-1)} = \begin{cases} \sqrt{\Omega/\bar{W}^{(0)}} & \text{for } k = 1 \\ \sqrt{\bar{W}^{(k-2)}/\bar{W}^{(k-1)}} & \text{for } k > 1 \end{cases}$$

  step # **4**: evaluate stresses at yield:

$$\sigma_1^{Y(k-1)} = \left[1 - \Gamma^{(k-1)}\right]\frac{\alpha_T W}{\sqrt{F_{11}}} + \Gamma^{(k-1)}\sigma_1^{e(k-1)};$$

$$\sigma_2^{Y(k-1)} = \left[1 - \Gamma^{(k-1)}\right]\frac{\beta_T W}{\sqrt{F_{22}}} + \Gamma^{(k-1)}\sigma_2^{e(k-1)};$$

$$\sigma_6^{Y(k-1)} = \Gamma^{(k-1)}\sigma_6^{e(k-1)}$$

  step # **5**: set $\dot{\varepsilon}_j^{c(k-1)} = \dot{\varepsilon}_j^{e(k-1)}$, $\dot{u}_i^{c(k-1)} = \dot{u}_i^{e(k-1)}$ and evaluate the upper bound multiplier

$$P_{UB}^{(k)} = \frac{\int_V \sigma_j^{Y(k-1)}\dot{\varepsilon}_j^{c(k-1)}\mathrm{d}V}{\int_{\partial V_t}\bar{p}_i\dot{u}_i^{c(k-1)}\mathrm{d}(\partial V)}$$

- *End layers loop*
- *End elements loop*

  step # **6**: check for convergence

$$\left|P_{UB}^{(k)} - P_{UB}^{(k-1)}\right| \leq \mathrm{TOL} \quad \begin{cases} \mathrm{YES} \Rightarrow \mathrm{EXIT} \\ \mathrm{NOT} \Rightarrow \mathrm{CONTINUE} \end{cases}$$

- *Start elements loop*
- *Start layers loop*

  step # **7**: compute the $E_j^{(k)}$ distribution accomplishing the matching at each GP of each layer to be utilized at next iteration, namely:

$$E_j^{(k)} = E_j^{(k-1)}\left[\Gamma^{(k-1)}\right]^2, \quad j = 1, 2, 6$$

  step # **8**: average the updated $E_j^{(k)}$ values within each element layer.
- *End layers loop*
- *End elements loop*

  set $k = k - 1$ and GOTO step #1
- *End iterative procedure*

5.2.2 Flow-Chart of the ECM Iterative Procedure

- *Initialization*
  Assign to all FEs layers the material elastic parameters, i.e.:

$$E_1^{(0)}; \quad E_2^{(0)}; \quad E_6^{(0)}; \quad \nu_{12};$$

  set also: $k = 1$, $P_D = 1$ (for $k = 1$, P_D can be a design load value).
- *Start iterative procedure*
- *Start elements loop*
- *Start layers loop*

  step # **1**: perform an elastic analysis with material parameters $E_j^{(k-1)}$, ν_{12} and loads $P_D \bar{p}_i$ ($\bar{p}_i :=$ reference loads), computing the stresses at Gauss points of each layer, namely: $\sigma_j^{e(k-1)}$.
  step # **2**: average the stress values inside each element layer so computing the stress vector $\boldsymbol{\sigma}_{\#e}^{e}$ and the corresponding stress at yield $\boldsymbol{\sigma}_{\#e}^{Y}$.
  step # **3**:

  IF $P_D = 1$
  update the young moduli within the current layer according to:

$$E_{\#ej}^{(k)} := E_{\#ej}^{(k-1)} \left[\frac{|\boldsymbol{\sigma}_{\#e}^{Y}|^{(k-1)}}{|\boldsymbol{\sigma}_{\#e}^{e}|^{(k-1)}} \right]^2 \quad \text{(Eq. (4))},$$

  ELSE
  update the young moduli within the current layer according to the above equation (Eq. (4)) only when:

$$\left|\boldsymbol{\sigma}_{\#e}^{e}\right|^{(k-1)} > \left|\boldsymbol{\sigma}_{\#e}^{Y}\right|^{(k-1)}$$

  ENDIF

  step # **4**: detect the "maximum stress" $\boldsymbol{\sigma}_R$ in the whole mesh (i.e. whose corresponding stress point is the one farthest away from the Tsai-Wu type surface) and evaluate the pertinent stress at yield $\boldsymbol{\sigma}_R^Y$
- *End layers loop*
- *End elements loop*

  step # **5**: check if compensated stress $\boldsymbol{\sigma}_R$ just reaches (is below) the yield value

$$|\boldsymbol{\sigma}_R| > \left|\boldsymbol{\sigma}_R^Y\right| \quad \begin{cases} \text{YES} \Rightarrow \text{GOTO step \# } \mathbf{8} \\ \text{NOT} \Rightarrow \text{CONTINUE} \end{cases}$$

  step # **6**: compute a lower bound as:

$$P_L := \left|\boldsymbol{\sigma}_R^Y\right| \frac{P_D}{|\boldsymbol{\sigma}_R|}$$

  step # **7**: set $P_D > P_L$, set also $k = 1$ and GOTO step # **1** to perform a new sequence of elastic analyses

step # **8**:

IF

$$|\boldsymbol{\sigma}_R|^{(k)} \geq |\boldsymbol{\sigma}_R|^{(k-1)}$$

set $P_L = P_D$ of the previous sequence and *EXIT*

ELSE

set $k = k - 1$ and GOTO step #**1** to start a new elastic analysis

ENDIF

- *End iterative procedure*

6 Numerical Versus Experimental Findings

6.1 Pinned Joints in FRP Plates: Single- and Multi-hole Fasteners

As already pointed out in the previous sections, the expounded numerical procedures have been validated by reproducing a considerable number of experimental tests for load bearing capacity experimental evaluation available in the literature and concerning single- as well as multi-pin joints composite plates. Four main different configurations have been considered. For all the examined cases, overall 177, the proposed approach has been applied to predict either the upper and lower bounds to the joint peak load value or the joint failure modes. In all cases, due to the symmetry of loading, geometry and material with respect to the longitudinal axis y of the plate, only half of the mechanical problem shown in Figs. 4 and 5 has been considered.

In particular, the first configuration refers to a multilayer composite laminate with a single hole, like the one sketched in Fig. 4 where geometrical, boundary and loading conditions are specified. In this first case, to simulate the action of the pin inside the hole a cosine load normal distribution T_i is assumed with P applied reference load, assumed equal to 1 kN, n_i the unit vector normal to the inner hole surface and ϑ a clockwise angle varying in the range $[-\pi/2, \pi/2]$. The numerical study has involved six different lay-ups (specimen-type), each one with eight different geometries excepted for the sixth specimen-type where seven different geometries have been analyzed, so considering 47 different specimens. For these 47 specimens, the experimental findings are the ones given by Okutan Baba [22] and Aktas and Dirikolu [2]. For benefit of clarity, the 6 layer stacking sequences (*LSS*), identifying 6 different specimen types, are listed in Table 1 together with the thickness of the laminate and the diameter of the fastener hole. Moreover, Table 2 shows the mechanical parameters of the two types of unidirectional laminae forming the examined laminates, i.e. glass-fiber/epoxy and carbon/epoxy. Specimens belonging to this first configuration have been analyzed either following a single layer approach, with 16 nodes single layer shell elements, or using higher order isoparametric multilayered shell elements, referred as DISP 16 in the ADINA code. The number of elements has been varied from 250 to 330 depending on the considered geometry.

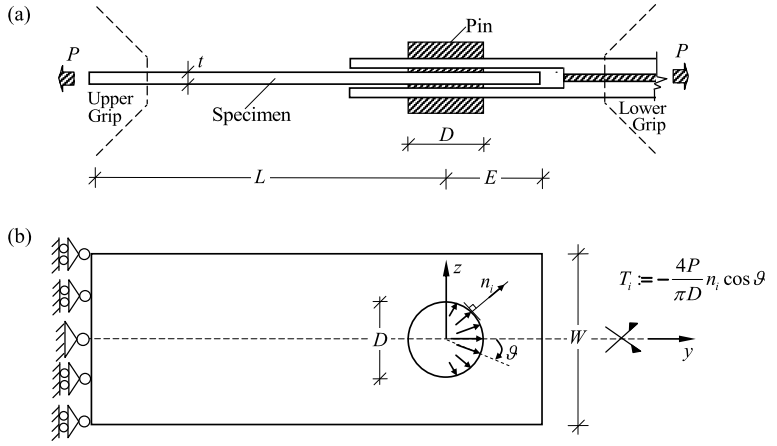

Fig. 4 Schematic representation of a single-pin-loaded composite rectangular plate: (**a**) fixture test for load bearing capacity evaluation; (**b**) mechanical model, boundary and loading conditions

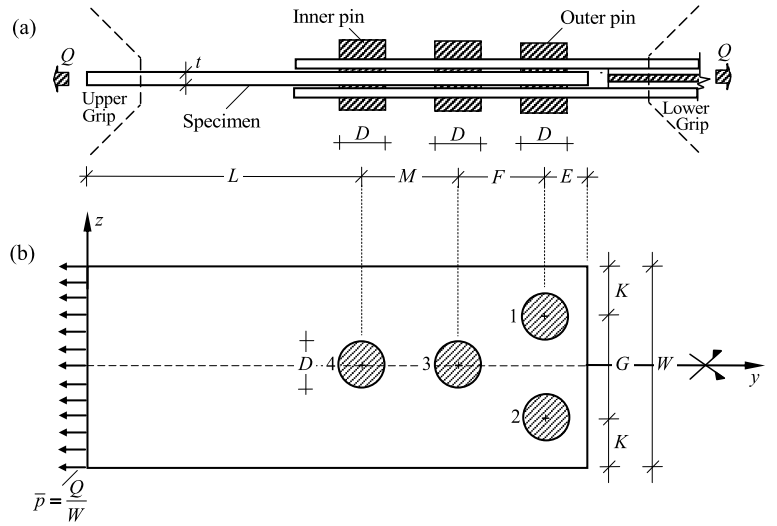

Fig. 5 Schematic representation of the multi-pin joints composite plate: (**a**) fixture test for load bearing capacity evaluation; (**b**) mechanical model

Configurations second, third and fourth, concern multi-pin joints plates. In these cases, the plate is subjected to a tensile load distribution (equivalent to a global load Q) acting on the plate mid-plane and applied to one edge. Also in these cases a reference load of global value equal to $Q = 1$ kN has been assumed (the P_{UB} and P_{LB} multiplier are numerically coincident with the predicted peak load value for all the run examples). The pins, assumed rigid, react to the applied load inducing high level of stresses around the fastener holes. A schematic representation of the

Table 1 Layer stacking sequence (*LSS*) and geometrical properties of the single-hole specimens

Specimen type	Material	*LSS*	t (mm)	D (mm)
A	glass-fiber epoxy	$[0°/\pm45°]_S$	4.4	5
B	glass-fiber epoxy	$[90°/\pm45°]_S$	4.4	5
C	glass-fiber epoxy	$[0^0/90°/0°]_S$	3.3	5
D	glass-fiber epoxy	$[90^0/0°/90°]_S$	3.3	5
E	glass-fiber epoxy	$[\pm45°]_{2S}$	4.8	5
F	carbon epoxy	$[90°/\pm45°/0°]_S$	2.64	6.35

Table 2 Mechanical parameters of the unidirectional laminae forming the composite laminates with a single-pin joint

Glass-fiber epoxy[a]					
Elastic moduli (GPa) and Poisson ratio	E_1	E_2	G_{12}	υ_{12}	
	44	10.5	3.74	0.36	
Strength (MPa)	X_t	X_c	Y_t	Y_c	S
	800	350	50	125	120
Carbon epoxy[b]					
Elastic moduli (GPa) and Poisson ratio	E_1	E_2	G_{12}	υ_{12}	
	88	8.8	2.8	0.28	
Strength (MPa)	X_t	X_c	Y_t	Y_c	S
	811	457.7	47.3	109.5	132

[a] After Okutan Baba [22]

[b] After Aktas and Dirikolu [2]

multi-pin joints fixture test together with the corresponding mechanical model is given in Fig. 5. The latter shows the distributed edge load as well as the shaded rigid pins fixed to the external world. As said in Sect. 5.1 boundary conditions of contact type are assumed between the pins and the fastener holes. With reference to Fig. 5: W and t are the width and thickness plate respectively; the length G indicates the distance between two parallel holes; K their distance from the longer edge; M the distance between two serial holes in the y direction; F the distance between two generic holes in the y direction. Finally, L and E are the distances between the inner and outer holes from the plate edges respectively.

In detail, the second configuration refers to a $[0°/90°/\pm45°]_S$ laminate with a three pins joint tested in the technical report of Karakuzu et al. [14]. Referring again to Fig. 5, the three holes are located in the positions 1, 2, 3. Each glass-epoxy lamina, forming the composite laminate, is characterized by the mechanical properties reported in Table 3, while the geometrical parameters are: $L = 90$ mm, $t = 1.7$ mm, $D = 5$ mm; finally, the distance K is equal to 10 mm. For this specimen type, 45 different geometries were tested with values of the ratio E/D ranging from 1 to 5, ratio G/D ranging from 3 to 5 and considering also three different ratios for F/D, namely: 2, 4, 6. A number of elements ranging from 544 to 662 has been used for this configuration together with the proposed layered approach.

The third configuration refers to a woven glass/vinylester laminate with two serial pins joint tested in the paper of Karakuzu et al. [12]. The two holes are located in the

Table 3 Mechanical parameters utilized for the numerical simulations of composite laminates with multi-pins joints

Glass/epoxy lamina[a]					
Elastic moduli (GPa) and Poisson ratio	E_1	E_2	G_{12}	v_{12}	
	38	8	4	0.27	
Strength (MPa)	X_t	X_c	Y_t	Y_c	S
	687	223	74	109	78
Glass/vinylester laminate[b]					
Elastic moduli (GPa) and Poisson ratio	E_1	E_2	G_{12}	v_{12}	
	20.77	20.77	4.13	0.09	
Strength (MPa)	X_t	X_c	Y_t	Y_c	S
	395	260	395	260	75

[a]After Karakuzu et al. [14]

[b]After Karakuzu et al. [12]

positions 3 and 4 of Fig. 5. The mechanical properties of the laminate are reported in Table 3, while its geometrical parameters are: $L = 85$ mm, $t = 2.8$ mm, $D = 5$ mm. For this specimen type, 40 different geometries were tested considering the ratios $W/D = 2, 4$ and M/D and E/D variable from 2 to 5 and from 1 to 5, respectively. In this case the FE models utilized had a number of 16 nodes single layer shell elements varying from 275 to 530.

Finally, the fourth configuration refers again to a woven glass/vinylester laminate but with two parallel pins joint (see e.g. Karakuzu et al. [13]). With reference to Fig. 5 the two holes are located in the positions 1 and 2. In this case the geometrical and mechanical parameters of the laminate are the same of configuration three, while the 45 different geometries considered are obtained by varying the ratio K/D from 2 to 4, the ratio E/D from 1 to 5, and considering the ratios $M/D = 2, 4, 5$. For this specimen type a FE modelling involving 16 nodes single layer shell elements has been again employed with a number of elements variable from 448 to 725.

6.2 Peak Load Prediction

For sake of synthesis, the obtained numerical results are organized in diagram format. In particular Figs. 6, 7 report, for the 6 specimen types related to the first laminate configuration, the comparison between the experimental findings and the numerical predictions in terms of peak load. Each Figure reports different couples of E/D and W/D ratios, the pertinent experimentally detected values of peak load and the predicted values, in terms of upper and lower bounds, given by the layer-by-layer and equivalent layer formulation of LMM and ECM. Precisely, the plots given in Fig. 6 refer to $E/D = 4$ and W/D variable, while the plots in Fig. 7 refer to $W/D = 4$ and E/D variable. The upper bound values predicted by the proposed layer-by-layer limit analysis are always above, or are practically coincident with the experimental ones. The same is definitely not true for the single layer treatment

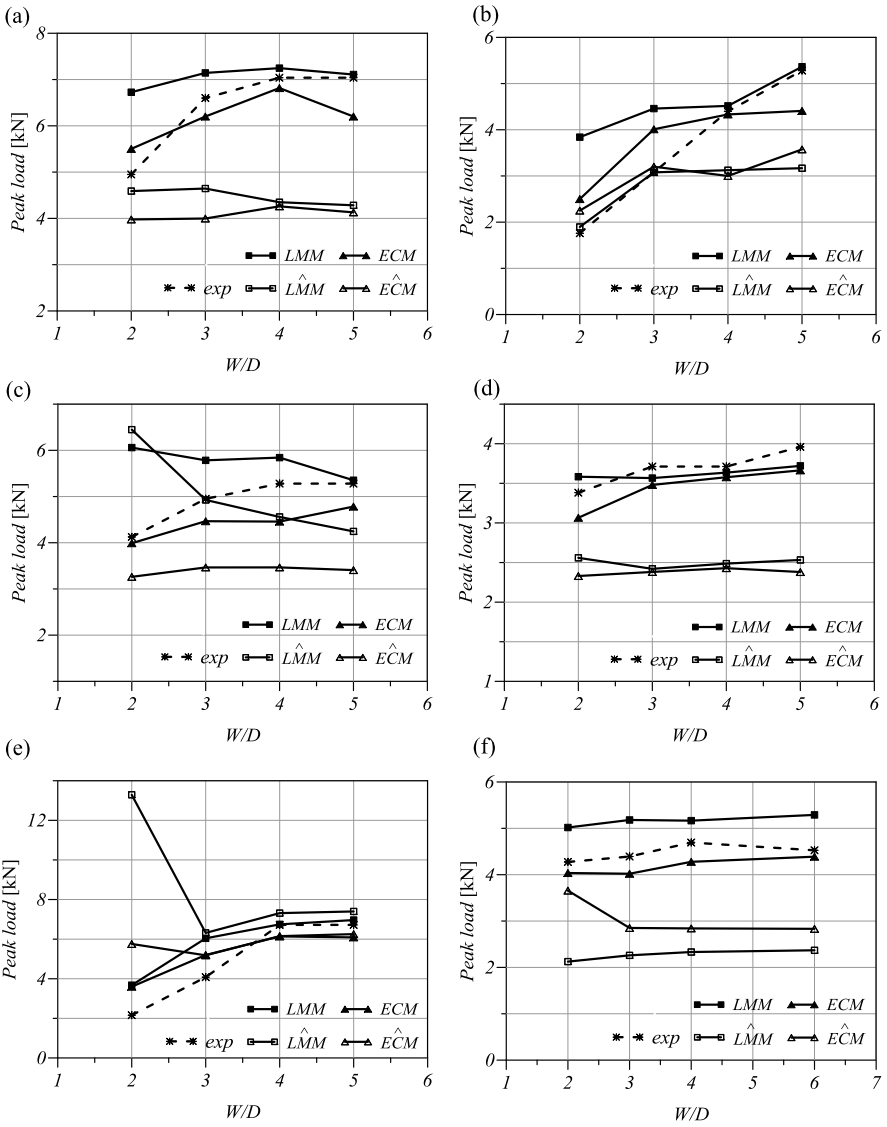

Fig. 6 Peak load values for fixed ratio $E/D = 4$; comparison between experimental data, dashed lines with asterisk marker, and values predicted by LMM and ECM respectively. (**a**) Specimen type A; (**b**) Specimen type B; (**c**) Specimen type C; (**d**) Specimen type D; (**e**) Specimen type E; (**f**) Specimen type F

where the evaluated upper bounds appear far, and even below, from the experimental values. Analogously, the lower bounds evaluated with the layer-by-layer analyses are closer (from below) to the experimental values than the ones given by the single layer treatment, too much conservative. As expected, good accuracy is attained by

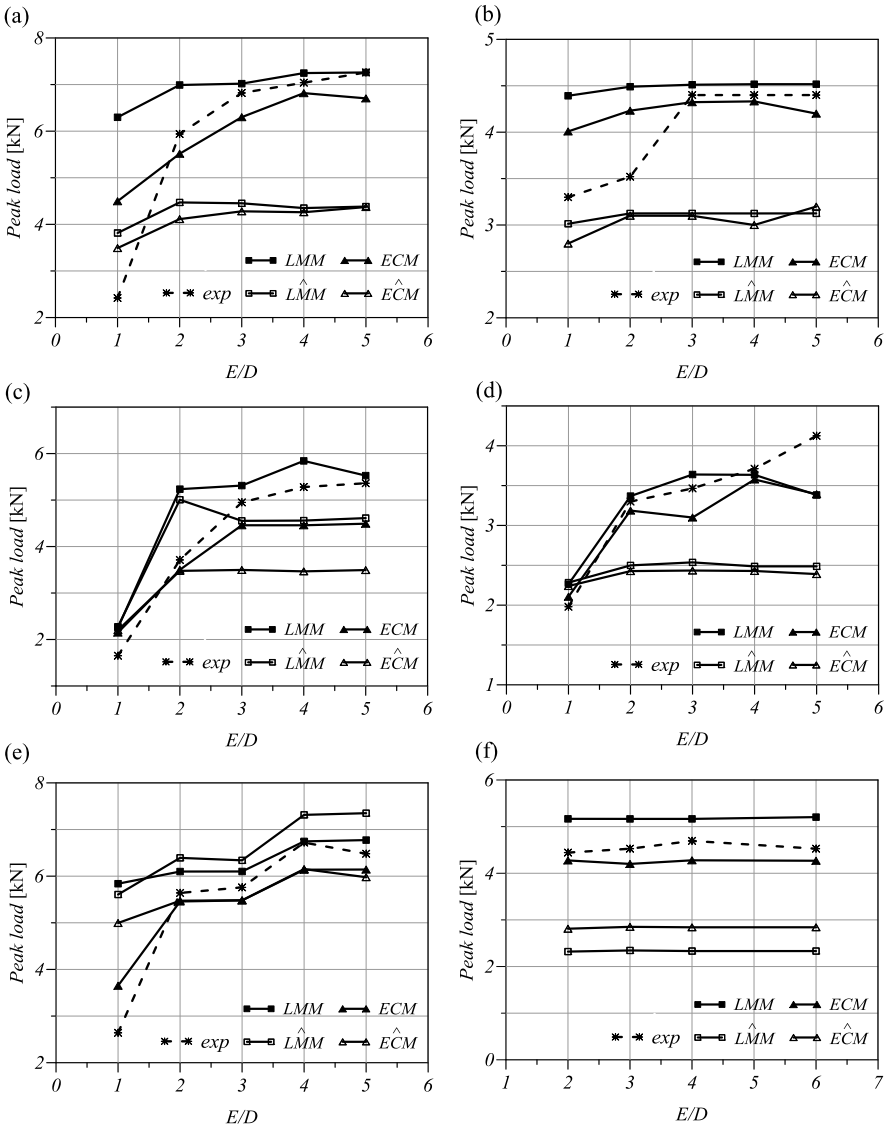

Fig. 7 Peak load values for fixed ratio $W/D = 4$; comparison between experimental data, dashed lines with asterisk marker, and values predicted by LMM and ECM respectively. (**a**) Specimen type A; (**b**) Specimen type B; (**c**) Specimen type C; (**d**) Specimen type D; (**e**) Specimen type E; (**f**) Specimen type F

both single and layer-by-layer procedures when dealing with laminate lay-ups of the type $[\pm 45^\circ]_{ns}$, as the one of specimen E of Figs. 6(e) and 7(e), for which the anisotropy of each layer is mitigated by the sequence itself. The average relative errors, computed as the absolute value of the difference between the experimental

Table 4 Average relative error of the peak load values computed with the layer-by-layer and the single layer approach

Specimen type	*LMM*	$L\hat{M}M$	*ECM*	$E\hat{C}M$
A	0.29	0.34	0.17	0.36
B	0.29	0.19	0.17	0.23
C	0.20	0.23	0.12	0.28
D	0.07	0.29	0.08	0.32
E	0.33	0.92	0.20	0.39
F	0.15	0.49	0.06	0.34

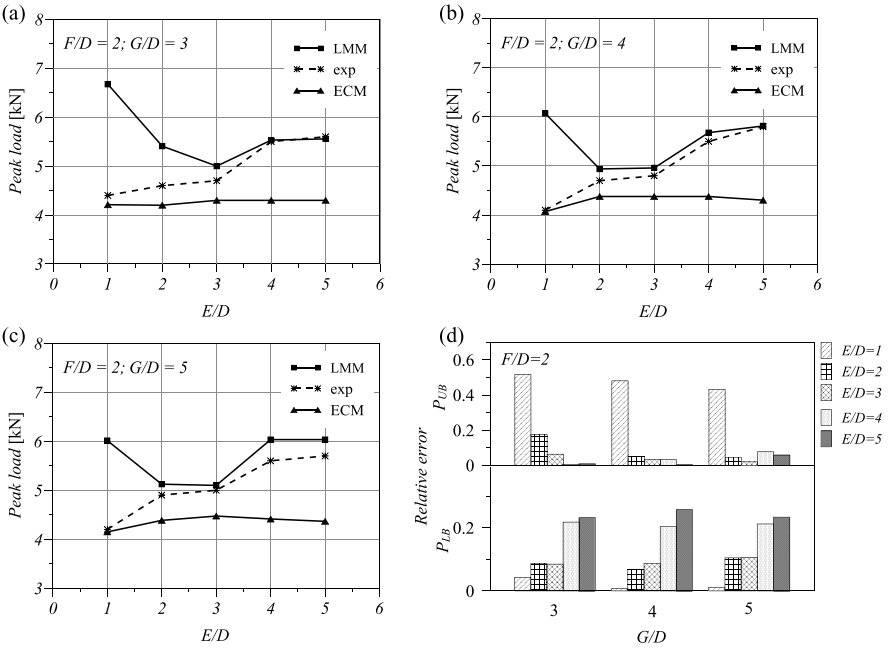

Fig. 8 Peak load values of the multi-layer specimens $[0°/90°/\pm 45°]_S$ for $F/D = 2$. (**a**) $G/D = 3$; (**b**) $G/D = 4$; (**c**) $G/D = 5$; (**d**) Plot of the relative error given by the two procedures

and the numerical detected peak load values over the experimental ones, are shown in Table 4 for the layered analysis and for the single layer one. As it appears the range of the computed load values bracketing the real one is, by far, more accurate for the layered approach.

With reference to the second configuration (a three holes joint), Figs. 8, 9 and 10 report the comparison between the experimental findings and the numerical predictions in terms of peak load for fixed values of F/D and different values of E/D and G/D. In addition, Figs. 8(d), 9(d) and 10(d) give the relative errors of the numerically predicted P_{UB} and P_{LB} with respect to the corresponding experimentally detected values.

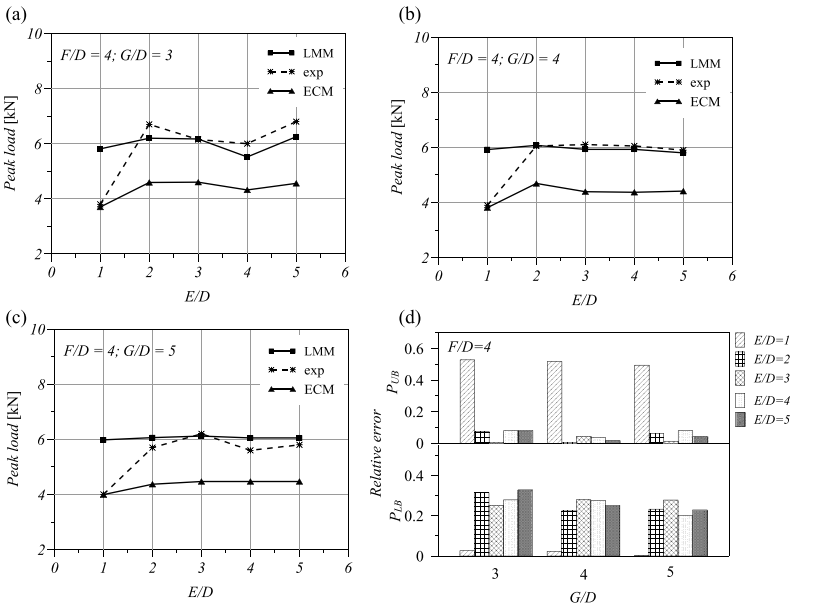

Fig. 9 Peak load values of the multi-layer specimens $[0°/90°/\pm 45°]_S$ for $F/D = 4$. (**a**) $G/D = 3$; (**b**) $G/D = 4$; (**c**) $G/D = 5$; (**d**) Plot of the relative error given by the two procedures

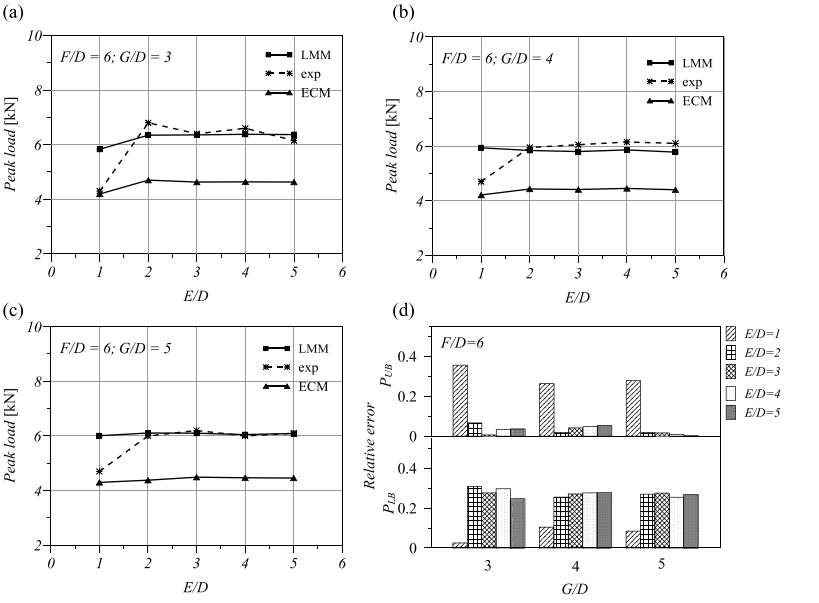

Fig. 10 Peak load values of the multi-layer specimens $[0°/90°/\pm 45°]_S$ for $F/D = 6$. (**a**) $G/D = 3$; (**b**) $G/D = 4$; (**c**) $G/D = 5$; (**d**) Plot of the relative error given by the two procedures

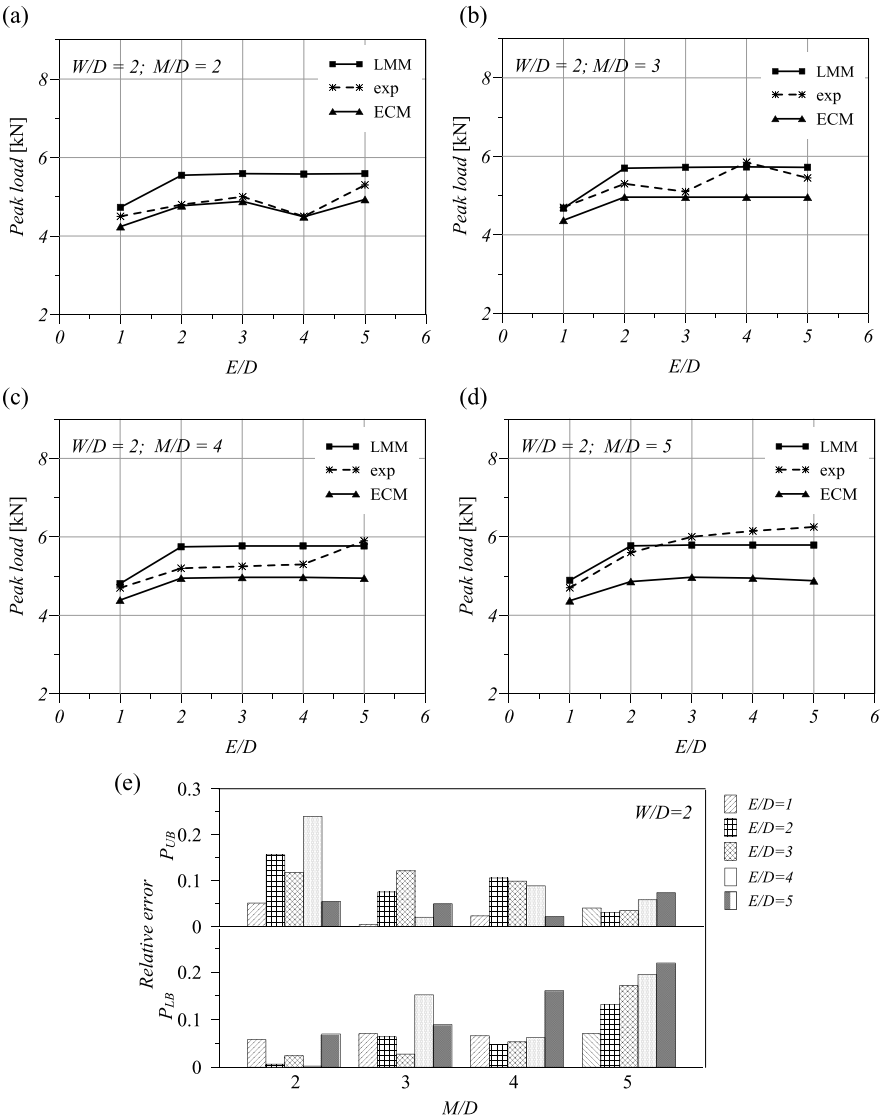

Fig. 11 Peak load values of the specimens with two serial fastener holes for $W/D = 2$. (**a**) $M/D = 2$; (**b**) $M/D = 3$; (**c**) $M/D = 4$; (**d**) $M/D = 5$; (**e**) Plot of the relative error given by the two procedures

For the third configuration (joint with two serial pins), the experimental and predicted peak load values are reported in Figs. 11, 12 for fixed values of W/D and different values of E/D and M/D.

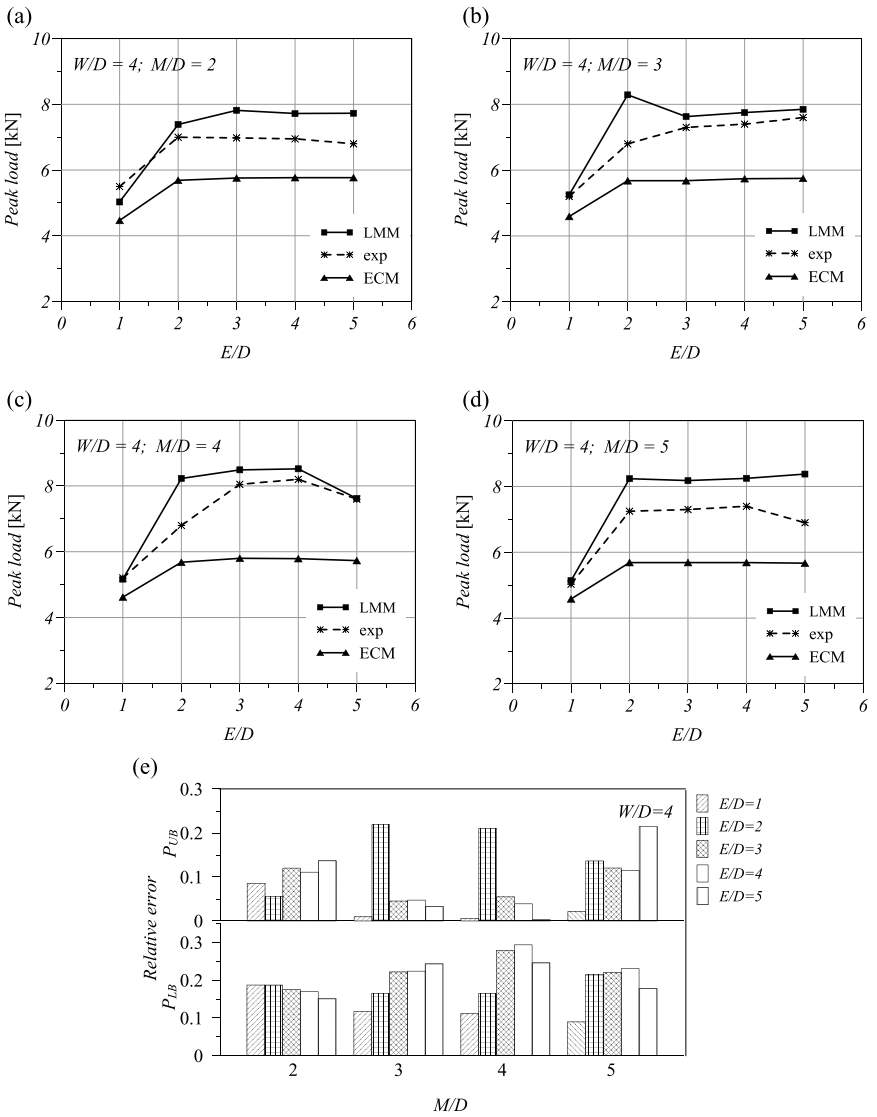

Fig. 12 Peak load values of the specimens with two serial fastener holes for $W/D = 4$. (**a**) $M/D = 2$; (**b**) $M/D = 3$; (**c**) $M/D = 4$; (**d**) $M/D = 5$; (**e**) Plot of the relative error given by the two procedures

Finally Figs. 13, 14 and 15 report the experimental and predicted peak load values for the two parallel pins joint (fourth configuration), for fixed values of M/D and different values of E/D and K/D.

By inspection of the obtained results, in 23 over the 177 examined cases the experimental peak value lies outside the range numerically predicted, such cases are

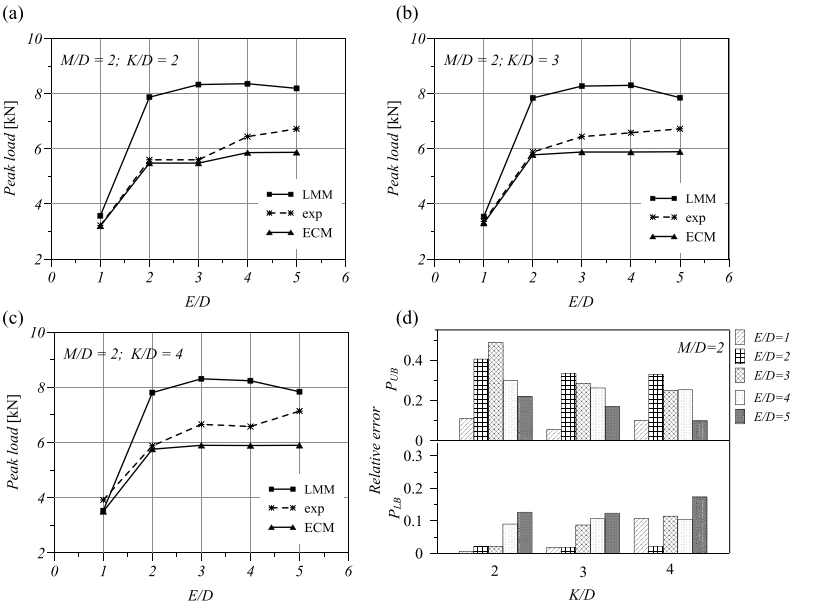

Fig. 13 Peak load values of the specimens with two parallel fastener holes for $M/D = 2$. (**a**) $K/D = 2$; (**b**) $K/D = 3$; (**c**) $K/D = 4$; (**d**) Plot of the relative error given by the two procedures

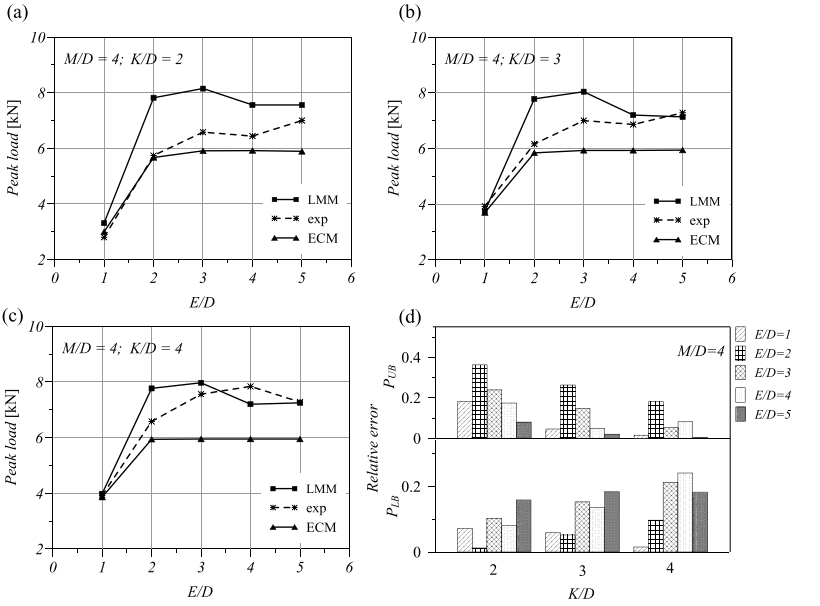

Fig. 14 Peak load values of the specimens with two parallel fastener holes for $M/D = 4$. (**a**) $K/D = 2$; (**b**) $K/D = 3$; (**c**) $K/D = 4$; (**d**) Plot of the relative error given by the two procedures

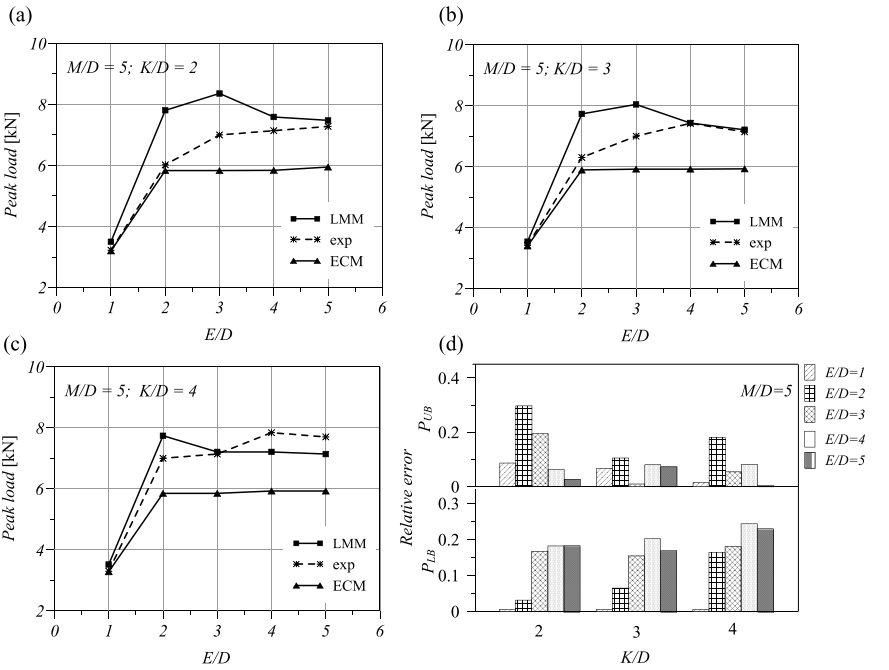

Fig. 15 Peak load values of the specimens with two parallel fastener holes for $M/D = 5$. (**a**) $K/D = 2$; (**b**) $K/D = 3$; (**c**) $K/D = 4$; (**d**) Plot of the relative error given by the two procedures

simply wrong predictions of the adopted methodology. A threefold reasons induced the authors to accept such circumstance: (i) the overall percentage of wrong predictions is about 13 %, i.e. a low value from an engineering point of view; (ii) the relative error, also in such cases, is very low; (iii) the wrong predictions are mainly concerned, in 21 over 23 cases, the upper bound to the peak load value, a value not directly affecting the design choices as the lower bound does. The P_{LB} being in practice always correct. Nevertheless, further investigations to this concern might be necessary.

Finally, Fig. 16 shows, for eight of the 177 analyzed specimens (i.e. two for each different laminate configuration considered), the plots of the upper and the lower bounds to the peak load versus the iterations number. In all cases a monotonic and rapid convergence of the methods is assured by a condition for convergence given in Ponter et al. [29]. Such circumstance, essential for any iterative based procedure, is met in all the examined cases but here is not reported for brevity.

The proposed methodology seems, at least for all the examined specimens, definitely able to predict, with good accuracy, the peak load of a multi-pin joints laminate.

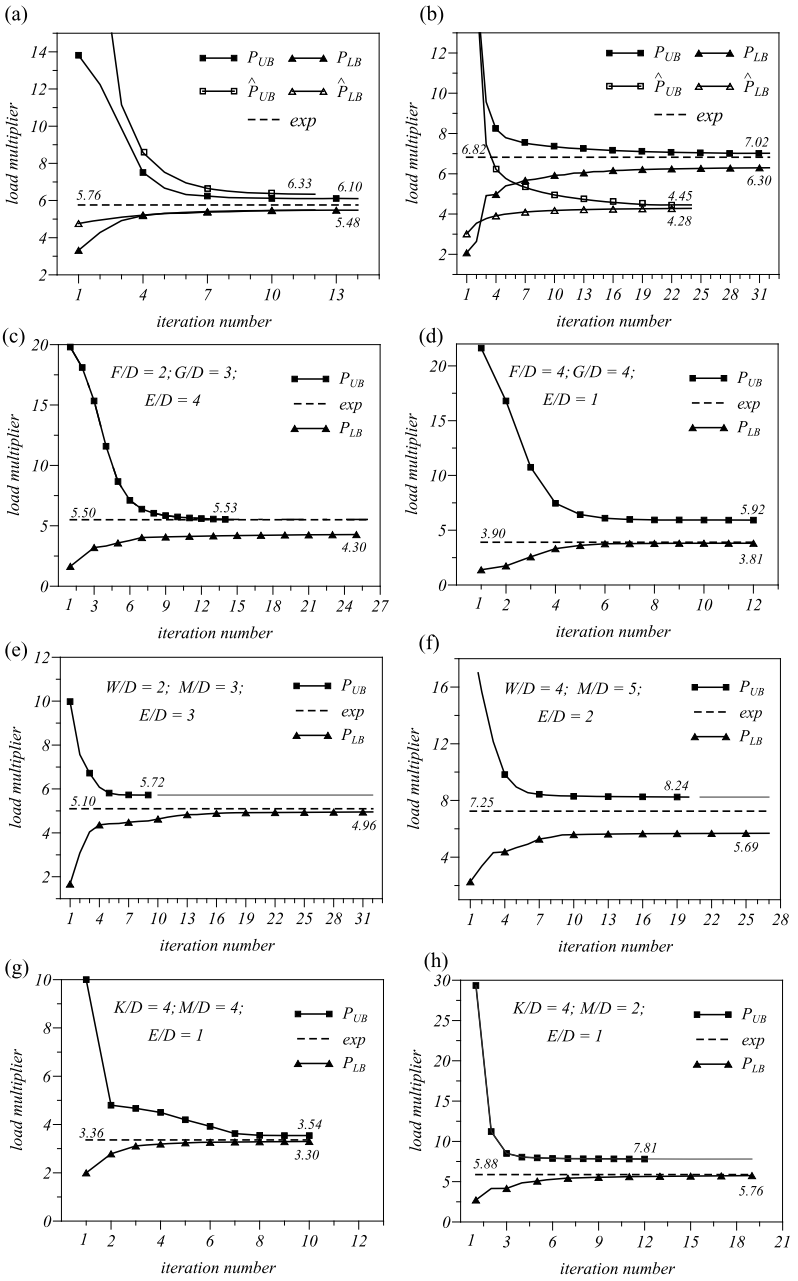

Fig. 16 Values of the upper (P_{UB}) and lower (P_{LB}) bounds to the collapse load multiplier versus iteration number. LMM prediction, solid lines with rectangular markers; ECM prediction, solid lines with triangular markers; collapse experimental threshold, finer dashed lines. (**a**) and (**b**): multilayer specimens E3 and A3 with single fastener hole; (**c**) and (**d**): multilayer specimens with three fastener holes; (**e**) and (**f**): woven specimens with two serial fastener holes; (**g**) and (**h**): woven specimens with two parallel fastener holes

Table 5 Failure modes: experimental data against predicted ones for the multi-layer specimens with one fastener hole

LSS	*E*/*D*	*W*/*D*	LMM	exp[a]
$[90°/\pm45°]_S$	5	5	B	B
$[90°/0°/90°]_S$	4	3	B	B
$[0°/90°/0°]_S$	2	5	S	S
$[0°/90°/0°]_S$	2	4	S	S
$[\pm45°]_{2S}$	3	4	B	N

[a]After Okutan Baba [22]

Table 6 Failure modes: experimental data against predicted ones for the multi-layer specimens $[0°/90°/\pm45°]_S$ with three fastener holes

E/*D*	*G*/*D* = 3		*G*/*D* = 4		*G*/*D* = 5	
	LMM	exp[a]	LMM	exp[a]	LMM	exp[a]
F/*D* = 2						
1	S/S/B	S/S/B	S/S/B	S/S/B	S/S/B	S/S/B
2	B/B/B	B/B/B	B/B/B	B/B/B	B/B/B	B/B/B
3	B/B/B	B/B/B	B/B/B	B/B/B	B/B/B	B/B/B
4	B/B/B	B/B/B	B/B/B	B/B/B	B/B/B	B/B/B
5	B/B/B	B/B/B	B/B/B	B/B/B	B/B/B	B/B/B
F/*D* = 4						
1	S/S/B	S/S/B	S/S/B	S/S/B	S/S/B	S/S/B
2	B/B/B	B/B/B	B/B/B	B/B/B	B/B/B	B/B/B
3	B/B/B	B/B/B	B/B/B	B/B/B	B/B/B	B/B/B
4	B/B/B	B/B/B	B/B/B	B/B/B	B/B/B	B/B/B
5	B/B/B	B/B/B	B/B/B	B/B/B	B/B/B	B/B/B
F/*D* = 6						
1	S/S/B	S/S/B	S/S/B	S/S/B	S/S/B	S/S/B
2	B/B/B	B/B/B	B/B/B	B/B/B	B/B/B	B/B/B
3	B/B/B	B/B/B	B/B/B	B/B/B	B/B/B	B/B/B
4	B/B/B	B/B/B	B/B/B	B/B/B	B/B/B	B/B/B
5	B/B/B	B/B/B	B/B/B	B/B/B	B/B/B	B/B/B

[a]After Karakuzu et al. [14]

6.3 Failure Modes Prediction

In order to gain a deeper comprehension of the mechanical joint behaviour, beside the evaluation of the peak load it is of equally importance the prediction of the joint failure mode. Typically, with reference to a single fastener/pin hole, three main/primary failure modes can be individuated (bearing, net-tension, shear-out), other modes (tear-out, cleavage, ...) being a combination of them, also called secondary modes. When a multi-pin fastening is considered the real failure modes can be more complex for the mutual interaction of the fastenings affected by their ge-

Table 7 Failure modes: experimental data against predicted ones for the woven specimens with two serial fastener holes

E/D	$M/D=2$		$M/D=3$		$M/D=4$		$M/D=5$	
	LMM	exp[a]	LMM	exp[a]	LMM	exp[a]	LMM	exp[a]
$W/D=2$								
1	N/N	N/N	N/S	N/N	N/S	N/N	N/–	N/N
2	N/–	N/–	N/–	N/–	N/–	N/–	N/–	N/–
3	N/–	N/–	N/–	N/–	N/–	N/–	N/–	N/–
4	N/–	N/–	N/–	N/–	N/–	N/–	N/–	N/–
5	N/–	N/–	N/–	N/–	N/–	N/–	N/–	N/–
$W/D=4$								
1	B/SN	B/S	B/S	B/S	B/S	B/S	B/S	B/S
2	BS/BS	B/B	B/BS	B/B	B/BS	B/B	B/BS	B/B
3	B/B	B/B	B/BN	B/B	B/B	B/B	B/B	B/B
4	B/BN	B/B	B/BN	B/B	B/B	B/B	B/B	B/B
5	B/BN	B/B	B/BN	B/B	B/B	B/B	B/B	B/B

[a]After Karakuzu et al. [12]

Table 8 Failure modes: experimental data against predicted ones for the woven specimens with two parallel fastener holes

E/D	$K/D=2$		$K/D=3$		$K/D=4$	
	LMM	exp[a]	LMM	exp[a]	LMM	exp[a]
$M/D=2$						
1	S	S	S	S	S	S
2	S	BN	S	BS	S	BS
3	BS	BN	BS	BS	BS	BS
4	BNS	BN	BS	BS	BS	BS
5	BN	BN	B	B	B	B
$M/D=4$						
1	S	S	S	S	S	S
2	S	B	S	B	S	B
3	B	B	B	B	B	B
4	B	B	B	B	B	B
5	B	B	B	B	B	B
$M/D=5$						
1	S	S	S	S	S	S
2	S	B	S	B	S	B
3	B	B	B	B	BS	B
4	B	B	B	B	B	B
5	B	B	B	B	B	B

[a]After Karakuzu et al. [13]

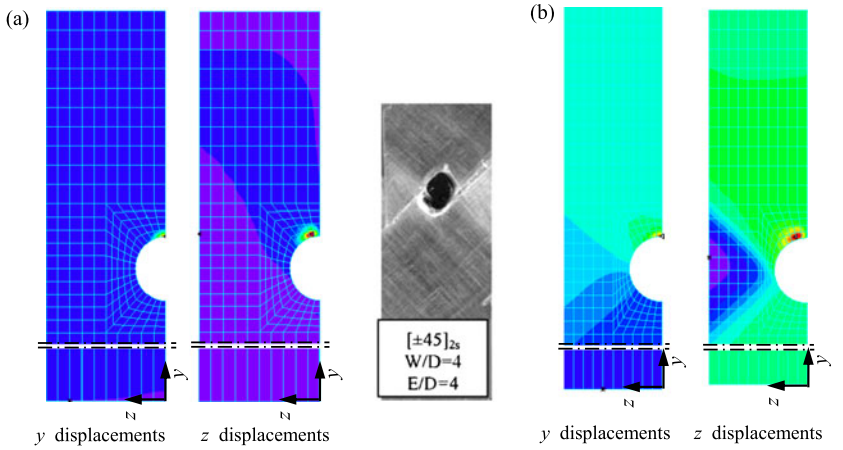

Fig. 17 Pin-loaded plate of Fig. 4: (**a**) predicted collapse mechanism of bearing type obtained for specimen #E4 with $W/D = 4$; (**b**) predicted collapse mechanism of net-tension type for specimen #E4 with $W/D = 3$ against experimental one (after Okutan Baba [22])

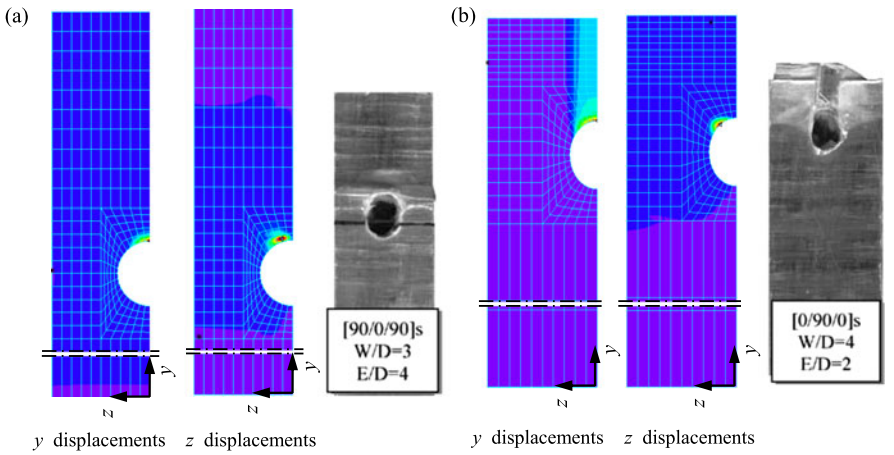

Fig. 18 Pin-loaded plate of Fig. 4: (**a**) predicted collapse mechanism of bearing type against experimental one for specimen #D7; (**b**) predicted collapse mechanism of shear-out type against experimental one for specimen #C2 (after Okutan Baba [22])

ometrical distribution (see e.g. [37]) and the possibility of a numerical prediction becomes more important.

The prediction of the failure mode is herein pursued numerically making use of the LMM which builds the collapse mechanism the joint exhibits when the loads attain their peak value or, more exactly, they reach the evaluated upper bound value to such peak. The obtained results are organized either in tabular or in band plots format. In particular, Tables 5, 6, 7 and 8 report the comparison between the experi-

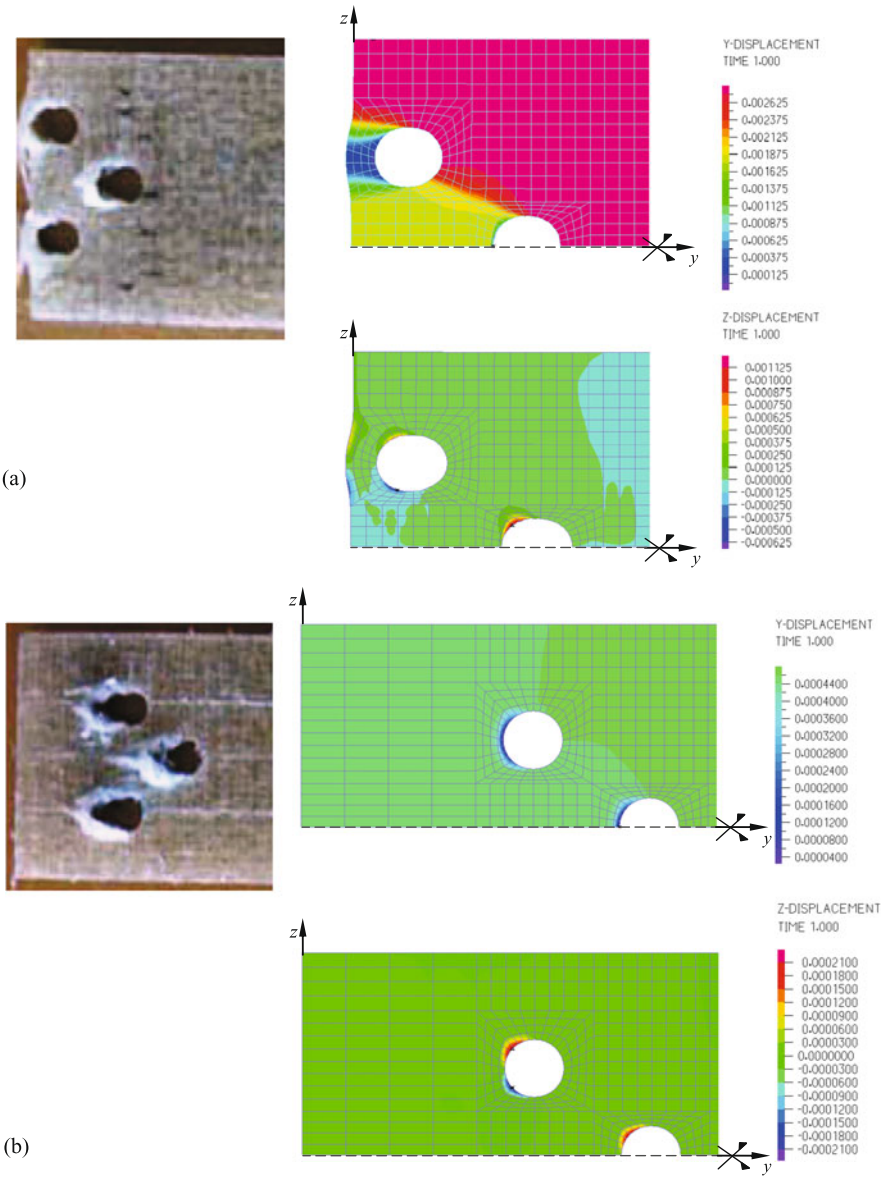

Fig. 19 Three-pins-loaded plate of Fig. 5. Failure modes predicted by numerical simulations against experimentally detected ones (after Karakuzu et al. [14]): (**a**) Shear-out at outer holes and Bearing at inner hole for $F/D = 2$, $G/D = 3$, $E/D = 1$; (**b**) Bearing at outer and inner holes for $F/D = 2$, $G/D = 3$, $E/D = 4$

mental findings and the numerical predictions in terms of collapse/failure modes for all the geometries analyzed, all grouped with respect to the four considered config-

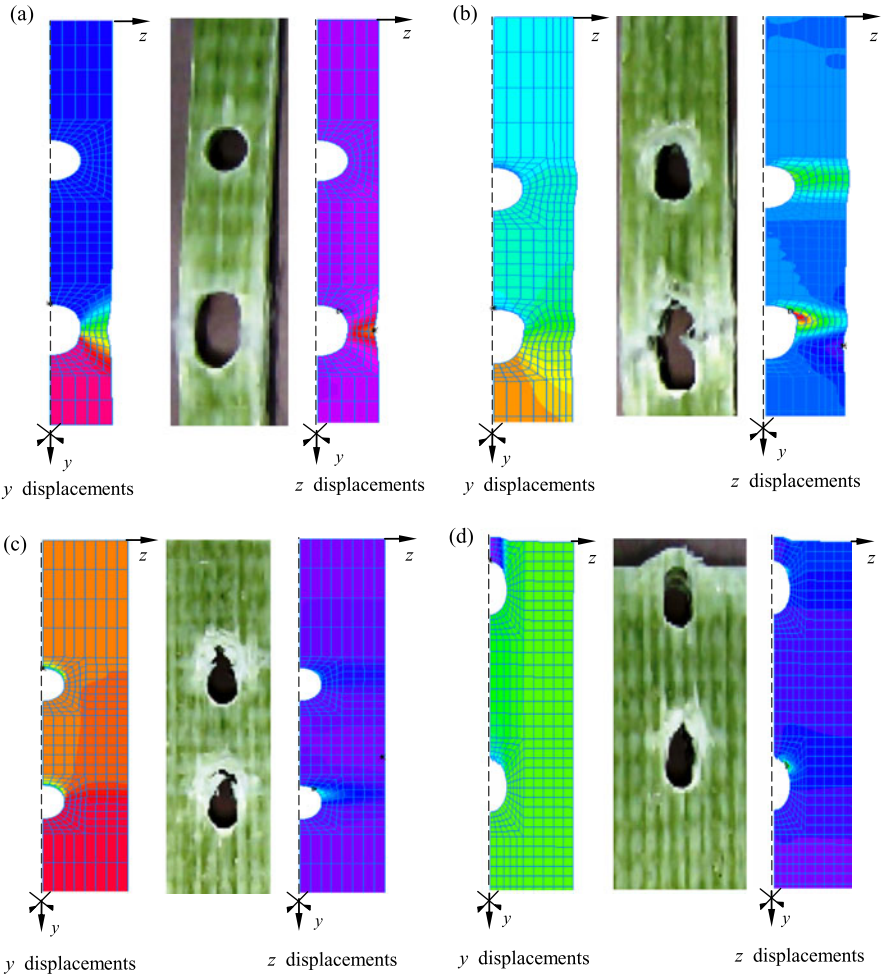

Fig. 20 Two-serial pins-loaded plate of Fig. 5. Failure modes predicted by numerical simulations against experimentally detected ones (after Karakuzu et al. [12]): (**a**) Net-tension at inner hole and no failure at outer hole for $W/D = 2$, $M/D = 4$, $E/D = 4$; (**b**) Net-tension at inner hole and bearing at outer hole for $W/D = 3$, $M/D = 4$, $E/D = 5$; (**c**) Bearing at inner hole and bearing at outer hole for $W/D = 4$, $M/D = 4$, $E/D = 5$; (**d**) Bearing at inner hole and shear-out at outer hole for $W/D = 5$, $M/D = 4$, $E/D = 1$

urations. In the above tables, as usual in the relevant literature, the symbol B means bearing, N net-tension, S shear-out, while when more symbols appear separated by slash (/) the first refers to the failure mode of the outer hole the second to that of the inner hole; eventually the symbol (–) means that no failure occurred at the considered hole.

In Figs. 17–21 the photographs of some tested specimens, at the joint failure stage, are reported together with the band plots, on the FE mesh, of the node dis-

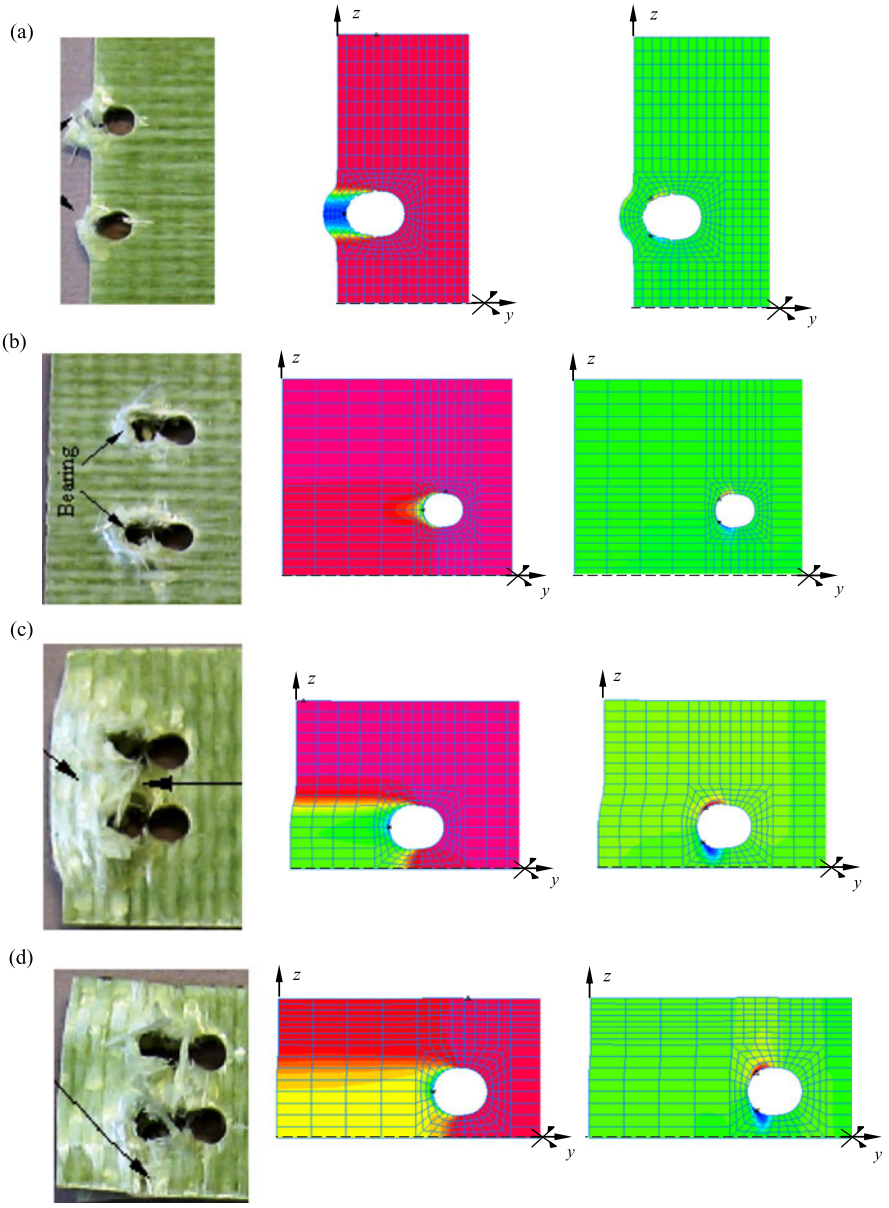

Fig. 21 Two-parallel pins-loaded plate of Fig. 5. Failure modes predicted by numerical simulations against experimentally detected ones (after Karakuzu et al. [13]): (**a**) Shear-out for $K/D = 4$, $M/D = 4$, $E/D = 1$; (**b**) Bearing for $K/D = 4$, $M/D = 4$, $E/D = 5$; (**c**) Bearing and Shear-out for $K/D = 3$, $M/D = 2$, $E/D = 3$; (**d**) Bearing and net-tension for $K/D = 2$, $M/D = 2$, $E/D = 4$

placement rates components (in y and z directions) at collapse. The latter, evaluated at last converged iteration of the LMM procedure, locate the distribution of the displacement rates the real structure exhibits at a state of incipient collapse, i.e. the one attained when the loads reach their peak value or, the computed upper bound value on it. Such distribution furnishes the searched failure mode but, obviously, only from a qualitative point of view; what it is meaningful is, in practice, only the direction of the computed displacement rates. By inspection of these figures it can be stated that the present procedure seems able to predict, in a quite good manner, the three multi-pin joints basic failure modes of bearing, shear-out and net-tension.

7 Concluding Remarks

The results of recent studies, concerning a design methodology based on numerical limit analysis and aimed at the evaluation of the load bearing capacity of single- and multi-pin joints in orthotropic composite laminates, have been presented.

The proposed methodology uses two numerical methods for limit analysis: the Linear Matching Method and the Elastic Compensation Method. The lack of associativity, postulated for the adopted Tsai-Wu-type yield criterion for orthotropic laminates, obliges to search for an upper and a lower bound to the joint peak load multiplier, the former pursued by the LMM, the latter by the ECM.

Both methods have been rephrased and adapted to the assumed yield criterion and to a layered treatment of the tackled mechanical problem. It is worth noting that the limit analysis carried out at lamina level, taking into account the stacking sequence of the laminate, appears very effective to deal with many of the through-thickness effects influencing the joint behaviour. Such layered formulation is indeed of general applicability.

The results, obtained for a remarkable number of tests on real prototypes, show a good ability of the expounded methodology to bracket the peak load detected via laboratory tests; a fairly good skillfulness to localize the collapse zone and to predict the related collapse mode; a good performance of the layered approach when dealing with different joint geometries and laminate lay-ups.

Such information are definitively very useful, at least at a preliminary stage of a design process. Concerning the tackled problem for example, limit analysis can be used for some design choices either related to the laminate setting, e.g. better lay-up, or appropriate components, for example, or the joint setting, in terms of fastener holes distribution, holes dimensions, ratios between fasteners and laminate geometrical parameters, etc. Once a good prototype has been settled more accurate and expensive numerical analyses or experimental tests can be carried out on it with considerable saving of money and time. Extension of such approach to other problems of engineering interest seem straightforward.

References

1. ADINA R & D Inc (2002) Theory and modeling guide. ADINA R & D, Watertown
2. Aktas A, Dirikolu MH (2004) An experimental and numerical investigation of strength characteristics of carbon-epoxy pinned-joint plates. Compos Sci Technol 64:1605–1611
3. Ascione F, Feo L, Maceri F (2009) An experimental investigation on the bearing failure load of glass fibre/epoxy laminates. Composites, Part B, Eng 40:197–205
4. Ascione F, Feo L, Maceri F (2010) On the pin-bearing failure load of GFRP bolted laminates: an experimental analysis on the influence of bolt diameter. Composites, Part B, Eng 41:482–490
5. Bathe KJ (1996) Finite element procedures. Prentice-Hall, New Jersey
6. Camanho PP, Matthews FL (1997) Stress analysis and strength prediction of mechanically fasteners joints in FRP: a review. Composites, Part A, Appl Sci Manuf 28(A):529–547
7. Capsoni A, Corradi L, Vena P (2001) Limit analysis of anisotropic structures based on the kinematic theorem. Int J Plast 17:1531–1549
8. Chen HF, Ponter ARS (2001) Shakedown and limit analyses for 3-D structures using the linear matching method. Int J Press Vessels Piping 78(6):443–451
9. Feo L, Marra G, Mosallam AS (2012) Stress analysis of multi-bolted joints for FRP pultruded composite structures. Compos Struct 94:3769–3780
10. Godwin EW, Matthews FL (1980) Review of the strengths of joints in fibre-reinforced plastics, part 1: mechanically fastened joints. Composites 11(3):155–160
11. Guillermin O, Kojić M, Bathe KJ (1990) Linear and nonlinear analysis of composite shells. In: Proceedings STRUCOME 90, Paris, France
12. Karakuzu R, Çalişkan CR, Aktaş M, İçten BM (2008) Failure behavior of laminated composite plates with two serial pin-loaded holes. Compos Struct 82:225–234
13. Karakuzu R, Taylak N, İçten BM, Aktaş M (2008) Effects of geometric parameters on failure behavior of laminated composite plates with two parallel pin-loaded holes. Compos Struct 85:1–9
14. Karakuzu R, Demirgoren O, İçten BM, Deniz ME (2010) Failure behavior of quasi-isotropic laminates with three-pin loaded holes. Mater Des 31:3029–3032
15. Krabbenhøft K, Lyamin AV, Sloan SW (2007) Formulation and solution of some plasticity problems as conic programs. Int J Solids Struct 44:1533–1549
16. Le CV, Hguyen-Xuan H, Nguyen-Dang H (2010) Upper and lower bound limit analysis of plates using FEM and second-order cone programming. Comput Struct 88:65–73
17. Lubliner J (1990) Plasticity theory. Macmillan, New York
18. Mackenzie D, Boyle JT (1993) A method of estimating limit loads by iterative elastic analysis, parts I, II, III. Int J Press Vessels Piping 53:77–142
19. Makrodimopoulos A, Martin M (2006) Lower bound limit analysis of cohesive-frictional materials using second-order cone programming. Int J Numer Methods Eng 66:604–634
20. Makrodimopoulos A, Martin M (2007) Upper bound limit analysis using simplex strain elements and second-order cone programming. Int J Numer Anal Methods Geomech 31:835–865
21. Mackerle J (2003) Finite element analysis of fastening and joining: a bibliography (1990–2002). Int J Press Vessels Piping 80:253–271
22. Okutan Baba B (2006) Behavior of pin-loaded laminated composites. Exp Mech 46:589–600
23. Pisano AA, Fuschi P (2007) A numerical approach for limit analysis of orthotropic composite laminates. Int J Numer Methods Eng 70:71–93
24. Pisano AA, Fuschi P (2011) Mechanically fastened joints in composite laminates: evaluation of load bearing capacity. Composites, Part B, Eng 42:949–961
25. Pisano AA, Fuschi P, De Domenico D (2012) A layered limit analysis of pinned-joints composite laminates: numerical versus experimental findings. Composites, Part B, Eng 43:940–952
26. Pisano AA, Fuschi P, De Domenico D (2013) Peak load prediction of multi-pin joints FRP laminates by limit analysis. Compos Struct 96:763–772

27. Pisano AA, Fuschi P, De Domenico D (2013) Failure modes prediction of multi-pin joints FRP laminates by limit analysis. Composites, Part B, Eng 46:179–206
28. Ponter ARS, Carter KF (1997) Limit state solutions, based upon linear elastic solutions with spatially varying elastic modulus. Comput Methods Appl Mech Eng 140:237–258
29. Ponter ARS, Fuschi P, Engelhardt M (2000) Limit analysis for a general class of yield conditions. Eur J Mech A, Solids 19:401–421
30. Radenkovic D (1961) Théorèmes limites pour un materiau de Coulomb à dilatation non standardisée. C R Acad Sci Paris 252:4103–4104
31. Rowlands RE (1985) Strength (failure) theories and their experimental correlation. In: Sih GC, Skudra AM (eds) Handbook of composites, vol 3: failure mechanics of composites. Elsevier, Amsterdam, pp 71–125
32. Salençon J (1972) Écoulement plastique libre et analyse limite pour les matériaux standards et non standards. Ann ITBTP 295–296:90–100
33. Salençon J (1977) Application of the theory of plasticity in soil mechanics. Wiley, Chichester
34. Soden PD, Kaddour AS, Hinton MJ (2004) Recommendations for designer and researchers resulting from the word-wide failure exercise. Compos Sci Technol 64:589–604
35. Staat M, Heitzer M (2001) LISA—a European project for FEM-based limit and shakedown analysis. Nucl Eng Des 206:151–166
36. Staat M, Schwartz M, Lang H, Wirtz K, Heitzer M (2003) Design by analysis of pressure components by non-linear optimization. In: Zeman JL (ed) Pressure vessel technology. Proceedings ICPVT-10. Österreichische Gesellschaft für Schweißtechik, Vienna, pp 59–65
37. Thoppul SD, Finegan J, Gibson RF (2009) Mechanics of mechanically fastened joints in polymer-matrix composite structures-a review. Compos Sci Technol 69:301–329
38. Tsai SW, Hann HT (1980) Introduction to composite materials. Technomic, Westport
39. Tsai SW, Wu EM (1971) A general theory of strength for anisotropic materials. J Compos Mater 5:58–80
40. Vu DK, Staat M, Tran IT (2007) Analysis of pressure equipment by application of the primal-dual theory of shakedown. Commun Numer Methods Eng 23:213–225
41. Weichert D, Ponter ARS (2009) Limit states of materials and structures—direct methods. Springer, Berlin

Shakedown Analysis of Kinematically Hardening Structures in n-Dimensional Loading Spaces

Jaan-Willem Simon

Abstract Determining the load bearing capacity is essential for the design of engineering structures subjected to varying thermo-mechanical loadings. The according computations can be carried out most conveniently by using shakedown analysis. In order to obtain realistic results, however, limited kinematical hardening needs to be taken into account. Moreover, it is necessary to consider arbitrary numbers of loadings leading to n-dimensional loading spaces. Even so, the numerical tools available for shakedown analysis are—up to now—restricted to either perfectly-plastic material behavior or to a maximum of two independently varying loadings. Thus, the aim of this paper is to present a numerical procedure, which allows the consideration of limited kinematical hardening in n-dimensional loading spaces. The method is based on the lower bound shakedown theorem by Melan, which has been extended to limited kinematical hardening by use of a two-surface model. To solve the resulting nonlinear optimization problem, which is typically characterized by a large number of variables and constraints, an interior-point algorithm is implemented. Finally, the potential of the procedure is shown by application to a flanged pipe subjected to three independently varying thermal and mechanical loadings accounting for different yield stress to ultimate stress ratios.

1 Introduction

Determining the load bearing capacity is essential for the design of engineering structures subjected to varying thermo-mechanical loadings. This is a demanding task if the loads exceed the structure's elastic limit and problems of practical relevance are considered. In principle, two different methods can be used for this, the conventional step-by-step methods or so-called direct methods.

In the step-by-step methods, the loading path is divided into sufficiently small loading steps and a full analysis of the evolution of stresses and strains is carried out for each step. Besides the question of running time, the most obvious disadvantage

J.-W. Simon (✉)
Institute of Applied Mechanics, RWTH Aachen University, Mies-van-der-Rohe-Str. 1, 52074 Aachen, Germany
e-mail: jaan.simon@rwth-aachen.de

K. Spiliopoulos, D. Weichert (eds.), *Direct Methods for Limit States in Structures and Materials*, DOI 10.1007/978-94-007-6827-7_3,

of these methods is the fact that the exact knowledge of the complete loading history is essential for the calculation, which is not realistic in many cases.

This disadvantage can be overcome by the use of direct methods [26, 32, 78, 79]—comprising limit and shakedown analysis. Here, the loading path needs not to be given deterministically but only its bounding envelope. The basement of direct methods is constituted by the theorems of Koiter [25] and Melan [37, 38]. In the present work, the statical approach by Melan is used, which gives a lower bound of the loading factor. From practical point of view, the determination of the lower bound is of special interest because it leads in principle to conservative solutions.

Since in many engineering applications the materials exhibit kinematical hardening, the latter needs to be incorporated into the procedure in order to obtain realistic results. The statical shakedown theorem in its original formulation is valid for elastic-perfectly plastic continua as well as for unlimited kinematical hardening ones. Notably, accounting for only unlimited kinematical hardening does not cover incremental collapse but solely alternating plasticity, see e.g. [26, 27, 53, 81].

Thus, accounting for limited (or bounded) kinematical hardening is inevitable, and consequently has been addressed by several authors in the field of shakedown analysis, e.g. [13, 16, 20, 35, 43, 47–52, 57, 64–67, 76]. The first explicit formulation for limited kinematical hardening materials has been given by Weichert and Groß-Weege [76], who introduced a two-surface model. Almost at the same time, Stein and coauthors proposed another approach based on an overlay model [65–67], which leaded to an equivalent formulation. Later, Heitzer [24] showed how to transfer these approaches one to the other.

However, Melan's theorem leads to nonlinear optimization problems, which are typically characterized by large numbers of variables and constraints. In the present work, these optimization problems are solved via the widely used *interior-point method* [14, 15, 56, 80]. Commonly used codes based on interior-point methods are IPOPT [72–74], LOQO [6, 18, 69] and KNITRO [11, 75]. Comparative studies can be found in e.g. [7, 40, 72] and a valuable commented overview of existing optimization codes is given in [39]. In addition, in the last years the program MOSEK [3, 4] came into the picture of direct methods and has been applied for both (piecewise) linear and second-order conic problems, e.g. [8, 17, 29, 33, 46, 68] at least for reference solutions.

All of the above mentioned programs have already proven their abilities and robustness. Nonetheless, independent interior-point algorithms have been developed by several authors, e.g. [1, 21, 28, 30, 44, 45, 70, 71]. Compared to the above mentioned general codes, these algorithms are distinguished by problem-tailored solution strategies. This is extremely important especially in field of direct methods, because of the usually high number of variables and subsidiary conditions.

It should be mentioned, that a variety of alternative methods have been developed in recent years. For example, in [82] an eigen-mode method has been proposed, whereas the so-called Linear Matching Method has been suggested in [54, 55]. Further, a bipotential approach has been invented in [9, 10], and a homogenized method has been examined e.g. in [31]. In addition, in [5, 42] a piece-wise linearization of the yield surface is presented, while a strain-driven strategy is given in [17]. More

recently, a new direct method has been suggested in [63], in which the cyclic nature of the expected residual stress distribution at the steady cycle is investigated.

In any case, in the present paper, the convex optimization problem resulting from the statical shakedown theorem is solved via the interior-point algorithm IPSA recently developed by the author, which is especially tailored to shakedown analysis problems for von Mises-type materials. Founded on a previous interior-point algorithm IPDCA [1, 22, 23], which has been developed for elastic-perfectly plastic engineering problems with either one or two varying loads, the new algorithm is distinguished by a particularly problem-oriented solution strategy [58–60]. Moreover, IPSA is capable to solve shakedown problems with n-dimensional loading spaces [62], such that the examined structures can be subjected to arbitrary numbers of loadings. This is important, because only few other methods can deal with more than two loadings, see e.g. [34].

In addition, limited kinematical hardening has already been introduced for two-dimensional loading spaces [61]. In this paper, an extension of this algorithm is presented, such that limited kinematical hardening can be considered in n-dimensional loading spaces. The method's potential is illustrated by application to a numerical example. In particular, the shakedown domain for a flanged pipe subjected to three independently varying thermo-mechanical loads is presented.

2 Lower Bound Shakedown Analysis

The current formulation is based on the statical shakedown theorem by MELAN [38]. This states that a structure will shake down, if there exists a time-independent residual stress field $\bar{\boldsymbol{\rho}}(\boldsymbol{X})$, such that the yield condition $f[\boldsymbol{\sigma}(\boldsymbol{X},t)] \leq 0$ is satisfied for any loading path in the considered loading domain at any time t and in any point $\boldsymbol{X}$ of the structure. For the mathematical formulation, the total stress $\boldsymbol{\sigma}(\boldsymbol{X},t)$ is decomposed into an elastic stress $\boldsymbol{\sigma}^E(\boldsymbol{X},t)$ and a residual stress $\boldsymbol{\rho}(\boldsymbol{X},t)$ induced by the evolution of plastic strains

$$\boldsymbol{\sigma}(\boldsymbol{X},t) = \boldsymbol{\sigma}^E(\boldsymbol{X},t) + \boldsymbol{\rho}(\boldsymbol{X},t). \tag{1}$$

Here, $\boldsymbol{\sigma}^E(\boldsymbol{X},t)$ denotes the stress state, which would occur in a fictitious purely elastic reference body under the same conditions as the original one. Clearly, the residual stresses satisfy the equilibrium condition, which can be transferred to a system of linear equations using the principle of virtual work, as shown e.g. in [19]

$$\sum_{r=1}^{NG} \mathbb{C}_r \cdot \bar{\boldsymbol{\rho}}_r = \mathbf{0}. \tag{2}$$

Hereby, the system has been discretized using the finite element method (FEM) and thus the stresses are approximately evaluated in the GAUSS points $r \in [1, NG]$. The equilibrium matrices $\mathbb{C}_r$ depend on the geometry and the chosen element type.

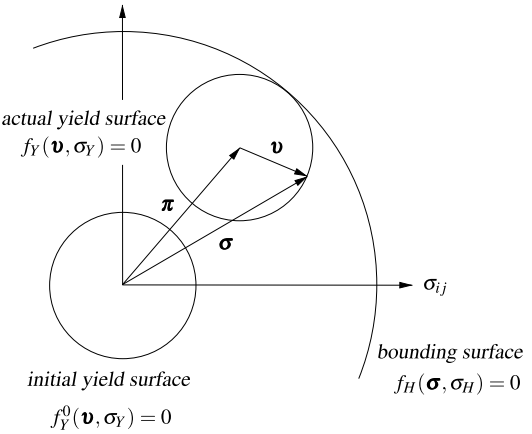

Fig. 1 Kinematical hardening considered as translation of the yield surface in stress space

The kinematical boundary conditions are taken into account considering the virtual displacements to be kinematical admissible.

Let the considered body be subjected to NL varying loads. Then, the according loading domain is polyhedral with $NC = 2^{NL}$ corners. As shown in [26], it is sufficient to only consider these corners to ensure shakedown for all possible loading paths inside of the loading domain. Then, introducing the loading factor $\alpha > 1$, Melan's statical shakedown theorem can be formulated as an optimization problem:

$$(\mathcal{P}_{Melan}) \quad \alpha_{SD} = \max \alpha$$

$$\sum_{r=1}^{NG} \mathbb{C}_r \cdot \bar{\boldsymbol{\rho}}_r = \mathbf{0}, \tag{3a}$$

$$f\left(\alpha \boldsymbol{\sigma}_r^{E,j} + \bar{\boldsymbol{\rho}}_r, \sigma_{Y,r}\right) \leq 0, \quad \forall j \in [1, NC],\ \forall r \in [1, NG]. \tag{3b}$$

3 Accounting for Limited Kinematical Hardening

In order to take into account the limited kinematical hardening we use the two-surface model proposed by WEICHERT and GROSS-WEEGE [76]. The kinematical hardening is considered as a rigid body motion of the yield surface in stress space, which is described by the six-dimensional vector of back-stresses $\boldsymbol{\pi}$ representing the translation of the yield surface's center, Fig. 1. Through the introduction of a second surfaces corresponding to the ultimate stress σ_H, the motion of the yield surface is bounded.

Thereby, the total stresses are divided into the back stresses $\boldsymbol{\pi}$ and the reduced stresses $\boldsymbol{\upsilon}$, which are responsible for the occurrence of plastic strains

$$\boldsymbol{\sigma}(\boldsymbol{X}, t) = \boldsymbol{\pi}(\boldsymbol{X}, t) + \boldsymbol{\upsilon}(\boldsymbol{X}, t). \tag{4}$$

As before, the total stresses are decomposed, $\boldsymbol{\sigma}_r^j = \alpha \boldsymbol{\sigma}_r^{E,j} + \bar{\boldsymbol{\rho}}_r$. In an analogous manner, the reduced stresses $\boldsymbol{\upsilon}_r^j$ can be formulated, keeping in mind that the back stresses are time-independent and thus not dependent on the considered corner j of the loading domain, because the bounding surface is fixed in stress space

$$\boldsymbol{\upsilon}_r^j = \boldsymbol{\sigma}_r^j - \bar{\boldsymbol{\pi}}_r = \alpha \boldsymbol{\sigma}_r^{E,j} + \bar{\boldsymbol{\rho}}_r - \bar{\boldsymbol{\pi}}_r. \tag{5}$$

Thereby, Melan's theorem accounting for limited kinematical hardening reads as follows:

$$\begin{aligned}
\left(\mathcal{P}_{Melan}^H\right) \quad & \alpha_{SD} = \max \alpha \\
& \sum_{r=1}^{NG} \mathbb{C}_r \cdot \bar{\boldsymbol{\rho}}_r = \mathbf{0}, && \text{(6a)} \\
& \forall j \in [1, NC],\ \forall r \in [1, NG]: \\
& f_H\left(\alpha \boldsymbol{\sigma}_r^{E,j} + \bar{\boldsymbol{\rho}}_r, \sigma_{H,r}\right) \leq 0, && \text{(6b)} \\
& f_Y\left(\alpha \boldsymbol{\sigma}_r^{E,j} + \bar{\boldsymbol{\rho}}_r - \bar{\boldsymbol{\pi}}_r, \sigma_{Y,r}\right) \leq 0. && \text{(6c)}
\end{aligned}$$

4 Solution with Interior-Point Method

For a clear presentation, the problem is rewritten in the following form. To achieve this, several transformations are necessary, which are not in the scope of this paper but can be followed in [59, 60]

$$\begin{aligned}
\left(\mathcal{P}_{IP}^H\right) \quad & \min f(\boldsymbol{x}) = -\alpha \\
& \boldsymbol{A}_H \cdot \boldsymbol{x} = \mathbf{0}, && \text{(7a)} \\
& \boldsymbol{c}_H(\boldsymbol{x}) \geq \mathbf{0}, && \text{(7b)} \\
& \boldsymbol{c}_Y(\boldsymbol{x}) \geq \mathbf{0}, && \text{(7c)} \\
& \boldsymbol{x} \in \mathbb{R}^n. && \text{(7d)}
\end{aligned}$$

The problem $(\mathcal{P}_{IP}^H)$ consists of n variables, merged to the solution vector $\boldsymbol{x}$, m_E equality constraints, represented by the affine linear system equation (7a), and $2m_I$ nonlinear concave inequality constraint equations (7b) and (7c). The equality constraints can be interpreted as equilibrium condition for the residual stress equations (2), whereas the inequality constraints represent the yield and the bounding condition Eqs. (6b) and (6c), respectively. The inequality constraints are converted into equality constraints by introducing slack variables $\boldsymbol{w}_H \in \mathbb{R}^{m_I}$ and $\boldsymbol{w}_Y \in \mathbb{R}^{m_I}$. Moreover, split variables $\boldsymbol{y} \in \mathbb{R}^n$ and $\boldsymbol{z} \in \mathbb{R}^n$ are used in order to avoid numerical instabilities due to the unboundedness of the solution vector Eq. (7d). Then, applying the interior-point method the objective function is perturbed by logarithmic barrier

terms, which penalize directions leading outside of the feasible region. Thereby, the barrier parameter μ is introduced, which is tending to zero during the iteration.

$$f_\mu(\boldsymbol{x}, \boldsymbol{y}, \boldsymbol{z}, \boldsymbol{w}_H, \boldsymbol{w}_Y) = f(\boldsymbol{x}) - \mu \left[\sum_{i=1}^{n} \log(y_i) + \sum_{i=1}^{n} \log(z_i) + \sum_{j=1}^{m_I} \log(w_{H,j}) + \sum_{j=1}^{m_I} \log(w_{Y,j}) \right]. \quad (8)$$

The resulting optimization problem can then be expressed as follows:

$$\begin{aligned} \left(\mathcal{P}_\mu^H\right) \quad & \min f_\mu(\boldsymbol{x}, \boldsymbol{y}, \boldsymbol{z}, \boldsymbol{w}_H, \boldsymbol{w}_Y) \\ & \boldsymbol{A}_H \cdot \boldsymbol{x} = \boldsymbol{0}, && (9a) \\ & \boldsymbol{c}_H(\boldsymbol{x}) - \boldsymbol{w}_H = \boldsymbol{0}, && (9b) \\ & \boldsymbol{c}_Y(\boldsymbol{x}) - \boldsymbol{w}_Y = \boldsymbol{0}, && (9c) \\ & \boldsymbol{x} - \boldsymbol{y} + \boldsymbol{z} = \boldsymbol{0}, && (9d) \\ & \boldsymbol{w}_H > \boldsymbol{0}, \qquad \boldsymbol{w}_Y > \boldsymbol{0}, \qquad \boldsymbol{y} > \boldsymbol{0}, \qquad \boldsymbol{z} > \boldsymbol{0} && (9e) \end{aligned}$$

Since the underlying optimization problem $(\mathcal{P}_{IP}^H)$ is convex and regular, the KARUSH-KUHN-TUCKER condition is both necessary and sufficient, which states that the solution is optimal if the Lagrangian $\mathcal{L}_H$ of the problem possesses a saddle point

$$\begin{aligned} \mathcal{L}_H = f_\mu(\boldsymbol{x}, \boldsymbol{y}, \boldsymbol{z}, \boldsymbol{w}_H, \boldsymbol{w}_Y) - \boldsymbol{\lambda}_E \cdot (\boldsymbol{A}_H \cdot \boldsymbol{x}) - \boldsymbol{\lambda}_H \cdot \left(\boldsymbol{c}_H(\boldsymbol{x}) - \boldsymbol{w}_H\right) \\ - \boldsymbol{\lambda}_Y \cdot \left(\boldsymbol{c}_Y(\boldsymbol{x}) - \boldsymbol{w}_Y\right) - \boldsymbol{s} \cdot (\boldsymbol{x} - \boldsymbol{y} + \boldsymbol{z}), \end{aligned} \quad (10)$$

where $\boldsymbol{\lambda}_E \in \mathbb{R}^{m_E}$, $\boldsymbol{\lambda}_H \in \mathbb{R}_+^{m_I}$, $\boldsymbol{\lambda}_Y \in \mathbb{R}_+^{m_I}$ and $\boldsymbol{s} \in \mathbb{R}_+^n$ are appropriate Lagrange multipliers. Thereby, the saddle point condition reads as follows:

$$\begin{aligned} \nabla_x \mathcal{L}_H &= \nabla_x f(\boldsymbol{x}) - \boldsymbol{A}_H^T \cdot \boldsymbol{\lambda}_E - \boldsymbol{C}_H^T(\boldsymbol{x}) \cdot \boldsymbol{\lambda}_H - \boldsymbol{C}_Y^T(\boldsymbol{x}) \cdot \boldsymbol{\lambda}_Y - \boldsymbol{s} = \boldsymbol{0}, && (11a) \\ \nabla_y \mathcal{L}_H &= -\mu \boldsymbol{Y}^{-1} \cdot \boldsymbol{e} + \boldsymbol{s} = \boldsymbol{0}, && (11b) \\ \nabla_z \mathcal{L}_H &= -\mu \boldsymbol{Z}^{-1} \cdot \boldsymbol{e} - \boldsymbol{s} = \boldsymbol{0}, && (11c) \\ \nabla_{w_H} \mathcal{L}_H &= -\mu \boldsymbol{W}_H^{-1} \cdot \boldsymbol{e} + \boldsymbol{\lambda}_H = \boldsymbol{0}, && (11d) \\ \nabla_{w_Y} \mathcal{L}_H &= -\mu \boldsymbol{W}_Y^{-1} \cdot \boldsymbol{e} + \boldsymbol{\lambda}_Y = \boldsymbol{0}, && (11e) \\ \nabla_{\lambda_E} \mathcal{L}_H &= -(\boldsymbol{A}_H \cdot \boldsymbol{x}) = \boldsymbol{0}, && (11f) \\ \nabla_{\lambda_H} \mathcal{L}_H &= -\left(\boldsymbol{c}_H(\boldsymbol{x}) - \boldsymbol{w}_H\right) = \boldsymbol{0}, && (11g) \\ \nabla_{\lambda_Y} \mathcal{L}_H &= -\left(\boldsymbol{c}_Y(\boldsymbol{x}) - \boldsymbol{w}_Y\right) = \boldsymbol{0}, && (11h) \\ \nabla_s \mathcal{L}_H &= -(\boldsymbol{x} - \boldsymbol{y} + \boldsymbol{z}) = \boldsymbol{0} && (11i) \end{aligned}$$

where: $\boldsymbol{C}_H(\boldsymbol{x}) = \boldsymbol{c}_H(\boldsymbol{x}) \nabla_x \in \mathbb{R}^{m_I \times n}$ and $\boldsymbol{C}_Y(\boldsymbol{x}) = \boldsymbol{c}_Y(\boldsymbol{x}) \nabla_x \in \mathbb{R}^{m_I \times n}$.

For consistency during the iteration, the new variable $\boldsymbol{r} = -\boldsymbol{s}$ is introduced into Eq. (11c). Both of these variables are tending to zero during the iteration. In addition, Eqs. (11b)–(11e) are multiplied by the matrices $\boldsymbol{Y}$, $\boldsymbol{Z}$, $\boldsymbol{W}_H$ and $\boldsymbol{W}_Y$, respectively. Merging all variables of the problem to the vector $\boldsymbol{\Pi}$, the resulting system of optimality conditions can be expressed by the function $\boldsymbol{F}_{\mu}^{H}(\boldsymbol{\Pi})$:

$$\boldsymbol{F}_{\mu}^{H}(\boldsymbol{\Pi}) = -\begin{pmatrix} -\nabla_x f(\boldsymbol{x}) + \boldsymbol{A}_H^T \cdot \boldsymbol{\lambda}_E + \boldsymbol{C}_H^T(\boldsymbol{x}) \cdot \boldsymbol{\lambda}_H + \boldsymbol{C}_Y^T(\boldsymbol{x}) \cdot \boldsymbol{\lambda}_Y + \boldsymbol{s} \\ \mu \boldsymbol{e} - \boldsymbol{Y} \cdot \boldsymbol{S} \cdot \boldsymbol{e} \\ \mu \boldsymbol{e} - \boldsymbol{Z} \cdot \boldsymbol{R} \cdot \boldsymbol{e} \\ \mu \boldsymbol{e} - \boldsymbol{W}_H \cdot \boldsymbol{\Lambda}_H \cdot \boldsymbol{e} \\ \mu \boldsymbol{e} - \boldsymbol{W}_Y \cdot \boldsymbol{\Lambda}_Y \cdot \boldsymbol{e} \\ \boldsymbol{A}_H \cdot \boldsymbol{x} \\ \boldsymbol{c}_H(\boldsymbol{x}) - \boldsymbol{w}_H \\ \boldsymbol{c}_Y(\boldsymbol{x}) - \boldsymbol{w}_Y \\ \boldsymbol{x} - \boldsymbol{y} + z \\ \boldsymbol{r} + \boldsymbol{s} \end{pmatrix} = \boldsymbol{0}. \tag{12}$$

Equation (12) constitutes a system of nonlinear equations, which will be linearized using the NEWTON method. The variables $\boldsymbol{\Pi}_{k+1}$ of the subsequent iteration step $k+1$ are computed from the variables $\boldsymbol{\Pi}_k$ of the previous one k and the step values $\Delta\boldsymbol{\Pi}_k$:

$$\boldsymbol{\Pi}_{k+1} = \boldsymbol{\Pi}_k + \Upsilon_k \Delta\boldsymbol{\Pi}_k, \tag{13}$$

where Υ_k denotes a matrix of damping factors, which is introduced for numerical reasons. The step values $\Delta\boldsymbol{\Pi}_k$ are determined from the following linearized system of equations

$$\boldsymbol{J}(\boldsymbol{\Pi}_k) \cdot \Delta\boldsymbol{\Pi}_k = -\nabla_{\Pi}\mathcal{L}_H(\boldsymbol{\Pi}_k) \quad \text{where: } \boldsymbol{J}(\boldsymbol{\Pi}_k) = \nabla_{\Pi}\mathcal{L}_H(\boldsymbol{\Pi})\nabla_{\Pi}|_{\boldsymbol{\Pi}=\boldsymbol{\Pi}_k}. \tag{14}$$

The Jacobian $\boldsymbol{J}(\boldsymbol{\Pi})$ of the function $\boldsymbol{F}_{\mu}^{H}(\boldsymbol{\Pi})$ can be expressed as follows:

$$\boldsymbol{J}(\boldsymbol{\Pi}) = \begin{pmatrix} \nabla_x^2\mathcal{L}_H & \boldsymbol{0} & \boldsymbol{0} & \boldsymbol{0} & \boldsymbol{0} & -\boldsymbol{A}_H^T & -\boldsymbol{C}_H^T(\boldsymbol{x}) & -\boldsymbol{C}_Y^T(\boldsymbol{x}) & -\boldsymbol{I}_n & \boldsymbol{0} \\ \boldsymbol{0} & \boldsymbol{S} & \boldsymbol{0} & \boldsymbol{0} & \boldsymbol{0} & \boldsymbol{0} & \boldsymbol{0} & \boldsymbol{0} & \boldsymbol{Y} & \boldsymbol{0} \\ \boldsymbol{0} & \boldsymbol{0} & \boldsymbol{R} & \boldsymbol{0} & \boldsymbol{0} & \boldsymbol{0} & \boldsymbol{0} & \boldsymbol{0} & \boldsymbol{0} & \boldsymbol{Z} \\ \boldsymbol{0} & \boldsymbol{0} & \boldsymbol{0} & \boldsymbol{\Lambda}_H & \boldsymbol{0} & \boldsymbol{0} & \boldsymbol{W}_H & \boldsymbol{0} & \boldsymbol{0} & \boldsymbol{0} \\ \boldsymbol{0} & \boldsymbol{0} & \boldsymbol{0} & \boldsymbol{0} & \boldsymbol{\Lambda}_Y & \boldsymbol{0} & \boldsymbol{0} & \boldsymbol{W}_Y & \boldsymbol{0} & \boldsymbol{0} \\ -\boldsymbol{A}_H & \boldsymbol{0} & \boldsymbol{0} & \boldsymbol{0} & \boldsymbol{0} & \boldsymbol{0} & \boldsymbol{0} & \boldsymbol{0} & \boldsymbol{0} & \boldsymbol{0} \\ -\boldsymbol{C}_H(\boldsymbol{x}) & \boldsymbol{0} & \boldsymbol{0} & \boldsymbol{I}_{m_I} & \boldsymbol{0} & \boldsymbol{0} & \boldsymbol{0} & \boldsymbol{0} & \boldsymbol{0} & \boldsymbol{0} \\ -\boldsymbol{C}_Y(\boldsymbol{x}) & \boldsymbol{0} & \boldsymbol{0} & \boldsymbol{0} & \boldsymbol{I}_{m_I} & \boldsymbol{0} & \boldsymbol{0} & \boldsymbol{0} & \boldsymbol{0} & \boldsymbol{0} \\ -\boldsymbol{I}_n & \boldsymbol{I}_n & -\boldsymbol{I}_n & \boldsymbol{0} & \boldsymbol{0} & \boldsymbol{0} & \boldsymbol{0} & \boldsymbol{0} & \boldsymbol{0} & \boldsymbol{0} \\ \boldsymbol{0} & \boldsymbol{0} & \boldsymbol{0} & \boldsymbol{0} & \boldsymbol{0} & \boldsymbol{0} & \boldsymbol{0} & \boldsymbol{0} & -\boldsymbol{I}_n & -\boldsymbol{I}_n \end{pmatrix}. \tag{15}$$

The system Eq. (14) is reduced by successive elimination of those equations, which involve diagonal matrices. After substituting the variables $\Delta\boldsymbol{s}$, $\Delta\boldsymbol{r}$, $\Delta\boldsymbol{y}$, Δz,

$\Delta \boldsymbol{w}_H$ and $\Delta \boldsymbol{w}_Y$, the following system remains:

$$\begin{pmatrix} -(\nabla_x^2 \mathcal{L}_H + \boldsymbol{E}_1) & \boldsymbol{A}_H^T & \boldsymbol{C}_H^T(\boldsymbol{x}) & \boldsymbol{C}_Y^T(\boldsymbol{x}) \\ \boldsymbol{A}_H & \boldsymbol{0} & \boldsymbol{0} & \boldsymbol{0} \\ \boldsymbol{C}_H(\boldsymbol{x}) & \boldsymbol{0} & \boldsymbol{E}_H & \boldsymbol{0} \\ \boldsymbol{C}_Y(\boldsymbol{x}) & \boldsymbol{0} & \boldsymbol{0} & \boldsymbol{E}_Y \end{pmatrix} \cdot \begin{pmatrix} \Delta \boldsymbol{x} \\ \Delta \boldsymbol{\lambda}_E \\ \Delta \boldsymbol{\lambda}_H \\ \Delta \boldsymbol{\lambda}_Y \end{pmatrix} = \begin{pmatrix} \boldsymbol{d}_1 \\ \boldsymbol{d}_2 \\ \boldsymbol{d}_3^H \\ \boldsymbol{d}_3^Y \end{pmatrix}. \tag{16}$$

The right-hand side values are as follows:

$$\boldsymbol{d}_1 = \nabla_x f(\boldsymbol{x}) - \boldsymbol{A}_H^T \cdot \boldsymbol{\lambda}_E - \boldsymbol{C}_H^T(\boldsymbol{x}) \cdot \boldsymbol{\lambda}_H - \boldsymbol{C}_Y^T(\boldsymbol{x}) \cdot \boldsymbol{\lambda}_Y - \boldsymbol{s} + \boldsymbol{E}_1 \cdot \boldsymbol{b}_1, \tag{17a}$$

$$\boldsymbol{d}_2 = -\boldsymbol{A}_H \cdot \boldsymbol{x}, \tag{17b}$$

$$\boldsymbol{d}_3^H = -\boldsymbol{c}_H(\boldsymbol{x}) + \mu \boldsymbol{\Lambda}_H^{-1} \cdot \boldsymbol{e}, \tag{17c}$$

$$\boldsymbol{d}_3^Y = -\boldsymbol{c}_Y(\boldsymbol{x}) + \mu \boldsymbol{\Lambda}_Y^{-1} \cdot \boldsymbol{e} \tag{17d}$$

where:

$$\boldsymbol{b}_1 = \boldsymbol{x} + \boldsymbol{z} + \mu\left(\boldsymbol{R}^{-1} - \boldsymbol{S}^{-1}\right) \cdot \boldsymbol{e} + \boldsymbol{R}^{-1} \cdot \boldsymbol{Z} \cdot \boldsymbol{s}, \tag{17e}$$

$$\boldsymbol{E}_1 = \left(\boldsymbol{S}^{-1} \cdot \boldsymbol{Y} + \boldsymbol{R}^{-1} \cdot \boldsymbol{Z}\right)^{-1}, \tag{17f}$$

$$\boldsymbol{E}_H = \boldsymbol{W}_H \cdot \boldsymbol{\Lambda}_H^{-1}, \tag{17g}$$

$$\boldsymbol{E}_Y = \boldsymbol{W}_Y \cdot \boldsymbol{\Lambda}_Y^{-1}. \tag{17h}$$

5 Numerical Aspects

The new algorithm has already been presented in [59], and some numerical aspects have been discussed in [60]. Here, only the most important issues are briefly recapitulated. The algorithm's mode of operation is illustrated in Fig. 2.

As one can see, there exist two different iterations:

- The ***outer iteration*** is the major loop in Fig. 2, where in each iteration step the barrier parameter μ is reduced in accordance with the update-rule. Thereby, during the outer iteration process, μ is a sequence tending to zero.
- The ***inner iteration*** is the minor loop in Fig. 2, which ensures that the approximate solution of the linearized system is in the close proximity of the exact solution, such that the KKT conditions are satisfied sufficiently accurate.

Since the full Newton step $\Delta \boldsymbol{\Pi}_k$ computed from Eq. (14) may happen to be too large, it has to be damped in these cases. This is done by a linesearch procedure, which actually is a third iteration within the outer and the inner one.

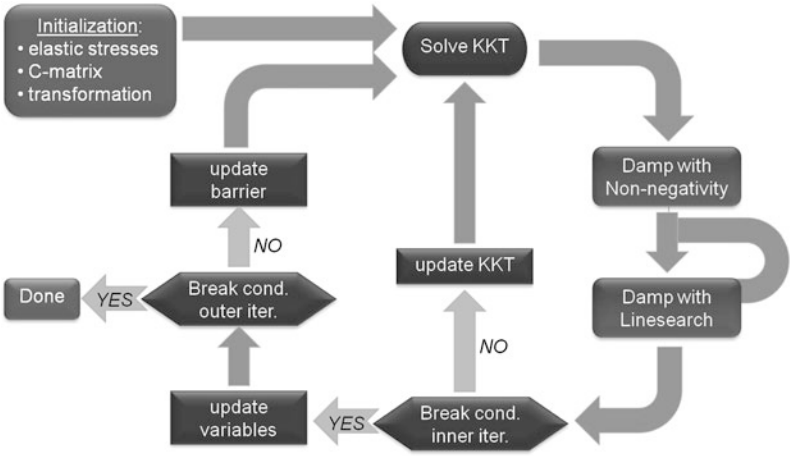

Fig. 2 Sketch of the algorithm's mode of operation

5.1 Starting Point Strategy

The choice of an admissible starting point is a critical issue when using interior-point methods. Fortunately, this does not hold for the specific problem considered here, because any solution vector $\boldsymbol{x}$ representing a stress state within the elastic limit domain is admissible. Thus, the initial solution vector $\boldsymbol{x}_0$ is computed from the elastic limit stresses and the back-stresses are initialized with zeroes. In order to stay inside of the strict interior of the elastic domain, these values are multiplied by the constant factor $\alpha_0 = 0.995$.

$$\boldsymbol{x}_0 = \boldsymbol{x}(\boldsymbol{\sigma} = \alpha_0 \boldsymbol{\sigma}_{el}). \tag{18}$$

With this choice for the initial solution vector, the condition Eq. (9a) is satisfied *a priori*. The other variables can be fitted such that the remaining conditions from Eq. (12) are satisfied as well. Note, that one of the variables can be chosen arbitrarily. Moreover, the condition $\boldsymbol{r} = -\boldsymbol{s}$ cannot be satisfied by any choice of positive $\boldsymbol{r}_0$ and $\boldsymbol{s}_0$. This condition is necessary to enforce $\boldsymbol{r}$ and $\boldsymbol{s}$ to be sequences tending to zero during the iteration, though. Except of this, the starting point $\boldsymbol{\Pi}_0$ is feasible.

5.2 Damping of the Newton Step

The full Newton step $\Delta\boldsymbol{\Pi}_k$ computed from Eq. (14) may happen to be too large in the sense that one or more of the Lagrange multipliers, the slack or the split variables become negative. Since these have to be nonnegative by definition, the Newton step is damped in these cases.

For this reason, the damping factors α_i are introduced, which are merged into the diagonal matrix $\boldsymbol{\Upsilon}_k$ in Eq. (13). In principle, damping factors can be defined for each of the variables separately. Nonetheless, it is common practice in linear and nonlinear programs to use two different values α_P for the primal variables $\boldsymbol{\Pi}_P$ and α_D for the dual variables $\boldsymbol{\Pi}_D$

$$\boldsymbol{\Pi}_P = [\boldsymbol{x}, \boldsymbol{y}, \boldsymbol{z}, \boldsymbol{w}_Y, \boldsymbol{w}_H]^T, \tag{19a}$$

$$\boldsymbol{\Pi}_D = [\boldsymbol{\lambda}_E, \boldsymbol{\lambda}_Y, \boldsymbol{\lambda}_H, \boldsymbol{s}, \boldsymbol{r}]^T. \tag{19b}$$

The two according sets of enforced nonnegative variables are denoted by $\boldsymbol{\Pi}_P^* = [\boldsymbol{y}, \boldsymbol{z}, \boldsymbol{w}_Y, \boldsymbol{w}_H]^T$ and $\boldsymbol{\Pi}_D^* = [\boldsymbol{\lambda}_Y, \boldsymbol{\lambda}_H, \boldsymbol{s}, \boldsymbol{r}]^T$, respectively

$$\boldsymbol{\Pi}_P^* = [\boldsymbol{y}, \boldsymbol{z}, \boldsymbol{w}_Y, \boldsymbol{w}_H]^T, \tag{20a}$$

$$\boldsymbol{\Pi}_D^* = [\boldsymbol{\lambda}_Y, \boldsymbol{\lambda}_H, \boldsymbol{s}, \boldsymbol{r}]^T. \tag{20b}$$

Then, the damping factors for the nonnegativity condition read as follows:

$$\tilde{\alpha}_P = \max\left\{\bar{\alpha} \;\middle|\; \boldsymbol{\Pi}_P^* + \bar{\alpha}\Delta\boldsymbol{\Pi}_P^* \geq \boldsymbol{0};\ \boldsymbol{\Pi}_P^* = [\boldsymbol{y}, \boldsymbol{z}, \boldsymbol{w}_Y, \boldsymbol{w}_H]^T\right\}, \tag{21a}$$

$$\tilde{\alpha}_D = \max\left\{\bar{\alpha} \;\middle|\; \boldsymbol{\Pi}_D^* + \bar{\alpha}\Delta\boldsymbol{\Pi}_D^* \geq \boldsymbol{0};\ \boldsymbol{\Pi}_D^* = [\boldsymbol{\lambda}_Y, \boldsymbol{\lambda}_H, \boldsymbol{s}, \boldsymbol{r}]^T\right\}. \tag{21b}$$

In order to prevent hitting the boundary, these values are multiplied by the constant factor $\alpha_0 = 0.995$.

Damping of the Newton step with the nonnegativity condition may still not be sufficient, because it is possible that the resulting step values do not lead to a descent direction in both the infeasibilities and the objective function. In order to ensure that the computed direction is a decreasing one, the following merit function $\Phi_{\mu,\nu}$ is introduced for a linesearch procedure. The term in squared brackets [.] is optional but should be used in order to avoid the Maratos effect [36]

$$\Phi_{\mu,\nu}(\boldsymbol{\Pi}) = f_\mu(\boldsymbol{x}, \boldsymbol{y}, \boldsymbol{z}, \boldsymbol{w}_Y, \boldsymbol{w}_H) + \frac{\nu}{2}\left\|\begin{pmatrix} \boldsymbol{A}\cdot\boldsymbol{x} \\ \boldsymbol{c}_Y(\boldsymbol{x}) - \boldsymbol{w}_Y \\ \boldsymbol{c}_H(\boldsymbol{x}) - \boldsymbol{w}_H \\ \boldsymbol{x} - \boldsymbol{y} + \boldsymbol{z} \end{pmatrix}\right\|_2^2 + \left[(\boldsymbol{A}\cdot\boldsymbol{x})\cdot\boldsymbol{\lambda}_E\right]. \tag{22}$$

Here, ν denotes the penalty parameter, which is updated if necessary in each iteration step before the linesearch starts.

With help of the linesearch, the supplementary damping factor α_T is determined. Starting from the initial value 1, the factor α_T is halved as often as is necessary such that the Armijo condition Eq. (23) is satisfied. As proposed in e.g. [75], this reduction is carried out in dependence of the primal values only. For the Armijo-factor we set $\beta = 10^{-3}$

$$\begin{aligned} &\Phi_{\mu,\nu}(\boldsymbol{\Pi} + \bar{\alpha}\Delta\boldsymbol{\Pi}) \leq \Phi_{\mu,\nu}(\boldsymbol{\Pi}) + \beta\bar{\alpha}\Phi'_{\mu,\nu}(\boldsymbol{\Pi}; \Delta\boldsymbol{\Pi}) \\ &\quad \text{where: } \bar{\alpha} = \alpha_T\alpha_0\tilde{\alpha}_P. \end{aligned} \tag{23}$$

Table 1 Dimensions in mm

Length L	386.9
Inner radius R_i	60.0
Outer radius $R_{a,1}$	68.1
Outer radius $R_{a,2}$	77.8
Outer radius $R_{a,3}$	90.5

Once the value α_T is determined, the total damping factors can be calculated.

$$\alpha_P = \alpha_T \alpha_0 \tilde{\alpha}_P, \qquad \alpha_D = \alpha_T \alpha_0 \tilde{\alpha}_D. \tag{24}$$

Concerning the penalty parameter ν, a new update-rule is used, which has been recently developed by the author. It is based on the necessary condition of a decreasing direction, $\Phi'(\boldsymbol{\Pi}; \Delta\boldsymbol{\Pi}) < 0$. For details, the reader is referred to [59].

5.3 Update-Rule of the Barrier Parameter

Once the inner iteration has converged, the barrier parameter μ has to be updated. For this, a modification of the update-rule given in [2] is used, which takes into account the distance from the solution.

$$\begin{aligned}
&\text{IF } (\bar{\mu}_i < 0.1\mu_k)\text{: if } \left(\mu_k < 10^{-4}\right)\text{:} \quad \mu_{k+1} = \min\left\{0.85\mu_k;\, 10 \cdot (0.85)^{k+2\sigma}\,\bar{\mu}_o\right\} \\
&\qquad\qquad\qquad\qquad \text{else:} \quad \mu_{k+1} = \min\left\{0.85\mu_k;\, 10 \cdot (0.85)^{k+\sigma}\,\bar{\mu}_o\right\} \\
&\text{ELSE:} \quad \mu_{k+1} = \min\left\{0.95\mu_k;\, 10 \cdot (0.95)^{k}\,\bar{\mu}_o\right\} \\
&\text{where: } \bar{\mu}_i = \frac{1}{\theta}\max\left\{\textit{scaled infeasibility}(\mu)\right\} \text{ and } \bar{\mu}_o = \bar{\mu}_i|_{\mu=0}.
\end{aligned} \tag{25}$$

The maximum scaled infeasibility can be taken from the computation of the break conditions. As suggested in [2], we use $\sigma = 5$.

6 Numerical Example

The proposed method was applied to a flanged pipe with three different outer radii, see Fig. 3(a), already considered by MOUHTAMID [41] and WEICHERT et al. [77]. Both the dimensions as well as the material data were adopted from [41], see Tables 1 and 2. The FEM-analysis was carried out with the software package ANSYS using the isoparametric hexahedral solid element *solid45*. Taking advantage of the system's rotational symmetry—as shown in Fig. 3(b)—the applied mesh consisted of 265 elements and 678 nodes, where one element across the thickness was used.

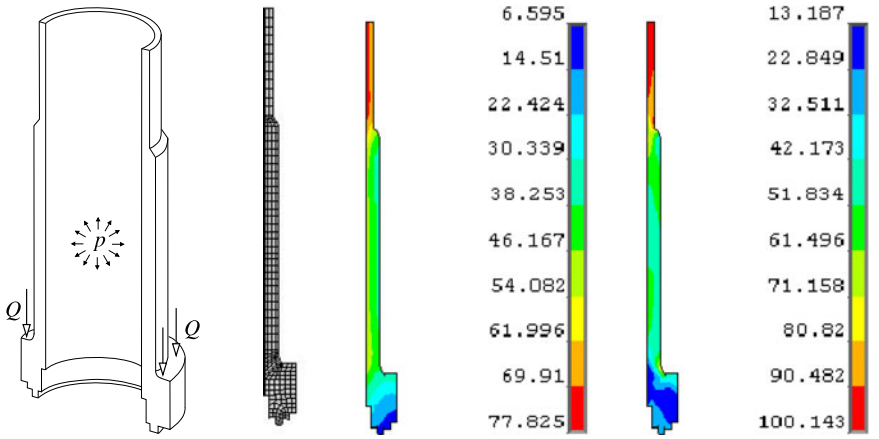

(a) System and loading (b) Model (c) Equivalent elastic stresses due to pressure (d) Equivalent elastic stresses due to axial force

Fig. 3 System, model and equivalent elastic stresses for the flanged pipe

Table 2 Thermal and mechanical characteristics

Young's modulus [MPa]	2.0×10^5
Yield stress [MPa]	200
Poisson's ratio	0.3
Density [kg/m^3]	7.9×10^3
Thermal conductivity [W/(m·K)]	15
Specific heat capacity [J/(kg·K)]	500
Coefficient of thermal expansion [1/K]	1.6×10^{-5}

6.1 Two-Dimensional Loading Space

To validate the method, the system was first investigated in a two-dimensional loading space. In particular, the pipe was subjected to an internal pressure p and an axial force Q, which varied independently in the ranges $p \in [0; p_{max}]$ and $Q \in [0; Q_{max}]$, respectively. In order to compute the elastic stresses presented in Figs. 3(c) and 3(d), the arbitrary values $p = 10$ MPa and $Q = 113.097$ kN were applied, respectively.

As a result of the shakedown analysis, Fig. 4 presents: the elastic domain and twice the elastic domain (dotted lines); the shakedown domains without consideration of hardening for the yield stress $\sigma_Y = 200$ MPa (solid line), and for multiples of the yield stress $\sigma^*_{Y,1} = 1.25\sigma_Y$ and $\sigma^*_{Y,2} = 1.5\sigma_Y$ (dash-dot lines); the shakedown domains including hardening with different values of ultimate stresses $\sigma_{H,1} = 1.25\sigma_Y$ and $\sigma_{H,2} = 1.5\sigma_Y$ (solid lines); the shakedown domain with unlimited kinematical hardening (solid line). Both axes are scaled to the according value $p_0 = 28.85$ MPa and $Q_0 = 416.7$ kN, respectively, for perfectly plastic material behavior.

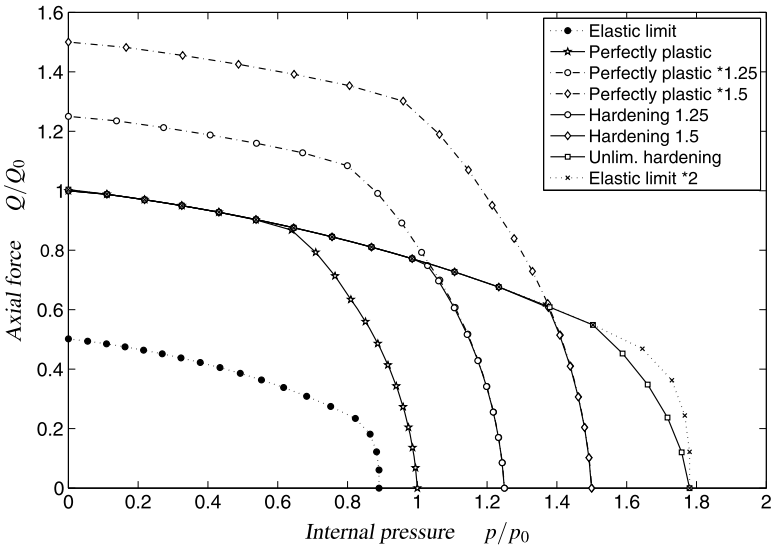

Fig. 4 Results of shakedown analysis of the flanged pipe

In all cases—both the perfectly plastic and the hardening one—the two mechanisms of alternating plasticity and incremental collapse can be clearly distinguished: In case of predominating axial force, all shakedown curves coincide with the one for unlimited hardening, indicating that alternating plasticity is decisive here. Hence, no influence of hardening can be observed.

By contrast, failure is due to incremental collapse in the regime of predominating internal pressure, where the limited kinematical hardening leads to an increase of the according shakedown domains in direct proportion with the ratio σ_H/σ_Y. Thus, the hardening curves (solid lines) coincide with the corresponding none-hardening ones with premultiplied yield stress (dash-dot lines) in this range. In all cases, the two curves pass into each other seamlessly.

It should be noticed, that the unlimited hardening curve does only accord partly with double the elastic domain. Even so, it is frequently stated in the literature, that these curves have to accord in the whole domain, which simply is wrong. In fact, they have to coincide only at the axis intercepts. In the remaining domain, they may—but do not must—be the same.

For validation, in Fig. 5 the results obtained by the new method are compared to those reported in [41], which have been computed on the basis of the augmented Lagrangian method using the program LANCELOT [12]. In general, matching of the results is satisfying, especially for limited kinematical hardening with $\sigma_H = 1.5\sigma_Y$. However, slight differences exist resulting from different elastic solutions. These can be explained by the use of different meshes. In particular, the maximum equivalent stress under axial force is 106.465 MPa in [41], whereas the current calculation yields 100.143 MPa.

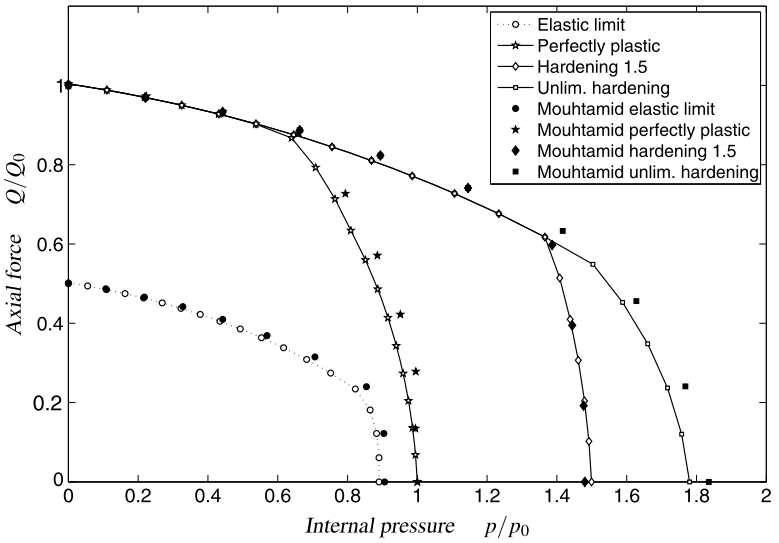

Fig. 5 Comparison with results from MOUHTAMID [41]

6.2 Three-Dimensional Loading Space

To illustrate the influence of hardening in a three-dimensional loading space, a temperature load $\Delta T \in [0; \Delta T_{max}]$ was applied additionally. The according FEM-analysis was carried out in two steps: (1) using the hexahedral thermal element *solid70*, the body temperature distribution was computed resulting from prescribed temperature bounding conditions of $T_i = 100$ K and $T_o = 20$ K at the inner and the outer surface of the pipe, respectively, see Fig. 6(a); (2) based on the body temperature distribution, nodal temperature loadings were defined for the structural analysis with element *solid45*, leading to the equivalent elastic stress distribution shown in Fig. 6(b).

Noteworthy, in the whole calculation, all material parameters were assumed to be temperature-independent. Furthermore, only steady-state processes were considered.

Applying the proposed algorithm, the three-dimensional shakedown domain was computed for elastic-perfectly plastic material, see Fig. 7. Further, the influence of limited kinematical hardening was investigated by calculations with different ultimate stresses: $\sigma_H = 1.1\sigma_Y$ (Fig. 8 and blue dash-dot line), $\sigma_H = 1.25\sigma_Y$ (Fig. 9 and blue dashed line), and $\sigma_H = 1.5\sigma_Y$ (Fig. 10 and black dash-dot line). Subsequently, the domain was determined for unlimited hardening (Fig. 11 and black solid line).

As in the two-dimensional case, the two mechanisms alternating plasticity and incremental collapse can be clearly distinguished. To highlight this, all computed points leading to alternating plasticity are marked by red circles.

In the regime of predominating temperature, all shakedown domains coincide, which implicates alternating plasticity to be decisive. Here, hardening does not af-

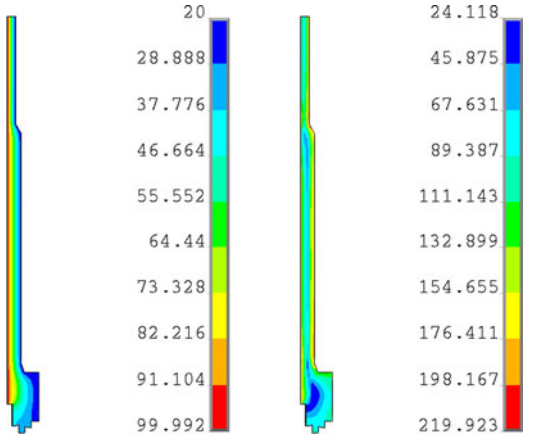

(a) Distribution of body temperature

(b) Equivalent elastic stresses due to temperature loading

Fig. 6 Body temperature distribution and resulting equivalent elastic stresses

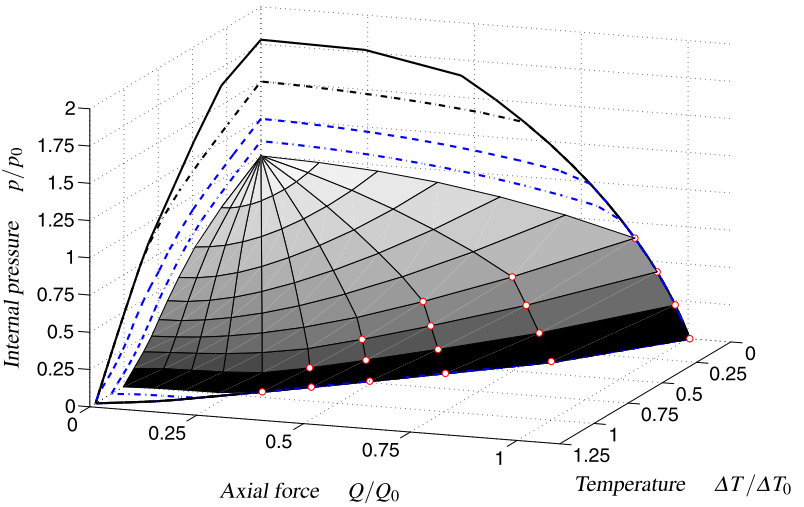

Fig. 7 Three-dimensional shakedown domain without hardening

fect the solution. By contrast, an influence of hardening can be observed in the regime of predominating axial force. While incremental collapse leads to failure in the elastic-perfectly plastic case as well as when considering limited hardening with $\sigma_H = 1.1\sigma_Y$, further increasing the ultimate stress has no impact, because alternating plasticity occurs starting from $\sigma_H = 1.2\sigma_Y$. Finally, when the internal pressure is superior, hardening enlarges the shakedown domain in direct proportion with the ratio σ_H/σ_Y in all calculations with limited hardening. Only for unlimited hardening, its effect its restricted and alternating plasticity appears.

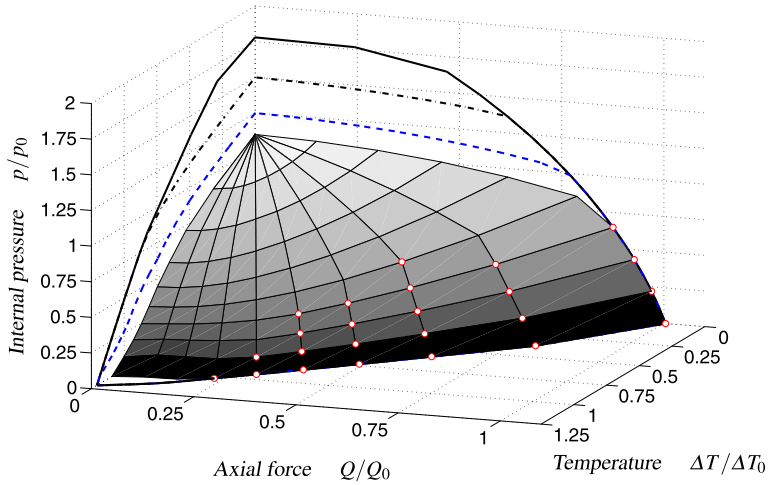

Fig. 8 Three-dimensional shakedown domain with hardening $\sigma_H = 1.1\sigma_Y$

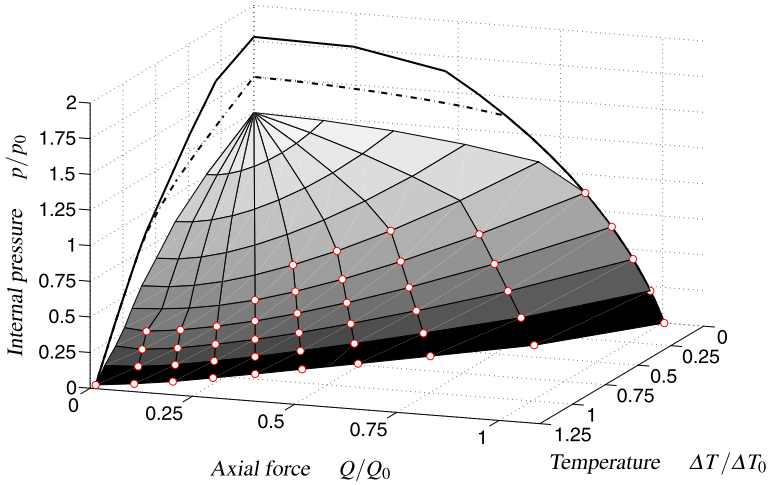

Fig. 9 Three-dimensional shakedown domain with hardening $\sigma_H = 1.25\sigma_Y$

Closing, the characteristic numerical details are reported in Table 3. As one can see, the number of iterations is not as much affected as the running time. Moreover, in the considered example, the number of loadings has a larger impact than the hardening, even though the numbers of variables and constraints are comparable.

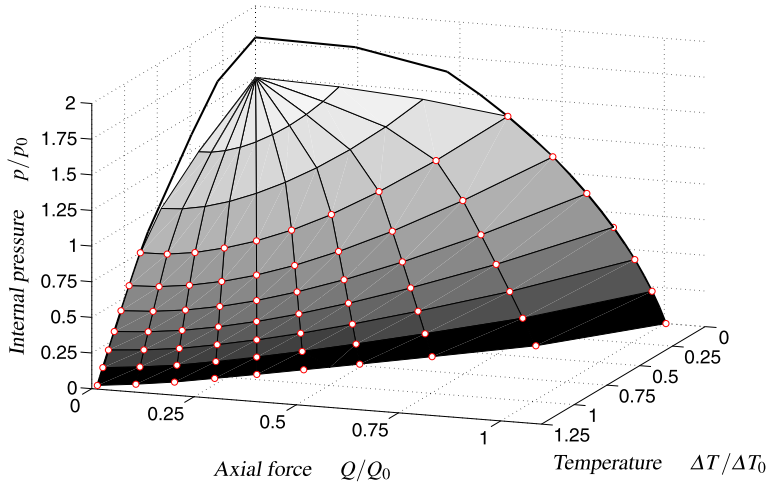

Fig. 10 Three-dimensional shakedown domain with hardening $\sigma_H = 1.5\sigma_Y$

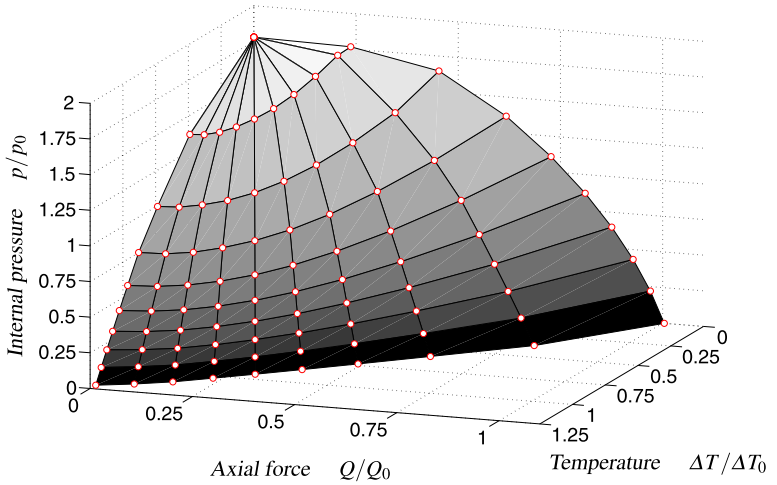

Fig. 11 Three-dimensional shakedown domain with unlimited hardening

7 Conclusion

In this paper, a method to compute the shakedown factors of engineering structures subjected to varying thermal and mechanical loadings has been presented using the lower bound approach. The method allows for taking into account limited kinematical hardening by application of a two-surface model, where both the yield and the bounding surface are described by the von Mises criterion. Further, it is capable of considering arbitrary numbers of thermal and mechanical loadings. The method's

Table 3 Influence of hardening on numerical details

	2 independent loads		3 independent loads	
	Perfectly plastic	Hardening	Perfectly plastic	Hardening
n	44521	86921	86921	171721
m_E	33834	65634	76234	150434
m_I	8480	16960	16960	33920
∅ Iterations	400	481	2318	3017
∅ CPU-time [s][a]	48	57	295	837

[a] *Dell Precision T7500* with *Xeon E5620*-processor with 2400 MHz and 12 GB RAM

potential has been illustrated by application to a numerical example from the field of power plant engineering.

Acknowledgements I cordially thank Prof. Dieter Weichert for the fruitful discussions and the support, which made this work possible.

References

1. Akoa FB, Hachemi A, An LTH, Mouhtamid S, Tao PD (2007) Application of lower bound direct method to engineering structures. J Glob Optim 37(4):609–630
2. Akrotirianakis I, Rustem B (2000) A primal-dual interior-point algorithm with an exact and differentiable merit function for general nonlinear programming problems. Optim Methods Softw 14(1/2):1–36
3. Andersen ED, Jensen B, Jensen J, Sandvik R, Worsøe U (2009) MOSEK version 6. Technical report TR-2009-3
4. Andersen ED, Roos C, Terlaky T (2003) On implementing a primal-dual interior-point method for conic quadratic optimization. Math Program 95(2):249–277
5. Ardito R, Cocchetti G, Maier G (2008) On structural safety assessment by load factor maximization in piecewise linear plasticity. Eur J Mech A, Solids 27:859–881
6. Benson HY, Shanno DF, Vanderbei RJ (2002) Interior-point methods for nonconvex nonlinear programming: filter methods and merit functions. Comput Optim Appl 23(2):257–272
7. Benson HY, Shanno DF, Vanderbei RJ (2003) A comparative study of large-scale nonlinear optimization algorithms. In: Di Pillo G, Murli A (eds) High performance algorithms and software for nonlinear optimization. Kluwer Academic, Princeton, pp 95–127
8. Bisbos CD, Makrodimopoulos A, Pardalos PM (2005) Second-order cone programming approaches to static shakedown analysis in steel plasticity. Optim Methods Softw 20(1):25–52
9. Bouby C, De Saxcé G, Tritsch J-B (2009) Shakedown analysis: comparison between models with the linear unlimited, linear limited and non-linear kinematic hardening. Mech Res Commun 36:556–562
10. Bousshine L, Chaaba A, De Saxce G (2003) A new approach to shakedown analysis for non-standard elastoplastic material by the bipotential. Int J Plast 19(5):583–598
11. Byrd RH, Hribar ME, Nocedal J (2000) An interior point algorithm for large-scale nonlinear programming. SIAM J Optim 9(4):877–900
12. Conn AR, Gould NIM, Toint PL (1992) In: LANCELOT: a Fortran package for large-scale nonlinear optimization (release A). Springer series in computational mathematics, vol 17. Springer, Heidelberg

13. Corigliano A, Maier G, Pycko S (1995) Kinematic criteria of dynamic shakedown extended to nonassociate constitutive laws with saturation nonlinear hardening. Rend Accad Lincei IX 6:55–64
14. El-Bakry AS, Tapia RA, Tsuchiya T, Zhang Y (1996) On the formulation and theory of the Newton interior-point method for nonlinear programming. J Optim Theory Appl 89:507–541
15. Forsgren A, Gill PE, Wright MH (2002) Interior methods for nonlinear optimization. SIAM Rev 44(4):525–597
16. Fuschi P (1999) Structural shakedown for elastic-plastic materials with hardening saturation surface. Int J Solids Struct 36:219–240
17. Garcea G, Leonetti L (2011) A unified mathematical programming formulation of strain driven and interior point algorithms for shakedown and limit analysis. Int J Numer Methods Eng 88(11):1085–1111
18. Griva I, Shanno DF, Vanderbei RJ, Benson HY (2008) Global convergence analysis of a primal-dual interior-point method for nonlinear programming. Algorithmic Oper Res 3(1):12–19
19. Groß-Weege J (1997) On the numerical assessment of the safety factor of elastic-plastic structures under variable loading. Int J Mech Sci 39(4):417–433
20. Groß-Weege J, Weichert D (1992) Elastic-plastic shells under variable mechanical and thermal loads. Int J Mech Sci 34:863–880
21. Hachemi A, An LTH, Mouhtamid S, Tao PD (2004) Large-scale nonlinear programming and lower bound direct method in engineering applications. In: An LTH, Tao PD (eds) Modelling, computation and optimization in information systems and management sciences. Hermes Science, London, pp 299–310
22. Hachemi A, Mouhtamid S, Nguyen AD, Weichert D (2009) Application of shakedown analysis to large-scale problems with selective algorithm. In: Weichert D, Ponter ARS (eds) Limit states of materials and structures. Springer, Berlin, pp 289–305
23. Hachemi A, Mouhtamid S, Weichert D (2005) Progress in shakedown analysis with applications to composites. Arch Appl Mech 74:762–772
24. Heitzer M (1999) Traglast- und Einspielanalyse zur Bewertung der Sicherheit passiver Komponenten. PhD thesis, Forschungszentrum Jülich, RWTH Aachen, Germany
25. Koiter WT (1960) General theorems for elastic-plastic solids. In: Sneddon IN, Hill R (eds) Progress in solid mechanics. North-Holland, Amsterdam, pp 165–221
26. König JA (1987) Shakedown of elastic-plastic structures. Elsevier, Amsterdam
27. König JA, Siemaszko A (1988) Shakedown of elastic-plastic structures. Ing-Arch 58:58–66
28. Krabbenhøft K, Damkilde L (2003) A general nonlinear optimization algorithm for lower bound limit analysis. Int J Numer Methods Eng 56:165–184
29. Krabbenhøft K, Lyamin AV, Sloan SW (2007) Formulation and solution of some plasticity problems as conic programs. Int J Solids Struct 44:1533–1549
30. Krabbenhøft K, Lyamin AV, Sloan SW, Wriggers P (2007) An interior-point algorithm for elastoplasticity. Int J Numer Methods Eng 69:592–626
31. Magoariec H, Bourgeois S, Débordes O (2004) Elastic plastic shakedown of 3d periodic heterogeneous media: a direct numerical approach. Int J Plast 20(8–9):1655–1675
32. Maier G, Pastor J, Ponter ARS, Weichert D (2003) Direct methods of limit and shakedown analysis. In: de Borst R, Mang HA (eds) Comprehensive structural integrity—fracture of materials from nano to macro. Numerical and computational methods, vol 3. Elsevier, Amsterdam, pp 637–684
33. Makrodimopoulos A (2006) Computational formulation of shakedown analysis as a conic quadratic optimization problem. Mech Res Commun 33:72–83
34. Malena M, Casciaro R (2008) Finite element shakedown analysis of reinforced concrete 3d frames. Comput Struct 86(11–12):1176–1188
35. Mandel J (1976) Adaptation d'une structure plastique ecrouissable et approximations. Mech Res Commun 3:483–488
36. Maratos N (1978) Exact penalty function algorithms for finite dimensional and control opimization problems. PhD thesis, University of London, UK

37. Melan E (1938) Der Spannungszustand eines „Mises-Hencky'schen" Kontinuums bei veränderlicher Belastung. Sitzungsber Akad Wiss Wien, Math-Nat Kl, Abt IIa 147:73–87
38. Melan E (1938) Zur Plastizität des räumlichen Kontinuums. Ing-Arch 9:116–126
39. Mittelmann H (2010) Decision tree for optimization software. http://plato.asu.edu/guide.thml
40. Morales JL, Nocedal J, Waltz RW, Lie G, Goux J-P (2003) Assessing the potential of interior methods for nonlinear optimization. In: Biegler LT, Ghattas O, Heinkenschloss M, van Bloemen Waander B (eds) Large-scale PDE-constrained optimization, vol 30. Springer, Berlin, pp 167–183
41. Mouhtamid S (2007) Anwendung direkter Methoden zur industriellen Berechnung von Grenzlasten mechanischer Komponenten. PhD thesis, Institute of General Mechanics, RWTH Aachen University, Germany
42. Ngo N, Tin-Loi F (2007) Shakedown analysis using the p-adaptive finite element method and linear programming. Eng Struct 29(1):46–56
43. Nguyen Q-S (2003) On shakedown analysis in hardening plasticity. J Mech Phys Solids 51:101–125
44. Pastor F, Loute E (2010) Limit analysis decomposition and finite element mixed method. J Comput Appl Math 234(7):2213–2221
45. Pastor F, Loute E, Pastor J, Trillat M (2009) Mixed method and convex optimization for limit analysis of homogeneous Gurson materials: a kinematic approach. Eur J Mech A, Solids 28:25–35
46. Pastor F, Thoré P, Loute E, Pastor J, Trillat M (2008) Convex optimization and limit analysis: application to Gurson and porous Drucker-Prager materials. Eng Fract Mech 75:1367–1383
47. Pham DC (2007) Shakedown theory for elastic plastic kinematic hardening bodies. Int J Plast 23:1240–1259
48. Pham DC (2008) On shakedown theory for elastic-plastic materials and extensions. J Mech Phys Solids 56:1905–1915
49. Pham DC, Weichert D (2001) Shakedown analysis for elastic-plastic bodies with limited kinematical hardening. Proc R Soc Lond A 457:1097–1110
50. Pham PT, Vu DK, Tran TN, Staat M (2010) An upper bound algorithm for shakedown analysis of elastic-plastic bounded linearly kinematic hardening bodies. In: Proc ECCM 2010
51. Polizzotto C (1986) A convergent bounding principle for a class of elastoplastic strain-hardening solids. Int J Plast 2(4):359–370
52. Polizzotto C (2010) Shakedown analysis for a class of strengthening materials within the framework of gradient plasticity. Int J Plast 26(7):1050–1069
53. Ponter ARS (1975) A general shakedown theorem for elastic plastic bodies with work hardening. In: Proc SMIRT-3, p L5/2
54. Ponter ARS (2002) A linear matching method for shakedown analysis. In: Weichert D, Maier G (eds) Inelastic behaviour of structures under variable repeated loading—direct analysis methods, pp 267–318
55. Ponter ARS, Chen HF (2005) Direct methods for limits in plasticity. Arch Mech 57:171–188
56. Potra FA, Wright SJ (2000) Interior-point methods. J Comput Appl Math 124:281–302
57. Pycko S, Maier G (1995) Shakedown theorems for some classes of nonassociative hardening elastic-plastic material models. Int J Plast 11(4):367–395
58. Simon J-W, Chen M, Weichert D (2012) Shakedown analysis combined with the problem of heat conduction. J Press Vessel Technol 134(2):021206
59. Simon J-W, Weichert D (2011) Numerical lower bound shakedown analysis of engineering structures. Comput Methods Appl Mech Eng 200:2828–2839
60. Simon J-W, Weichert D (2012) Interior-point method for lower bound shakedown analysis of von mises-type materials. In: de Saxcé G, Oueslati A, Charkaluk E, Tritsch J-B (eds) Limit states of materials and structures—direct methods, vol 2. Springer, Berlin, pp 103–128
61. Simon J-W, Weichert D (2012) Shakedown analysis of engineering structures with limited kinematical hardening. Int J Solids Struct 49(4):2177–2186
62. Simon J-W, Weichert D (2012) Shakedown analysis with multidimensional loading spaces. Comput Mech 49(4):477–485

63. Spiliopoulos KV, Panagiotou KD (2012) A direct method to predict cyclic steady states of elastoplastic structures. Comput Methods Appl Mech Eng 223(224):186–198
64. Staat M, Heitzer M (2002) The restricted influence of kinematical hardening on shakedown loads. In: Proc WCCM V
65. Stein E, Zhang G, Huang Y (1993) Modeling and computation of shakedown problems for nonlinear hardening materials. Comput Methods Appl Mech Eng 103(1–2):247–272
66. Stein E, Zhang G, König JA (1992) Shakedown with nonlinear strain-hardening including structural computation using finite element method. Int J Plast 8(1):1–31
67. Stein E, Zhang G, Mahnken R, König JA (1990) Micromechanical modelling and computation of shakedown with nonlinear kinematic hardening including examples for 2-D problems. In: Axelard DR, Muschik W (eds) Recent developments of micromechanics. Springer, Berlin
68. Trillat M, Pastor J (2005) Limit analysis and Gurson's model. Eur J Mech A, Solids 24:800–819
69. Vanderbei RJ (1999) LOQO: an interior point code for quadratic programming. Optim Methods Softw 11–12:451—484
70. Vu DK, Staat M (2007) Analysis of pressure equipment by application of the primal-dual theory of shakedown. Commun Numer Methods Eng 23(3):213–225
71. Vu DK, Yan AM, Nguyen-Dang H (2004) A primal-dual algorithm for shakedown analysis of structures. Comput Methods Appl Mech Eng 193:4663–4674
72. Wächter A (2002) An interior point algorithm for large-scale nonlinear optimization with applications in process engineering. PhD thesis, Carnegie Mellon University, Pittsburgh, Pennsylvania
73. Wächter A, Biegler LT (2005) Line-search filter methods for nonlinear programming: motivation and global convergence. SIAM J Optim 16(1):1–31
74. Wächter A, Biegler LT (2006) On the implementation of an interior-point filter line-search algorithm for large-scale nonlinear programming. Math Program 106(1):25–57
75. Waltz RA, Morales JL, Nocedal J, Orban D (2006) An interior algorithm for nonlinear optimization that combines line search and trust region steps. Math Program 107(3):391–408
76. Weichert D, Groß-Weege J (1988) The numerical assessment of elastic-plastic sheets under variable mechanical and thermal loads using a simplified two-surface yield condition. Int J Mech Sci 30(10):757–767
77. Weichert D, Hachemi A, Mouhtamid S, Nguyen AD (2008) On recent progress in shakedown analysis and applications to large-scale problems. In: IUTAM symposium on theoretical, computational and modelling aspects of inelastic media, vol 11, pp 349–359
78. Weichert D, Maier G (2000) Inelastic analysis of structures under variable repeated loads. Kluwer Academic, Dordrecht
79. Weichert D, Ponter ARS (2009) Limit states of materials and structures. Springer, Wien
80. Wright MH (2004) The interior-point revolution in optimization: history, recent developments and lasting consequences. Bull Am Math Soc 42(1):39–56
81. Zarka J, Casier J (1981) Elastic-plastic response of a structure to cyclic loading: practical rule. In: Nemat-Nasser S (ed) Mechanics today, vol 6. Pergamon, New York
82. Zhang T, Raad L (2002) An eigen-mode method in kinematic shakedown analysis. Int J Plast 18:71–90

Computation of Bounds for Anchor Problems in Limit Analysis and Decomposition Techniques

J.J. Muñoz, N. Rabiei, A. Lyamin, and A. Huerta

Abstract Numerical techniques for the computation of strict bounds in limit analyses have been developed for more than thirty years. The efficiency of these techniques have been substantially improved in the last ten years, and have been successfully applied to academic problems, foundations and excavations. We here extend the theoretical background to problems with anchors, interface conditions, and joints. Those extensions are relevant for the analysis of retaining and anchored walls, which we study in this work. The analysis of three-dimensional domains remains as yet very scarce. From the computational standpoint, the memory requirements and CPU time are exceedingly prohibitive when mesh adaptivity is employed. For this reason, we also present here the application of decomposition techniques to the optimisation problem of limit analysis. We discuss the performance of different methodologies adopted in the literature for general optimisation problems, such as primal and dual decomposition, and suggest some strategies that are suitable for the parallelisation of large three-dimensional problems. The proposed decomposition techniques are tested against representative problems.

J.J. Muñoz (✉) · N. Rabiei · A. Huerta
Laboratori de Càlcul Numèric (LaCàN), Universitat Politècnica de Catalunya (UPC), Barcelona, Spain
e-mail: j.munoz@upc.edu

N. Rabiei
e-mail: nima.rabiei@upc.edu

A. Huerta
e-mail: antonio.huerta@upc.edu

A. Lyamin
Center for Geothecnical and Materials Modelling, University of Newcastle, Newcastle, Australia
e-mail: a.lyamin@newcastle.edu.au

K. Spiliopoulos, D. Weichert (eds.), *Direct Methods for Limit States in Structures and Materials*, DOI 10.1007/978-94-007-6827-7_4,

1 Introduction

1.1 Limit Analysis Problem

According to the lower (primal) and upper (dual) bound theorem of limit analysis, the bearing capacity of a structure is equal to (i) the maximum load factor λ^* under equilibrium conditions and with plastically admissible stresses $\boldsymbol{\sigma}$ (i.e. they belong to a set $\mathscr{B}$), or alternatively, to (ii) the minimum dissipation energy $D(\boldsymbol{v})$ of a kinematically admissible velocity field $\boldsymbol{v}$. Mathematically, the resulting bearing capacity has the structure of a saddle point problem that can be written as [6],

$$\lambda^* = \min_{\ell(\boldsymbol{v})=1} \max_{\substack{\boldsymbol{\sigma}\in\mathscr{B} \\ a(\boldsymbol{\sigma},\boldsymbol{v})=\lambda\ell(\boldsymbol{v})}} a(\boldsymbol{\sigma},\boldsymbol{v}) \tag{1}$$

where the linear form $\ell(\boldsymbol{v})$ is the power dissipated by the external loads, while the bilinear form $a(\boldsymbol{\sigma},\boldsymbol{v})$ is the internal dissipated power. For a given domain Ω, subjected to external surface load $\boldsymbol{g}$ and body load $\boldsymbol{f}$, these forms are explicitly given by:

$$\ell(\boldsymbol{v}) = \int_\Omega \boldsymbol{f}\cdot\boldsymbol{v}\, d\Omega + \int_{\partial\Omega} \boldsymbol{g}\cdot\boldsymbol{v}\, d\Gamma,$$

$$a(\boldsymbol{\sigma},\boldsymbol{v}) = \int_\Omega \boldsymbol{\sigma} : \boldsymbol{\varepsilon}(\boldsymbol{v})\, d\Omega + \int_\Gamma \boldsymbol{\sigma} : \left(\llbracket\boldsymbol{v}\rrbracket \bar{\otimes} \boldsymbol{n}\right) d\Gamma$$

with Γ the (unknown) region of Ω where the velocity is discontinuous, $\llbracket\boldsymbol{v}\rrbracket$ the velocity discontinuity, and $\boldsymbol{n}$ the normal vector at this discontinuity. The operator $\bar{\otimes}$ is the symmetrised dyadic product such that $\boldsymbol{a}\bar{\otimes}\boldsymbol{b} = \frac{1}{2}(\boldsymbol{a}\otimes\boldsymbol{b} + \boldsymbol{b}\otimes\boldsymbol{a})$ (see also [16] for equivalent definitions of discontinuous velocities). The saddle point problem or min max problem can be also rewritten as,

$$\lambda^* = \max_{\substack{\boldsymbol{\sigma}\in\mathscr{B} \\ a(\boldsymbol{\sigma},\boldsymbol{v})=\lambda\ell(\boldsymbol{v}),\forall\boldsymbol{v}}} \lambda \tag{2}$$

$$= \min_{\ell(\boldsymbol{v})=1} D(\boldsymbol{v}) \tag{3}$$

where the dissipated energy $D(\boldsymbol{v})$ is defined by,

$$D(\boldsymbol{v}) = \max_{\substack{\boldsymbol{\sigma}\in\mathscr{B} \\ a(\boldsymbol{\sigma},\boldsymbol{v})=\lambda\ell(\boldsymbol{v})}} a(\boldsymbol{\sigma},\boldsymbol{v}).$$

Equations (2) and (3) are the primal and dual form of the saddle point problem in (1). From the dual form in (3), it turns out that the velocities must be associated, that is, that $\boldsymbol{\varepsilon}(\boldsymbol{v}) \in \partial\mathscr{B}$ and $\llbracket\boldsymbol{v}\rrbracket \otimes \boldsymbol{n} \in \partial\mathscr{B}$, with $\partial\mathscr{B}$ the sub-gradient of set $\mathscr{B}$.

The analytical saddle point problem in (1) is illustrated in Fig. 1(a). A stress field such that $\boldsymbol{\sigma} \in \mathscr{B}$ and for which the equilibrium condition $a(\boldsymbol{\sigma},\boldsymbol{v}) = \lambda\ell(\boldsymbol{v}), \forall\ell(\boldsymbol{v})$

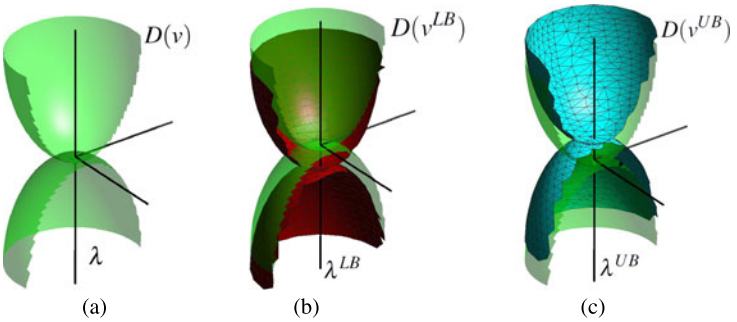

Fig. 1 Illustration of saddle point problem for the (**a**) analytical solution of limit analysis problem, (**b**) lower bound discrete limit analysis problem, and (**c**) upper bound discrete limit analysis problem

is satisfied everywhere is so-called a *statically admissible* stress space. Similarly, a velocity field such that $\ell(\boldsymbol{v}) = 1$ and for which the associative conditions $[\![\boldsymbol{v}]\!] \otimes \boldsymbol{n}, \boldsymbol{\varepsilon}(\boldsymbol{v}) \in \partial\mathscr{B}$ is satisfied everywhere is so-called a *kinematically admissible* space. The saddle point problem in (1) states that the bearing capacity (or maximum load factor) of a structure is equal to the internal dissipated energy of a statically admissible stress space $\boldsymbol{\sigma}^*$ and a kinematically admissible velocity space $\boldsymbol{v}^*$.

1.2 Discrete Upper and Lower Bound Formulations

By choosing an appropriate discrete statically admissible space $(\boldsymbol{\sigma}^{LB}, \boldsymbol{v}^{LB})$ that satisfies the maximisation conditions in (1), and a kinematically admissible space $(\boldsymbol{\sigma}^{UB}, \boldsymbol{v}^{UB})$ that satisfies the minimisation conditions in (1), we can construct strict bounds of the load factor λ^* as,

$$\lambda^{LB} = a\left(\boldsymbol{\sigma}^{LB}, \boldsymbol{v}^{LB}\right) \leq \lambda^* \leq a\left(\boldsymbol{\sigma}^{UB}, \boldsymbol{v}^{UB}\right) = \lambda^{UB}.$$

A schematic of discrete spaces $(\boldsymbol{\sigma}^{LB}, \boldsymbol{v}^{LB})$ and $(\boldsymbol{\sigma}^{LB}, \boldsymbol{v}^{LB})$ that satisfy those conditions are given in Fig. 2. The reader is referred to [12, 13] for a justification of those spaces. When resorting to them, the saddle point problem is consequently modified, as illustrated in Figs. 1(b)–(c). The max min problem in (1) turns into a lower bound problem when the first pair of spaces is used, and into an upper bound problem when the second pair is used.

Therefore, after using these interpolation spaces $(\boldsymbol{\sigma}^{UB}, \boldsymbol{v}^{UB})$ and $(\boldsymbol{\sigma}^{LB}, \boldsymbol{v}^{LB})$ in the exact optimisation problem in (2) or (3), we are able to compute exact upper and lower bounds of the optimal factor λ^*. In particular, the lower bound problem turns

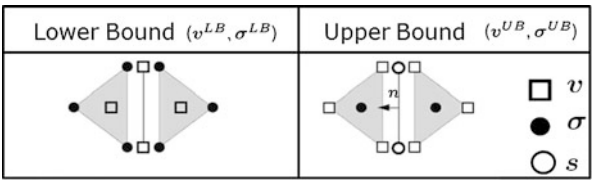

Fig. 2 Interpolation spaces for the lower and upper bound problem. *Symbols at nodes* denote a elementwise linear space, while *symbols at the center of the element* denote elementwise constant space

into the following form,

$$\lambda^{LB} = \max_{\boldsymbol{\sigma}^{UB}} \lambda$$
$$\text{s.t.} \begin{cases} \bar{\mathbf{A}}^{eq1}\boldsymbol{\sigma}^{LB} + \lambda \boldsymbol{F}^{eq1} = \mathbf{0}, \\ \bar{\mathbf{A}}^{eq2}\boldsymbol{\sigma}^{LB} = \mathbf{0}, \\ \bar{\mathbf{A}}^{eq3}\boldsymbol{\sigma}^{LB} + \lambda \boldsymbol{F}^{eq3} = \mathbf{0}, \\ \boldsymbol{\sigma}_i^{LB,e} \in \mathscr{B}, \quad e = 1, \ldots, N_e, i = 1, \ldots, n_{sd} + 1 \end{cases} \tag{4}$$

whereas the upper bound problem reads,

$$\lambda^{UB} = \min_{\boldsymbol{v}^{UB}} D\big(\boldsymbol{v}^{UB}\big)$$
$$\text{s.t.} \begin{cases} l(\boldsymbol{v}^{UB}) = 1 \\ -\boldsymbol{\varepsilon}(\boldsymbol{v}_i^{UB,e}) \in \partial\mathscr{B}^*, \quad e = 1, \ldots, N_e, \ i = 1, \ldots, n_{sd} + 1, \\ -[\![\boldsymbol{v}^{UB}]\!]_j^{\xi} \bar{\otimes} \boldsymbol{n}^{\xi} \in \partial\mathscr{B}^*, \quad \xi = 1, \ldots, N_\xi, \ j = 1, \ldots, n_{sd} \end{cases} \tag{5}$$

where n_{sd} is the number of space dimensions, and the three block equations in (4) correspond respectively to the intra-element equilibrium, the inter-element equilibrium, and the Neumann boundary conditions. The vectors $\boldsymbol{\sigma}^{LB}$ and $\boldsymbol{v}^{UB}$ contain the collection of all nodal stresses $\boldsymbol{\sigma}_i^{LB,e}$ of element e, and the velocities $\boldsymbol{v}_i^{UB,e}$ and $\boldsymbol{v}_j^{UB,\xi}$ for each node i of element e or each node j of edge ξ, respectively.

The problems above can be solved efficiently using available optimisation programs [1, 17, 18]. Moreover, for the usual plasticity criteria such as von Mises or Mohr-Coulomb in two dimensions, we can apply linear transformations of the stress variables that turn the membership conditions $\boldsymbol{\sigma} \in \mathscr{B}$ into second order cones (SOC), which can be handled by the mentioned optimisation software. After applying in such transformations, the optimisation problems above turn into,

$$\lambda^{LB} = \max_{\boldsymbol{x}} \lambda$$
$$\text{s.t.} \begin{cases} \mathbf{A}^{eq1}\boldsymbol{x} + \lambda \boldsymbol{F}^{eq1} = \boldsymbol{b}^{eq1}, \\ \mathbf{A}^{eq2}\boldsymbol{x} = \mathbf{0}, \\ \mathbf{A}^{eq3}\boldsymbol{x} + \lambda \boldsymbol{F}^{eq3} = \boldsymbol{b}^{eq3}, \\ \boldsymbol{x}_i^{LB,e} \in \mathscr{K}, \quad e = 1, \ldots, N_e, i = 1, \ldots, n_{sd} + 1, \end{cases}$$

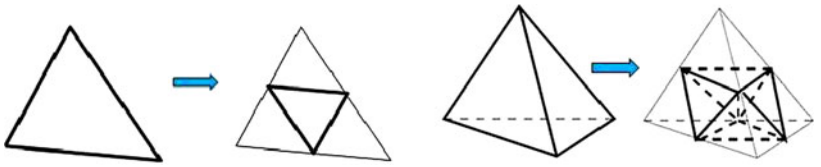

(a) (b)

Fig. 3 Subdivision of a triangular element in 2D (**a**) and tetrahedron in 3D (**b**), when their elemental gap contribution $\Delta\lambda^a$ is larger than a pre-defined threshold

$$\lambda^{UB} = \min_{\boldsymbol{v}^{UB}} \boldsymbol{b} \cdot \boldsymbol{v}^{UB} \tag{6}$$

$$\text{s.t.} \begin{cases} l(\boldsymbol{v}^{UB}) = 1 \\ \boldsymbol{v}_i^{UB,e} \in \mathscr{K}^*, & e = 1, \ldots, N_e,\ i = 1, \ldots, n_{sd}+1, \\ [\![\boldsymbol{v}^{UB}]\!]_i^{\xi} \bar{\otimes} \boldsymbol{n}^{\xi} \in \mathscr{K}^*, & \xi = 1, \ldots, N_\xi,\ i = 1, \ldots, n_{sd} \end{cases}$$

with $\mathscr{K}$ a second order cone, and $\mathscr{K}^*$ the dual cone of $\mathscr{K}$ [4].

1.3 Mesh Adaptivity

The optimum values of the lower and upper bound problem can be used to compute a set of elemental and edge contributions to the total gap, which are defined by [7, 13]:

$$\Delta\lambda^e = \int_{\Omega^e} \boldsymbol{\sigma}^{UB} : \boldsymbol{\varepsilon}\left(\boldsymbol{v}^{UB}\right) d\Omega + \int_{\Omega^e} \nabla \cdot \boldsymbol{\sigma}^{LB} \cdot \boldsymbol{v}^{UB}\, d\Omega - \int_{\partial\Omega} \boldsymbol{\sigma}^{LB}\boldsymbol{n} \cdot \boldsymbol{v}^{UB}\, d\Gamma,$$

$$\Delta\lambda^{\xi} = \int_{\Gamma^{\xi}} \boldsymbol{\sigma}^{UB,\xi} \cdot [\![\boldsymbol{v}^{UB}]\!]\, d\Gamma - \int_{\Gamma^{\xi}} \boldsymbol{\sigma}^{LB}\boldsymbol{n} \cdot [\![\boldsymbol{v}^{UB}]\!]\, d\Gamma.$$

These bound gaps satisfy the properties, $\lambda^{UB} - \lambda^{LB} = \sum_e \Delta\lambda^e + \sum_\xi \Delta\lambda^\xi$, $\Delta\lambda^e \geq 0$ and $\Delta\lambda^\xi \geq 0$, which make them good candidates to estimate the errors of the lower and upper bound solution. These quadratures are obtained only if appropriate quadratures are employed to compute the integrals: Gauss quadrature for all the terms excepting the first integral in $\Delta\lambda^\xi$ (see [14] for the justification of this). We have used them to design an adaptive remeshing strategy employed in the results Sect. 4. Any element or edge with a gap contribution higher than a certain threshold will be subdivided according to the pattern shown in Fig. 3.

2 Extension to Anchors, Joints and Frictional Interfaces

We will develop next specific conditions for common interface conditions encountered in geomechanics. In all cases we add specific constraints that preserve the strictness of the bounds. The studied and implemented situations are:

1. Interface material that splits two different materials with specific admissibility criterion for the common boundary.
2. Duplicated edges: in two-dimensional applications, it may convenient to overlap materials or structural elements such as ties or anchors. In these situations, it is required to have edges that joint one element on one side and two elements, B and B', on the other side.
3. Modelling of joints such as articulated joints in anchors and anchor-wall interface.

We briefly describe how to include in each case the corresponding constraints in the optimisation problem (see [15] for further details).

2.1 Interface Conditions

Specific admissibility conditions for the stresses can be introduced by adding new nodal variables $\boldsymbol{\sigma}_i^I$ at the interface, with new membership sets $\mathscr{B}_I$, that are different from the two materials at each side of the interface. These new nodal variables are equivalent to extending the spaces given in Sect. 1.2, and adding equilibrium constraints such as,

$$\left(\boldsymbol{\sigma}_i^A - \boldsymbol{\sigma}_i^B\right) \cdot \boldsymbol{n} = \mathbf{0}, \quad i = 1, 2, \tag{7}$$

$$\left(\boldsymbol{\sigma}_i^A - \boldsymbol{\sigma}_i^I\right) \cdot \boldsymbol{n} = \mathbf{0}, \quad i = 1, 2 \tag{8}$$

and adding the following membership constraints at the interface,

$$\boldsymbol{\sigma}_i^I \in \mathscr{B}_I, \quad i = 1, 2. \tag{9}$$

The vector $\boldsymbol{n}$ is the normal to the interface edge or face in 3D. Some of admissible sets that may be employed in common problems are depicted in Fig. 4. We also note that the nodal velocities at the two edges between A and B, indicated in Fig. 4(a) with circles, correspond in fact to the Lagrange multipliers associated with these constraints: the velocities at one edge are associated with Eq. (7) while those at the other edge correspond to Eq. (8).

Figure 5 shows the usual admissible domain $\mathscr{B}_I$ for the stresses at the interfaces. The criteria in Fig. 5(c) has been included for completeness reasons, but it is unrealistic and has not practical interest. The subscript σ_N and σ_T denote the normal and tangential components of the traction vector $\boldsymbol{\sigma} \cdot \boldsymbol{n}$ at the interface. In our implementation, we impose admissibility domains for the stress tensors $\boldsymbol{\sigma}^I$, which imply the usual admissibility conditions for the traction vectors $\boldsymbol{\sigma}^I \cdot \boldsymbol{n}$.

2.2 Duplicated Edges

The modelling of two-dimensional problems with anchors, ties or reinforcements can be achieved by superimposing the latter elements onto the soil elements. This

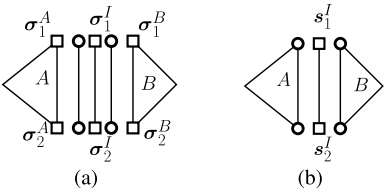

Fig. 4 Discrete spaces considered for the lower (**a**) and upper (**b**) bound problems when modelling interfaces

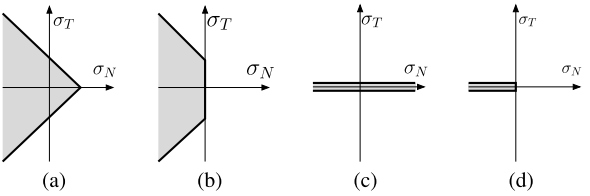

Fig. 5 Interface conditions: Rough interface, equal to soil properties (**a**), rough with no tension (**b**), smooth interface (**c**), and smooth with no tension (**d**)

is an idealisation of the real three-dimensional situation. We consider the two-dimensional plane strain analysis with additional superimposed elements (reinforcements, ties or anchors) that are analysed in plane-stress and connected to the soil. We have modelled the structural elements as solid elements and not linear elements, which prevents the presence of point loads and therefore allows us to preserve the strictness of the bounds.

Computationally, we need to deal with edges where the soil elements on side A are connected to two types of elements: other soil elements (with variables B) and those superimposed elements that model the structural elements (with variables B'). Figure 6 shows such an edge in the lower and upper bound formulation. We will call those edges as *duplicated edges*.

In the lower bound formulation, we need to modify the equilibrium constraints of the edges, which now read,

$$\left(\boldsymbol{\sigma}_i^A - \boldsymbol{\sigma}_i^B - \boldsymbol{\sigma}_i^{B'}\right) \cdot \boldsymbol{n} = \mathbf{0}, \quad i = 1, 2$$

where $\boldsymbol{\sigma}_i^A$, $\boldsymbol{\sigma}_i^B$ an $\boldsymbol{\sigma}_i^{B'}$ are respectively the nodal stresses at sides A, B nd B'. Since there is one equilibrium equation per common node, each duplicated edge requires two nodal velocities, as indicated with circles in Fig. 6(a).

In the upper bound formulation, the dissipation power at the edge corresponds to the sum of the power dissipated between elements A and B, and the dissipated power between elements A and B'. Formally, the total dissipation power at the edge correspond to the sum of two integrals along the common edge:

$$a_\xi(\boldsymbol{\sigma}, \boldsymbol{v}) = \int_{\Gamma^\xi} \boldsymbol{\sigma}^{A-B} \cdot \left(\boldsymbol{v}^B - \boldsymbol{v}^A\right) d\Gamma + \int_{\Gamma^\xi} \boldsymbol{\sigma}^{A-B'} \cdot \left(\boldsymbol{v}^{B'} - \boldsymbol{v}^A\right) d\Gamma.$$

This expression of the dissipated power is equivalent to extending the stress space at the edges with two superimposed linear stress spaces, $\boldsymbol{\sigma}^{A-B}$ and $\boldsymbol{\sigma}^{A-B'}$, indicated by two pairs of squares in Fig. 6(b). By imposing that each one of the four nodal

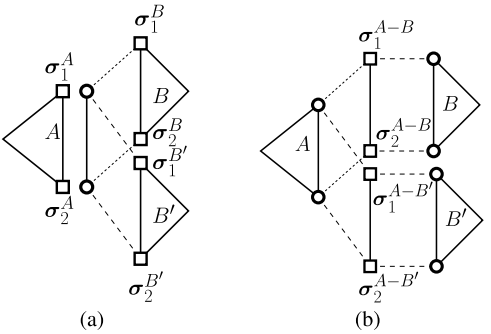

Fig. 6 Discrete spaces considered for the lower (**a**) and upper (**b**) bound problems when modelling duplicated edges. Elements B and B' are geometrically superimposed

variables is admissible, that is:

$$\begin{cases} \boldsymbol{\sigma}_i^{A-B} \in \mathscr{B}_I, \\ \boldsymbol{\sigma}_i^{A-B'} \in \mathscr{B}_I, \end{cases} \qquad i = 1, 2,$$

with $\mathscr{B}_I$ the admissible set for the interface conditions, the admissibility of the corresponding velocity jumps $\boldsymbol{v}_i^A - \boldsymbol{v}_i^B$ and $\boldsymbol{v}_i^A - \boldsymbol{v}_i^{B'}$ is ensured, and therefore the strictness of the upper bound is guaranteed. The nodal velocities are indicated with circles in Fig. 6(b).

2.3 Joints

Some of the practical problems in limit analysis include anchors, ties or other structural elements that are connected through joints. In this case, the kinematic constraints must be included in the exact problem described in Sect. 1.1, and also modelled in such a way that the strictness of the bounds is preserved. In the lower bound formulation, the presence of joints is modelled by including solely a point-to-point equilibrium condition, that is,

$$\int \left(\boldsymbol{\sigma}^A - \boldsymbol{\sigma}^B\right) \cdot \boldsymbol{n} d\Gamma = \mathbf{0}, \tag{10}$$

which replaces the equilibrium along the whole edge between elements. In the upper bound problem, the construction of a kinematically admissible space for the velocities is constructed by constricting the relative displacements of the joints in such a manner that only rotations with respect to the joint centre are allowed. Formally, this is achieved by replacing the associative velocity field at the joint by the following constraint in the upper bound problem in (5):

$$[\![\boldsymbol{v}]\!]_1 + [\![\boldsymbol{v}]\!]_2 = \mathbf{0}. \tag{11}$$

Figure 7 shows a schematic of the stress and velocity spaces employed for the modelling of the joints in the lower and upper bound problem. We point out that

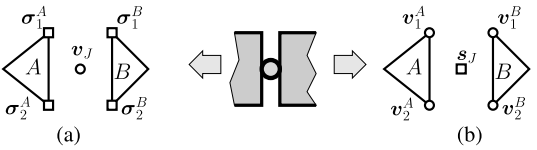

Fig. 7 Rotational joint and discrete spaces considered for the lower (**a**) and upper (**b**) bound problem

the joint is without friction, since no dissipated energy is associated to the relative rotation at the joint. This is computational made explicit by not imposing any equilibrium relation associated to the rotations in Eq. (10), and imposing exactly the kinematic relation in (11), i.e. the associated Lagrangian multiplier (variable $\boldsymbol{s}_J$ in Fig. 7) is free.

3 Decomposition Techniques

In order to reduce the memory requirement of realistic three dimensional problems we propose a decomposition of the optimization problems, which is based on the ideas explained in [5, 8]. While the decomposition techniques for optimisation problems is a relatively recent topic, its application to limit analysis and other plasticity problems has found far less attention [11]. We also refer the reader to [10], where alternative decomposition techniques of the limit analysis problem has been introduced. We here first briefly describe some of the general ideals of decomposition of optimisation problems.

3.1 Decomposition of Optimisation Problems

3.1.1 Primal Decomposition

To illustrate the decomposition techniques, we state the following linear optimization problem:

$$\begin{aligned} \boldsymbol{c}^T \boldsymbol{x}^* = \min_{\boldsymbol{x}} \ & \boldsymbol{c}^T \boldsymbol{x} \\ & \mathbf{A}\boldsymbol{x} = \boldsymbol{b}, \\ & \boldsymbol{x} \geq \mathbf{0}, \end{aligned} \tag{12}$$

whose dual reads,

$$\begin{aligned} \boldsymbol{b}^T \boldsymbol{y}^* = \max_{\boldsymbol{y}} \ & \boldsymbol{b}^T \boldsymbol{y} \\ & \mathbf{A}^T \boldsymbol{y} \leq \boldsymbol{c}. \end{aligned}$$

The primal decomposition consists on rewriting the problem (12) as:

$$\begin{aligned} \min_{\boldsymbol{x}_1,\boldsymbol{x}_2} \ & \boldsymbol{c}_1^T\boldsymbol{x}_1 + \boldsymbol{c}_2^T\boldsymbol{x}_2 \\ & \mathbf{A}_1\boldsymbol{x}_1 + \mathbf{A}_2\boldsymbol{x}_2 = \boldsymbol{b}, \\ & \boldsymbol{x}_1 \geq \mathbf{0}, \quad \boldsymbol{x}_2 \geq \mathbf{0}. \end{aligned} \tag{13}$$

In other words, we split the primal $\boldsymbol{x}$ variable as $\boldsymbol{x} = (\boldsymbol{x}_1, \boldsymbol{x}_2)$. The problem above is equivalent to:

$$\begin{aligned} \min_{\boldsymbol{t}} \min_{\boldsymbol{x}_1,\boldsymbol{x}_2} \ & \boldsymbol{c}_1^T\boldsymbol{x}_1 + \boldsymbol{c}_2^T\boldsymbol{x}_2 \\ & \mathbf{A}_1\boldsymbol{x}_1 = \frac{\boldsymbol{b}}{2} + \boldsymbol{t}, \\ & \mathbf{A}_2\boldsymbol{x}_2 = \frac{\boldsymbol{b}}{2} - \boldsymbol{t}, \\ & \boldsymbol{x}_1 \geq 0, \quad \boldsymbol{x}_2 \geq 0, \quad \boldsymbol{t} \text{ is free.} \end{aligned} \tag{14}$$

Given a fixed value of $\boldsymbol{t}$, the optimum value may be obtained as a result of the inner minimums,

$$\begin{aligned} f_i(\boldsymbol{t}) = \min_{\boldsymbol{x}_i} \ & \boldsymbol{c}_i^T\boldsymbol{x}_i \\ & \mathbf{A}_i\boldsymbol{x}_i = \frac{b}{2} + (-1)^{i+1}\boldsymbol{t}, \\ & \boldsymbol{x}_i \geq \mathbf{0} \quad (i = 1, 2), \end{aligned} \tag{15}$$

so called sub-problems or slave problems and the following master problem:

$$\min_{\boldsymbol{t}} \ f_1(\boldsymbol{t}) + f_2(\boldsymbol{t}), \tag{16}$$

which only depends on the global variable $\boldsymbol{t}$. The Lagrangian function of problem (14) is given by:

$$\begin{aligned} & L(\boldsymbol{x}_1, \boldsymbol{x}_2; \boldsymbol{y}_1, \boldsymbol{y}_2, \boldsymbol{w}_1, \boldsymbol{w}_2) \\ & = \boldsymbol{c}_1^T\boldsymbol{x}_1 + \boldsymbol{c}_2^T\boldsymbol{x}_2 + \boldsymbol{y}_1^T\left(\frac{\boldsymbol{b}}{2} + \boldsymbol{t} - \mathbf{A}_1\boldsymbol{x}_1\right) + \boldsymbol{y}_2^T\left(\frac{\boldsymbol{b}}{2} - \boldsymbol{t} - \mathbf{A}_2\boldsymbol{x}_2\right) - \mathbf{w}_1^T\boldsymbol{x}_1 \\ & \quad - \mathbf{w}_2^T\boldsymbol{x}_2 \\ & = \boldsymbol{c}_1^T\boldsymbol{x}_1 + \boldsymbol{y}_1^T\left(\frac{b}{2} - \mathbf{A}_1\boldsymbol{x}_1\right) + \boldsymbol{c}_2^T\boldsymbol{x}_2 + \boldsymbol{y}_2^T\left(\frac{\boldsymbol{b}}{2} - \mathbf{A}_1\boldsymbol{x}_1\right) + \boldsymbol{t}^T(\boldsymbol{y}_1 - \boldsymbol{y}_2) \\ & = L_1(\boldsymbol{x}_1, \boldsymbol{t}; \boldsymbol{y}_1, \boldsymbol{w}_1) + L_2(\boldsymbol{x}_2, \boldsymbol{t}; \boldsymbol{y}_2, \boldsymbol{w}_2), \end{aligned}$$

with

$$L_i(\boldsymbol{x}_i, \boldsymbol{t}; \boldsymbol{y}_i, \boldsymbol{w}_i) = \boldsymbol{c}_i^T \boldsymbol{x}_1 + \boldsymbol{y}_i^T \left(\frac{\boldsymbol{b}}{2} + (-1)^{i+1} \boldsymbol{t} - \mathbf{A}_1 \boldsymbol{x}_1 \right) - \boldsymbol{w}_i^T \boldsymbol{x}_i \quad (i = 1, 2).$$

It then follows that we can rewrite the optimum primal objective $\boldsymbol{c}^T \boldsymbol{x}^*$ as,

$$\boldsymbol{c}^T \boldsymbol{x}^* = \boldsymbol{c}_1^T \boldsymbol{x}_1^* + \boldsymbol{c}_2^T \boldsymbol{x}_2^* = \min_{\boldsymbol{t}} \sum_{i=1}^{2} \min_{\boldsymbol{x}_i} \max_{\boldsymbol{y}_i, \boldsymbol{w}_i} L_i(\boldsymbol{x}_i, \boldsymbol{t}; \boldsymbol{y}_i, \boldsymbol{w}_i).$$

After observing the equation above, we have that $\nabla_{\boldsymbol{t}} L = (\boldsymbol{y}_1 - \boldsymbol{y}_2)$, and therefore we can update the master variables with the following descent method,

$$\boldsymbol{t}^{k+1} = \boldsymbol{t}^k - \alpha^k \left(\boldsymbol{y}_1^k - \boldsymbol{y}_2^k \right) = \boldsymbol{t}^k + \alpha^k \left(\boldsymbol{y}_2^k - \boldsymbol{y}_1^k \right), \tag{17}$$

where $\boldsymbol{y}_1$ and $\boldsymbol{y}_2$ are the sub-gradient of functions f_1 and f_2 respectively. α^k is a step length that can be chosen in any of the standard ways [3].

3.1.2 Dual Decomposition

We recall the same problem in (13). Dual decomposition for this example is straightforward. We form the Lagrangian function as follows:

$$\begin{aligned}
&L(\boldsymbol{x}_1, \boldsymbol{x}_2, \boldsymbol{y}, \boldsymbol{w}_1, \boldsymbol{w}_2) \\
&= \boldsymbol{c}_1^T \boldsymbol{x}_1 + \boldsymbol{c}_2^T \boldsymbol{x}_2 + \boldsymbol{y}^T \left(\frac{\boldsymbol{b}}{2} - \mathbf{A}_1 \boldsymbol{x}_1 + \frac{\boldsymbol{b}}{2} - \mathbf{A}_2 \boldsymbol{x}_2 \right) - \boldsymbol{w}_1^T \boldsymbol{x}_1 - \boldsymbol{w}_2^T \boldsymbol{x}_2 \\
&= \left(\boldsymbol{c}_1^T \boldsymbol{x}_1 + \boldsymbol{y}^T \left(\frac{\boldsymbol{b}}{2} - \mathbf{A}_1 \boldsymbol{x}_1 \right) - \boldsymbol{w}_1^T \boldsymbol{x}_1 \right) \\
&\quad + \left(\boldsymbol{c}_2^T \boldsymbol{x}_2 + \boldsymbol{y}^T \left(\frac{\boldsymbol{b}}{2} - \mathbf{A}_2 \boldsymbol{x}_2 \right) - \boldsymbol{w}_2^T \boldsymbol{x}_2 \right),
\end{aligned}$$

so we can minimize over $\boldsymbol{x}_1$ and $\boldsymbol{x}_2$ separately given the dual variable $\boldsymbol{y}$, to find $g(\boldsymbol{y}) = g_1(\boldsymbol{y}) + g_2(\boldsymbol{y})$ where $g(\boldsymbol{y})$ is given as,

$$g(\boldsymbol{y}) = \min_{\boldsymbol{x}_1, \boldsymbol{x}_2} L(\boldsymbol{x}_1, \boldsymbol{x}_2, \boldsymbol{y}, \boldsymbol{w}_1, \boldsymbol{w}_2) = \min_{\boldsymbol{x}_1, \boldsymbol{x}_2} L_1(\boldsymbol{x}_1, \boldsymbol{y}, \boldsymbol{w}_1) + L_2(\boldsymbol{x}_2, \boldsymbol{y}, \boldsymbol{w}_2).$$

In order to find $g_1(\boldsymbol{y})$ and $g_2(\boldsymbol{y})$, respectively, we solve the following two subproblems:

$$g_1(\boldsymbol{y}) = \min_{\boldsymbol{x}_1 \geq 0} \boldsymbol{c}_1^T \boldsymbol{x}_1 + \boldsymbol{y}^T \left(\frac{\boldsymbol{b}}{2} - \mathbf{A}_1 \boldsymbol{x}_1 \right) = \min_{\boldsymbol{x}_1 \geq 0} \left(\boldsymbol{c}_1^T - \mathbf{A}_1^T \boldsymbol{y} \right) \boldsymbol{x}_1 + \boldsymbol{y}^T \frac{\boldsymbol{b}}{2},$$

$$g_2(\boldsymbol{y}) = \min_{\boldsymbol{x}_2 \geq 0} \boldsymbol{c}_2^T \boldsymbol{x}_2 + \boldsymbol{y}^T \left(\frac{\boldsymbol{b}}{2} - \mathbf{A}_2 \boldsymbol{x}_2 \right) = \min_{\boldsymbol{x}_2 \geq 0} \left(\boldsymbol{c}_2^T - \mathbf{A}_2^T \boldsymbol{y} \right) \boldsymbol{x}_2 + \boldsymbol{y}^T \frac{\boldsymbol{b}}{2}.$$

The master algorithm updates $\boldsymbol{y}$ based on sub-gradient as follows:

$$\boldsymbol{y} = \boldsymbol{y} + \beta\left(\frac{\boldsymbol{b}}{2} - \mathbf{A}_1\boldsymbol{x}_1 + \frac{\boldsymbol{b}}{2} - \mathbf{A}_2\boldsymbol{x}_2\right) = \boldsymbol{y} + \beta(\boldsymbol{b} - \mathbf{A}\boldsymbol{x}), \tag{18}$$

where β is a step length that can be chosen in any of the standard ways [3].

3.1.3 Bender's Decomposition

One of the main disadvantages of the previous decomposition is the update of the master variables. Since the minimised/maximised functions are non-smooth, the updated in (17) and (18) is not always optimal. For this reason, we have also studied the implementation of Bender's decomposition [2, 9]. The latter may be applied to the simple form of the linear problem in (14) as the solution of the following two sub-problems,

$$\left.\begin{aligned} &\min_{\boldsymbol{x}_i} \boldsymbol{c}_i^T\boldsymbol{x}_i \\ &\mathbf{A}_i\boldsymbol{x}_i = \frac{\boldsymbol{b}}{2} + (-1)^{i+1}\boldsymbol{t}, \\ &\boldsymbol{x}_i \geq 0, \end{aligned}\right\} \quad i = 1, 2 \tag{19}$$

and the solution of the following master problem:

$$\begin{aligned} &\min_{\alpha,\boldsymbol{t}} \alpha_1 + \alpha_2 \\ &0 \geq \left(\frac{\boldsymbol{b}}{2} + (-1)^{i+1}\boldsymbol{t}\right)\cdot \boldsymbol{y}_i^p, \quad p = 1, \ldots, p_k, \\ &\alpha_i \geq \left(\frac{\boldsymbol{b}}{2} + (-1)^{i+1}\boldsymbol{t}\right)\cdot \boldsymbol{y}_i^q, \quad q = 1, \ldots, q_k. \end{aligned} \tag{20}$$

The first and second sets of inequalities in (20) are respectively so-called feasibility cuts or optimality constraints, where $\boldsymbol{y}_i^p$ and $\boldsymbol{y}_i^q$ are the whole set optimal dual variables and extreme rays of the dual problem of (19) computed up to iteration $k = p_k + q_k$. Further details on the Bender's decomposition may be found in [8].

3.2 Decomposition of Limit Analysis Optimisation Problem

The decomposition techniques described in Sect. 3 are here adapted to optimization problem encountered in limit analysis. When applying these ideas, it must be taken into account the particular structure of the lower and upper bound optimization problems. Indeed, the objective function is only formed by the load factor in the lower bound problem, the constraints correspond to the equilibrium constrains, as a

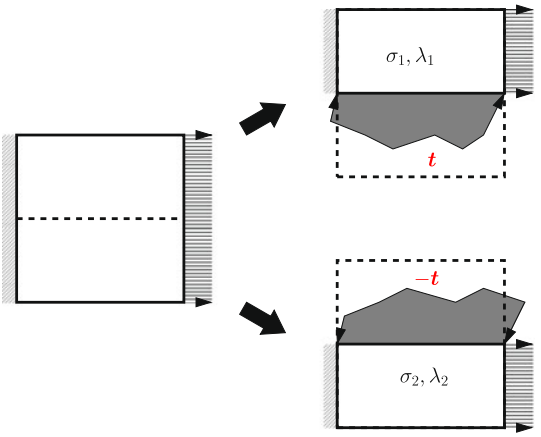

Fig. 8 Decomposition of the global domain of a limit analysis problem (*left*) into two domains, with the fictitious Neumann boundary shaded (*right*)

function of the stress variables which belongs to a non-linear set. As explained in Sect. 1 the constraints become linear equations of variables that belong to second-order cones. In the sequel we apply the decomposition technique described to the lower bound (LB) problem in limit analysis.

3.2.1 Decomposition of LB Problem

The decomposition of LB problem corresponds to splitting the nodal stress variables $\boldsymbol{\sigma}$ into two sets $\boldsymbol{\sigma}^1$ and $\boldsymbol{\sigma}^2$, which in turn is also equivalent to splitting the variable $\boldsymbol{x}$ into two variables $\boldsymbol{x}_1$ and $\boldsymbol{x}_2$. In this case, the constrains may be decomposed like in the primal technique, by using additional traction variables $\boldsymbol{t}$ between domains, as depicted in Fig. 8. In other words we split our domain in two sub-problems with local variables $\boldsymbol{x}_i$, and a master(global) variable $\boldsymbol{t}$ that in the LB problem corresponds to the internal tractions between the sub-domains. Such variables may be seen as a (non-proportional) fictitious Neumann condition. We next deduce in detail the decomposed form of the lower bound optimisation problem.

As described in Sect. 1, equation $\bar{\mathbf{A}}^{eq1}\boldsymbol{\sigma} + \boldsymbol{F}^{eq1} = 0$ in (4) is related to the equilibrium constraint, which can be decomposed into two separate equations as follows:

$$\begin{aligned} \bar{\mathbf{A}}^{eq1,1}\boldsymbol{\sigma}^1 + \lambda \boldsymbol{F}^{eq1,1} &= \mathbf{0}, \\ \bar{\mathbf{A}}^{eq1,2}\boldsymbol{\sigma}^2 + \lambda \boldsymbol{F}^{eq1,2} &= \mathbf{0}. \end{aligned} \tag{21}$$

When the vector $\boldsymbol{\sigma}$ is split into two vectors $\boldsymbol{\sigma}^1$ and $\boldsymbol{\sigma}^2$, the domain of the problem is also split into two parts with a common boundary that couples some of the two set of variables. This means that the vectors $\boldsymbol{\sigma}^1$ and $\boldsymbol{\sigma}^2$ may be decomposed into two vectors $\boldsymbol{\sigma}^1 = (\boldsymbol{\sigma}^{1,1}, \boldsymbol{\sigma}^{1,2})$ and $\boldsymbol{\sigma}^2 = (\boldsymbol{\sigma}^{2,1}, \boldsymbol{\sigma}^{2,2})$ such that the vectors $\boldsymbol{\sigma}^{1,1}$ and $\boldsymbol{\sigma}^{2,2}$

are coupled through the inter-element equilibrium constraints as follows:

$$\begin{aligned}
&\bar{\mathbf{A}}^{eq2,1}\boldsymbol{\sigma}^1 = 0,\\
&\bar{\mathbf{A}}^{eq2,2}\boldsymbol{\sigma}^2 = 0,\\
&\bar{\mathbf{B}}^{eq2,1}\boldsymbol{\sigma}^1 + \bar{\mathbf{B}}^{eq2,2}\boldsymbol{\sigma}^2 = 0.
\end{aligned} \tag{22}$$

We note that the last equation in (22) is a complicating constraint. The equation $\bar{\mathbf{A}}^3\boldsymbol{\sigma} + \lambda \boldsymbol{F}^{eq3} = 0$ is separable and can be in turn decomposed as,

$$\begin{aligned}
&\bar{\mathbf{A}}^{eq3,1}\boldsymbol{\sigma}^1 + \lambda \boldsymbol{F}^{eq3,1} = 0,\\
&\bar{\mathbf{A}}^{eq3,2}\boldsymbol{\sigma}^2 + \lambda \boldsymbol{F}^{eq3,2} = 0.
\end{aligned} \tag{23}$$

Consequently, after applying the linear transformation to variable $\boldsymbol{\sigma}^i$, we can rewrite the optimisation problem in (6) as,

$$\begin{aligned}
\min_{\boldsymbol{x}_1,\boldsymbol{x}_2,\lambda}\ & -\lambda\\
& \mathbf{A}^{eq1,i}\boldsymbol{x}^i + \lambda \boldsymbol{F}^{eq1,i} = \boldsymbol{b}^{eq1,i}, \quad i = 1,2,\\
& \mathbf{A}^{eq2,i}\boldsymbol{x}^i = 0, \quad i = 1,2,\\
& \mathbf{A}^{eq3,i}\boldsymbol{x}^i + \lambda \boldsymbol{F}^{eq3,i} = \boldsymbol{b}^{eq3,i}, \quad i = 1,2,\\
& \mathbf{B}^{eq2,1}\boldsymbol{x}^1 + \mathbf{B}^{eq2,2}\boldsymbol{x}^2 = 0,\\
& \boldsymbol{x}^1 \in K_1, \quad \boldsymbol{x}^2 \in K_2; \quad \lambda \text{ free}.
\end{aligned} \tag{24}$$

The last equation in the previous optimisation problem (24) is a complicating constraint of the local variables $\boldsymbol{x}_1$ and $\boldsymbol{x}_2$, while the variable λ can be regarded as a global variable. In order to decompose the problem in (24) we first introduce a variable $\boldsymbol{t}$ such that

$$\mathbf{B}^{eq2,1}\boldsymbol{x}^1 = \boldsymbol{t}.$$

Then we can rewrite the optimisation problem in the following form:

$$\begin{aligned}
\min_{\boldsymbol{t},\boldsymbol{x}_i,\lambda}\ & -\lambda\\
& \mathbf{A}^{eq1,i}\boldsymbol{x}^i + \lambda \boldsymbol{F}^{eq1,i} = \boldsymbol{b}^{eq1,i},\\
& \mathbf{A}^{eq2,i}\boldsymbol{x}^i = 0,\\
& \mathbf{A}^{eq3,i}\boldsymbol{x}^i + \lambda \boldsymbol{F}^{eq3,i} = 0,\\
& \mathbf{B}^{eq2,i}\boldsymbol{x}^i = (-1)^{i+1}t,\\
& \boldsymbol{x}_i \in K_i, \quad \boldsymbol{t}, \lambda \text{ free} \quad (i = 1,2)
\end{aligned} \tag{25}$$

Note that since the complicating constraint in optimisation problem (25) is built through the common boundary, the coupling constraint can be interpreted as fictitious Newman condition for each sub-domain.

By introducing new variables $\boldsymbol{t}_i$ $(i = 1, 2)$, we can rewrite our problem in the following form:

$$\begin{aligned}
\min\ & \left(-\frac{\lambda_1}{2}\right) + \left(-\frac{\lambda_2}{2}\right), \\
& \mathbf{A}^{eq1,i}\boldsymbol{x}^i + \lambda_i \boldsymbol{F}^{eq1,i} = \boldsymbol{b}^{eq1.i}, \\
& \mathbf{A}^{eq2,i}\boldsymbol{x}^i = 0, \\
& \mathbf{A}^{eq3,i}\boldsymbol{x}^i + \lambda_i \boldsymbol{F}^{eq3,i} = \boldsymbol{b}^{eq3,i}, \\
& \mathbf{B}^{eq2,i}\boldsymbol{x}^i = (-1)^{i+1}\boldsymbol{t}_i, \\
& \boldsymbol{t}_1 = \boldsymbol{t}_2, \\
& \lambda_1 = \lambda_2.
\end{aligned}$$

Let C_i $(i = 1, 2)$ be local constraints that are defined as follows:

$$C_i = \left\{ \left\{ \boldsymbol{t}_i, \boldsymbol{x}^i, \lambda^i \right\} \middle| \begin{array}{l} \mathbf{A}^{eq1,i}\boldsymbol{x}^i + \lambda_i \boldsymbol{F}^{eq1,i} = \boldsymbol{b}^{eq1,i}, \\ \mathbf{A}^{eq2,i}\boldsymbol{x}^i = 0, \\ \mathbf{A}^{eq3,i}\boldsymbol{x}^i + \lambda_i \boldsymbol{F}^{eq3,i} = \boldsymbol{b}^{eq3,i}, \\ \mathbf{B}^{eq2,i}\boldsymbol{x}^i = \boldsymbol{t}_i, \\ \boldsymbol{x}^i \in K_i,\ \boldsymbol{t}_i, \lambda_i \ \text{ free.} \end{array} \right\}$$

In the above problem, $\boldsymbol{t}_1, \lambda_1, \boldsymbol{t}_2, \lambda_2$ are public variables and $\boldsymbol{x}^1, \boldsymbol{x}^2$ are private variables. Let us collect all the public variables together into one variable $\boldsymbol{y} = (\boldsymbol{t}_1, \lambda_1, \boldsymbol{t}_2, \lambda_2) = (\boldsymbol{y}_1, \boldsymbol{y}_2)$ where $\boldsymbol{y}_1 = (\boldsymbol{t}_1, \lambda_1)$, $\boldsymbol{y}_2 = (\boldsymbol{t}_2, \lambda_2)$. If we introduce a vector $\boldsymbol{z}$ that gives the common values of the public variables, then we can express the coupling constraints as $\boldsymbol{y} = \mathbf{E}\boldsymbol{z}$ where $\mathbf{E}$ is a matrix with components equal to zero or one, that is:

$$\boldsymbol{z} = \left\{ \begin{array}{c} \boldsymbol{t} \\ \lambda \end{array} \right\}, \qquad \boldsymbol{y}_i = \mathbf{E}_i \boldsymbol{z} \quad \text{where } \mathbf{E}_i = \begin{bmatrix} \mathbf{I} & 0 \\ 0 & 1 \end{bmatrix},\ \boldsymbol{y} = \mathbf{E}\boldsymbol{z} \text{ where } \mathbf{E} = \begin{bmatrix} \mathbf{E}_1 \\ \mathbf{E}_2 \end{bmatrix}.$$

Let us set $f_i(\boldsymbol{x}_i, \boldsymbol{y}_i) = f(\boldsymbol{x}_i, \boldsymbol{t}_i, \lambda_i) = -\frac{\lambda_i}{2}$ $(i = 1, 2)$. Then our problem has the followings form:

$$\begin{aligned}
\min_{\boldsymbol{x},\boldsymbol{y},\boldsymbol{z}}\ & f_1(\boldsymbol{x}_1, \boldsymbol{y}_1) + f_2(\boldsymbol{x}_2, \boldsymbol{y}_2) \\
& (\boldsymbol{x}_1, \boldsymbol{y}_1) \in C_1, \quad (\boldsymbol{x}_2, \boldsymbol{y}_2) \in C_2, \\
& \boldsymbol{y}_i = \mathbf{E}_i \boldsymbol{z}, \quad i = 1, 2, \\
& \boldsymbol{x} = (\boldsymbol{x}_1, \boldsymbol{x}_2), \quad \boldsymbol{y} = (\boldsymbol{y}_1, \boldsymbol{y}_2), \quad \boldsymbol{y}_i = (\boldsymbol{t}_i, \lambda_i) \quad (i = 1, 2),
\end{aligned} \tag{26}$$

with variables $\boldsymbol{x}_i$, $\boldsymbol{y}_i$, and $\boldsymbol{z}$. We then have a problem that is separable for fixed values of $\boldsymbol{z}$.

3.2.2 Primal Decomposition of LB Problem

In primal decomposition, at each iteration we fix the vector $\boldsymbol{z}$ and we fix the public variables as $\boldsymbol{y}_i = \mathbf{E}_i \boldsymbol{z}$. The problem is now separable. Each sub-problem can separately find optimal values for its local variables $\boldsymbol{x}_i$. Let us denote $q_i(\boldsymbol{y}_i) = q_i(\mathbf{E}\boldsymbol{z})$ the optimal value of the sub-problem

$$\begin{aligned} q_i(\boldsymbol{y}_i) = \min_{\boldsymbol{x}_i} \; & f_i(\boldsymbol{x}_i, \boldsymbol{y}_i) \\ & (\boldsymbol{x}_i, \boldsymbol{y}_i) \in C_i \quad (i = 1, 2), \end{aligned}$$

with variable $\boldsymbol{x}_i$, as a function of $\boldsymbol{y}_i$. The original problem (26) is equivalent to the primal master problem

$$\min_{\boldsymbol{z}} q(\boldsymbol{z}) = q_1(\mathbf{E}_1 \boldsymbol{z}) + q_2(\mathbf{E}_2 \boldsymbol{z}),$$

with variable $\boldsymbol{z}$. In order to find a sub-gradient of q, denoted by $\boldsymbol{g}$, we find $\boldsymbol{g}_i \in \partial q_i(\boldsymbol{y}_i)$ (which can be done separately), and then compute $\boldsymbol{g}$ as,

$$\boldsymbol{g} = \mathbf{E}_1^T \boldsymbol{g}_1 + \mathbf{E}_2^T \boldsymbol{g}_2.$$

3.2.3 Dual Decomposition of LB Problem

We form the partial Lagrangian of problem (26),

$$\begin{aligned} L(\boldsymbol{x}, \boldsymbol{y}, \boldsymbol{z}, \boldsymbol{v}) &= f_1(\boldsymbol{x}_1, \boldsymbol{y}_1) + f_2(\boldsymbol{x}_2, \boldsymbol{y}_2) + \boldsymbol{v}^T(-\boldsymbol{y} + \mathbf{E}\boldsymbol{z}) \\ &= \big(f_1(\boldsymbol{x}_1, \boldsymbol{y}_1) - \boldsymbol{v}_1^T \boldsymbol{y}_1\big) + \big(f_2(\boldsymbol{x}_2, \boldsymbol{y}_2) - \boldsymbol{v}_2^T \boldsymbol{y}_2\big) + \boldsymbol{v}^T \mathbf{E}\boldsymbol{z}, \end{aligned}$$

where $\boldsymbol{v}$ is the Lagrangian multiplier associated with $\boldsymbol{y} = \mathbf{E}\boldsymbol{z}$. To find the dual function, we first minimize over $\boldsymbol{z}$, which results in the condition $\mathbf{E}^T \boldsymbol{v} = 0$. In other words

$$\begin{aligned} q(\boldsymbol{v}) &= q(\boldsymbol{v}_1, \boldsymbol{v}_2) \\ &= \min_{\boldsymbol{x}_1, \boldsymbol{x}_2, \boldsymbol{y}_1, \boldsymbol{y}_2} \; \min_{\boldsymbol{z}} \big(f_1(\boldsymbol{x}_1, \boldsymbol{y}_1) - \boldsymbol{v}_1^T \boldsymbol{y}_1\big) + \big(f_2(\boldsymbol{x}_2, \boldsymbol{y}_2) - \boldsymbol{v}_2^T \boldsymbol{y}_2\big) + \boldsymbol{v}^T \mathbf{E}\boldsymbol{z} \\ & \qquad (\boldsymbol{x}_1, \boldsymbol{y}_i) \in C_i \quad (i = 1, 2), \end{aligned}$$

then

$$q(\boldsymbol{v}) = q(\boldsymbol{v}_1, \boldsymbol{v}_2) = \min_{\boldsymbol{x}_1, \boldsymbol{x}_2, \boldsymbol{y}_1, \boldsymbol{y}_2} \big(f_1(\boldsymbol{x}_1, \boldsymbol{y}_1) - \boldsymbol{v}_1^T \boldsymbol{y}_1\big) + \big(f_2(\boldsymbol{x}_2, \boldsymbol{y}_2) - \boldsymbol{v}_2^T \boldsymbol{y}_2\big)$$

$$\mathbf{E}^T \boldsymbol{v} = 0,$$
$$(\boldsymbol{x}_i, \boldsymbol{y}_i) \in C_i \quad (i = 1, 2).$$

We define $q_i(\boldsymbol{v}_i),\ (i = 1, 2)$ as the optimal value of the sub-problems $(i = 1, 2)$,

$$\begin{aligned} q_i(\boldsymbol{v}_i) = \min_{\boldsymbol{x}_i, \boldsymbol{y}_i} \left(f_i(\boldsymbol{x}_i, \boldsymbol{y}_i) - \boldsymbol{v}_i^T \boldsymbol{y}_i \right) \\ (\boldsymbol{x}_i, \boldsymbol{y}_i) \in C_i, \end{aligned} \tag{27}$$

as a function of $\boldsymbol{v}_i$. A sub-gradient of q_i at $\boldsymbol{v}_i$ is just $-\boldsymbol{y}_i$, an optimal value of $\boldsymbol{y}_i$ in the sub-problem (27). Therefore the dual of the original problem (26) is

$$\max\ q(\boldsymbol{v}) = q_1(\boldsymbol{v}_1) + q_2(\boldsymbol{v}_2)$$
$$\mathbf{E}^T \boldsymbol{v} = 0,$$

with variable $\boldsymbol{v}$. We can solve this dual decomposition master problem using a projected sub-gradient method. The projection onto the feasible set $\{\boldsymbol{v} | \mathbf{E}^T \boldsymbol{v} = 0\}$, is given by the following operator:

$$\mathbf{I} - \mathbf{E}\left(\mathbf{E}^T \mathbf{E}\right)^{-1} \mathbf{E}^T.$$

4 Numerical Results

4.1 Bearing Capacity of Anchors

The extensions described in Sect. 2 have been employed to test the pull out capacity of multi-belled anchors. The linearity of the limit tension with respect to the number of bells has been verified.

Five different anchor/soil conditions have been employed: rough (same properties as the soil), smooth (no resistance to shear), no tension condition, rough condition with no tension, and smooth condition with no-tension. Although the mechanisms do not significantly depend on these conditions, the pull out capacity does, and has been shown to be much larger for rough conditions. On the other hand, while for clay materials (zero internal friction angle, but non-zero cohesion) the failure mechanism is localised around the anchor (see Fig. 9(a)), in other sand materials the slide-lines propagate up to the soil surface (see Fig. 9(b)). The computed limiting height agrees satisfactorily with experimental results and other numerical models that use incremental plasticity [15].

4.2 Retaining Walls

The maximum height of a simply supported and anchored retaining wall has been computed using the techniques explained in Sect. 2. Figure 10 shows the dissipation

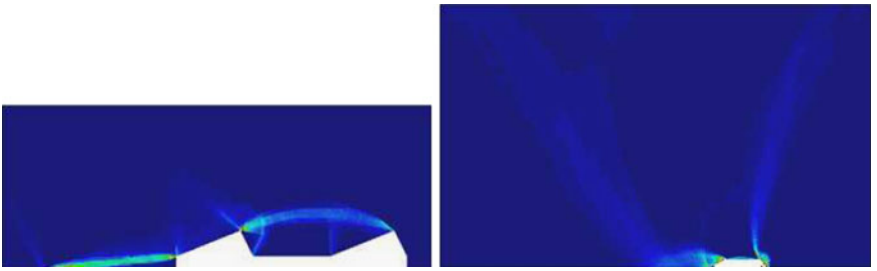

(a) (b)

Fig. 9 Dissipation energy of double bell anchor. (**a**) Clay soil, with sliding conditions and no tension at the anchor-soil interface. (**b**) Sand soil with internal friction angle $\phi = 20°$, and rough interface conditions with no tension

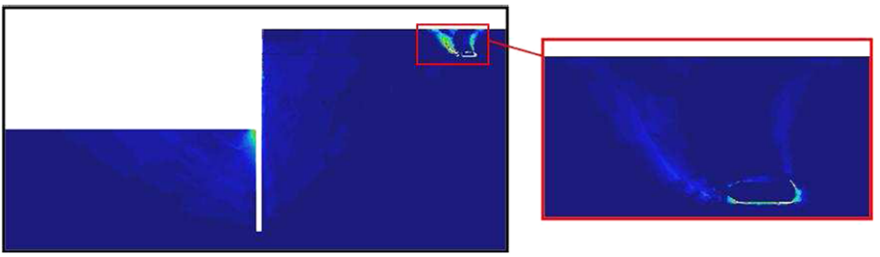

Fig. 10 Contour plot of the dissipation power on an anchored wall. *Left*: domain without the wall. *Right*: zoom on the domain surrounding the anchor. Interface soil-anchor and soil-wall conditions are rough with no tension

power of an anchored wall, with a zoom on the region surrounding the anchor. For an anchor length equal to the height of the wall, the collapse mechanism surround the whole wall-anchor system, while for longer anchors, the mechanism tends to be localised around the anchor. Figure 11 shows the mesh obtained after 4 successive iterations. As it can be observed, the smaller elements localise in the regions with higher dissipation power and at the slidelines.

The tests have been run for different ratios of d/h where $h =$ free wall height, and $d =$ total height of the wall. The collapse of the wall was obtained for a certain factor λ of the gravity acceleration. As the ratio h/d is increased, the value of λ was decreasing. The limiting free height is the value for which $\lambda = 1$. The plots in Figure 12 show the evolution of λ, and indicate the limiting ratios for different wall conditions and admissibility conditions of the wall-soil and anchor-soil interfaces. These values agree with some experimental values published in [19].

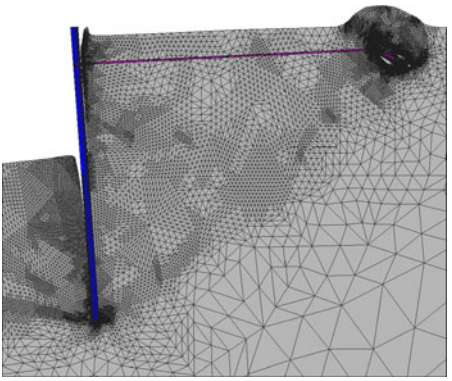

Fig. 11 Upper bound velocities of anchored wall with the resulting mesh after 4 meshing strategies

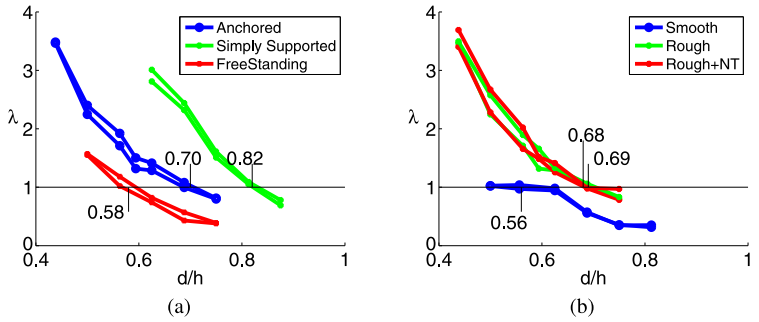

Fig. 12 (**a**) Upper and lower bound of the bearing capacity of a retaining wall with a rough interface with no traction. (**b**) Bounds for the anchored wall with different anchor-soil conditions. *Horizontal axis* corresponds to the ratio d/h, while the values in the *vertical axis* corresponds to the factor multiplying the gravity acceleration at collapse

4.3 Decomposition Techniques

We have applied the dual decomposition technique described in Sect. 3.2.3 with dynamic step size [3] to the LB problem using a mesh with 128 elements and 1537 primal variables (see Fig. 13(a)). The domain is subjected to a horizontal traction field at the right boundary, and to a fully homogeneous Dirichlet conditions on its left boundary.

Figure 13(b) shows the evolution of the upper and lower bounds of the LB optimization problem, which after successive iteration converges to the exact value $\lambda^* = \lambda^{LB} = 2$. The algorithm converges to tolerance of 10^{-3} for the relative difference of upper and lower bound, the number of master iterations are between 10 and 15.

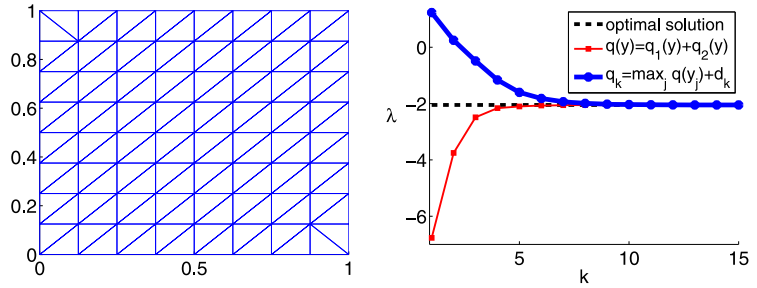

(a) (b)

Fig. 13 (**a**) Domain and mesh employed in the decomposition analysis of the lower bound problem. The domain is subjected to a homogeneous Dirichlet conditions (zero velocities) at the left boundary, and a horizontal tensile traction at the right boundary. (**b**) Evolution of the upper and lower bound of the optimal solution of the LB limit analysis problem when using a variable step–size in the dual decomposition method

5 Conclusions

We have presented some recent extension of the lower and upper bound formulation of limit analysis for problems with specific frictional interfaces, duplicated edges and joints. Such extensions are motivated by the limit analysis of practical problems with anchors and other structural elements.

We have also described how the optimisation problems that current computational limit analysis encounters may be decomposed for its eventual parallelisation. Although only simple domains problems with limited number of elements have been analysed, the methodology presented here is general and may be applied for more general problems. This generalisation, and other techniques are currently under investigation.

References

1. MOSEK ApS (2005) The MOSEK optimization tools version 3.2 (revision 8). User's manual and reference. http://www.mosek.com
2. Benders JF (1962) Partitioning procedures for solving mixed-variables programming problems. Numer Math 4:238–252
3. Bertsekas DP (2003) Convex analysis and optimization, 3rd edn. Athena Scientific, Cambridge
4. Boyd S, Vandenberghe L (2004) Convex optimization. Cambridge University Press, Cambridge
5. Boyd S, Xiao L, Mutapcic A, Mattingley J (2007) Notes on decomposition methods. Technical report, Stanford University. Notes of EE364B course
6. Christiansen E (1996) Limit analysis of collapse states. In: Handbook of numerical analysis, vol IV. North Holland, Amsterdam, pp 193–312
7. Ciria H, Peraire J, Bonet J (2008) Mesh adaptive computation of upper and lower bounds in limit analysis. Int J Numer Methods Eng 75:899–944

8. Conejo AJ, Castillo E, Mínguez R, García-Bertrand R (2006) Decomposition techniques in mathematical programming. Springer, The Netherlands
9. Geoffrion AM (1972) Generalized Benders decomposition. J Optim Theory Appl 10(4):238–252
10. Kammoun Z, Pastor F, Smaoui H, Pastor J (2010) Large static problem in numerical limit analysis: a decomposition approach. Int J Numer Anal Methods Geomech 34:1960–1980
11. Kaneko I (1983) A decomposition procedure for large-scale optimum plastic design problems. Int J Numer Methods Eng 19:873–889
12. Lyamin AV, Sloan SW, Krabbenhøft K, Hjiaj M (2005) Lower bound limit analysis with adaptive remeshing. Int J Numer Methods Eng 63:1961–1974
13. Muñoz JJ, Bonet J, Huerta A, Peraire J (2009) Upper and lower bounds in limit analysis: adaptive meshing strategies and discontinuous loading. Int J Numer Methods Eng 77:471–501
14. Muñoz JJ, Bonet J, Huerta A, Peraire J (2012) A note on upper bound formulations in limit analysis. Int J Numer Methods Eng 91(8):896–908
15. Muñoz JJ, Lyamin A, Huerta A (2012) Stability of anchored sheet wall in cohesive-frictional soils by FE limit analysis. Int J Numer Anal Methods Geomech. doi:10.1002/nag.2090
16. Salençon J (2002) De l'élasto-plasticité au calcul à la rupture. Les Éditions de l'École Polytechnique, Paris
17. Sturm JF (1999) Using SeDuMi 1.02, a MATLAB toolbox for optimization over symmetric cones. Optim Methods Softw 11–12:625–653. Version 1.05 available from http://sedumi.ie.lehigh.edu
18. Tütüncü RH, Toh KC, Todd MJ (2003) Solving semidefinite-quadratic-linear programs using SDPT3. Math Program, Ser B 95:189–217. http://www.math.nus.edu.sg/~mattohkc/sdpt3.html
19. Vossoughi KC (2001) Étude numérique du comportement des ouvrages de soutènement à la rupture. PhD thesis, Ecole Centrale Paris, Paris, France

Shakedown Analysis of Reissner-Mindlin Plates Using the Edge-Based Smoothed Finite Element Method

Thanh Ngọc Trần and M. Staat

Abstract This paper concerns the development of a primal-dual algorithm for limit and shakedown analysis of Reissner-Mindlin plates made of von Mises material. At each optimization iteration, the lower bound of the shakedown load multiplier is calculated simultaneously with the upper bound using the duality theory. An edge-based smoothed finite element method (ES-FEM) combined with the discrete shear gap (DSG) technique is used to improve the accuracy of the solutions and to avoid the transverse shear locking behaviour. The method not only possesses all inherent features of convergence and accuracy from ES-FEM, but also ensures that the total number of variables in the optimization problem is kept to a minimum compared with the standard finite element formulation. Numerical examples are presented to demonstrate the effectiveness of the present method.

1 Introduction

In practical engineering, the calculation of the load carrying capacity for structures has been a problem of great interest to many designers. In the early 20th century, it could be relatively easily obtained by limiting the stress intensity at a certain point of the structure equal to the yield stress of the material. This implies that structural failure occurs at initiating local plastic flow. However, many materials, for example the majority of metals, exhibit distinct, plastic properties. Such materials can deform considerably without breaking, even after the stress intensity attains the yield stress. This implies that if the stress intensity reaches the critical (yield) value, the structure does not necessarily fail or deform extensively. To this case, elastic-plastic structural analysis becomes more general and is capable of providing the much needed safety

T.N. Trần · M. Staat (✉)
Institute for Bioengineering, Biomechanics Lab., Aachen University of Applied Sciences, Heinrich-Mußmann-Str. 1, Jülich Campus, 52428 Jülich, Germany
e-mail: m.staat@fh-aachen.de

T.N. Trần
Chair of Mechanics and Robotics, University of Duisburg-Essen, Lotharstr. 1, 47057 Duisburg, Germany

K. Spiliopoulos, D. Weichert (eds.), *Direct Methods for Limit States in Structures and Materials*, DOI 10.1007/978-94-007-6827-7_5,

evaluation capability for enhanced diagnosis of aging infrastructure and the economical and safe design of new structures. Among the plasticity methods, Limit and Shakedown Analysis (LISA) seems to be the most powerful one. In Europe LISA have been developed as direct plasticity methods for the design and the safety analysis of severely loaded engineering structures, such as nuclear power plants and chemical plants, offshore structures, etc. [18]. Annex B of the new European pressure vessel standard EN 134453 is based on LISA (European standard, 2005-06), thus indicating the industrial need for LISA software.

Limit analysis of plates and slabs has been studied analytically [8, 14] and numerically [3, 5, 10]. In this work, the limit load was studied either by the lower bound approach which is based on the static theorem or by the upper bound approach which is based on the kinematic theorem. Tran et al. [19] developed a kinematic formulation for the shakedown analysis of thin plates and shells using the exact Ilyushin yield surface and nonlinear programming. Recently, a primal-dual algorithm for shakedown analysis of Kirchhoff plates made of von Mises material has been developed using DKQ plate elements [20]. It has been pointed out by the author that duality theory is indeed a very effective approach for shakedown analysis of structures.

After more than half a century of development, the finite element method (FEM) has become a very powerful technique for numerical simulations in engineering and science. However, when using finite element software, one frequently encounters problems with mesh generation. For accuracy reasons, one wants to use quadrilateral or hexahedron elements, but such a mesh is quite difficult to generate and requires a number of manual operations to cut the domain into proper pieces. In searching for alternatives, Liu et al. have introduced the strain smoothing technique [6] into the FEM formulating a cell/element-based smoothed finite element method (SFEM or CS-FEM) [11] and a node-based smoothed finite element method (NS-FEM) [13]. It was shown that the SFEM achieves more accurate results and a higher convergence rate than FEM without increasing computational costs. More important, as no mapping or coordinate transformation is involved in the SFEM, its elements are allowed to be of arbitrary shape and the problem of mesh distortion can be avoided when using SFEM.

CS-FEM is formulated using smoothing domains located inside the elements and proven effectively in solving 2D solid mechanics problems by using a proper number of smoothing cells in each element (for example four smoothing cells). The CS-FEM has also been extended to plate and shell structures [15, 16]. NS-FEM uses node-based smoothing domains associated from the predefined parts of all adjacent elements around the node. It can provide upper bound solutions in the strain energy and is also immune to volumetric locking naturally. However, the NS-FEM was found temporally unstable, and cannot be applied directly to dynamic problems. To overcome such a temporal instability, the edge-based smoothed finite element method (ES-FEM) has been recently proposed for analyses of solid 2D mechanics problems [12] and has then been extended for static, free vibration and buckling analyses of Reissner-Mindlin plates using triangular elements [17]. In that method, ES-FEM was incorporated with the discrete shear gap (DSG) technique [2] together

with a stabilization technique [1] in order to avoid the transverse shear locking and to improve the accuracy of the numerical solution. With T3 elements ES-FEM has been applied succesfully to probabilistic limit and shakedown analysis of 2D structures [21].

This paper presents a numerical algorithm for shakedown analysis of Reissner-Mindlin plates made of von Mises material. The algorithm is based upon a primal-dual approach in which the lower bound of the shakedown load multiplier is calculated simultaneously with the upper one through a dual problem. The edge-based smoothed finite element method (ES-FEM, [13]) and the DSG technique [2] were used for the discretization of the problem domain. This technique has been recently developed by Nguyen-Xuan et al. [17] in order to avoid the transverse shear locking and to improve the accuracy of the numerical solution of Reissner-Mindlin plates. Several benchmark plate problems in literature are investigated to test the performance of the method in which the thickness of the plate varies from very thick to very thin (below the Kirchhoff limit). Numerical examples demonstrate that the proposed method not only exhibits excellent convergence and accuracy of solutions, but also ensures that the total number of variables in the optimization problem is kept to a minimum compared with the standard finite element formulation.

2 Governing Equations of Mindlin Plates

Consider a plate whose mid-surface occupies a closed area Ω with static boundary $\partial\Omega_\sigma$ and kinematical boundary $\partial\Omega_u$ as shown in Fig. 1. Let t be the plate thickness, σ_y, E and ν the uniaxial yield stress, Young's modulus and Poisson's ratio of the material, respectively. The normalized vectors of moments $\mathbf{m}$, shear forces $\mathbf{s}$, curvatures $\boldsymbol{\kappa}$ and shear strains $\boldsymbol{\gamma}$ can be defined as

$$\begin{aligned} \mathbf{m} &= \frac{1}{M_0}\begin{pmatrix} M_{xx} \\ M_{yy} \\ M_{xy} \end{pmatrix}, \qquad \mathbf{s} = \frac{1}{S_0}\begin{pmatrix} S_{xx} \\ S_{yy} \end{pmatrix}, \\ \boldsymbol{\kappa} &= \frac{1}{\kappa_0}\begin{pmatrix} \kappa_{xx} \\ \kappa_{yy} \\ 2\kappa_{xy} \end{pmatrix}, \qquad \boldsymbol{\gamma} = \frac{1}{\gamma_0}\begin{pmatrix} \gamma_{xz} \\ \gamma_{yz} \end{pmatrix}, \end{aligned} \tag{1}$$

in which $M_0 = \sigma_y t^2/4$, $S_0 = \sigma_y t$, $\gamma_0 = \sigma_y(1-\nu^2)/E$, $\kappa_0 = 4\gamma_0/t$ are normalized quantities. Note that κ_0 is defined by assuming the relation $M_0\kappa_0 = S_0\gamma_0$ to hold. The non-dimensional stress and strain resultant vectors are introduced as follows

$$\hat{\boldsymbol{\sigma}} = \begin{bmatrix} \mathbf{m} & \mathbf{s} \end{bmatrix}^T, \qquad \hat{\boldsymbol{\varepsilon}} = \begin{bmatrix} \boldsymbol{\kappa} & \boldsymbol{\gamma} \end{bmatrix}^T. \tag{2}$$

We denote the nodal variables of the plate element by $\mathbf{q} = [\, w\ \theta_x\ \theta_y \,]^T$ and loading $\mathbf{g} = [\, 0\ 0\ p \,]^T$ acting on the plate where w is the transverse displacement; θ_x, θ_y are the rotations around the y- and x-axes; and p is the transverse load. Using the

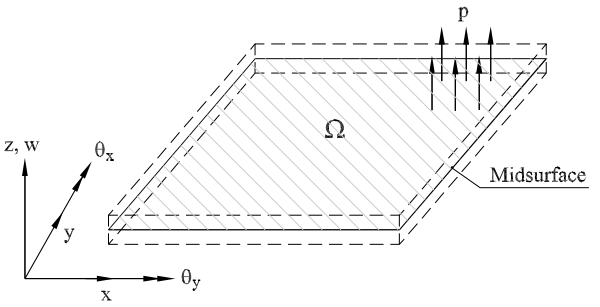

Fig. 1 Plate subjected to transverse load

stress and strain resultant vectors introduced above, the equilibrium conditions of plates can be written as follows

$$\mathbf{R}\hat{\boldsymbol{\sigma}} - \mathbf{g} = \mathbf{0}, \quad \mathbf{R} = \begin{bmatrix} M_0\frac{\partial}{\partial x} & 0 & M_0\frac{\partial}{\partial y} & S_0 & 0 \\ 0 & M_0\frac{\partial}{\partial y} & M_0\frac{\partial}{\partial x} & 0 & S_0 \\ 0 & 0 & 0 & S_0\frac{\partial}{\partial x} & S_0\frac{\partial}{\partial y} \end{bmatrix}. \tag{3}$$

The kinematic relations can also be expressed by

$$\hat{\boldsymbol{\varepsilon}} = \mathbf{L}\mathbf{q}, \quad \mathbf{L} = \begin{bmatrix} 0 & 0 & 0 & \frac{1}{\gamma_0}\frac{\partial}{\partial x} & \frac{1}{\gamma_0}\frac{\partial}{\partial y} \\ \frac{1}{\kappa_0}\frac{\partial}{\partial x} & 0 & \frac{1}{\kappa_0}\frac{\partial}{\partial y} & -\frac{1}{\gamma_0} & 0 \\ 0 & \frac{1}{\kappa_0}\frac{\partial}{\partial y} & \frac{1}{\kappa_0}\frac{\partial}{\partial x} & 0 & -\frac{1}{\gamma_0} \end{bmatrix}^T. \tag{4}$$

The von Mises yield condition in the space of stress resultants takes the form

$$f(\hat{\boldsymbol{\sigma}}) = \sqrt{\hat{\boldsymbol{\sigma}}^T \mathbf{P} \hat{\boldsymbol{\sigma}}} - 1 = 0, \tag{5}$$

in which the matrix $\mathbf{P}$ is composed of moment and shear force components $\mathbf{P}^b$ and $\mathbf{P}^s$ as follows

$$\mathbf{P} = \begin{bmatrix} \mathbf{P}^b & \mathbf{0} \\ \mathbf{0} & \mathbf{P}^s \end{bmatrix}, \qquad \mathbf{P}^b = \begin{bmatrix} 1 & -1/2 & 0 \\ -1/2 & 1 & 0 \\ 0 & 0 & 3 \end{bmatrix}, \qquad \mathbf{P}^s = \begin{bmatrix} 3 & 0 \\ 0 & 3 \end{bmatrix}. \tag{6}$$

The plastic dissipation function per unit area of the plate is defined as

$$D^p(\dot{\boldsymbol{\kappa}}, \dot{\boldsymbol{\gamma}}) = M_0\sqrt{\dot{\boldsymbol{\kappa}}^T \mathbf{Q}^b \dot{\boldsymbol{\kappa}} + \frac{16}{t^2}\dot{\boldsymbol{\gamma}}^T \mathbf{Q}^s \dot{\boldsymbol{\gamma}}} = M_0\kappa_0\sqrt{\dot{\hat{\boldsymbol{\varepsilon}}}^T \mathbf{Q} \dot{\hat{\boldsymbol{\varepsilon}}}}, \tag{7}$$

where

$$\mathbf{Q} = \mathbf{P}^{-1} = \begin{bmatrix} \mathbf{Q}^b & \mathbf{0} \\ \mathbf{0} & \mathbf{Q}^s \end{bmatrix},$$
$$\mathbf{Q}^b = \left(\mathbf{P}^b\right)^{-1} = \begin{bmatrix} 4/3 & 2/3 & 0 \\ 2/3 & 4/3 & 0 \\ 0 & 0 & 1/3 \end{bmatrix}, \qquad \mathbf{Q}^s = \left(\mathbf{P}^s\right)^{-1} = \begin{bmatrix} 1/3 & 0 \\ 0 & 1/3 \end{bmatrix}. \tag{8}$$

3 The Edge-Based Smoothed Discrete Shear Gap Triangular Element (ES-DSG3)

Similar to the FEM, the ES-FEM also uses a mesh of elements. When 3-node triangular elements are used, the shape functions used in the ES-FEM are also identical to those in the FEM, and hence the displacement field in the ES-FEM is also ensured to be continuous on the whole problem domain. However, in the ES-FEM the strains are "smoothed" over local smoothing domains. These local smoothing domains are constructed based on edges of the elements such that $\Omega = \bigcup_{i=1}^{N_{ed}} \Omega^{(i)}$ and $\Omega^{(i)} \cap \Omega^{(j)} = \emptyset$ for $i \neq j$, in which N_{ed} is the total number of edges of all elements in the entire problem domain. For triangular elements T3, the smoothing domain $\Omega^{(i)}$ associated with the edge i is created by connecting two end-points of the edge to centroids of adjacent elements as shown in Fig. 2. The smoothed strains over the smoothing domain $\Omega^{(i)}$ are defined by

$$\tilde{\boldsymbol{\varepsilon}}_i = \frac{1}{A^{(i)}} \int_{\Omega^{(i)}} \hat{\boldsymbol{\varepsilon}}(\mathbf{x}) d\Omega, \tag{9}$$

where $A^{(i)}$ is the area of the smoothing domain $\Omega^{(i)}$. Let a point on the problem domain Ω be identified by a vector variable $\mathbf{x}$. In terms of nodal variable vectors $\mathbf{q}_I$, the smoothing strain vector $\tilde{\boldsymbol{\varepsilon}}_i$ can be written as

$$\tilde{\boldsymbol{\varepsilon}}_i = \sum_{I=1}^{N_n^{(i)}} \tilde{\mathbf{B}}_I(\mathbf{x}_i)\mathbf{q}_I, \tag{10}$$

where $N_n^{(i)}$ is the total number of nodes of elements containing the common edge i. For inner edges (see Fig. 2) $N_n^{(i)} = 4$, for boundary edges $N_n^{(i)} = 3$. $\tilde{\mathbf{B}}_I(\mathbf{x}_i)$ is the smoothed strain matrix on the domain $\Omega^{(i)}$ which is calculated numerically by an assembly process similar to the standard FEM

$$\tilde{\mathbf{B}}(\mathbf{x}_i) = \sum_{I=1}^{N_n^{(i)}} \tilde{\mathbf{B}}_I(\mathbf{x}_i) = \frac{1}{A^{(i)}} \sum_{j=1}^{N_e^{(i)}} \frac{1}{3} A_j \mathbf{B}_j, \tag{11}$$

in which $N_e^{(i)}, A_j, \mathbf{B}_j$ are the number of elements, the area and the strain matrix of the jth element around the edge i, respectively. For inner edges (see Fig. 2)

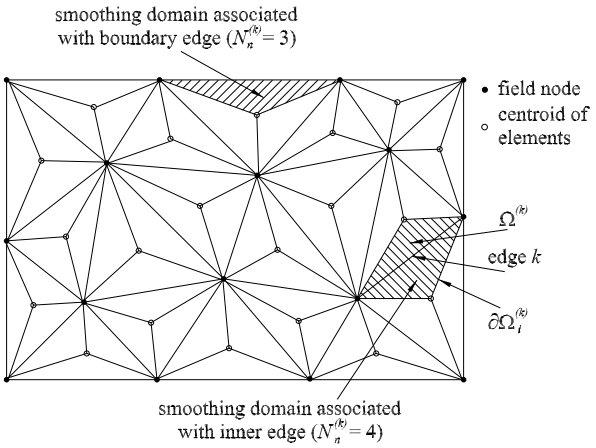

Fig. 2 Division of the domain into triangular elements and smoothing cells $\Omega^{(k)}$ connected to edge k of triangular elements

$N_e^{(i)} = 2$, for boundary edges $N_e^{(i)} = 1$. The matrix $\mathbf{B}_j$ is exactly the strain matrix of the T3 element in the standard FEM. When linear elements are used, the entries of $\mathbf{B}_j$ and therefore of $\tilde{\mathbf{B}}_I(\mathbf{x}_i)$ are also constants.

For thick plate elements, the strain-displacement matrix $\mathbf{B}$ and material matrix $\mathbf{D}$ are composed of moment and shear force components $\mathbf{B}^b$, $\mathbf{D}^b$ and $\mathbf{B}^s$, $\mathbf{D}^s$ as follows

$$\mathbf{B} = \begin{bmatrix} \mathbf{B}^b \\ \mathbf{B}^s \end{bmatrix}, \qquad \mathbf{D} = \begin{bmatrix} \mathbf{D}^b & 0 \\ 0 & \mathbf{D}^s \end{bmatrix}. \tag{12}$$

The moment components $\mathbf{B}^b$ and $\mathbf{D}^b$ are defined similarly to the standard T3 plate elements. In order to avoid the transverse shear locking, the stabilized DSG technique proposed by Bischoff and Bletzinger [1] is used to formulate the shear force components $\mathbf{B}^s$ and $\mathbf{D}^s$ to give a so-called edge-based smoothed discrete shear gap T3 element (ES-DSG3). Details of the formulations of $\mathbf{B}^s$ and $\mathbf{D}^s$ can be found in Nguyen-Xuan et al. [17].

The stiffness matrix of the smoothing domain $\Omega^{(i)}$ is calculated by

$$\tilde{\mathbf{K}}_{(i)} = \int_{\Omega^{(i)}} \tilde{\mathbf{B}}_I^T \mathbf{D} \tilde{\mathbf{B}}_I d\Omega = A^{(i)} \tilde{\mathbf{B}}_I^T \mathbf{D} \tilde{\mathbf{B}}_I, \tag{13}$$

and the global stiffness matrix is then assembled from all domain stiffness matrices $\tilde{\mathbf{K}}_{(i)}$ by a similar process as in the FEM.

4 Shakedown Analysis of Mindlin Plates

4.1 Lower Bound Formulation

Consider a convex polyhedral load domain $\mathcal{L}$ and a special loading path consisting of all load vertices $\hat{P}_k$ $(k = 1, \ldots, m)$ of $\mathcal{L}$. The convex property of the load domain

and yield function allow us to replace the time-dependent stress field $\hat{\boldsymbol{\sigma}}(\mathbf{x}, t)$ by its values calculated at load vertices $\hat{\boldsymbol{\sigma}}(\mathbf{x}, \hat{P}_k)$. Let the fictitious elastic stress resultant vector be $\hat{\boldsymbol{\sigma}}^E$ and a statically admissible time-independent stress resultant field be $\bar{\boldsymbol{\rho}}$. Based on the static shakedown theorem, the lower bound shakedown load multiplier α^- can be found from a constrained maximization problem as follows

$$\begin{aligned} &\alpha^- = \max \alpha \\ &\text{subjected to: } \begin{cases} \mathbf{R}\bar{\boldsymbol{\rho}}(\mathbf{x}) = \mathbf{0} & \text{in } \Omega, \\ f(\alpha \hat{\boldsymbol{\sigma}}^E(\mathbf{x}, \hat{P}_k) + \bar{\boldsymbol{\rho}}(\mathbf{x})) \le 0 & \forall k = \overline{1, m}; \text{in } \Omega. \end{cases} \end{aligned} \tag{14}$$

The first constraint in (14) ensures that the equilibrium of the residual stress field $\bar{\boldsymbol{\rho}}$ is fulfilled. The second constraint means that the actual stress resultant field $\hat{\boldsymbol{\sigma}} = \alpha \hat{\boldsymbol{\sigma}}^E + \bar{\boldsymbol{\rho}}$ does not anywhere violate the yield condition in (5). Using ES-FEM to discretize the weak form of the equilibrium equations and the yield condition, the maximization problem (14) can be reformulated as

$$\begin{aligned} &\alpha^- = \max \alpha \\ &\text{subjected to: } \begin{cases} \sum_{i=1}^{N_{ed}} A^{(i)} \tilde{\mathbf{B}}_i^T \bar{\boldsymbol{\rho}}_i = \mathbf{0}, \\ f(\alpha \tilde{\boldsymbol{\sigma}}_{ik}^E + \bar{\boldsymbol{\rho}}_i) \le 0 \quad \forall i = \overline{1, N_{ed}}, \forall k = \overline{1, m} \end{cases} \end{aligned} \tag{15}$$

in which $\tilde{\boldsymbol{\sigma}}_{ik}^E$ is the fictitious elastic stress resultant vector on the smoothing domain i at load vertex $\hat{P}_k$.

4.2 Upper Bound Formulation

Let $\Delta\dot{\hat{\boldsymbol{\varepsilon}}}$ denote the strain resultant rates accumulated over the loading cycle which goes through all load vertices $\hat{P}_k$ of $\mathcal{L}$, thus we have $\Delta\dot{\hat{\boldsymbol{\varepsilon}}} = \sum_{k=1}^m \dot{\hat{\boldsymbol{\varepsilon}}}_k$. At each load vertex, the kinematical condition may not be satisfied, however the accumulated strains over a load cycle $\Delta\dot{\hat{\boldsymbol{\varepsilon}}}$ must be kinematically compatible i.e. $\Delta\dot{\hat{\boldsymbol{\varepsilon}}} = \mathbf{L}\dot{\mathbf{q}}$. According to the kinematic theorem of shakedown, the upper bound shakedown load multiplier α^+ may be formulated by the following form

$$\begin{aligned} &\alpha^+ = \min \sum_{k=1}^m \int_\Omega D^p(\dot{\hat{\boldsymbol{\varepsilon}}}_k) d\Omega \\ &\text{subjected to: } \begin{cases} \Delta\dot{\hat{\boldsymbol{\varepsilon}}} = \sum_{k=1}^m \dot{\hat{\boldsymbol{\varepsilon}}}_k = \mathbf{L}\dot{\mathbf{q}} \quad \text{in } \Omega, \\ \sum_{k=1}^m \int_\Omega M_0 \kappa_0 \hat{\boldsymbol{\sigma}}^E(\mathbf{x}, \hat{P}_k)^T \dot{\hat{\boldsymbol{\varepsilon}}}_k d\Omega = 1, \end{cases} \end{aligned} \tag{16}$$

in which the second constraint is the normalization of the external power of loading. By using ES-FEM and the plastic dissipation defined in (7), the discretized form of the minimization problem (16) is rewritten as

$$\alpha^+ = \min \sum_{k=1}^{m} \sum_{i=1}^{N_{ed}} A^{(i)} M_0 \kappa_0 \sqrt{\dot{\tilde{\boldsymbol{\varepsilon}}}_{ik}^T \mathbf{Q} \dot{\tilde{\boldsymbol{\varepsilon}}}_{ik}}$$

$$\text{subjected to:} \begin{cases} \displaystyle\sum_{k=1}^{m} \dot{\tilde{\boldsymbol{\varepsilon}}}_{ik} = \tilde{\mathbf{B}}_i \dot{\mathbf{q}} \quad \forall i = \overline{1, N_{ed}}, \\ \displaystyle\sum_{k=1}^{m} \sum_{i=1}^{N_{ed}} A^{(i)} M_0 \kappa_0 \dot{\tilde{\boldsymbol{\varepsilon}}}_{ik}^T \tilde{\boldsymbol{\sigma}}_{ik}^E = 1. \end{cases} \tag{17}$$

Note that when $m = 1$, i.e. the loads are constant, the formulations (15) and (17) reduce to those of limit analysis.

5 Duality Between Lower and Upper Bounds

The minimum and maximum problems resulting from the static and kinematic theorems presented above are actually dual. To prove this duality, we first introduce some new notations

$$\dot{\mathbf{e}}_{ik} = A^{(i)} \mathbf{Q}^{1/2} \dot{\tilde{\boldsymbol{\varepsilon}}}_{ik}, \qquad \mathbf{t}_{ik} = M_0 \kappa_0 \left(\mathbf{Q}^{-1/2}\right)^T \tilde{\boldsymbol{\sigma}}_{ik}^E, \qquad \hat{\mathbf{B}}_i = A^{(i)} \mathbf{Q}^{1/2} \tilde{\mathbf{B}}_i, \tag{18}$$

so that these following relations hold

$$\mathbf{Q}^{1/2} \mathbf{Q}^{-1/2} = \mathbf{I}, \qquad \mathbf{Q} = \left(\mathbf{Q}^{1/2}\right)^T \mathbf{Q}^{1/2}. \tag{19}$$

Introducing these new notations into Eq. (17) gives (primal problem)

$$\alpha^+ = \min \sum_{k=1}^{m} \sum_{i=1}^{N_{ed}} M_0 \kappa_0 \sqrt{\dot{\mathbf{e}}_{ik}^T \dot{\mathbf{e}}_{ik}}$$

$$\text{subjected to:} \begin{cases} \displaystyle\sum_{k=1}^{m} \dot{\mathbf{e}}_{ik} - \hat{\mathbf{B}}_i \dot{\mathbf{q}} = \mathbf{0} \quad \forall i = \overline{1, N_{ed}}, \\ \displaystyle\sum_{k=1}^{m} \sum_{i=1}^{N_{ed}} \dot{\mathbf{e}}_{ik}^T \mathbf{t}_{ik} - 1 = 0. \end{cases} \tag{20}$$

Now, we can write the Lagrangian for the primal problem (20)

$$L = \sum_{i=1}^{N_{ed}} \left\{ \sum_{k=1}^{m} M_0 \kappa_0 \sqrt{\dot{\mathbf{e}}_{ik}^T \dot{\mathbf{e}}_{ik}} - \boldsymbol{\beta}_i^T \left(\sum_{k=1}^{m} \dot{\mathbf{e}}_{ik} - \hat{\mathbf{B}}_i \dot{\mathbf{q}} \right) \right\} - \alpha \left(\sum_{k=1}^{m} \sum_{i=1}^{N_{ed}} \dot{\mathbf{e}}_{ik}^T \mathbf{t}_{ik} - 1 \right), \tag{21}$$

with the Lagrange multipliers β_i, α. The duality between the upper and lower bounds is proven through the two following propositions.

Proposition 1 *If there exists a finite solution α^+ for the upper bound shakedown load multiplier (20), then α^+ has its dual form as*

$$\alpha^+ = \max_{\beta_i,\alpha} \alpha$$
$$\text{subjected to: } \begin{cases} \sum_{i=1}^{N_{ed}} \hat{\mathbf{B}}_i^T \beta_i = \mathbf{0}, & \text{(a)} \\ \|\beta_i + \mathbf{t}_{ik}\alpha\| \le M_0\kappa_0. & \text{(b)} \end{cases} \tag{22}$$

Proof By using the Lagrangian introduced in (21), the dual problem of the primal problem takes the form

$$\max_{\beta_i,\alpha}\left(\min_{\dot{\mathbf{e}}_{ik},\dot{\mathbf{q}}} L\right). \tag{23}$$

Since a finite solution for the problem (20) exists, the two constraints in (20) are affine, the objective function in (20) is convex, thus according to the strong duality theorem, there exists no gap between primal and dual problems. It follows that

$$\min_{\mathbf{h}(\dot{\mathbf{e}}_{ik},\dot{\mathbf{q}})=\mathbf{0}} \sum_{k=1}^{m}\sum_{i=1}^{N_{ed}} M_0\kappa_0\sqrt{\dot{\mathbf{e}}_{ik}^T\dot{\mathbf{e}}_{ik}} = \max_{\beta_i,\alpha}\left(\min_{\dot{\mathbf{e}}_{ik},\dot{\mathbf{q}}} L\right), \tag{24}$$

in which $\mathbf{h}(\dot{\mathbf{e}}_{ik}, \dot{\mathbf{q}}) = \mathbf{0}$ stands for two linear constraints in (20). The Lagrangian in (21) may be rewritten as

$$L = \sum_{i=1}^{N_{ed}}\sum_{k=1}^{m}\left(\frac{M_0\kappa_0\dot{\mathbf{e}}_{ik}}{\sqrt{\dot{\mathbf{e}}_{ik}^T\dot{\mathbf{e}}_{ik}}} - \beta_i - \mathbf{t}_{ik}\alpha\right)^T\dot{\mathbf{e}}_{ik} + \sum_{i=1}^{N_{ed}}\beta_i^T\hat{\mathbf{B}}_i\dot{\mathbf{q}} + \alpha. \tag{25}$$

Note that in Eq. (25) we accepted a convention that if the vector norm of the strain rate $\|\dot{\mathbf{e}}_{ik}\|$ is equal to zero, then $M_0\kappa_0\dot{\mathbf{e}}_{ik}^T\dot{\mathbf{e}}_{ik}/\sqrt{\dot{\mathbf{e}}_{ik}^T\dot{\mathbf{e}}_{ik}} = 0$. Since there is no gap between the primal and dual problems, it is required that for any solution set of Lagrange multipliers β_i, α, the Lagrange dual function $g(\boldsymbol{\beta}_i, \alpha) = \min_{\dot{\mathbf{e}}_{ik},\dot{\mathbf{q}}} L$ must have a finite value. To fulfill this, the following system must be satisfied

$$\begin{cases} \left(\frac{M_0\kappa_0\dot{\mathbf{e}}_{ik}}{\sqrt{\dot{\mathbf{e}}_{ik}^T\dot{\mathbf{e}}_{ik}}} - \beta_i - \mathbf{t}_{ik}\alpha\right)^T\dot{\mathbf{e}}_{ik} \ge 0 \quad \forall\dot{\mathbf{e}}_{ik}, & \text{(a)} \\ \sum_{i=1}^{N_{ed}}\beta_i^T\hat{\mathbf{B}}_i\dot{\mathbf{q}} = \mathbf{0} \quad \forall\dot{\mathbf{q}}. & \text{(b)} \end{cases} \tag{26}$$

Otherwise the following situation may occur

$$g(\boldsymbol{\beta}_i, \alpha) = \min_{\dot{\boldsymbol{e}}_{ik}, \dot{\mathbf{q}}} L \to -\infty, \tag{27}$$

which of course violates the strong duality theorem. Taking the system (26) into (25) leads to the conclusion

$$g(\boldsymbol{\beta}_i, \alpha) = \min_{\dot{\boldsymbol{e}}_{ik}, \dot{\mathbf{q}}} L = \alpha. \tag{28}$$

The condition (16b) is equivalent to

$$\sum_{i=1}^{N_{ed}} \hat{\mathbf{B}}_i^T \beta_i = \mathbf{0}. \tag{29}$$

Furthermore, we can prove that the condition (26a) is equivalent to the following inequality constraint

$$\|\beta_i + \mathbf{t}_{ik}\alpha\| \leq M_0\kappa_0 \quad \forall i, k. \tag{30}$$

Firstly, if the inequality (30) holds, then the Cauchy-Schwartz inequality permits us to write

$$(\beta_i + \mathbf{t}_{ik}\alpha)^T \dot{\mathbf{e}}_{ik} \leq \|\beta_i + \mathbf{t}_{ik}\alpha\| \cdot \|\dot{\mathbf{e}}_{ik}\| \leq M_0\kappa_0 \|\dot{\mathbf{e}}_{ik}\| = M_0\kappa_0 \sqrt{\dot{\mathbf{e}}_{ik}^T \dot{\mathbf{e}}_{ik}} \quad \forall \dot{\mathbf{e}}_{ik}, \tag{31}$$

which is equivalent to the condition (26a). Secondly, if on the contrary we find a set (β_i, α) satisfying

$$\|\beta_i + \mathbf{t}_{ik}\alpha\| > M_0\kappa_0, \tag{32}$$

we can always choose a strain rate vector $\tilde{\dot{\mathbf{e}}}_{ik}$ such that the angle between this vector and the vector $\mathbf{b} = \beta_i + \mathbf{t}_{ik}\alpha$ is equal to zero, or $\mathbf{b}^T \tilde{\dot{\mathbf{e}}}_{ik} = \|\mathbf{b}\| \cdot \|\tilde{\dot{\mathbf{e}}}_{ik}\|$. It follows that

$$\mathbf{b}^T \tilde{\dot{\mathbf{e}}}_{ik} = \|\mathbf{b}\| \cdot \|\tilde{\dot{\mathbf{e}}}_{ik}\| > M_0\kappa_0 \|\tilde{\dot{\mathbf{e}}}_{ik}\| = M_0\kappa_0 \sqrt{\tilde{\dot{\mathbf{e}}}_{ik}^T \tilde{\dot{\mathbf{e}}}_{ik}} = M_0\kappa_0 \frac{\tilde{\dot{\mathbf{e}}}_{ik}^T \tilde{\dot{\mathbf{e}}}_{ik}}{\sqrt{\tilde{\dot{\mathbf{e}}}_{ik}^T \tilde{\dot{\mathbf{e}}}_{ik}}}, \tag{33}$$

or

$$\left(\frac{M_0\kappa_0 \tilde{\dot{\mathbf{e}}}_{ik}}{\sqrt{\dot{\mathbf{e}}_{ik}^T \dot{\mathbf{e}}_{ik}}} - \beta_i - \mathbf{t}_{ik}\alpha \right)^T \tilde{\dot{\mathbf{e}}}_{ik} < 0, \tag{34}$$

which violates the condition (26a). Equalities (28), (29) and inequality (30) conclude our proof. □

Proposition 2 *If there exists a finite solution α^+ for the upper bound shakedown load multiplier (20), then the static formulation (15) is exactly the dual problem of*

the kinematic problem (20) *such that*

$$\alpha^{+} = \min_{\mathbf{h}(\dot{\mathbf{e}}_{ik},\dot{\mathbf{q}})=\mathbf{0}} \sum_{k=1}^{m}\sum_{i=1}^{N_{ed}} M_0\kappa_0\sqrt{\dot{\mathbf{e}}_{ik}^T\dot{\mathbf{e}}_{ik}} = \max_{\substack{\sum_{i=1}^{N_{ed}} A^{(i)}\tilde{\mathbf{B}}_i^T\bar{\boldsymbol{\rho}}_i=\mathbf{0} \\ f(\alpha\tilde{\boldsymbol{\sigma}}_{ik}^E+\bar{\boldsymbol{\rho}}_i)\le 0}} \alpha = \alpha^{-}. \tag{35}$$

Proof The left-hand side of the inequality (22b) can be rewritten as

$$\begin{aligned}
\|\beta_i + \mathbf{t}_{ik}\alpha\| &= \left\|\beta_i + M_0\kappa_0\left(\mathbf{Q}^{-1/2}\right)^T\tilde{\boldsymbol{\sigma}}_{ik}^E\alpha\right\| \\
&= \left\|M_0\kappa_0\left(\mathbf{Q}^{-1/2}\right)^T\left[\frac{(\mathbf{Q}^{1/2})^T\beta_i}{M_0\kappa_0} + \tilde{\boldsymbol{\sigma}}_{ik}^E\alpha\right]\right\| \\
&= M_0\kappa_0\left\{\left[\frac{(\mathbf{Q}^{1/2})^T\beta_i}{M_0\kappa_0} + \tilde{\boldsymbol{\sigma}}_{ik}^E\alpha\right]^T\right. \\
&\quad \left.\times\,\mathbf{Q}^{-1/2}\left(\mathbf{Q}^{-1/2}\right)^T\left[\frac{(\mathbf{Q}^{1/2})^T\beta_i}{M_0\kappa_0} + \tilde{\boldsymbol{\sigma}}_{ik}^E\alpha\right]\right\}^{1/2} \\
&= M_0\kappa_0\left\{\left[\frac{(\mathbf{Q}^{1/2})^T\beta_i}{M_0\kappa_0} + \tilde{\boldsymbol{\sigma}}_{ik}^E\alpha\right]^T\mathbf{Q}^{-1}\left[\frac{(\mathbf{Q}^{1/2})^T\beta_i}{M_0\kappa_0} + \tilde{\boldsymbol{\sigma}}_{ik}^E\alpha\right]\right\}^{1/2}.
\end{aligned} \tag{36}$$

Using (5), (7), (8) and (36), the inequality (22b) now becomes

$$f\left(\alpha\tilde{\boldsymbol{\sigma}}_{ik}^E + \bar{\boldsymbol{\rho}}_i\right) \le 0, \tag{37}$$

with $\bar{\boldsymbol{\rho}}_i = (\mathbf{Q}^{1/2})^T\beta_i/M_0\kappa_0$. Substitute $\hat{\mathbf{B}}_i$ by $\tilde{\mathbf{B}}_i$ from (18) and then $(\mathbf{Q}^{1/2})^T\beta_i$ by $M_0\kappa_0\bar{\boldsymbol{\rho}}_i$ in (22a), one has

$$\sum_{i=1}^{N_{ed}}\hat{\mathbf{B}}_i^T\beta_i = \sum_{i=1}^{N_{ed}}A^{(i)}\tilde{\mathbf{B}}_i^T\left(\mathbf{Q}^{1/2}\right)^T\beta_i = M_0\kappa_0\sum_{i=1}^{N_{ed}}A^{(i)}\tilde{\mathbf{B}}_i^T\bar{\boldsymbol{\rho}}_i = \mathbf{0} \tag{38}$$

or

$$\sum_{i=1}^{N_{ed}}A^{(i)}\tilde{\mathbf{B}}_i^T\bar{\boldsymbol{\rho}}_i = \mathbf{0}. \tag{39}$$

Equality (39) and inequality (37) conclude our proof. □

The vector $\bar{\boldsymbol{\rho}}_i = (\mathbf{Q}^{1/2})^T\beta_i/M_0\kappa_0$ can be interpreted as the time-independent residual stress resultant vector: the value of this vector is calculated on each smoothing domain, independently of load vertices or, in other words, independently of time. On the other hand, the Lagrange multiplier α represents the lower bound shakedown load factor.

Based on the duality between lower and upper bounds, an iterative primal-dual optimization algorithm was proposed to calculate both the upper and lower bounds

of the shakedown load of plates. Firstly, we can write the Karush-Kuhn-Tucker (KKT) optimality conditions of the Lagrangian in (21) as follows

$$\begin{aligned}
\frac{\partial L}{\partial \dot{\mathbf{e}}_{ik}} &= \left(M_0 \kappa_0 \frac{\dot{\mathbf{e}}_{ik}}{\sqrt{\dot{\mathbf{e}}_{ik}^T \dot{\mathbf{e}}_{ik}}} \right) - \beta_i - \alpha \mathbf{t}_{ik} = 0, \\
\frac{\partial L}{\partial \dot{\mathbf{q}}} &= \beta_i^T \hat{\mathbf{B}}_i = 0, \\
\frac{\partial L}{\partial \alpha} &= \left(\sum_{k=1}^{m} \sum_{i=1}^{N_{ed}} \dot{\mathbf{e}}_{ik}^T \mathbf{t}_{ik} - 1 \right) = 0.
\end{aligned} \tag{40}$$

By using the Newton's method to solve the optimality conditions (40) and after some manipulations, we get the following system of linear equations

$$\mathbf{K} d\dot{\mathbf{q}} = -\mathbf{K}\dot{\mathbf{q}} + \mathbf{f}_1 + \mathbf{f}_2(\alpha + d\alpha), \tag{41}$$

where

$$\begin{aligned}
\mathbf{K} &= \sum_{i=1}^{N_{ed}} \hat{\mathbf{B}}_i^T \mathbf{E}_i^{-1} \hat{\mathbf{B}}_i, \\
\mathbf{f}_1 &= -\sum_{i=1}^{N_{ed}} \hat{\mathbf{B}}_i^T \mathbf{E}_i^{-1} \sum_{k=1}^{m} \mathbf{M}_{ik}^{-1} (\boldsymbol{\beta}_i + \alpha \mathbf{t}_{ik}) \frac{\dot{\mathbf{e}}_{ik}^T \dot{\mathbf{e}}_{ik}}{\sqrt{\dot{\mathbf{e}}_{ik}^T \dot{\mathbf{e}}_{ik} + \varepsilon_0^2}}, \\
\mathbf{f}_2 &= \sum_{i=1}^{N_{ed}} \hat{\mathbf{B}}_i^T \mathbf{E}_i^{-1} \sum_{k}^{m} \mathbf{M}_{ik}^{-1} \sqrt{\dot{\mathbf{e}}_{ik}^T \dot{\mathbf{e}}_{ik} + \varepsilon_0^2} \mathbf{t}_{ik}, \\
\mathbf{M}_{ik} &= M_0 \kappa_0 \mathbf{I} + (\boldsymbol{\beta}_i + \alpha \mathbf{t}_{ik}) \frac{\dot{\mathbf{e}}_{ik}^T}{\sqrt{\dot{\mathbf{e}}_{ik}^T \dot{\mathbf{e}}_{ik} + \varepsilon_0^2}}, \\
\mathbf{E}_i &= \sum_{k}^{m} \mathbf{M}_{ik}^{-1} \sqrt{\dot{\mathbf{e}}_{ik}^T \dot{\mathbf{e}}_{ik} + \varepsilon_0^2}
\end{aligned} \tag{42}$$

and ε_0^2 is a small positive number, e.g. 10^{-20}. The system (41) can be considered as the linear system arising in purely elastic computations with the global stiffness matrix $\mathbf{K}$ and the elastic matrix $\mathbf{E}_i^{-1}$. At each optimization iteration, by solving this system we will get the incremental vector of nodal variables $d\dot{\mathbf{q}}$ and then the incremental vectors $d\dot{\mathbf{e}}_{ik}$, $d\boldsymbol{\beta}_i$ and $d\alpha$. The vectors $d\dot{\mathbf{q}}$, $d\dot{\mathbf{e}}_{ik}$, $d\boldsymbol{\beta}_i$ and $d\alpha$ are actually Newton directions which assure that a suitable step along them will lead to a decrease of the objective function of the primal problem (20) and to an increase of the objective function of the dual problem (22). Iterating these steps a stable set of $\dot{\mathbf{q}}$, $\dot{\mathbf{e}}_{ik}$, $\boldsymbol{\beta}_i$ and α is obtained satisfying all conditions in (20) and (22). A detailed explanation of the primal-dual algorithm can be found in Vu et al. [22].

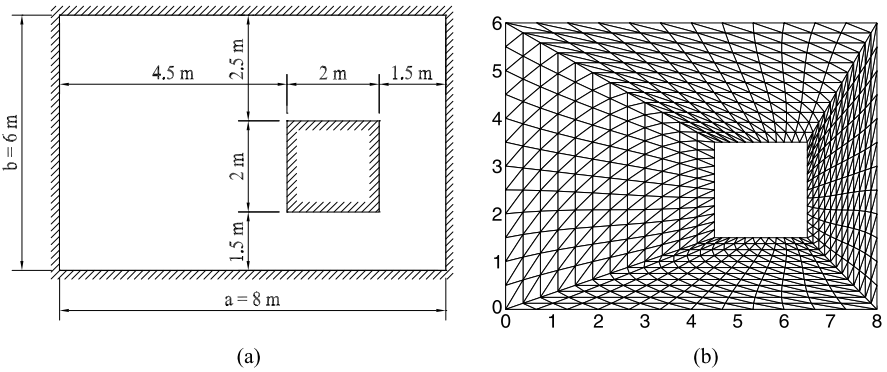

Fig. 3 Geometrical dimensions (**a**) and FE-mesh (**b**) of rectangular plate with eccentric square cutout

6 Validations

In this section, two numerical examples are presented to evaluate the performance of the proposed method. Two plates that have different slenderness ratios, subjected either to uniform out-of-plane pressure loading or concentrated load are considered. In all examples, the structures are made of elastic-perfectly plastic material and 3-node triangular element T3 is used to discretize the structural domains. For each test case, some existing analytical and numerical solutions found in literature are briefly represented and compared.

6.1 Rectangular Plate with Eccentric Square Cutout

Consider a rectangular plate of thickness t with an eccentric square cutout subjected to an out-of-plane uniform pressure as depicted in Fig. 3(a). This problem was examined previously using the adaptive element-free Galerkin method, kinematic limit analysis and the Kirchhoff plate assumptions [9]. All external and internal edges of the plate are simply supported or built-in and the pressure p can be constant or vary within a range $p \in [0, p_{\max}]$. The plate is modelled by 1152 T3 elements (Fig. 3(b)).

Figure 4 depicts the convergence of the upper and lower bounds of the plastic collapse and shakedown load multipliers, given in dimensionless form pab/M_0, for the case of a simply supported plate with the slenderness ratio $b/t = 40$. The lower and upper bounds are nearly stationary after 5 optimization iterations for both limit and shakedown analyses. The normalized plastic collapse load factor is 48.684 which is comparable with 51.45 obtained by Le [9]. Solutions for the corresponding Reissner-Mindlin plate are not found in literature.

The plastic collapse and shakedown loads of the plate are calculated for the different boundary conditions with several plate slenderness ratios, and presented in

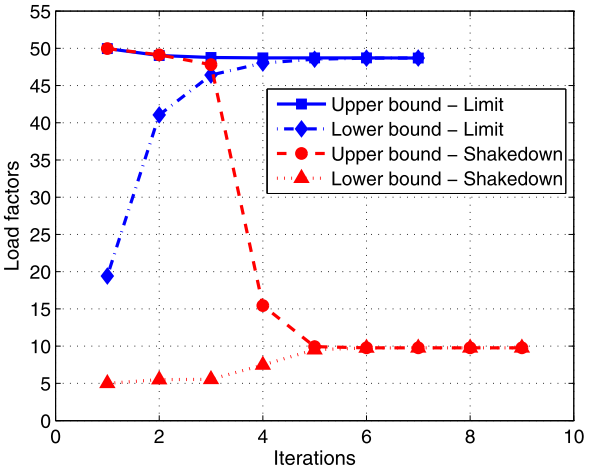

Fig. 4 Convergence of plastic collapse and shakedown load factors of a rectangular plate

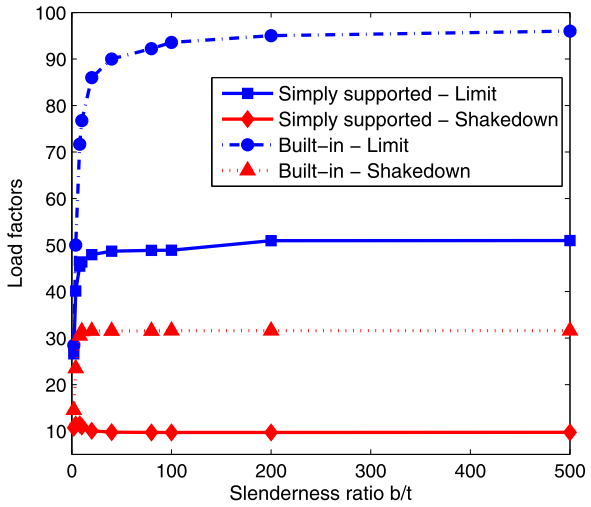

Fig. 5 Plastic collapse and shakedown loads of a rectangular plate

Fig. 5. In all cases, only one value is presented since the lower bound is identical with the upper one and the results are normalized with pab/M_0. It is seen that the performance of the proposed method is effective and free of locking when the slenderness ratio becomes very large.

6.2 Rhombic Plates

The next example involves rhombic plates under an out-of-plane uniform load p. Geometry and FE mesh are shown in Fig. 6. This problem was previously studied either analytically by Mansfield [14] or numerically by Capsoni and Vicente da

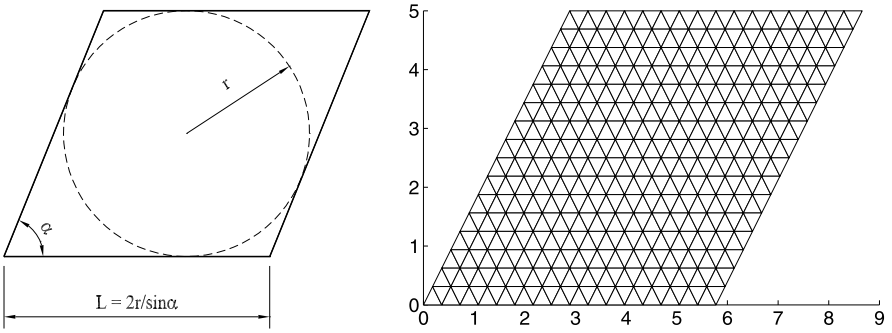

Fig. 6 Geometrical dimensions (**a**) and FE-mesh (**b**) of a rhombic plate

Table 1 Limit loads of thin rhombic plates subjected to a uniform pressure (pr^2/M_0) with $2r/t = 20$

$\alpha(^\circ)$	Simply supported		Clamped	
	Kirchhoff, upper bound, [3]	Reissner-Mindlin	Kirchhoff, upper bound, [3]	Reissner-Mindlin
30	5.140	4.807	9.757	9.359
45	5.609	5.403	10.596	10.488
60	5.966	5.827	11.394	11.303
75	6.197	6.019	11.893	11.799
90	6.278	6.278	12.062	11.928

Silva [4] using the Kirchhoff plate assumptions. All edges of the plate are simply supported or built-in and the uniform load p can be constant or varying within a range $p \in [0, p_{\max}]$.

We consider first thin rhombic plates with the slenderness ratio $2r/t = 20$. Numerical limit analysis for the different skewness angles α was carried out and the results are collected in Table 1 and compared with the least upper bounds obtained by Capsoni and Vicente da Silva [4]. It is seen that our numerical solutions are always smaller than those of Capsoni and Vicente da Silva (the maximum difference is 6.5 % and 4.1 % for $\alpha = 30^\circ$) except for the case of simply supported edges with $\alpha = 90^\circ$, in which they are identical. This difference may be interpreted by the two following observations: (1) The solutions obtained by Capsoni and Vicente da Silva are pure upper bounds and (2) for skew plates ($\alpha \neq 90^\circ$), the bending moments at obtuse corners tend to zero for the Reissner-Mindlin plate while they tend to infinity for the Kirchhoff plate as pointed out by Häggblad and Bathe [7].

Figure 7 depicts the convergence of the upper and lower bounds of the plastic collapse and shakedown load multipliers, given in dimensionless form pr^2/M_0, for the case of simply supported plate with $\alpha = 60^\circ$.

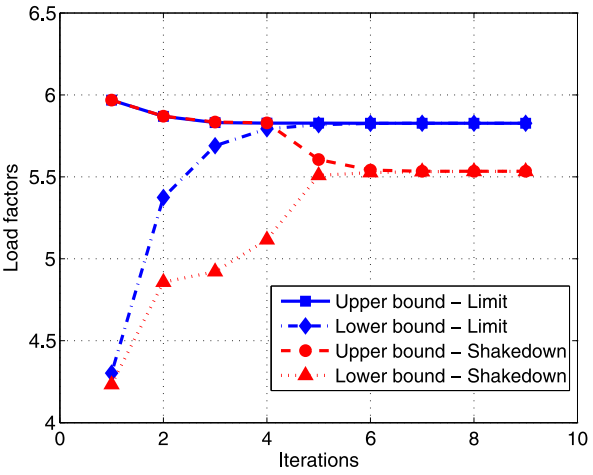

Fig. 7 Convergence of plastic collapse and shakedown load factors of rhombic plate

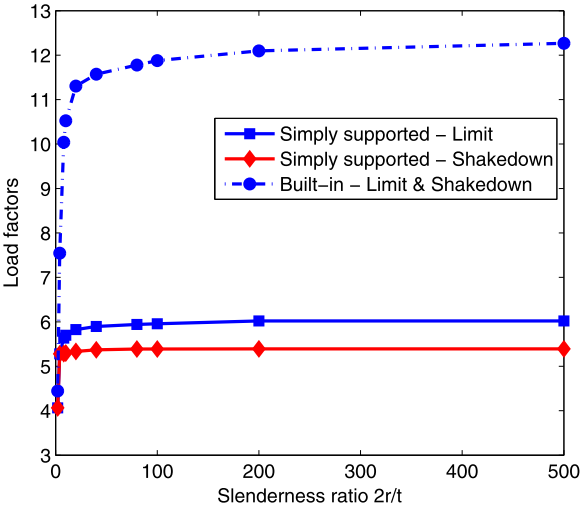

Fig. 8 Plastic collapse and shakedown loads of rhombic plate with skewness angles $\alpha = 60°$

Choosing the rhombic plate with the skewness angle $\alpha = 60°$, we study now the performance of the present method for several plate slenderness ratios. The graph in Fig. 8 shows the normalized plastic collapse and shakedown loads calculated for different boundary conditions. We may also see that the results are nearly unchanged even if the thickness of the plate becomes very small (below the Kirchhoff limit).

References

1. Bischoff M, Bletzinger KU (2001) Stabilized DSG plate and shell elements. In: Wall WA, Bletzinger K-U, Schweizerhof K (eds) Trends in computational structural mechanics. CIMNE, Barcelona, pp 253–263

2. Bletzinger KU, Bischoff M, Ramm E (2000) A unified approach for shear-locking free triangular and rectangular shell finite elements. Comput Struct 75:321–334
3. Capsoni A, Corradi L (1999) Limit analysis of plates—a finite element formulation. Struct Eng Mech 8:325–341
4. Capsoni A, Vicente da Silva M (2011) A finite element formulation of Mindlin plates for limit analysis. Int J Numer Methods Biomed Eng 27:143–156
5. Cecchi A, Milani G, Tralli A (2007) A Reissner-Mindlin limit analysis model for out-of-plane loaded running bond masonry walls. Int J Solids Struct 44:1438–1460
6. Chen JS, Wu CT, Yoon S, You Y (2001) A stabilized conforming nodal integration for Galerkin mesh-free methods. Int J Numer Methods Eng 50:435–466
7. Häggblad B, Bathe KJ (1990) Specifications of boundary conditions for Reissner/Mindlin plate bending finite elements. Int J Numer Methods Eng 30:981–1011
8. Hopkins HG, Wang AJ (1954) Load-carrying capacities for circular plates of perfectly-plastic material with arbitrary yield condition. J Mech Phys Solids 3:117–129
9. Le VC (2009) Novel numerical procedures for limit analysis of structures. PhD thesis, University of Sheffield, UK
10. Le VC, Gilbert M, Askes H (2010) Limit analysis of plates and slabs using a meshless equilibrium formulation. Int J Numer Methods Eng 83:1739–1758
11. Liu GR, Dai KY, Nguyen TT (2007) A smoothed finite element method for mechanics problem. Comput Mech 39:859–877
12. Liu GR, Nguyen-Thoi T, Lam KY (2009) An edge-based smoothed finite element method (ES-FEM) for static, free and forced vibration analyses of solids. J Sound Vib 320:1100–1130
13. Liu GR, Nguyen-Thoi T, Nguyen-Xuan H, Lam KY (2009) A node-based smoothed finite element method (NS-FEM) for upper bound solutions to solid mechanics problems. Comput Struct 87:14–26
14. Mansfield EH (2000) Collapse pressures for rhombic plates. Int J Mech Sci 42:635–643
15. Nguyen-Thanh N, Rabczuk T, Nguyen-Xuan H, Bordas S (2008) A smoothed finite element method for shell analysis. Comput Methods Appl Mech Eng 198:165–177
16. Nguyen-Xuan H, Rabczuk T, Bordas S, Debongnie JF (2008) A smoothed finite element method for plate analysis. Comput Methods Appl Mech Eng 197:1184–1203
17. Nguyen-Xuan H, Liu GR, Thai-Hoang C, Nguyen-Thoi T (2010) An edge-based smoothed finite element method (ES-FEM) with stabilized discrete shear gap technique for analysis of Reissner-Mindlin plates. Comput Methods Appl Mech Eng 199:471–489
18. Staat M, Heitzer M (eds) (2003) Numerical methods for limit and shakedown analysis. Deterministic and probabilistic approach. NIC series, vol 15. John von Neumann Institute for Computing, Jülich. http://hdl.handle.net/2128/2926
19. Tran TN, Kreißig R, Vu DK, Staat M (2008) Upper bound limit and shakedown analysis of shells using the exact Ilyushin yield surface. Comput Struct 86:1683–1695
20. Tran TN (2011) A dual algorithm for shakedown analysis of plate bending. Int J Numer Methods Eng 86:862–875
21. Trần TN, Staat M (2013) An edge-based smoothed finite element method for primal-dual shakedown analysis of structures under uncertainty. In: de Saxcé G, Oueslati A, Charkaluk E, Tritsch J-B (eds) Limit states of materials and structures: direct methods, vol 2. Springer, Dordrecht, pp 89–102
22. Vu DK, Yan YM, Nguyen-Dang H (2004) A primal-dual algorithm for shakedown analysis of structure. Comput Methods Appl Mech Eng 193:4663–4674

Progress in Plastic Design of Composites

Min Chen and Abdelkader Hachemi

Abstract In this paper, the lower-bound of direct methods is applied to fiber reinforced metal matrix periodic composites. Three boundary conditions for the localization problem are discussed and the influence of hardening matrix material is studied. Furthermore, in combination with homogenization theory, plastic material parameters are predicted by using yield loci fitting on the macroscopic limit stress domain. The proposed approach is validated through a numerical example of unidirectional periodic composites with square fiber patterns.

1 Introduction

To predict safe service conditions of structures or structural elements made of heterogeneous materials under variable loads beyond elasticity is a challenging task in civil and mechanical engineering. There are two major difficulties: to consider variable loads with unknown evolution in time and to determine the effective material properties. The former difficulty can be overcome by direct methods (DM), namely limit and shakedown analysis. Limit analysis only requires the load range, and shakedown analysis needs the envelope of the independent loads [13]. Therefore, the application of DM to composites arose many interests these years. To solve the latter difficulty, multi-scale modeling method and homogenization theory are involved [27]. Either using the lower-bound [14, 23, 33, 34] or upper-bound [3, 21, 22] approach, periodic composites are investigated at the representative volume element (RVE) level with the elastic perfectly plastic material properties of each phase.

DM has been formulated for structures assuming elastic perfectly plastic material behavior. However, work-hardening occurs most notably for ductile materials, like metals. Thus DM for plasticity models with hardening has also been investigated for long time [15, 16, 18, 20, 32], where the studied objects are homogeneous global

M. Chen (✉) · A. Hachemi
Institute of General Mechanics, RWTH-Aachen, Templergraben 64, 52062 Aachen, Germany
e-mail: min@iam.rwth-aachen.de

A. Hachemi
e-mail: hachemi@iam.rwth-aachen.de

K. Spiliopoulos, D. Weichert (eds.), *Direct Methods for Limit States in Structures and Materials*, DOI 10.1007/978-94-007-6827-7_6,

structures [2, 19, 25]. In this work, we applied the lower-bound approach of DM to periodic composites with the consideration of work-hardening.

As the global effective material properties are concerned, in [7], homogenized elastic parameters are obtained basing on the homogenization theory and the constitutive laws of elastic materials. The plastic properties are only studied for the composites under plane stress case by using yield loci fitting. Here, the predictions for unidirectional periodic composites are discussed.

The numerical tools required for the lower-bound approach are the finite-element method and non-linear optimization. To reduce the scale of optimization problem, non-conforming three-dimensional finite elements are used to discretize the RVE, and the interior-point-algorithm based optimization tool (IPOPT) [29, 31] together with the pre-programming language AMPL [11] are used.

2 Direct Methods Applied to Composites

2.1 Elements of Homogenization Theory

For periodic heterogeneous media, two different scales are adopted: the macroscopic (or global) scale and the mesoscopic (or local) scale. The homogenization method describes the relation between these two scales mainly by two stages: localization and globalization [27].

With $\boldsymbol{x}$ and $\boldsymbol{\xi}$ as the global and local coordinates (Fig. 1), respectively, the following relationship holds:

$$\boldsymbol{\xi} = \frac{\boldsymbol{x}}{\delta}, \tag{1}$$

δ is a small scale parameter, which determines the size of the representative volume element (RVE). It plays an important role in studying the heterogeneous material, especially for non-uniform structures. For a heterogeneous material with periodic distribution, the smallest possible unit is normally defined as the RVE. The macroscopic strain $\boldsymbol{E}$ and stress $\boldsymbol{\Sigma}$ are linked to mesoscopic strain $\boldsymbol{\epsilon}$ and stress $\boldsymbol{\sigma}$ by:

$$\boldsymbol{E}(\boldsymbol{x}) = \frac{1}{V}\int_V \boldsymbol{\epsilon}(\boldsymbol{\xi})\,\mathrm{d}V = \langle \boldsymbol{\epsilon}(\boldsymbol{\xi})\rangle, \tag{2}$$

$$\boldsymbol{\Sigma}(\boldsymbol{x}) = \frac{1}{V}\int_V \boldsymbol{\sigma}(\boldsymbol{\xi})\,\mathrm{d}V = \langle \boldsymbol{\sigma}(\boldsymbol{\xi})\rangle. \tag{3}$$

Here, $\langle\cdot\rangle$ stands for the averaging operator. In DM for periodic heterogeneous materials, the macroscopic stress is decomposed as [34]:

$$\boldsymbol{\Sigma} = \frac{1}{V}\int_V \left(\alpha\boldsymbol{\sigma}^E + \bar{\boldsymbol{\rho}}\right)\mathrm{d}V = \frac{1}{V}\int_V \alpha\boldsymbol{\sigma}^E\,\mathrm{d}V + \frac{1}{V}\int_V \bar{\boldsymbol{\rho}}\,\mathrm{d}V \quad \text{with } \frac{1}{V}\int_V \bar{\boldsymbol{\rho}}\,\mathrm{d}V = 0 \tag{4}$$

where α is the safety factor, $\boldsymbol{\sigma}^E$ is the purely elastic stress field and $\bar{\boldsymbol{\rho}}$ is the time-independent residual stress field.

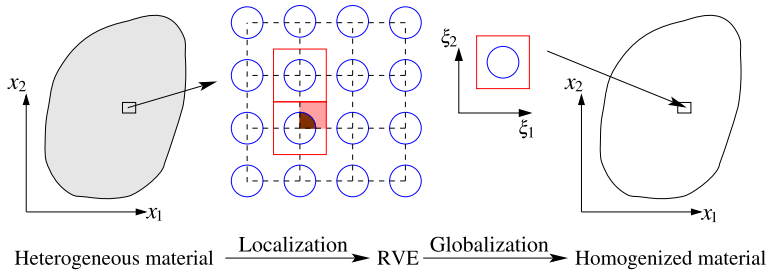

Fig. 1 Homogenization theory

2.2 Boundary Conditions

One of the difficulties in the localization problem lies in introducing appropriate boundary conditions. Usually, three types of boundary conditions are considered on the local scale [1, 27].

Strain approach Uniform strain is imposed on ∂V,

$$\boldsymbol{u} = \boldsymbol{E} \cdot \boldsymbol{\xi} \quad \text{on } \partial V. \tag{5}$$

Stress approach Uniform stress is imposed on ∂V,

$$\boldsymbol{\sigma} \cdot \boldsymbol{n} = \boldsymbol{\Sigma} \cdot \boldsymbol{n} \quad \text{on } \partial V. \tag{6}$$

Periodicity Constraints are required for both fields.

- The stress vectors on the opposite sides have the same value but opposite direction,

$$\boldsymbol{\sigma} \cdot \boldsymbol{n} \quad \text{anti-periodic.} \tag{7}$$

- The local strain can be split into an overall strain $\boldsymbol{E}$ and a fluctuating field $\boldsymbol{\epsilon}^{\text{per}}$, where the average of $\boldsymbol{\epsilon}^{\text{per}}$ over RVE vanishes,

$$\boldsymbol{\epsilon}(\boldsymbol{u}) = \boldsymbol{E} + \boldsymbol{\epsilon}\left(\boldsymbol{u}^{\text{per}}\right) = \boldsymbol{E} + \boldsymbol{\epsilon}^{\text{per}}, \tag{8}$$

$$\left\langle \boldsymbol{\epsilon}^{\text{per}} \right\rangle = 0. \tag{9}$$

In the numerical implementation, to carry out the strain approach, uniform displacement is imposed on the boundary, see Fig. 2(L). For Stress approach, besides the uniform stress imposed on the boundary, one degree of freedom of the boundary is coupled in order to maintain the periodic deformation, as shown in Fig. 2(M).

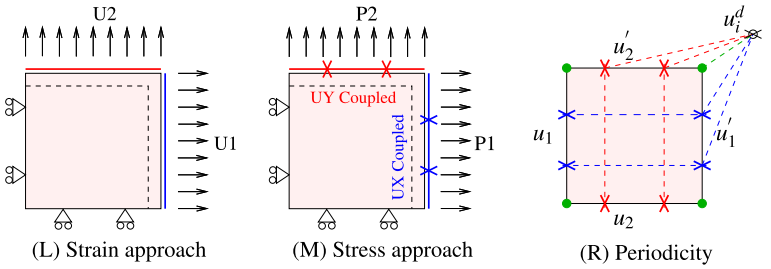

Fig. 2 Boundary conditions

Fig. 3 Deformations of the non-periodic RVE under different boundary conditions

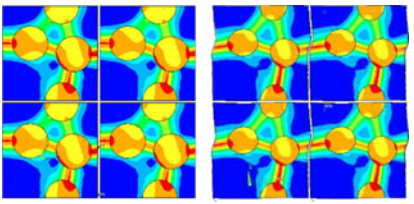

These two approaches are normally suitable for the periodic RVE, while the third one is more realistic, especially for non-periodic unit cell. Figure 2(R) describes the constraints for periodicity method:

$$u_i' - u_i + u_i^d = 0 \tag{10}$$

here, u_i' and u_i are the displacements of the relative opposite periodic node pairs and u_i^d is the macroscopic displacement. Figure 3 illustrates the deformations of a non-periodic RVE under pure thermal loading by using strain approach and periodicity approach, respectively.

The common ground in these three approaches is the consistent deformation of boundaries. The strain energies, by using different boundary conditions, are ordered in the following way [27]:

$$\boldsymbol{E} : \hat{\boldsymbol{d}}^{\text{hom}} : \boldsymbol{E} \leq \boldsymbol{E} : \boldsymbol{d}_{\text{per}}^{\text{hom}} : \boldsymbol{E} \leq \boldsymbol{E} : \tilde{\boldsymbol{d}}^{\text{hom}} : \boldsymbol{E}. \tag{11}$$

$\hat{\boldsymbol{d}}^{\text{hom}}$, $\boldsymbol{d}_{\text{per}}^{\text{hom}}$ and $\tilde{\boldsymbol{d}}^{\text{hom}}$ are the 4th order tensors of elastic stiffness, under uniform stress, periodicity and uniform strain, respectively, which depend on the micro variable ξ.

The objective studied in this work is the periodic composites under mechanical loading, and the strain approach was adopted as the boundary condition. The local-

ization of the elastic mechanical problem can be written as [14]:

$$P_{\text{strain}} = \begin{cases} \text{div}\boldsymbol{\sigma}^E = 0 & \text{in } V, \\ \boldsymbol{\sigma}^E = \boldsymbol{d} : (\boldsymbol{E} + \boldsymbol{\epsilon}^{\text{per}}) & \text{in } V, \\ \boldsymbol{\sigma}^E \cdot \boldsymbol{n} & \text{anti-periodic on } \partial V, \\ \boldsymbol{u}^{\text{per}} & \text{periodic on } \partial V, \\ \langle \boldsymbol{\epsilon} \rangle = \boldsymbol{E}. \end{cases} \tag{12}$$

The residual stress field $\bar{\boldsymbol{\rho}}$ should satisfy the self-equilibrium condition and periodicity conditions:

$$P_{\text{strain}}^{\text{res}} = \begin{cases} \text{div}\bar{\boldsymbol{\rho}} = 0 & \text{in } V, \\ \bar{\boldsymbol{\rho}} \cdot \boldsymbol{n} & \text{anti-periodic on } \partial V. \end{cases} \tag{13}$$

Anti-periodicity means that either $\boldsymbol{\sigma}^E \cdot \boldsymbol{n}$ or $\bar{\boldsymbol{\rho}} \cdot \boldsymbol{n}$ has opposite values on opposite sides of ∂V. Periodicity of $\boldsymbol{u}^{\text{per}}$ indicates that the displacements at two opposite points of the boundary are the same. For strain approach, we assume that $\boldsymbol{u}^{\text{per}} = 0$ and $\boldsymbol{\epsilon}^{\text{per}} = 0$.

2.3 Finite Element Discretization

In order to satisfy the equilibrium conditions for the elastic stress $\boldsymbol{\sigma}^E$ and time-independent residual stress $\bar{\boldsymbol{\rho}}$ in weak form, the principle of virtual work, demanding that the external virtual work equals to the internal virtual work for unrelated but consistent displacements and strains, is used:

$$\int_V \{\delta\boldsymbol{\epsilon}\}^T \left\{\alpha\boldsymbol{\sigma}^E + \bar{\boldsymbol{\rho}}\right\} \text{d}V = \int_{\partial V} \{\delta\boldsymbol{u}\}^T \{\mathbf{p}\} \text{d}S + \int_V \{\delta\boldsymbol{u}\}^T \{\mathbf{f}\} \text{d}V. \tag{14}$$

Here, $\delta\boldsymbol{\epsilon}$ is the virtual strain, and δu is the virtual displacement. $\mathbf{p}$ and $\mathbf{f}$ are surface force and body force, respectively. For periodic heterogeneous materials, the external loads can be either macroscopic stresses $\boldsymbol{\Sigma}$ or macroscopic strains $\boldsymbol{E}$. The left side of Eq. (14) implies that the discretization here has to be carried out for the purely elastic stress field $\boldsymbol{\sigma}^E$ and the residual stress field $\bar{\boldsymbol{\rho}}$. Since the scale of the optimization problem is mainly determined by the type and the number of finite elements, the choice of a proper element type is very important. In this work, a non-conforming solid element was applied in the limit and shakedown analysis of composites because of its accuracy and efficiency [5].

The lower-bound problem of DM for periodic composites with elastic perfectly plastic material model can be formulated finally as the following mathematical programming:

$$\max \alpha \quad \begin{cases} [\boldsymbol{C}]\{\bar{\boldsymbol{\rho}}\} = 0, \\ F(\alpha\boldsymbol{\sigma}_{\boldsymbol{i}}^{\boldsymbol{E}}(P_k) + \bar{\boldsymbol{\rho}}_i, \sigma_{Yi}) \leq 0, \quad i \in [1, NGS]. \end{cases} \tag{15}$$

α is the load factor, P_k is the vertices of load envelope and NGS is the number of Gaussian points and σ_Y is the yield strength. F is the von Mises yield criterion.

2.4 Large Scale Optimization

The lower-bound approach of DM applied to a real structure or structural element will lead usually to a large scale optimization problem. To solve such kind of problem, there are many optimization algorithms and corresponding software packages, like LANCELOT [9], which is based on an augmented Lagrangian method, and IPDCA (Interior Point with DC regularization Algorithm), which is based on interior-point method and especially designed for shakedown problems. The efficiency of IPDCA was proved in [17]. However, the present version is suitable for elastic perfectly plastic material model. Another user-developed software package is IPSA [24, 25], which is also based on interior-point method. The additional selective algorithm makes the application of DM on large structures possible. In this work, AMPL+IPOPT are adopted as the numerical solver [4]. AMPL (A Modeling Language for Mathematical Programming) is a comprehensive and powerful algebraic modeling language for linear and nonlinear optimization problems with discrete or continuous variables [11]. IPOPT, short for "Interior Point OPTimizer" is an open software library for large scale nonlinear optimization of continuous systems [30].

3 Hardening Material Models

DM with hardening has been investigated for long time, however, the studied objects are only homogeneous global structures [2, 19, 24].

Here, the lower-bound approach of DM for periodic composites with the consideration of hardening matrix is applied on the RVE. The material model for the fiber is assumed as elastic perfectly plastic. Some abbreviations used in this work are introduced in Table 1.

3.1 Isotropic Hardening

The isotropic hardening material model assumes that the yield surface increases in size, but keeps its shape. The subsequent yield surface and initial yield surface have the same center, as shown in Fig. 4.

The lower-bound approach of DM with isotropic hardening matrix can be formulated as:

$$\max \alpha \quad \begin{cases} [\boldsymbol{C}]\{\bar{\boldsymbol{\rho}}\} = 0, \\ F(\alpha \boldsymbol{\sigma}_i^E(P_k) + \bar{\boldsymbol{\rho}}_i, \sigma_{Yi}^{\mathrm{f}}) \le 0, \quad i \in [1, NGSF], \\ F(\alpha \boldsymbol{\sigma}_j^E(P_k) + \bar{\boldsymbol{\rho}}_j, \sigma_{Uj}^{\mathrm{m}}) \le 0, \quad j \in [1, NGSM] \end{cases} \tag{16}$$

Table 1 Abbreviations of some terms

Term	Meaning
NE	Number of elements
NK	Number of nodes
NGE	Number of Gaussian points of each element (in this work, $NGE = 8$)
NGSF	Number of Gaussian points for Fiber
NGSM	Number of Gaussian points for Matrix
NGS	Number of total Gaussian points, $NGS = NGE \times NE = NGSF + NGSM$
NL	Number of load vertices: $NL = 1$, limit analysis; $NL = 2^n$, shakedown analysis. n is the number of independent loads

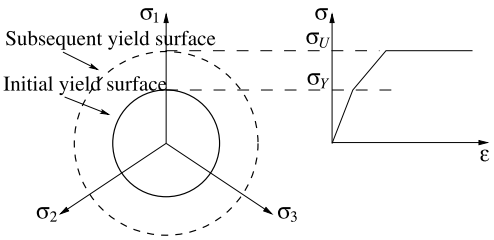

Fig. 4 Isotropic hardening

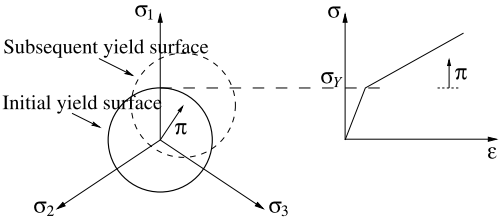

Fig. 5 Unlimited kinematic hardening

where σ_{Uj}^{m} is the ultimate strength for the matrix. Superscript 'm' and 'f' indicate matrix and fiber respectively.

3.2 Unlimited Kinematic Hardening

The kinematic hardening model allows the yield surface to translate, without changing its shape, as shown in Fig. 5. $\boldsymbol{\pi}$ is the time-independent back stress. The discretized formulation of the lower-bound problem for the linear unlimited kinematic hardening condition is:

$$\max \alpha \quad \begin{cases} [\boldsymbol{C}]\{\bar{\boldsymbol{\rho}}\} = 0, \\ F(\alpha \boldsymbol{\sigma}_i^E(P_k) + \bar{\boldsymbol{\rho}}_i, \sigma_{Yi}^{\mathrm{f}}) \le 0, \quad i \in [1, NGSF] \\ F(\alpha \boldsymbol{\sigma}_j^E(P_k) + \bar{\boldsymbol{\rho}}_j - \bar{\boldsymbol{\pi}}_j, \sigma_{Yj}^{\mathrm{m}}) \le 0, \quad j \in [1, NGSM] \end{cases} \tag{17}$$

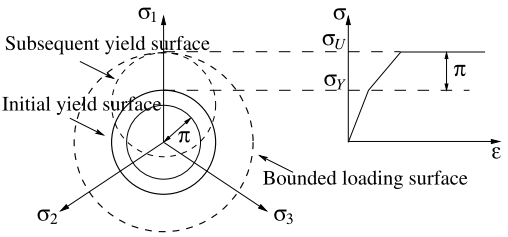

Fig. 6 Limited kinematic hardening

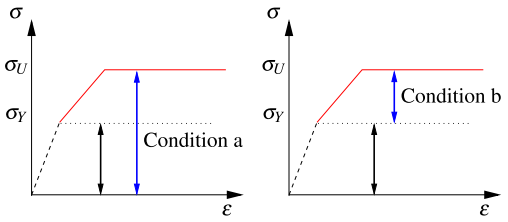

Fig. 7 Conditions a and b in limited kinematic hardening

where $\bar{\boldsymbol{\pi}}$ is the back stress field. It is important to note that, for matrix with unlimited kinematic hardening, there is no optimal solution for limit analysis, since the ultimate strength of the material is infinite.

3.3 Limited Kinematic Hardening

To overcome the shortcoming of the unlimited linear kinematic hardening material model, two-surface model of limited kinematic hardening has been introduced [32], as shown in Fig. 6. With the consideration of the linear limited kinematic hardening, the lower bound problem has an analogous discretized form like unlimited kinematic hardening. Moreover, due to the back stress limitation, there is an additional inequality constraint, as shown in (18a) or (18b).

$$\max \alpha \quad \begin{cases} [\boldsymbol{C}]\{\bar{\boldsymbol{\rho}}\} = 0, \\ F(\alpha \boldsymbol{\sigma}_i^E(P_k) + \bar{\boldsymbol{\rho}}_i, \sigma_{Yi}^{\mathrm{f}}) \le 0, \quad i \in [1, NGSF], \\ F(\alpha \boldsymbol{\sigma}_j^E(P_k) + \bar{\boldsymbol{\rho}}_j - \bar{\boldsymbol{\pi}}_j, \sigma_{Yj}^{\mathrm{m}}) \le 0, \quad j \in [1, NGSM], \\ F(\alpha \boldsymbol{\sigma}_j^E(P_k) + \bar{\boldsymbol{\rho}}_j, \sigma_{Uj}^{\mathrm{m}}) \le 0, \quad \text{(a)} \\ \text{or} \quad F(\bar{\boldsymbol{\pi}}_j, \boldsymbol{\sigma}_{Uj}^{\mathrm{m}} - \boldsymbol{\sigma}_{Yj}^{\mathrm{m}}) \le 0. \quad \text{(b)} \end{cases} \tag{18}$$

As shown in Fig. 7, Eq. (18a) indicates that the subsequent yield surfaces stays always inside the bounded loading surface [32]. Equation (18b) means that motion of the origin center of the subsequent yield surface is bounded by the back stress surface [26]. The mathematical equality of both conditions is proved in [19]. Nevertheless, the obtained optimized value of back stresses under the two conditions are slightly different [6].

Table 2 Sizes of optimization problem with different material models

Material model	No. Var	No. Eq	No. Ineq.
Elastic-perfectly plastic	$6NGS + 1$	$3NK + 9NE$	$NL \times NGS$
Isotropic hardening	$6NGS + 1$	$3NK + 9NE$	$NL \times NGS$
Unlimited kinematic hardening	$6NGS + 6NGSM + 1$	$3NK + 9NE$	$NL \times NGS$
Limited kinematic hardening (a)	$6NGS + 6NGSM + 1$	$3NK + 9NE$	$NL \times (NGS + NGSM)$
Limited kinematic hardening (b)	$6NGS + 6NGSM + 1$	$3NK + 9NE$	$NL \times NGS + NGSM$

With the assumption that the material model of fiber is elastic, the material model of matrix is elastic-perfectly, isotropic hardening, unlimited kinematic hardening and limited kinematic hardening, respectively, the sizes of static shakedown problem are shown in Table 2.

4 Failure Criterion for Composites

Every material has certain strength, expressed in terms of stress or strain, beyond which the structure fractures or fails to carry the load. For heterogeneous materials, consisting of two or more phases, the determination of failure criteria is in fact one of the most important issues in the design process. Some phenomenological failure criteria that use experimental data to determine material constants have been proposed, like maximum stress theory, maximum strain theory, distortional energy (Tsai-Hill) criterion, Tsai-Wu criterion, Hashin's criterion and so on [28].

In this section, a general method to identify material parameters for a given failure criterion for composites is proposed and discussed.

4.1 Definition of Homogenized Stress

The effective elastic material properties related to different fiber distributions and volume fractions, are predicted with the aid of homogenization theory and mechanical constitutive law [4], which can be generally described as:

$$\boldsymbol{\Sigma} = \boldsymbol{d}^{\text{hom}} : \boldsymbol{E}, \tag{19}$$

$\boldsymbol{d}^{\text{hom}}$ are the homogenized elasticity tensor.

Homogenized plastic material properties can be determined experimentally or numerically. Although the results from experiments are generally more accurate, the cost is normally very high and only the strength in one or more principle directions may be obtained. Through the numerical method, we provide a rough but complete prediction of plastic properties after neglecting some defects caused in the manufacturing process.

In our former work, the yield criterion of periodic composites under plane stress case are discussed [7]. Firstly, three states during the failure are defined [8, 12]:

- Onset of plasticity (Homogenized elastic stress): $\boldsymbol{\Sigma}_{EL} = \alpha_{EL}\langle\boldsymbol{\sigma}^E\rangle$.
- Shakedown state (Homogenized shakedown stress): $\boldsymbol{\Sigma}_{SD} = \alpha_{SD}\langle\boldsymbol{\sigma}^E\rangle$.
- Limit state (Homogenized limit stress): $\boldsymbol{\Sigma}_{LM} = \alpha_{LM}\langle\boldsymbol{\sigma}^E\rangle$.

$\langle\boldsymbol{\sigma}^E\rangle$ is the homogenized macroscopic stress of purely elastic stress field. Based on limit homogenized macroscopic stress domain, there are two possibilities to derive the yield criteria:

- To find the best fitted mathematical formulation;
- To identify the related parameters by using existing yield criteria.

The former approach seems quite difficult because of the uncertainty of the number of parameters. Therefore, the latter is adopted to seek a feasible solution. Since the studied object in the numerical example is the unidirectional fiber reinforced periodic composites, whose global material behavior can be treated as an orthotropic one, Hill's yield criterion is hypothesized to fit the limit domain.

However, the stress components, either in micro-/mesoscropic level σ_{ij} or in macroscopic level Σ_{ij} depend on the orientation of the coordinate system. Nevertheless, there are certain invariants associated with every tensor. The three principle stresses are calculated through the characteristic equation:

$$\boldsymbol{\sigma}^3 - I_1\boldsymbol{\sigma}^2 + I_2\boldsymbol{\sigma} + I_3 = 0, \tag{20}$$

I_1, I_2 and I_3 are the first, second, and third stress invariants, respectively.

4.2 Projection into π-Plane

In principle stresses, Hill's yield criterion is written as:

$$F(\sigma_2 - \sigma_3)^2 + G(\sigma_3 - \sigma_1)^2 + H(\sigma_1 - \sigma_2)^2 = 1 \tag{21}$$

with:

$$\begin{aligned} F &= \frac{1}{2}\left(\frac{1}{Y^2} + \frac{1}{Z^2} - \frac{1}{X^2}\right), \\ G &= \frac{1}{2}\left(\frac{1}{Z^2} + \frac{1}{X^2} - \frac{1}{Y^2}\right), \\ H &= \frac{1}{2}\left(\frac{1}{X^2} + \frac{1}{Y^2} - \frac{1}{Z^2}\right). \end{aligned} \tag{22}$$

Here X,Y and Z are axial strengths of the orthotropic material. $\sigma_1 = \sigma_2 = \sigma_3$ is defined as the *hydrostatic axis*, $\sigma_1 + \sigma_2 + \sigma_3 = 0$ is named as π*-plane* or *deviatoric*

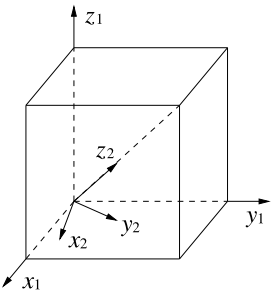

Fig. 8 Illustration of two coordinate systems

plane. Hill's yield surfaces in principal stress coordinate circumscribes an ellipse column around the hydrostatic axis.

Let $(x_1{-}y_1{-}z_1)$ and $(x_2{-}y_2{-}z_2)$ denote the original principle stress and transformed coordinate systems, respectively. As shown in Fig. 8, z_2 is coincident with the hydrostatic axis.

$(x_2{-}y_2{-}z_2)$ can be achieved using a specific sequence of intrinsic rotations (mobile frame rotations), whose values are called the Euler Angles of the target frame. Here we use "y-convention", i.e. (Z, Y', Z''):

- Rotate the $x_1y_1z_1$ -system about the z_1-axis (Z) by angle φ;
- Rotate the current system about the new y-axis (Y') by angle θ;
- Rotate the current system about the new z-axis (Z'') by angle ϕ.

$$\begin{Bmatrix} x_1 \\ y_1 \\ z_1 \end{Bmatrix} = T \begin{Bmatrix} x_2 \\ y_2 \\ z_2 \end{Bmatrix}. \tag{23}$$

T is the rotation matrix,

$$T_{x_1y_1z_1} = \begin{pmatrix} \cos\varphi & -\sin\varphi & 0 \\ \sin\varphi & \cos\varphi & 0 \\ 0 & 0 & 1 \end{pmatrix} \begin{pmatrix} \cos\theta & -\sin\theta & 0 \\ \sin\theta & \cos\theta & 0 \\ 0 & 0 & 1 \end{pmatrix} \begin{pmatrix} \cos\phi & -\sin\phi & 0 \\ \sin\phi & \cos\phi & 0 \\ 0 & 0 & 1 \end{pmatrix}. \tag{24}$$

Here, $\varphi = \frac{\pi}{4}$, $\theta = \tan^{-1}(\sqrt{2})$ and $\phi = -\frac{\pi}{4}$.

Let:

$$\begin{Bmatrix} \sigma_1 \\ \sigma_2 \\ \sigma_3 \end{Bmatrix} = T \begin{Bmatrix} \gamma_1 \\ \gamma_2 \\ \gamma_3 \end{Bmatrix},$$

the projection of Hill criterion into π-plane is:

$$(F + 1.866H + 0.134G)\gamma_1^2 + (F + 0.134H + 1.866G)\gamma_2^2 + (G - 2F + H)\gamma_1\gamma_2 = 1. \tag{25}$$

Equation (25) implies that the projection of Hill criterion onto π-plane is an ellipse.

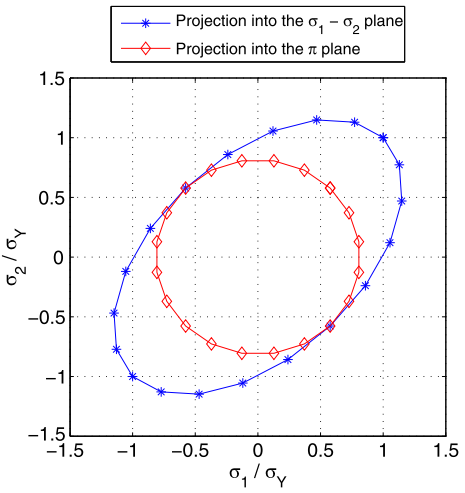

Fig. 9 Projection of the von Mises yield criterion

4.2.1 Homogeneous Material

For homogeneous material, $X = Y = Z$, i.e. $F = G = H$, which leads to the von Mises yield criterion, as shown in Eq. (26). It is a special case of Hill's yield criterion and there is only one parameter to determine:

$$(\sigma_1 - \sigma_2)^2 + (\sigma_2 - \sigma_3)^2 + (\sigma_3 - \sigma_1)^2 - 2\sigma_Y^2 \leq 0. \tag{26}$$

If the von Mises criterion is projected to π plane, Eq. (25) can be written as:

$$\gamma_1^2 + \gamma_2^2 = C \quad \text{with } C = \frac{1}{3F} = \frac{2}{3}\sigma_Y^2. \tag{27}$$

The projection of the von Mises yield criterion on (σ_1, σ_2)-plane and π-plane is shown in Fig. 9, and the ellipse from Hill's criterion becomes a circle.

4.2.2 Transversely Homogeneous Material

For transversely homogeneous material, with the assumption $Y = Z$, i.e. $G = H$, Eq. (25) can be written as:

$$(F + 2H)\gamma_1^2 + (F + 2H)\gamma_2^2 + (2H - 2F)\gamma_1\gamma_1 = 1. \tag{28}$$

There is two parameters to determine. From Eq. (22), we may obtain:

$$F = \frac{1}{2}\left(\frac{2}{Y^2} - \frac{1}{X^2}\right); \qquad G = H = \frac{1}{2}\left(\frac{1}{X^2}\right). \tag{29}$$

Rewrite Eq. (29):

$$X = \frac{1}{\sqrt{2H}}; \qquad Y = \frac{1}{\sqrt{F+H}}. \tag{30}$$

An ellipse in general position can be expressed parametrically as the path of a point $(x(t), y(t))$, where:

$$\begin{aligned} x(t) &= x_c + a\cos(t)\cos(\psi) - b\sin(t)\sin(\psi), \\ y(t) &= y_c + a\cos(t)\cos(\psi) + b\sin(t)\sin(\psi). \end{aligned} \tag{31}$$

Here, (x_c, y_c) is the center of the ellipse, ψ is the angle between the X-axis and the major axis of the ellipse, parameter t varies from 0 to 2π, a and b are major and minor radii, respectively.

In the case of transversely homogeneous material, $x_c = y_c = 0$ and $\psi = \frac{\pi}{4}$. Substitute the known value into Eq. (31), we get:

$$\begin{aligned} &\left(\frac{x+y}{\sqrt{2}a}\right)^2 + \left(\frac{x-y}{\sqrt{2}b}\right)^2 = 1 \quad \Longrightarrow \\ &\left(\frac{1}{2a^2} + \frac{1}{2b^2}\right)x^2 + \left(\frac{1}{2a^2} + \frac{1}{2b^2}\right)y^2 + \left(\frac{1}{a^2} - \frac{1}{b^2}\right)xy = 1. \end{aligned} \tag{32}$$

Comparing Eqs. (28) and (32), we get:

$$\begin{cases} F + 2H = \dfrac{1}{2a^2} + \dfrac{1}{2b^2}, \\ H - F = \dfrac{1}{2a^2} - \dfrac{1}{2b^2} \end{cases} \Longrightarrow \begin{cases} H = \dfrac{1}{3a^2}, \\ F = \dfrac{1}{2b^2} - \dfrac{1}{6a^2}. \end{cases} \tag{33}$$

4.2.3 General Orthotropic Material

For the general orthotropic material, there are three parameters to determine. Equation (31) can be written as a general implicit ellipse equation:

$$c_1x^2 + c_2xy + c_3y^2 + c_4x + c_5y + c_6 = 0. \tag{34}$$

In our case, $c_4 = c_5 = 0$ and $c_6 = -1$. Comparing Eqs. (25) and (34), we get the following three equations:

$$\begin{cases} F + 1.866H + 0.134G = c_1, \\ F + 0.134H + 1.866G = c_2, \\ G - 2F + H = c_3. \end{cases} \tag{35}$$

In conclusion, the methodology to determine the yield criterion of unidirectional fiber reinforced periodic metal matrix composites is:

1. Calculation of limit macroscopic stresses based on homogenization theory;
2. Calculation of stress invariants;
3. Projection of principle stresses into π plane;
4. Ellipse fit using least squares criterion;
5. Parameters determination of yield criterion.

5 Numerical Examples

Take the square patterned unidirectional fiber reinforced periodic metal matrix composites as an example, the RVE is shown in Fig. 10, with perfect interface. The fiber ratio is 40 %. Because of symmetry, the quarter of the RVE is used for the finite element analysis (see Fig. 11), with the dimension $l_x = l_y = 50$ mm. The RVE is subjected to two independent uniform displacement loadings, $U1^* = U2^* = U0 =$ 0.02 mm.

The material properties of each phase are shown in Table 3, with the assumption that each phase is isotropic.

8-node non-conforming elements are applied for the calculation of purely elastic stress field $\boldsymbol{\sigma}^E$ and the self-equilibrated constant matrix $[\boldsymbol{C}]$. Since the unidirectional fiber reinforced composites can be treated as plane strain case, all degrees of freedoms in the fiber direction are fixed, i.e. there is no displacement deformation in the fiber direction. AMPL+IPOPT are used as the optimization tool.

Besides the limit load factor α_{LM} and the shakedown load factor α_{SD}, the elastic load factor α_{EL} and the alternating plastic load factor α_{AP} are also calculated for the comparison in this work. The elastic load factor α_{EL} under two independent loads L_1 and L_2 is defined as:

$$\max \alpha_{EL} \quad F\left(\alpha \boldsymbol{\sigma}^i_E(P_k), \sigma_{Yi}\right) \leq 0, \quad i \in [1, NGS], \; k = 1 \tag{36}$$

where the load vertex P_1 indicates the combination of L_1 and L_2.

The alternating plasticity load factor α_{AP} under two independent loads L_1 and L_2 can be simplified as follows:

$$\max \alpha_{AP} \quad \begin{cases} F(\frac{1}{2}\alpha[\boldsymbol{\sigma}^E_i(L_1) + \boldsymbol{\sigma}^E_i(L_2)], \sigma_{Yi}) \leq 0, \\ F(\frac{1}{2}\alpha[\boldsymbol{\sigma}^E_i(L_1) - \boldsymbol{\sigma}^E_i(L_2)], \sigma_{Yi}) \leq 0, \quad i \in [1, NGS]. \end{cases} \tag{37}$$

Figure 12 shows the different load domains of the considered example, assuming that both phases have elastic perfectly plastic material behavior.

Considering the hardening, the shakedown domains for different matrix material models are shown in Fig. 13. We observe that the shakedown domain with isotropic hardening is only enlarged compared to the elastic perfectly plastic model. The shakedown domain with unlimited kinematic hardening is bounded by the alternating plasticity load domain.

If the RVE is under loading $U1 = U2$, the shakedown load factors of elastic perfectly plastic, limited kinematic hardening and unlimited kinematic hardening

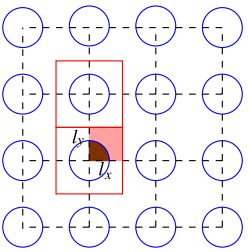

Fig. 10 Square patterned periodic composites

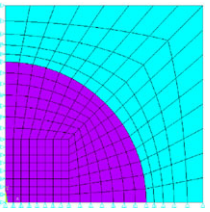

Fig. 11 Finite element model

Table 3 Material properties Al/Al_2O_3

	E (GPa)	ν	σ_Y (MPa)	σ_U (MPa)
Matrix(Al)	70	0.3	80	120
Fiber(Al_2O_3)	370	0.3	2000	

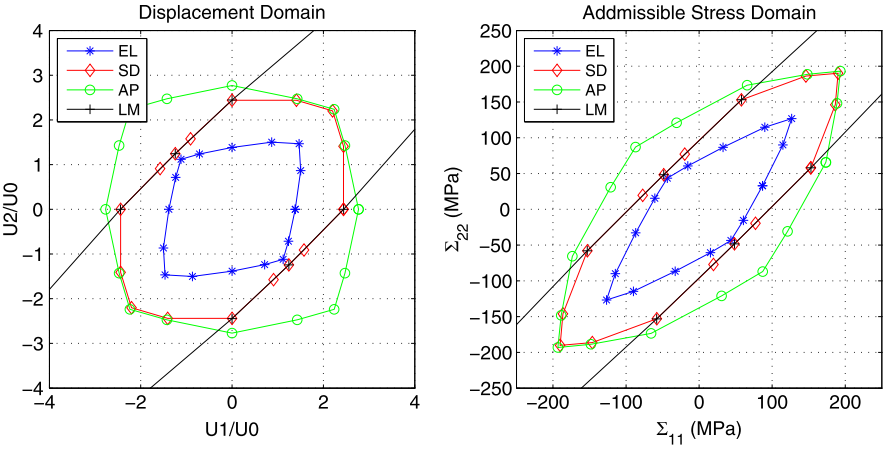

Fig. 12 Load domains of periodic composites with the fiber volume fraction 40 % under plane strain case, with EL: elastic load factor; SD: shakedown load factor; LM: limit load factor and AP: alternating plasticity load factor. (L) Displacement domain; (R) Macroscopic stress domain

have the same value, as shown Fig. 13. However, the mechanisms are obviously different. For example, under loading $U1 = U2 = -\alpha_{SD}U0$, the equivalent stress fields obtained under different material models are shown in Fig. 14.

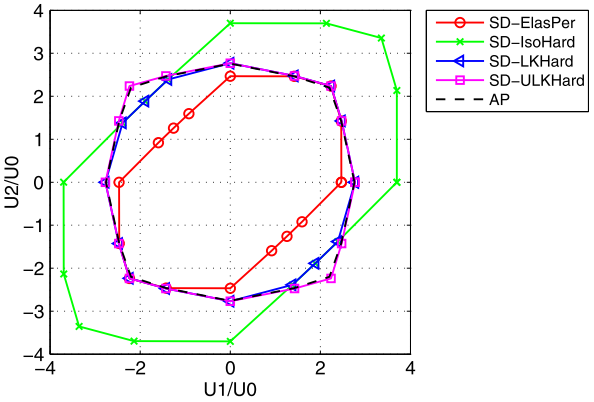

Fig. 13 Shakedown domains of all material models, with SD-ElasPer: elastic perfectly plastic; SD-IsoHard: isotropic hardening; SD-LKHard: Limited kinematic hardening; SDH-ULKHard: Unlimited kinematic hardening

Although based on the same elastic stress field $\boldsymbol{\sigma}^E$, the residual stress fields $\bar{\boldsymbol{\rho}}$ and back stress fields $\bar{\boldsymbol{\pi}}$, obtained from the optimization programming, are quite different. For the elastic perfectly plastic material model, obviously there is no back stress field. Nevertheless, the total equivalent stress fields of these three different material models are similar.

Figure 15 shows us merely the limit domains with elastic perfectly plastic and limited kinematic hardening material models, since there is no bound for limit load of matrix with unlimited kinematic hardening.

According to the limit displacement domain of the elastic perfectly plastic material model, with the aid of homogenization approach and stress invariant theory, the macroscopic principle stresses domain is obtained, as shown in Fig. 16(L), which is projected into π-plane afterwards, see Fig. 16(R). Based on the least square fitting method, the obtained parameters of Hill's criterion are as follow:

$$\text{Major axis of ellipse:} \quad a = 241.8306; \qquad \text{Minor axis of ellipse:} \quad b = 67.7779.$$

From Eqs. (33) and (30), we get the axial strength of the unidirectional periodic composites:

$$X = 296.1808\ \text{MPa} = 3.70\sigma_Y^m; \qquad Y = Z = 94.6217\ \text{MPa} = 1.18\sigma_Y^m.$$

According to the micromechanics of unidirectional composites [10], the effective yield tensile strength in fiber direction is defined as:

$$\Sigma_Y^X = \eta_{\text{m}} E_{\text{m}} \epsilon_c + \eta_{\text{f}} E_{\text{f}} \epsilon_c. \tag{38}$$

Indices 'f' and 'm' represent fiber and matrix, respectively. ϵ_c is the critical strain defined by:

$$\epsilon_c = \min\left\{\frac{\sigma_Y^{\text{m}}}{E_{\text{m}}}, \frac{\sigma_Y^{\text{f}}}{E_{\text{f}}}\right\}. \tag{39}$$

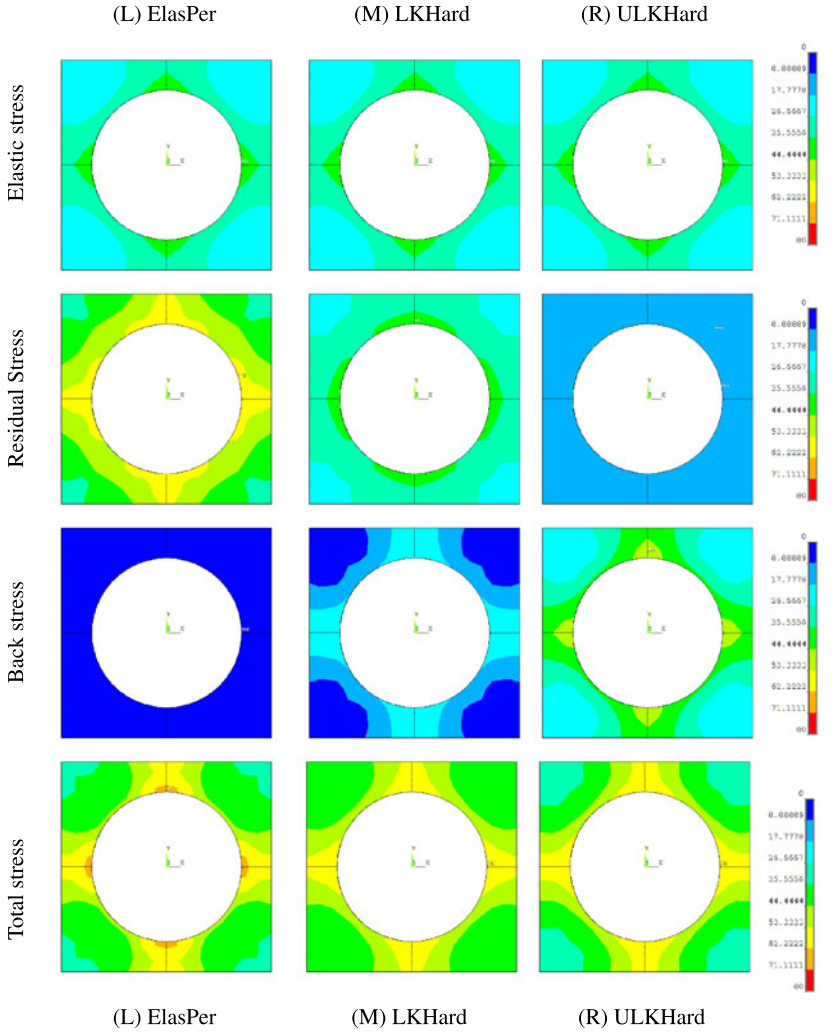

Fig. 14 Different stress fields under different material models: (**L**) Elastic perfectly plastic material model; (**M**) Limited kinematic hardening material model; (**R**) Unlimited kinematic hardening material model

Therefore, the effective yield strength based on micromechanics is:

$$\Sigma_Y^X = 217.14\ \text{MPa} = 2.17\sigma_Y^m.$$

The maximum tensile stress criterion is:

$$\Sigma_Y^{\text{t}} = \frac{1-\nu_{\text{m}}}{k_\sigma(1+\nu_{\text{m}})(1-2\nu_{\text{m}})}(\sigma_{\text{mt}} - \epsilon_{\text{rm}}E_{\text{m}}) \tag{40}$$

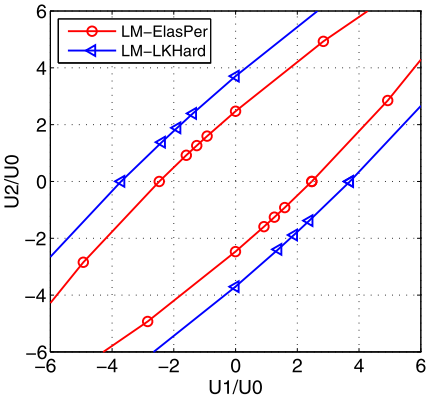

Fig. 15 Limit domains, with LM-ElasPer:elastic perfectly plastic; LM-LKHard: Limited kinematic hardening

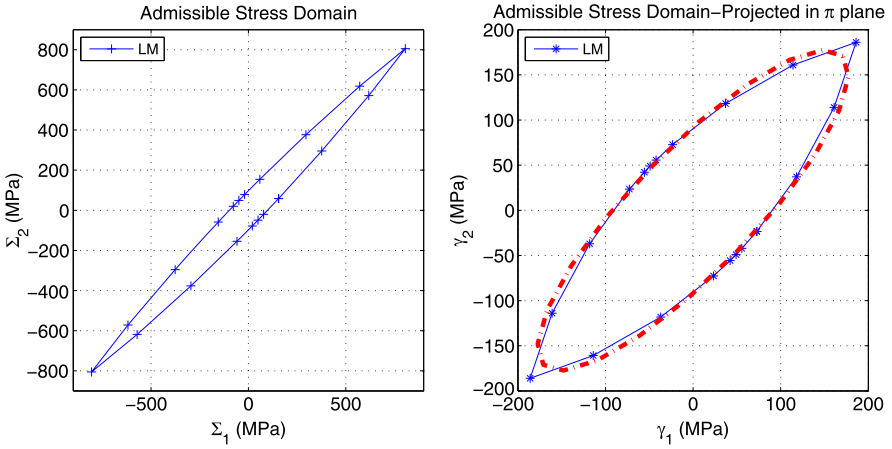

Fig. 16 Yield criterion fitting: (**L**) Homogenized stresses (Σ_1-Σ_2) domain; (**R**) Hill's yield criterion fitting based on the projection into π plane

where, index 't' means the transverse direction. ϵ_{rm} is the radial maximum residual strain, which is approximated to zero in our case. k_σ is the stress concentration factor, with the definition:

$$k_\sigma = \frac{\sigma_{\max}}{\sigma_p}, \tag{41}$$

σ_p is the outer force that is applied on the RVE or mesoscopic components. According to the numerical result, k_σ is around 1.15. Therefore, the effective transverse yield strength based on micromechanics is:

$$\Sigma_Y^Y = \Sigma_Y^Z = 93.65 \text{ MPa} = 1.17\sigma_Y^m.$$

When compared with the analytical results from microscopic mechanics, we observe that the predicted strength in transverse direction matches well. However, the

numerical value of the strength in fiber direction is bigger than the analytical one. The possible reason lies in the too restrict constraints in the numerical analysis: the degrees of freedom in fiber direction are completely fixed which leads to a greater homogenized elastic stress in fiber direction. Nevertheless, the advantages of numerical methods are obvious, which consist in the possibility to consider the fiber distributions, imperfect bounded interfaces, or other types of composites, instead of the unidirectional one.

6 Conclusions

In this paper, the lower-bound approach of DM is applied on periodic composites, including hardening material models for the matrix. As expected, for isotropic hardening, the shakedown domain is enlarged with the same shape as elastic perfectly plastic one. For unlimited kinematic hardening, there is no bound for the limit load and shakedown domain is bounded by alternating plasticity. Two yield surfaces of limited kinematic hardening model provide more realistic solutions. Furthermore, in combination with homogenization theory, plastic material parameters are predicted by using yield surface fitting on the macroscopic limit homogenized stress domain. However, the present work is based on the assumption that fiber and matrix have perfect interfaces. The debonding failure will be studied in the further work.

Acknowledgements We thank Professor D. Weichert for his support.

References

1. Kassem GA (2009) Micromechanical material models for polymer composites through advanced numerical simulation techniques. PhD thesis, Germany: RWTH-Aachen
2. Bouby C, de Saxcé G, Tritsch JB (2009) Shakedown analysis: comparison between models with linear unlimited, linear limited and non-linear kinematic hardening. Mech Res Commun 36:556–562
3. Carvelli V, Maier G, Taliercio A (1999) Shakedown analysis of periodic heterogeneous materials by a kinematic approach. J Mech Eng 50:229–240
4. Chen M (2011) Shakedown and optimization analysis of composite materials. PhD thesis, China: Southeast University
5. Chen M, Hachemi A, Weichert D (2010) Non-conforming element for limit analysis of periodic composites. Proc Appl Math Mech 10:405–406
6. Chen M, Hachemi A, Weichert D (2012) Shakedown analysis of periodic composites with kinematic hardening. Proc Appl Math Mech 12:271–272
7. Chen M, Hachemi A, Weichert D (2012) Shakedown and optimization analysis of periodic composites. In: Saxcé G, Oueslati A, Charkaluk E, Tritsch J-B (eds) Limit state of materials and structures, direct methods 2. Springer, Berlin, pp 45–69
8. Chen M, Zhang LL, Weichert D, Tang WC (2009) Shakedown and limit analysis of periodic composites. Proc Appl Math Mech 9:415–416
9. Conn AR, Gould NIM, Toint PL (1992) LANCELOT—a Fortran package for large-scale nonlinear optimization. Springer, Berlin

10. Daniel IM, Ishai O (2006) Engineering mechanics of composite materials, 2nd edn. Oxford University Press, New York
11. Fourer R, Gay DM, Kernighan BW (2003) In: AMPL: a modeling language for mathematical programming, 2nd edn. Duxbury, N. Scituate
12. Hachemi A, Chen M, Weichert D (2009) Plastic design of composites by direct methods. In: Simos TE, Psihoyios G, Tsitouras Ch (eds) Numerical analysis and applied mathematics, international conference, pp 319–323
13. König JA (1987) Shakedown of elastic-plastic structures. Elsevier, Amsterdam
14. Magoariec H, Bourgeois S, Débordes O (2004) Elastic plastic shakedown of 3d periodic heterogenous media: a direct numerical approach. Int J Plast 20:1655–1675
15. Maier G (1973) Shakedown matrix theory allowing for work hardening and second-order geometric effects. In: Sawczuk A (ed) Foundations of plasticity, pp 417–433
16. Melan E (1938) Zur Plastizität des räumlichen Kontinuums. Ing-Arch 8:116–126
17. Mouthamid S (2008) Anwendung direkter Methoden zur industriellen Berechnung von Grenzlasten mechanischer Komponenten. PhD thesis, RWTH-Aachen, Germany
18. Pham DC (2005) Shakedown static and kinematic theorems for elastic-plastic limited linear kinematic-hardening solids. Eur J Mech A, Solids 24:35–45
19. Pham PT (2011) Upper bound limit and shakedown analysis of elastic-plastic bounded linearly kinematic hardening structures. PhD thesis, RWTH-Aachen, Germany
20. Ponter ARS (1975) A general shakedown theorem for elastic plastic bodies with work hardening. In: Proc SMIRT-3, p L5/2
21. Ponter ARS, Leckie FA (1998) Bounding properties of metal-matrix composites subjected to cyclic thermal loading. J Mech Phys Solids 46:697–717
22. Ponter ARS, Leckie FA (1998) On the behaviour of metal matrix composites subjected to cyclic thermal loading. J Mech Phys Solids 46:2183–2199
23. Schwabe F (2000) Einspieluntersuchungen von Verbundwerkstoffen mit periodischer Mikrostruktur. PhD thesis, RWTH-Aachen, Germany
24. Simon JW, Weichert D (2011) Numerical lower bound shakedown analysis of engineering structures. Comput Methods Appl Mech Eng 200:2828–2839
25. Simon WJ (2011) Numerische Einspielunguntersuchungen mechanischer Komponenten mit begrenzt kinematisch verfestigendem Materialverhalten. PhD thesis, RWTH-Aachen, Germany
26. Stein E, Zhang G, König JA (1992) Shakedown with nonlinear hardening including structural computation using finite element method. Int J Plast 8:1–31
27. Suquet P (1982) Plasticité et homogénéisation. PhD thesis, Université Pierre et Marie Curie, France
28. Talreja R, Singh CV (2012) Damage and failure of composite materials. Cambridge University Press, Cambridge
29. Wächter A (2002) An Interior Point Algorithm for Large-Scale Nonlinear Optimization with Applications in Process Engineering. PhD thesis, Chemical Engineering, Carnegie Mellon University, Pennsylvania:
30. Wächter A (2009) Short tutorial: getting started with ipopt in 90 minutes. Technical report, IBM Research Report
31. Wächter A, Biegler LT (2006) On the implementation of a primal-dual interior-point filter line-search algorithm for large-scale nonlinear programming. Math Program 106:25–57
32. Weichert D, Gross-Weege J (1988) The numerical assessment of elastic-plastic sheets under variable mechanical and thermal loads using a simplified tow-surface yield condition. Int J Mech Sci 30:757–767
33. Weichert D, Hachemi A, Schwabe F (1999) Application of shakedown analysis to the plastic design of composites. Arch Appl Mech 69:623–633
34. Weichert D, Hachemi A, Schwabe F (1999) Shakedown analysis of composites. Mech Res Commun 26:309–318

The Residual Stress Decomposition Method (RSDM): A Novel Direct Method to Predict Cyclic Elastoplastic States

Konstantinos V. Spiliopoulos and Konstantinos D. Panagiotou

Abstract Instead of approaching the steady state behavior of an elastic–perfectly plastic structure, under cyclic loading, through time consuming incremental time-stepping calculations, one may alternatively use direct methods. A common feature of these methods is to estimate directly these cyclic states, profiting, thus, big savings in computer time. The elastic shakedown is the most important, in terms of structural safety, cyclic state. Most of the existing methods address this state through the solution of an optimization problem. In this work, a novel direct method that has a more physical understanding and may predict any cyclic steady stress state is exposed. The method is based on the expected cyclic nature of the residual stress distribution at the steady cycle. Having evaluated the elastic stress part of the total stress to equilibrate the external load, the unknown residual stress part is decomposed into Fourier series, whose coefficients are evaluated iteratively by satisfying compatibility and equilibrium with zero loads at time points inside the cycle. A computationally simple way to account for plasticity is considered. The procedure converges uniformly to a residual stress field which is either constant, marking the loading to be below the elastic shakedown limit, or to a cyclic residual stress field, from which possible alternating plasticity or ratcheting conditions may be realized. The procedure is formulated within the finite element method. A von Mises yield surface is typically used. Examples of application to a truss and a two dimensional plate under plane stress or strain are discussed.

1 Introduction

Nowadays structures are continuously designed to withstand repeated thermo-mechanical loading that forces them to enter the plastic regime. Such loading conditions are encountered either in civil or mechanical engineering. Typical examples of such structures are buildings and bridges under seismic loading on the one hand and nuclear reactors and aircraft gas propulsion engines on the other.

K.V. Spiliopoulos (✉) · K.D. Panagiotou
Department of Civil Engineering, Institute of Structural Analysis & Antiseismic Research, National Technical University of Athens, Zografou Campus, Zografos 157-80, Athens, Greece
e-mail: kvspilio@central.ntua.gr

K. Spiliopoulos, D. Weichert (eds.), *Direct Methods for Limit States in Structures and Materials*, DOI 10.1007/978-94-007-6827-7_7,

The life cycle assessment of such a structure constitutes an important task for a structural engineer. However, the long term response of a structure, subjected to a given thermo-mechanical loading which exhibits inelastic time independent plastic strains, is quite complex, because of the need to perform lengthy and expensive incremental calculations, especially for structures with a high degree of redundancy. In the case that the long term response turns out to be a stabilized state there are procedures called direct methods, which may lead directly to these states. Scleronomic or rheonomic stable materials guarantee the existence of such states [1]. Thus direct methods search for this asymptotic state right from the start of the calculations.

The most well known cyclic state is the elastic shakedown. The search for this state is based on the lower [2] and upper bound [3] shakedown theorems of plasticity. The formulation of these problems is normally done using mathematical programming (MP). One may refer to various such procedures like a nonlinear Newton-type algorithm [4] or the interior point methods (e.g. [5, 6]).

There are also very few approaches that are not based on MP. Internal parameters are introduced in [7] which characterize local inelastic mechanisms. Another procedure is the Linear Matching Method (LMM) [8] which is a generalization of the elastic compensation method [9] and is based on matching a linear problem to a plasticity problem. A sequence of linear solutions, with spatially varying moduli, is generated that provide upper bounds that monotonically converge to the least upper bound.

The method was further extended beyond shakedown, for loadings that can be decomposed into constant and time varying components, so as to provide an upper bound estimation of the ratchet boundary [10].

Besides the knowledge of safety margins, it is important to be able to determine the long-term effects on a structure for a given cyclic loading. For this purpose, an alternative to the cumbersome incremental procedure is a method called Direct Cycle Analysis (DCA) originally suggested in [11] and implemented in the commercial program Abaqus [12]. The main assumption of the method is that the displacements at the steady cycle will become cyclic. The method is quite involved and appears to be a mixture of an incremental and an iterative procedure. The displacements are decomposed into Fourier series whose coefficients are evaluated in an iterative way by linking them with the coefficients of the Fourier series of the out-of-balance load vector. This vector is evaluated as in an incremental procedure, and static admissibility is enforced by leading it to zero. The procedure seems to be suited for the cases of alternating plasticity but fails to converge for loadings that are close to ratcheting as also mentioned in [12] since, because of its main assumption, it can't predict such a case.

A new direct method to predict any long-term cyclic state of an elastic-perfectly structure under a given cyclic loading was quite recently suggested [13]. The method focuses on the cyclic nature of the residual stresses at the steady state. The method has been called Residual Stress Decomposition Method (RSDM) and is based on decomposing the residual stresses in Fourier series inside a cycle of loading. The decomposition of the residual stresses, so as to find a simplified way to predict creep cyclic steady stress states, was originally proposed in [14].

In the RSDM the coefficients of the Fourier series are evaluated in an iterative way by integrating the residual stress rates over the cycle. By satisfying equilibrium and compatibility at time points inside the cycle one may evaluate these rates. Plastic effects are accounted for by adding the elastic and the residual stress at the cycle points. If the sum exceeds the yield surface, the plastic strain rate may be represented by the stress in excess of the yield surface. This excess stress provides then input for iteration. If the plastic strain rates stabilize, in the form of a converged residual stress vector, the procedure stops. One can easily distinguish any of the three different cases, shakedown, alternating plasticity or ratcheting. A one-dimensional truss and a two-dimensional plate with a hole under plane stress have demonstrated in [13] the application of the procedure. For the plate, results are, in the present work, extended to include plane strain conditions. The whole approach is shown to be stable and computationally efficient, with uniform convergence.

2 Cyclic Steady-States

Let us consider a body of volume V and surface S. On one part of S we have zero displacement conditions and on the other part of the surface a cyclic loading of the form (1) is applied.

$$\mathbf{P}(t) = \mathbf{P}(t + nT) \tag{1}$$

where $\mathbf{P}(t)$ is the set of loads that act on S; t is the time point inside the cycle, T is the period of the cycle, $n = 1, 2, \ldots$, denotes the number of full cycles. Bold letters are used, herein, to denote vectors and matrices.

Let us suppose that our structure is made of an elastic-perfectly plastic material. At any time point $\tau = t/T$ inside the cycle the structure will develop a stress field $\boldsymbol{\sigma}(\tau)$ which may be decomposed into an elastic part $\boldsymbol{\sigma}^{\mathrm{el}}(\tau)$, that equilibrates the external loading $\mathbf{P}(\tau)$ assuming a completely elastic behavior, and a self-equilibrating residual stress part $\boldsymbol{\rho}(\tau)$ that is due to inelasticity. Therefore:

$$\boldsymbol{\sigma}(\tau) = \boldsymbol{\sigma}^{\mathrm{el}}(\tau) + \boldsymbol{\rho}(\tau). \tag{2}$$

An analogous decomposition holds for the strain rates:

$$\dot{\boldsymbol{\varepsilon}} = \dot{\mathbf{e}}^{\mathrm{el}}(\tau) + \dot{\boldsymbol{\varepsilon}}_r(\tau). \tag{3}$$

The residual strain rate itself may be decomposed into an elastic and a plastic part [15]. Thus the final compatibility equation is expressed as:

$$\dot{\boldsymbol{\varepsilon}} = \dot{\mathbf{e}}^{\mathrm{el}}(\tau) + \dot{\boldsymbol{\varepsilon}}_r^{\mathrm{el}}(\tau) + \dot{\boldsymbol{\varepsilon}}^{\mathrm{pl}}(\tau). \tag{4}$$

The elastic strain rates are related to the stress rates through the elasticity matrix $\mathbf{D}$, whereas the plastic strain rate vector through the gradient of the flow rule:

$$\begin{aligned} \dot{\boldsymbol{\sigma}}^{\mathrm{el}}(\tau) &= \mathbf{D} \cdot \dot{\mathbf{e}}, \\ \dot{\boldsymbol{\rho}}(\tau) &= \mathbf{D} \cdot \dot{\boldsymbol{\varepsilon}}_r^{\mathrm{el}}, \\ \dot{\boldsymbol{\varepsilon}}^{\mathrm{pl}} &= \lambda \cdot \frac{\partial f}{\partial \boldsymbol{\sigma}} \end{aligned} \tag{5}$$

where f is the yield surface.

Based on the Drucker's stability postulate for rheonomic or scleronomic materials it may be proved [16] that there always exists an asymptotic cyclic state that the stresses and strain rates stabilize and become periodic with the same period of the cyclic loading.

Depending on the amplitude of the load three different asymptotic states may be realized, based on the existence or not of the plastic strain rates:

(a) Elastic shakedown, meaning $\dot{\boldsymbol{\varepsilon}}^{\mathrm{pl}} \to \mathbf{0}$.
(b) Plastic shakedown, meaning $\dot{\boldsymbol{\varepsilon}}^{\mathrm{pl}} \neq \mathbf{0}$, but $\int_0^T \dot{\boldsymbol{\varepsilon}}^{\mathrm{pl}} dt = \mathbf{0}$.
(c) Ratcheting, meaning $\dot{\boldsymbol{\varepsilon}}^{\mathrm{pl}} \neq \mathbf{0}$, and $\int_0^T \dot{\boldsymbol{\varepsilon}}^{\mathrm{pl}} dt \neq \mathbf{0}$.

3 The Residual Stress Decomposition Method (RSDM)

Since the elastic stress under a cyclic load is cyclic, a cyclic steady stress state renders the residual stress distribution to be also cyclic. One may thus exploit this cyclic nature, decompose the residual stresses into Fourier series, and try to find the unknown Fourier coefficients. In this way we may write:

$$\boldsymbol{\rho}(\tau) = \frac{1}{2}\mathbf{a}_0 + \sum_{k=1}^{\infty}\left\{\cos(2k\pi\tau)\cdot\mathbf{a}_k + \sin(2k\pi\tau)\cdot\mathbf{b}_k\right\}. \tag{6}$$

Differentiating the above with respect to τ one may write the following expression for the derivative:

$$\dot{\boldsymbol{\rho}}(\tau) = 2\pi\sum_{k=1}^{\infty}\left\{-k\sin(2k\pi\tau)\cdot\mathbf{a}_k + k\cos(2k\pi\tau)\cdot\mathbf{b}_k\right\}. \tag{7}$$

Making use of (7) and the orthogonality properties of the trigonometric functions one may get expressions for the Fourier coefficients of the *cosine* and *sine* series in terms of the residual stress derivatives:

$$\begin{aligned}\mathbf{a}_k &= -\frac{1}{k\pi}\int_0^1 \sin(2k\pi\tau)\cdot\dot{\boldsymbol{\rho}}(\tau)d\tau,\\ \mathbf{b}_k &= \frac{1}{k\pi}\int_0^1 \cos(2k\pi\tau)\cdot\dot{\boldsymbol{\rho}}(\tau)d\tau.\end{aligned} \tag{8}$$

A more involved formula proves to be needed for the constant term, which uses the information at the beginning and at the end of the cycle [13]:

$$\frac{1}{2}\mathbf{a}_{0,e} = \left(\frac{1}{2}\mathbf{a}_{0,b} + \sum_{k=1}^{\infty}\mathbf{a}_{k,b}\right) - \sum_{k=1}^{\infty}\mathbf{a}_{k,e} + \int_0^1 \dot{\boldsymbol{\rho}}(\tau)d\tau \tag{9}$$

where the subscripts b and e denote the beginning and the end of the cycle respectively. As seen from Eqs. (8) and (9), because of (7), there is an implicit dependence of the Fourier coefficients and thus an iterative scheme may be used to estimate them, once the residual stress derivatives are calculated.

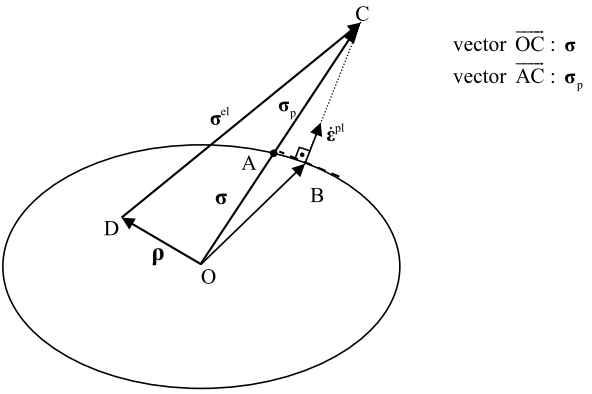

Fig. 1 Estimation of plastic straining (von Mises yield surface)

To find these derivatives one seeks to satisfy compatibility and equilibrium at some predefined time points inside the cycle. To this end we assume that our structure is discretized with finite elements (FEs). Using the rates of displacements of the nodes of the FE mesh one may write:

$$\dot{\boldsymbol{\varepsilon}} = \mathbf{B} \cdot \dot{\mathbf{r}}. \tag{10}$$

From Eqs. (4) and (5) we may write:

$$\dot{\boldsymbol{\rho}} = \mathbf{D} \cdot \left(\dot{\boldsymbol{\varepsilon}} - \dot{\boldsymbol{\varepsilon}}^{\mathrm{el}} - \dot{\boldsymbol{\varepsilon}}^{\mathrm{pl}} \right). \tag{11}$$

Since the strain rates are kinematically admissible, the residual stress rates are self-equilibrated, and fixed supports have been assumed, one may write, for a virtual strain field $\delta\dot{\boldsymbol{\varepsilon}}$, using the Principle of Virtual Work (PVW):

$$\int_V \delta\dot{\boldsymbol{\varepsilon}}^T \cdot \dot{\boldsymbol{\rho}} dV = 0. \tag{12}$$

Combining (10), (11) and (12), we end up with:

$$\left(\int_V \mathbf{B}^T \cdot \mathbf{D} \cdot \mathbf{B} dV \right) \cdot \dot{\mathbf{r}} = \int_V \mathbf{B}^T \cdot \dot{\boldsymbol{\sigma}}^{\mathrm{el}} dV + \int_V \mathbf{B}^T \cdot \mathbf{D} \cdot \dot{\boldsymbol{\varepsilon}}^{\mathrm{pl}} dV \tag{13}$$

or equivalently:

$$\mathbf{K} \cdot \dot{\mathbf{r}} = \dot{\mathbf{R}} + \int_V \mathbf{B}^T \cdot \mathbf{D} \cdot \dot{\boldsymbol{\varepsilon}}^{\mathrm{pl}} dV \tag{14}$$

where $\mathbf{K}$ is the stiffness matrix, $\dot{\mathbf{R}}$ is the rate vector of the external forces acting on the structure at the cycle time τ.

Plastic straining will occur whenever the total stress (Eq. (2)) exceeds the yield surface (Fig. 1). In such a case, the returning back on the yield surface will be, according to the closest point projection [17], along the vector $\overrightarrow{CB}$, with the plastic strain rate $\dot{\boldsymbol{\varepsilon}}^{\mathrm{pl}}$ directed along $\overrightarrow{BC}$. We use, instead, the vector $\overrightarrow{CA}$ which is $-\boldsymbol{\sigma}_{\mathrm{p}}$. This vector is a 'radial return' type of mapping along the known $\overrightarrow{OC}$. It may be easily determined, especially for a von Mises yield surface. It is an equivalent measure for the plastic straining in the sense that they either both exist or not.

3.1 Numerical Procedure

An iterative procedure has been written that updates the Fourier coefficients inside an iteration [13].

Firstly we solve for the external loading and its cycle rate assuming elastic behavior, and obtain, for each cycle point τ, the elastic stress $\boldsymbol{\sigma}^{\mathrm{el}}(\tau)$ and the elastic stress rate $\dot{\boldsymbol{\sigma}}^{\mathrm{el}}(\tau)$ at each Gauss point (GP) of a continuum finite element.

Let us suppose that after the completion of the iteration (μ) an estimate of the distribution of the Fourier coefficients $\mathbf{a}_0^{(\mu)}$, $\mathbf{a}_k^{(\mu)}$, $\mathbf{b}_k^{(\mu)}$ has been made. The following steps are now followed:

1. For a specific cycle point τ we compute $\boldsymbol{\rho}^{(\mu)}(\tau)$, at each GP, using (6):

$$\boldsymbol{\rho}^{(\mu)}(\tau) = \frac{1}{2}\mathbf{a}_0^{(\mu)} + \sum_{k=1}^{\infty}\left\{\cos(2k\pi\tau)\cdot\mathbf{a}_k^{(\mu)} + \sin(2k\pi\tau)\cdot\mathbf{b}_k^{(\mu)}\right\}. \tag{15}$$

2. Evaluate at each GP the total stress $\boldsymbol{\sigma}^{(\mu)}(\tau)$, using (2):

$$\boldsymbol{\sigma}^{(\mu)}(\tau) = \boldsymbol{\sigma}^{\mathrm{el}}(\tau) + \boldsymbol{\rho}^{(\mu)}(\tau). \tag{16}$$

3. Calculate whether, at each GP, $\bar{\sigma}^{(\mu)}(\tau) > \sigma_Y$. In such a case compute $\boldsymbol{\sigma}_p^{(\mu)}(\tau)$:

$$\xi = \frac{\bar{\sigma}^{(\mu)}(\tau) - \sigma_Y}{\bar{\sigma}^{(\mu)}(\tau)} \Rightarrow \boldsymbol{\sigma}_p^{(\mu)}(\tau) = \xi\cdot\boldsymbol{\sigma}^{(\mu)}(\tau). \tag{17}$$

4. Assemble for the whole structure the rate vector of the nodal forces $\dot{\mathbf{R}}'(\tau)$, which is the r.h.s. of Eqs. (13)–(14):

$$\dot{\mathbf{R}}'(\tau) = \dot{\mathbf{R}}(\tau) + \int_V \mathbf{B}^T\cdot\boldsymbol{\sigma}_p^{(\mu)}(\tau)dV. \tag{18}$$

5. Solve the following iterative form of Eq. (14) and obtain $\dot{\mathbf{r}}^{(\mu)}(\tau)$:

$$\mathbf{K}\dot{\mathbf{r}}^{(\mu)}(\tau) = \dot{\mathbf{R}}'(\tau). \tag{19}$$

6. Evaluate at each GP the residual stress derivative rates, using (11):

$$\dot{\boldsymbol{\rho}}^{(\mu)}(\tau) = \mathbf{DB}\dot{\mathbf{r}}^{(\mu)}(\tau) - \dot{\boldsymbol{\sigma}}^{\mathrm{el}}(\tau) - \boldsymbol{\sigma}_p^{(\mu)}(\tau). \tag{20}$$

7. Repeat the steps 1–6 for all the assumed cycle points.
8. Perform a numerical integration over the cycle points and update the Fourier coefficients, making use of Eqs. (8) and (9):

$$\begin{aligned}
\mathbf{a}_k^{(\mu+1)} &= -\frac{1}{k\pi}\int_0^1\left\{\left[\dot{\boldsymbol{\rho}}^{(\mu)}(\tau)\right](\sin 2k\pi\tau)\right\}d\tau,\\
\mathbf{b}_k^{(\mu+1)} &= \frac{1}{k\pi}\int_0^1\left\{\left[\dot{\boldsymbol{\rho}}^{(\mu)}(\tau)\right](\cos 2k\pi\tau)\right\}d\tau,\\
\frac{\mathbf{a}_0^{(\mu+1)}}{2} &= -\sum_{k=1}^{\infty}\mathbf{a}_k^{(\mu+1)} + \frac{\mathbf{a}_0^{(\mu)}}{2} + \sum_{k=1}^{\infty}\mathbf{a}_k^{(\mu)} + \int_0^1\left[\dot{\boldsymbol{\rho}}^{(\mu)}(\tau)\right]d\tau.
\end{aligned} \tag{21}$$

9. From the updated Fourier coefficients evaluate the updated distribution of the residual stresses, at all the Gauss points, using (15), and check the convergence through their norms at the end of the cycle:

$$\frac{\|\boldsymbol{\rho}^{(\mu+1)}(1)\|_2 - \|\boldsymbol{\rho}^{(\mu)}(1)\|_2}{\|\boldsymbol{\rho}^{(\mu+1)}(1)\|_2} \leq tol \tag{22}$$

where *tol* is a specified tolerance.

If (22) holds, the procedure stops as we have reached a cyclic stress state (cs), and $\boldsymbol{\rho}^{(\mu)} = \boldsymbol{\rho}^{(\mu+1)} = \boldsymbol{\rho}^{\text{cs}}$; otherwise we go back to step 1 and repeat the process.

Once a cyclic stress state has been attained, we look at $\boldsymbol{\sigma}_p^{\text{cs}} = \boldsymbol{\sigma}_p^{(\mu)} = \boldsymbol{\sigma}_p^{(\mu+1)}$, which was evaluated during the last iteration. We may determine the nature of the obtained solution, for each GP, by evaluating the following integral over the cycle:

$$\alpha_i = \int_0^1 \sigma_{p,i}^{\text{cs}}(\tau) d\tau \tag{23}$$

with i spanning all the components of $\boldsymbol{\sigma}_p^{\text{cs}}(\tau)$.

Depending on the values of α_i we may have:

(a) If $\alpha_i \neq 0$, a state of ratcheting exists at this GP. If $\alpha_i = 0$, we check the value of $\sigma_{p,i}^{\text{cs}}(\tau)$ for every cycle point τ.
(b) If $\sigma_{p,i}^{\text{cs}}(\tau) \neq 0$, the Gauss point is in a state of reverse plasticity, since this must hold for pairs of cycle points of equal value but of alternating sign.
(c) If $\sigma_{p,i}^{\text{cs}}(\tau) = 0$, the point has remained either elastic or has developed an elastic shakedown state.

For the case of all the Gauss points being either elastic or in a state of elastic shakedown, our structure, under the given external loading, will also shake down. On the other hand, if sufficient GPs are in a state of ratcheting, at the steady state, our structure will undergo incremental collapse. This, numerically, may be easily proved here, through the singularity of the stiffness matrix, which can be evaluated just at the end of the converged steady cycle, by zeroing the elasticity matrix **D** at the ratcheting GPs.

4 Application Examples

The method is applied to two structures one being a one dimensional and the other a two dimensional plate element with a hole under plane stress or plane strain conditions. A value of 10^{-4} for the tolerance proved quite accurate to stop the iterations.

4.1 Pin Jointed Framework

The truss structure (Fig. 2) that consists of five members, whose properties are listed in Table 1, was chosen as a first example of application of the proposed method.

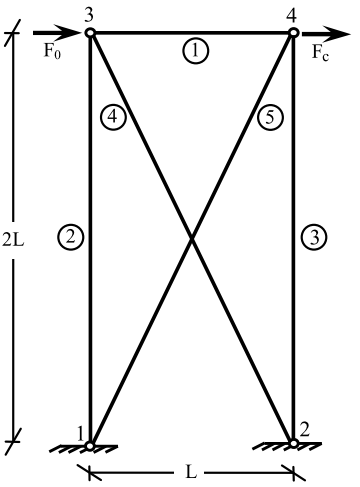

Fig. 2 Five bar truss example

Table 1 Properties of the truss elements

Element	Areas (cm^2)
1	1.806
2	30.825
3	24.940
4	34.583
5	27.908

Material data was assumed as $E = 0.21 \times 10^5$ kN/cm^2, $\sigma_y = 36$ kN/cm^2, whereas $L = 200$ cm.

A simple two node plane truss element was used to analyze the structure. The only change that needs to be applied in the numerical procedure, presented for the continuum, is to use the axial stress in each bar, for this one-dimensional problem, instead of the effective stress used for the continuum.

The truss was subjected to concentrated cyclic loads F_0 and F_c which are applied at nodes 3 and 4 respectively. Two cases of loading have been considered which lead to different cyclic steady states.

(a) The first cyclic loading case has the following variation with time:

$$F_c(t) = 100 \sin(2\pi t/T), \qquad F_0 = 400 \text{ kN}.$$

The procedure predicts that the structure will shakedown. The constant in time steady state residual stress may be seen in Fig. 3(a). In Fig. 3(b) one may also see the distribution of the total stress, for bar 1, inside the cycle, where nowhere the yield stress is exceeded. Analogous behavior is observed, of course, for all the other bars.

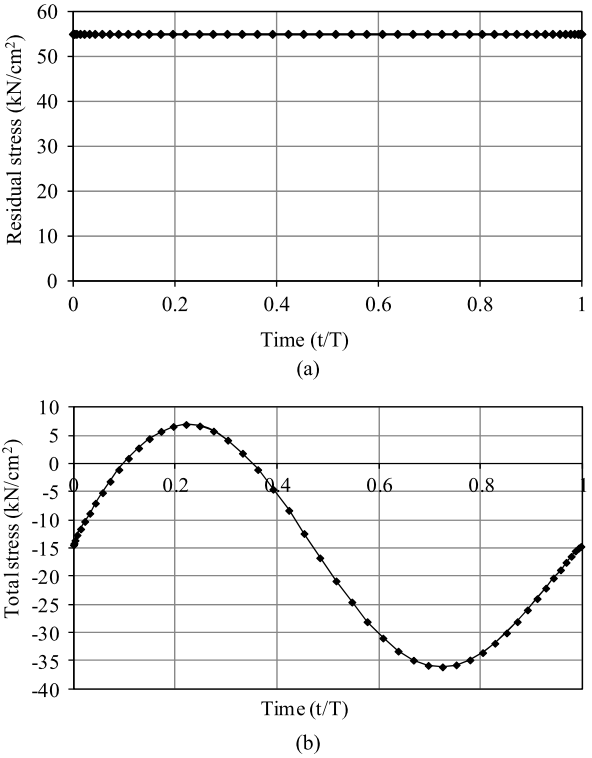

Fig. 3 Steady state stress distributions inside a cycle for element 1 (load case a—shakedown): (**a**) residual stress, (**b**) total stress

(b) The second cyclic loading case has the following variation with time:

$$F_c(t) = 200 \sin(2\pi t/T), \qquad F_0 = 200 \text{ kN}.$$

For this loading case the RSDM predicts that the structure is going to suffer from alternating plasticity. In Fig. 4 one may see the uniform convergence of the procedure towards the final steady state.

The distribution of the cyclic residual stress predicted for the middle bar 1 inside the steady cycle may be seen in Fig. 5. The procedure shows that in the steady state the middle bar suffers plastic strain rates, of alternating nature. These strains spread within the time intervals [0.169, 0.362] and [0.638, 0.851], inside the cycle, rendering the total plastic strain over the cycle (parameter α_1—expression (23), also equal to the total area under the curve, Fig. 6) equal to zero.

The results for both the two loading cases agree well with those in [18].

4.2 Plate with a Central Hole

The second example of application is the classical problem of a square plate having a circular hole in its center. The plate is subjected to two biaxial uniform loads applied

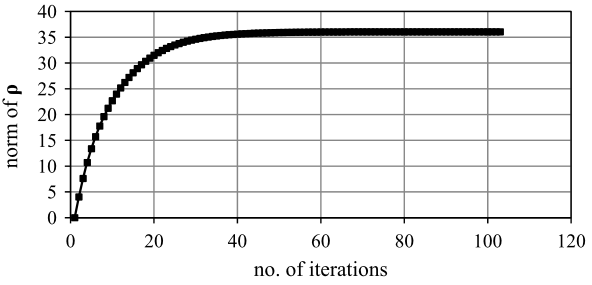

Fig. 4 Convergence of the iterative procedure—truss example (load case b)

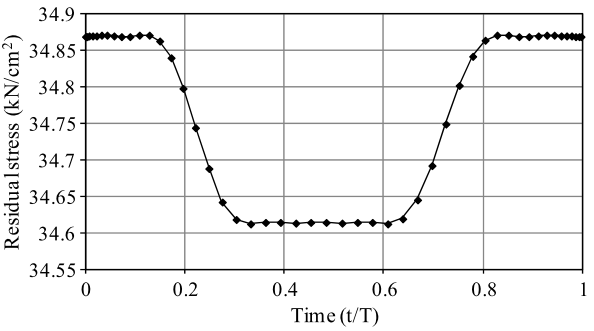

Fig. 5 Predicted steady state residual stress distribution for element 1 inside a cycle (load case b—alternating plasticity)

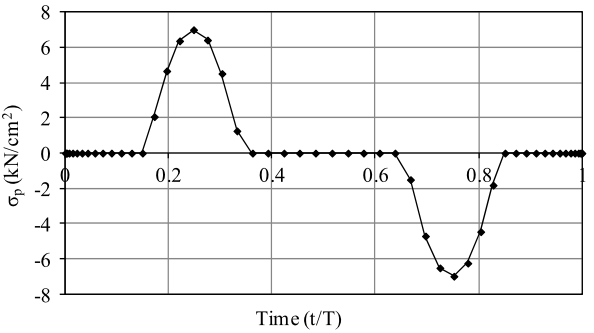

Fig. 6 Predicted $\sigma_p^{\mathrm{cs}}(t)$ distribution at steady state inside a cycle for element 1 (load case b—alternating plasticity)

at the edges of the plate. Due to the symmetry of the structure and the loading, only one quarter of the plate is considered.

The boundary conditions as well as its finite element mesh discretization are shown in Fig. 7. The ratio between the diameter d of the hole and the length L of the plate is equal to 0.2. Also the ratio of the depth of the plate and its length is equal to 0.05. Ninety-eight, eight-noded, isoparametric elements with 3×3 Gauss integration points were used.

The material data used was: Young's modulus $E = 0.21 \times 10^5$ kN/cm^2, Poisson's ratio $\nu = 0.3$ and yield stress $\sigma_y = 36$ kN/cm^2.

Both plane stress and plain strain conditions have been examined as the procedure 3.1 may be applied to both of them.

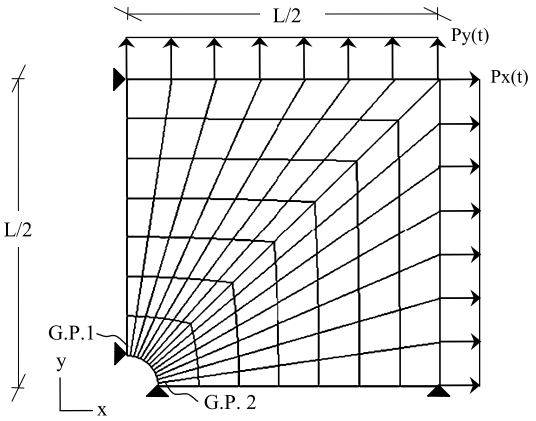

Fig. 7 The geometry, loading, and the finite element mesh of a quarter of a plate

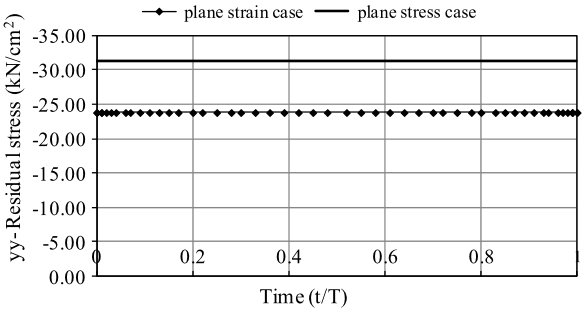

Fig. 8 Residual stress distribution at GP 2 inside a cycle at steady state under plane stress and plane strain conditions (load case a—shakedown)

The same vectors $\boldsymbol{\sigma} = \{\sigma_{xx}\ \sigma_{yy}\ \sigma_{xy}\ \sigma_{zz}\}^T$ and $\boldsymbol{\rho} = \{\rho_{xx}\ \rho_{yy}\ \rho_{xy}\ \rho_{zz}\}^T$ may be utilized at a GP for both cases. For each of the two cases the corresponding 3×3 elasticity matrix $\mathbf{D}$ should be used. As far as the fourth element of the stress vector is concerned, for the plane stress problem $\sigma_{zz}^{\mathrm{el}}, \rho_{zz} = 0$. The same holds for their derivatives.

For a plane strain problem, on the other hand, we should have $\sigma_{zz}^{\mathrm{el}} = \nu(\sigma_{xx}^{\mathrm{el}} + \sigma_{yy}^{\mathrm{el}})$, $\rho_{zz} = \nu(\rho_{xx} + \rho_{yy})$. The same, of course, holds for their derivatives. The non existence of the corresponding out of plane plastic strain is assured by setting $\sigma_{p,zz} = 0$.

Three different loading cases were taken into account, which lead the structure to either shakedown, reverse plasticity or ratcheting. Results are plotted for the generally most highly stressed points of the plate GP 1 or GP 2, depending on the loading case.

(a) The first cyclic loading case has the following variation with time:

$$P_y(t) = 0.65\sigma_y \sin^2(\pi t/T), \qquad P_x(t) = 0.$$

The predicted by the procedure behavior for the structure is a shakedown state and this complies with the fact that this loading is below the shakedown boundary estimated in [19]. In Fig. 8 the computed by the RSDM steady-state residual stress distribution is plotted for the GP 2, for both plane stress and plane strain conditions.

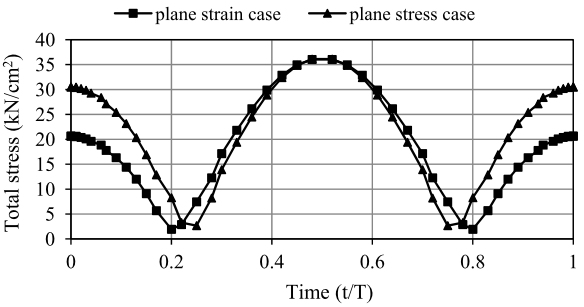

Fig. 9 Effective total stress distribution at GP 2 inside a cycle at steady-state (load case a—shakedown), plane stress and plane strain condition

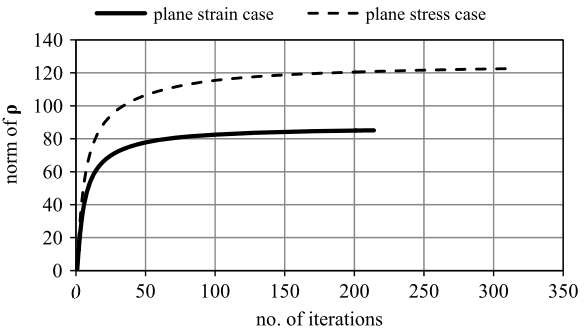

Fig. 10 Convergence of the iterative procedure (load case a—shakedown)

This residual stress distribution is unique and will be the same with the one that would be predicted from an incremental step-by-step analysis, e.g. [12] (see also examples in [13]). The total stress distribution for this point is plotted in Fig. 9. In Fig. 10 one may also see the convergence towards the final steady states.

(b) The second cyclic loading case has the following variation with time:

$$P_y(t) = 0.7223\sigma_y \sin^2(\pi t/T), \qquad P_x(t) = 0.$$

The value of this load, at many cycle points, is in excess of the shakedown limit computed by using a plane stress modeling, and below the shakedown limit assuming a plane strain condition [19]. The present numerical procedure (RSDM) also shows that this loading will lead the plate to shakedown for plane strain, but assuming plane stress conditions the loading leads some GPs to reverse plasticity. So, for the plane strain case, in Figs. 11, 12 one may see the computed by the RSDM steady-state residual stress distribution for the GP 2 and its effective total stress distribution, respectively.

On the other hand, for plane stress modelling, we plot, for the most strained point GP 2, the variation of the yy component of the excess stress vector $\boldsymbol{\sigma}_p^{\mathrm{cs}}$, which has the biggest values from the three components (Fig. 13). We may see that plastic straining occurs, alternately, inside the time intervals [0, 0.04], [0.45, 0.55] and [0.96, 1] at the steady cycle.

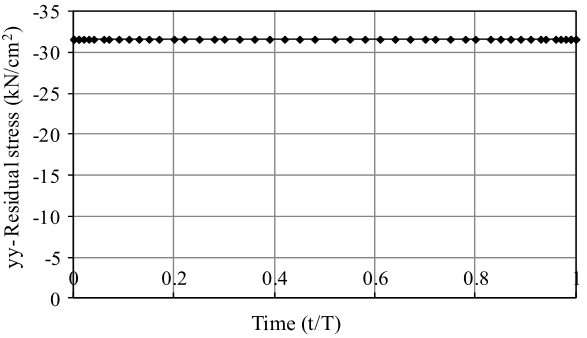

Fig. 11 Residual stress distribution at GP 2 inside a cycle at steady-state (load case b—shakedown), plane strain case

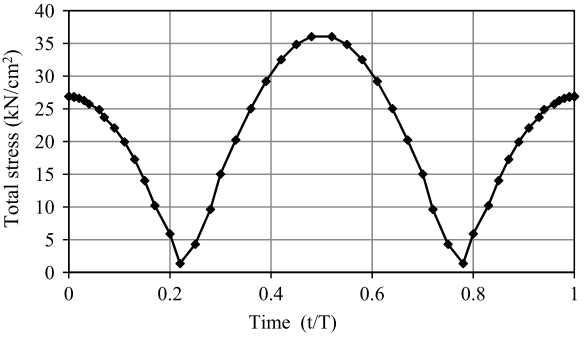

Fig. 12 Effective total stress distribution at GP 2 inside a cycle at steady-state (load case b—shakedown), plane strain case

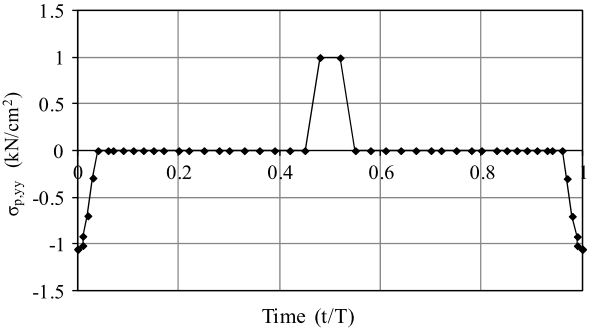

Fig. 13 Predicted cyclic steady-state distribution of the yy component of the stress vector at GP 2 (load case b—alternating plasticity), plane stress case

(c) The third cyclic loading case involves two loads, one constant in time and one varying with time:

$$P_y(t) = 0.5\sigma_y \sin^2(\pi t/T), \qquad P_x(t) = 0.93\sigma_y.$$

This loading, at many cycle points, is above the ratcheting boundary. The results for GP 1, assuming plane strain conditions, may be seen in Fig. 14, where plastic straining of the same positive sign inside the cycle intervals [0, 0.11] and [0.89, 1] at the steady cycle is observed. On the other hand, with a plane stress modeling, one may observe that plastic strains of the same positive sign appear during the whole cycle (Fig. 15). For both cases the xx direction of the component of the excess

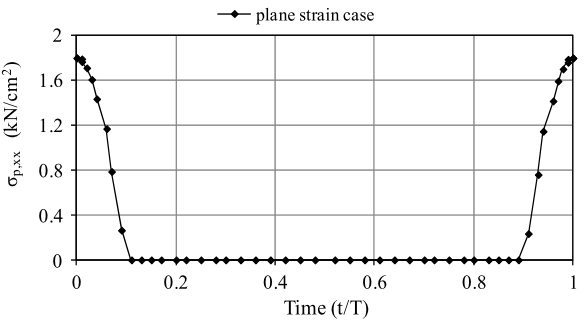

Fig. 14 Predicted cyclic steady-state distribution of the xx component of the stress vector at GP 1 (load case c—ratcheting), plane strain condition

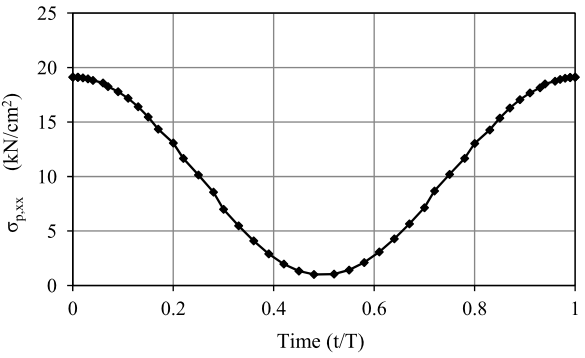

Fig. 15 Predicted cyclic steady-state distribution of the xx component of the stress vector at GP 1 (load case c—ratcheting), plane stress condition

stress vector $\boldsymbol{\sigma}_p^{\mathrm{cs}}$, which has the biggest values from the three components, is plotted. This ratcheting behavior is observed also for quite a few GPs around the structure, which definitely constitutes incremental collapse mechanisms for both plane strain and plane stress conditions that may be seen in Figs. 16, 17 respectively. We may observe that we have a much more spreading of ratcheting for the case of plane stress than for the case of plane strain.

In Fig. 18 one may see the convergence of the RSDM for this loading case, for both plane stress and plain strain conditions.

Reviewing the examples considered herein, we note that, within the adopted tolerance, the number of iterations ranged from a minimum of 80 for the case of reverse plasticity of the truss example, to a maximum number of 740 for the case of ratcheting of the plate example, under plane strain. The total CPU-time required to solve this last example was just 260 s, using an Intel Core i7 at 2.93 GHz with 4096 MB RAM.

The number of time points inside the cycle should be enough so that it may adequately represent the applied loading. Fifty time points inside the cycle were used for all the examples considered herein. Three terms of the Fourier series were found enough to represent the residual stress decomposition. The RSDM procedure proved to be quite stable, no matter which asymptotic behavior was reached. Another important fact of the computational efficiency of the approach is that the stiffness matrix needs to be decomposed once and for all at the start of the calculations.

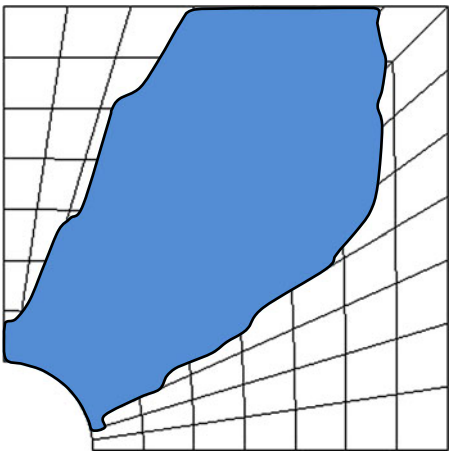

Fig. 16 Ratcheting mechanism—RSDM (plane strain condition)

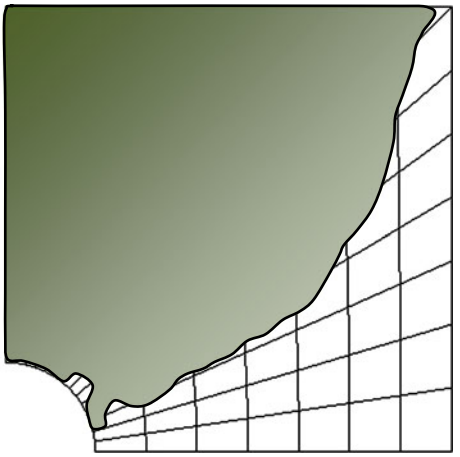

Fig. 17 Ratcheting mechanism—RSDM (plane stress condition)

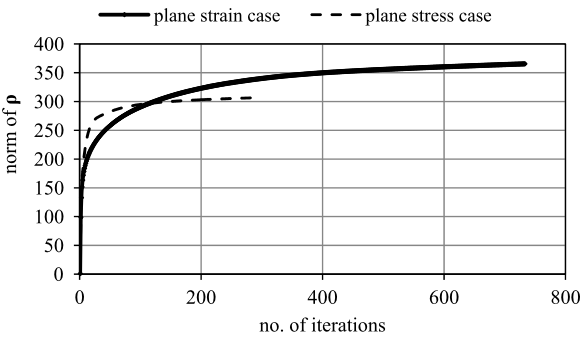

Fig. 18 Convergence of the iterative procedure (load case c)

5 Concluding Remarks

The Residual Stress Decomposition Method (RSDM) is a direct method that proves to be a simple and efficient procedure to estimate the long-term effects of the cyclic loading on a structure. For a given time history of this loading it may equally predict any possible steady state either it is elastic shakedown or alternating plasticity or ratcheting.

The method, although currently developed for elastic-perfectly plastic material and the von Mises yield surface, has the potential of extension to other types of behavior and yield surfaces.

It also appears to have the potential to provide safety margins for a cyclic loading the exact history of which is not known, but only its variation ranges, and work is being done towards this direction.

References

1. Drucker DC (1959) A definition of stable inelastic material. J Appl Mech 26:101–106
2. Melan E (1938) Zur plastizität des räumlichen Kontinuums. Ing-Arch 9:116–126
3. Koiter W (1960) In: Sneddon IN, Hill R (eds) General theorems for elastic-plastic solids. North-Holland, Amsterdam
4. Zouain N, Borges L, Silveira JL (2002) An algorithm for shakedown analysis with nonlinear yield function. Comput Methods Appl Mech Eng 191:2463–2481
5. Simon J-W, Weichert D (2011) Numerical lower bound shakedown analysis of engineering structures. Comput Methods Appl Mech Eng 200:2828–2839
6. Vu DK, Yan AM, Nguyen-Dang H (2004) A primal-dual algorithm for shakedown analysis of structures. Comput Methods Appl Mech Eng 193:4663–4674
7. Zarka J, Frelat J, Inglebert G, Kasmai-Navidi P (1990) A new approach to inelastic analysis of structures. Nijhoff, Dordrecht
8. Ponter ARS, Carter KF (1997) Shakedown state simulation techniques based on linear elastic solutions. Comput Methods Appl Mech Eng 140:259–279
9. Mackenzie D, Boyle T (1993) A method of estimating limit loads by iterative elastic analysis, I: simple examples. Int J Press Vessels Piping 53:77–95
10. Ponter ARS, Chen H (2001) A minimum theorem for cyclic load in excess of shakedown, with application to the evaluation of a ratchet limit. Eur J Mech A, Solids 20:539–553
11. Maitournam MH, Pommier B, Thomas J-J (2002) Détermination de la réponse asymptotique d'une structure anélastique sous chargement thermomécanique cyclique. C R, Méc 330:703–708
12. Abaqus 6.10, theory & user's manual, Dassault systèmes (2010)
13. Spiliopoulos KV, Panagiotou KD (2012) A direct method to predict cyclic steady states of elastoplastic structures. Comput Methods Appl Mech Eng 223–224:186–198
14. Spiliopoulos KV (2000) Simplified methods for the steady state inelastic analysis of cyclically loaded structures. In: Weichert D, Maier G (eds) Inelastic analysis of structures under variable loads. Kluwer Academic, Dordrecht, pp 213–232
15. Gokhfeld DA, Cherniavsky OF (1980) Limit analysis of structures at thermal cycling. Sijthoff & Noordhoff, Rockwille

16. Frederick CO, Armstrong PJ (1966) Convergent internal stresses and steady cyclic states of stress. J Strain Anal 1:154–169
17. Simo JC, Hughes TJR (1998) Computational inelasticity. Springer, Berlin
18. Palizzolo L (2004) Optimal design of trusses according to a plastic shakedown criterion. J Appl Mech 71:240–246
19. Chen HF, Ponter ARS (2001) Shakedown and limit analyses for 3-D structures using linear matching method. Int J Press Vessels Piping 78:443–451

Use of Layout Optimization to Solve Large-Scale Limit Analysis and Design Problems

Matthew Gilbert, Colin C. Smith, Samuel J. Hawksbee, and Andrew Tyas

Abstract Direct methods can be used to rapidly verify the safety of solid bodies and structures against collapse, and also to assist engineers wishing to rapidly identify structurally efficient designs for a specified load carrying capacity. *Layout optimization* is a direct method that can be used to solve very large-scale problems when adaptive solution schemes are employed, and the same underlying mathematical formulation is applicable to both analysis and design problems. Here the *truss layout optimization* formulation is applied to various benchmark design problems and the *discontinuity layout optimization* formulation applied to various plane strain limit analysis problems. It is observed that highly accurate solutions can be obtained, close to known analytical solutions. Finally future directions in the field of layout optimization are briefly considered.

1 Introduction

To verify the safety of solid bodies and structures against collapse, engineers have traditionally had to rely either on simplistic hand type calculations, or on significantly more complex computational tools which identify the collapse state in an indirect, iterative, manner. Such computational tools can be unreliable and often require large amounts of computer time and/or high levels of operator expertise. Additionally, in many engineering disciplines the initial design stage is carried out in an ad-hoc manner, with 'engineering intuition' often used to identify structurally

M. Gilbert (✉) · C.C. Smith · S.J. Hawksbee · A. Tyas
Department of Civil and Structural Engineering, University of Sheffield, Mappin Street, Sheffield S1 3JD, UK
e-mail: m.gilbert@sheffield.ac.uk

C.C. Smith
e-mail: c.c.smith@sheffield.ac.uk

S.J. Hawksbee
e-mail: s.hawksbee@sheffield.ac.uk

A. Tyas
e-mail: a.tyas@sheffield.ac.uk

K. Spiliopoulos, D. Weichert (eds.), *Direct Methods for Limit States in Structures and Materials*, DOI 10.1007/978-94-007-6827-7_8,

efficient designs. Direct analysis and design methods can potentially address both these issues, and similarities between analysis and design formulations can be exploited. Thus for example, a general integrated analysis and design framework has been recently developed at the University of Sheffield, allowing a range of potential applications to be explored. Highly efficient interior point linear programming (LP) solvers are used in conjunction with an adaptive solution scheme to allow large-scale problems to be solved.

A focus on both analysis and design problems also permits similarities in the underlying mathematical formulations to be studied in more detail. This led the authors to realize that the *truss layout optimization* design technique, developed almost half a century ago [5], could be modified so as to provide a powerful new direct analysis method for plasticity problems: *discontinuity layout optimization* [27]. In this chapter, both these direct methods will be described, with a simple adaptive solution scheme used to allow large-scale problems to be treated. The research has led to industrial applications (e.g. [6]), and the highly accurate solutions that can be obtained has allowed new analytical solutions to be identified for old problems.

2 Adaptive Solution Scheme

In the context of direct methods, an adaptive solution scheme entails initially solving a simplified 'reduced' problem and then successively adding (or modifying) variables and/or constraints to improve the solution (sometimes termed '*column generation*' or '*cut generation*' in the context of LP [2]). It might be argued that the use of an adaptive solution scheme impinges on the 'directness' of a direct method, since iteration is required; however in reality iteration is required in almost all numerical solution schemes (e.g. interior point methods[1] involve iteration [31]) and the purpose of the solution scheme presented here is simply to increase the size of limit analysis and design problems that can be solved using available computational resources.

2.1 Basic Algorithm

Before considering concrete examples, the basic adaptive solution algorithm used herein will be stated:

1. Formulate initial *reduced* problem.
2. Obtain a solution to the reduced problem using LP.
3. Loop through each element, checking for violations. Record violations in a list.

[1]Note that adaptive model refinement procedures will generally be most effective when interior point methods are used. This is because the collapse fields generated are more 'physically correct' [1] than when extreme-point methods, such as the traditional Simplex method, are used.

4. Sort list to identify largest violations, and use these to refine the reduced problem.
5. Repeat from step 2 until the violation list is empty.

The 'violations' listed in step 3 may be violations of a yield surface or perhaps violation of a virtual strain limit in the case of a truss layout optimization problem.

2.2 Example: Stability of Rigid Blocks

To illustrate how an adaptive solution scheme can be applied, the centuries old problem of assessing the stability of assemblages of rigid blocks will initially be considered. Such problems have been considered in the context of masonry structures by workers throughout history, notably Coulomb [15], and more recently Heyman [14] and Livesley [20]. A characteristic of these problems is the presence of discontinuities in pre-defined locations (i.e. at the joints), so that assessing their stability is much simpler, at least from a limit analysis perspective, than comparable continuum problems. However, behaviour at discontinuities may be non-linear, potentially making obtaining a numerical solution time-consuming, unless an adaptive solution scheme is employed.

Several rigid block formulations have been proposed; here a simple equilibrium formulation similar to that first proposed by Livesley [20] will be presented.

2.2.1 Standard Equilibrium Formulation

Consider a weakly bonded assemblage of rigid blocks, comprising n blocks and m discontinuities between blocks. With the equilibrium limit analysis formulation the usual goal is to establish the maximum factor λ on one or more live loads in the system subject to equilibrium and yield constraints:

$$\max \lambda$$

subject to:

$$\mathbf{B}\mathbf{q} - \lambda \mathbf{f}_{\mathrm{L}} = \mathbf{f}_{\mathrm{D}}, \tag{1}$$

$$\mathbf{N}^T \mathbf{q} \leq \mathbf{g},$$

where $\mathbf{B}$ is a $(3n \times 3m)$ equilibrium matrix and $\mathbf{q}$ and $\mathbf{f}$ are respectively $3m$ and $3n$ vectors of forces at discontinuities and block loads. Also $\mathbf{q}^T = \{N_1, M_1, S_1, N_2, M_2, S_2, \ldots, N_m, S_m, M_m\}$ and where N_i, M_i and S_i are respectively the normal force, shear force and moment acting at discontinuity i $(i = 1 \ldots m)$, $\mathbf{f} = \mathbf{f}_{\mathrm{D}} + \lambda \mathbf{f}_{\mathrm{L}}$, where $\mathbf{f}_{\mathrm{D}}$ and $\mathbf{f}_{\mathrm{L}}$ are respectively vectors of dead and live loads acting on blocks. $\mathbf{N}$ and $\mathbf{g}$ depend on the adopted yield criteria, which for an individual discontinuity i can be expressed as follows:

$$\mathbf{N}_i^T \mathbf{q}_i \leq \mathbf{g}_i \tag{2}$$

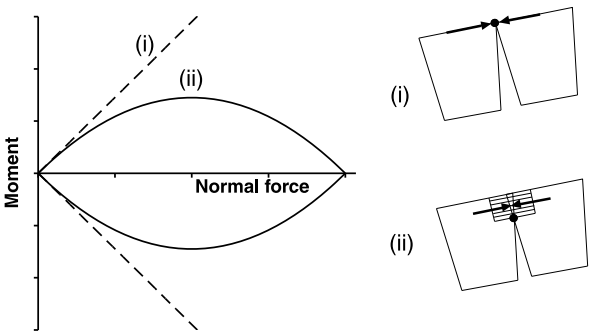

Fig. 1 Adaptive solution example: (i) linear and (ii) non-linear yield criteria

or, in expanded form for a joint where friction and/or rocking failure may occur as:

$$\begin{bmatrix} 1 & \tan\phi_i & 0 \\ -1 & \tan\phi_i & 0 \\ 0 & l_i/2 & 1 \\ 0 & l_i/2 & -1 \end{bmatrix} \begin{bmatrix} S_i \\ N_i \\ M_i \end{bmatrix} \leq \begin{bmatrix} 0 \\ 0 \\ 0 \\ 0 \end{bmatrix} \tag{3}$$

where l_i represents the length of each discontinuity, which is assumed to have angle of friction ϕ_i. The LP variables are therefore the discontinuity forces S_i, N_i and M_i and the live load factor λ.

2.2.2 Example: Modelling Compressive Failure at Hinge Points

A practical limitation of the standard equilibrium formulation of Eq. (1) is that it is implicitly assumed that the constituent blocks are rigid and incompressible, such that hinging of two adjacent blocks about an extreme point is possible. In $N - M$ space the corresponding yield criteria is labelled (i) in Fig. 1, whereas more realistic behaviour, which corresponds to a compressive stress block of finite depth, is labelled (ii).

This kind of problem would traditionally have been approached by adopting a piecewise linear approximation of the non-linear yield criteria, with perhaps 12, 24 or even 48 planes used to circumscribe the yield surface. More recently, use of second order cone programming has been favoured for problems which can be expressed in this form (e.g. [21]). However, an alternative is to use 'cut generation' to iteratively refine the yield surface. This has the advantage that: (i) only LP needs to be used to obtain a solution, and (ii) it is comparatively computationally inexpensive (a solution can typically be obtained in only a few iterations). Furthermore, as will be evident, the same basic approach can if necessary also be applied to more complex, non-convex, problems.

Figure 2 shows a solution obtained for a three span masonry arch railway bridge; the computed compressive stress block depths are indicated on the figure. To obtain a solution, additional constraints were added at each iteration in the adaptive

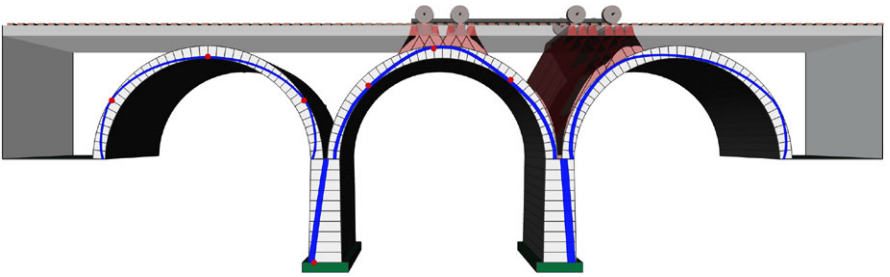

Fig. 2 Adaptive solution example: hinged failure mechanism of three span masonry viaduct

solution scheme. In this case three iterations were required to obtain a solution of the required accuracy, and the peak number of yield constraints required was less than 500. In contrast had 24 fixed planes been used to circumscribe the yield surface the number of yield constraints involved would have exceeded 3000, and the accuracy of the solution would have been lower. (The analysis was undertaken using the LimitState:RING software [18].)

2.2.3 Example: Modelling Non-associated Friction

As mentioned earlier, the same basic algorithm can also be applied to more complex, non-smooth, optimization problems. For example, consider the use of a non-associated friction model between blocks, which is usually considered more physically reasonable than the 'saw-tooth' friction model implicitly associated with Eq. (1).

To achieve this, the yield constraints in $N - S$ space can be rotated to achieve the level of dilatancy required (since 'flow' will always be normal to the yield surface when using an LP formulation), and then successively updated according to the magnitude of the normal force N until a converged solution is obtained. Though the solutions obtained are approximate, and have no formal status within the context of plasticity theory, it has been shown that these are comparable to solutions obtained using much more complex procedures [9], and that large problems can be tackled, as for example illustrated in Fig. 3. (Note that in this case the solution was obtained by changing the positions of existing linear yield constraints, rather than by adding new linear yield constraints.)

3 Layout Optimization of Trusses

Truss layout optimization involves finding the most efficient arrangement of truss bars capable of transmitting a given load or loads to defined support points. In the classical 'ground structure' method [5], the design domain is discretized with nodes

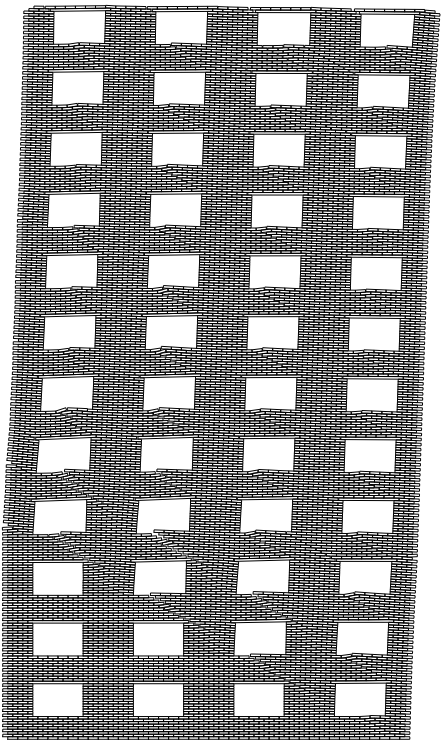

Fig. 3 Adaptive solution example: collapse of wall modelled with non-associated friction and subject to in-plane pseudo-static seismic load, after [9]

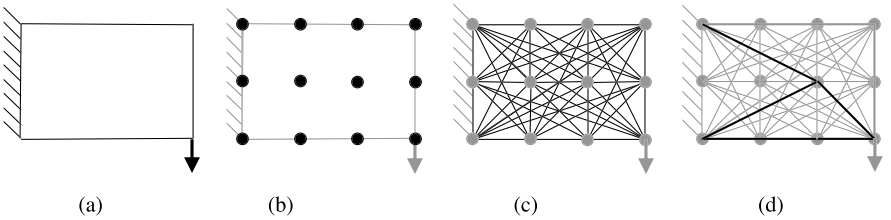

Fig. 4 Stages in truss layout optimization procedure: (**a**) starting problem (point load applied remote from support); (**b**) discretization of design domain using nodes; (**c**) interconnection of nodes with potential truss bars; (**d**) identification of optimal subset of potential bars using optimization (giving the optimal truss layout)

interconnected by bars, from which an optimal arrangement can subsequently be found. Stages in the procedure are indicated in Fig. 4.

The simplest design objective is to minimise the total volume (or mass) of the truss, whilst ensuring equilibrium is satisfied at each node, and also ensuring that limiting stresses in each bar are not exceeded. This is often termed the 'fully stressed' (or 'plastic') layout optimization problem, which can be solved using LP; the formulation will be outlined in the next section.

3.1 Truss Optimization: Mathematical Formulations

Consider a planar design domain which is discretized using n nodes and m potential connections (truss bars). The classical 'equilibrium' plastic truss layout optimization formulation for a single load case is defined in Eq. (4) as follows:

$$\min V = \mathbf{c}^T \mathbf{q}$$

subject to:

$$\mathbf{B}\mathbf{q} = \mathbf{f}, \tag{4}$$

$$\mathbf{q} \geq \mathbf{0},$$

where V is the total volume of the structure, $\mathbf{q}^T = \{q_1^+, q_1^-, q_2^+, q_2^-, \ldots, q_m^-\}$, and q_i^+, q_i^- are the tensile and compressive internal forces in bar i $(i = 1 \ldots m)$; $\mathbf{c}^T = \{l_1/\sigma_1, l_1/\sigma_1, l_2/\sigma_2, l_2/\sigma_2, \ldots, l_m/\sigma_m\}$, where l_i and σ_i are respectively the length and yield stress of bar i. $\mathbf{B}$ is a suitable $(2n \times 2m)$ equilibrium matrix and $\mathbf{f}^T = \{f_1^x, f_1^y, f_2^x, f_2^y, \ldots, f_n^y\}$ where f_j^x and f_j^y are the x and y components of the external load applied to node j $(j = 1 \ldots n)$. The presence of supports at nodes can be accounted for by omitting the relevant terms from $\mathbf{f}$, together with the corresponding rows from $\mathbf{B}$. This problem is in a form which can be solved using LP, with the bar forces in $\mathbf{q}$ being the LP variables.

An equivalent kinematic formulation can be derived using duality principles:

$$\max V = \mathbf{f}^T \mathbf{u} \tag{5}$$

subject to:

$$\mathbf{B}^T \mathbf{u} \leq \mathbf{c} \tag{6}$$

where $\mathbf{u}^T = \{u_1^x, u_1^y, u_2^x, u_2^y, \ldots, u_n^y\}$, and where u_j^x and u_j^y are the x and y components of the virtual displacements of node j. In this case the nodal displacements in $\mathbf{u}$ are the LP variables.

3.2 Adaptive Solution Scheme for Trusses

For the aforementioned truss optimization procedure to produce accurate results, it is essential that a bar connection can be made between any pair of nodes (using the prescribed nodal discretization). This is because if a partially connected ground structure is employed then a non-optimal solution may be identified, as demonstrated in Fig. 5. Unfortunately, the number of bars in a 'fully-connected' problem comprising n nodes, will be $n(n-1)/2$, which means that the problem becomes intractable for only moderately large problems. For example, a 2D problem with a square design domain discretized using 100×100 nodes would generate a total

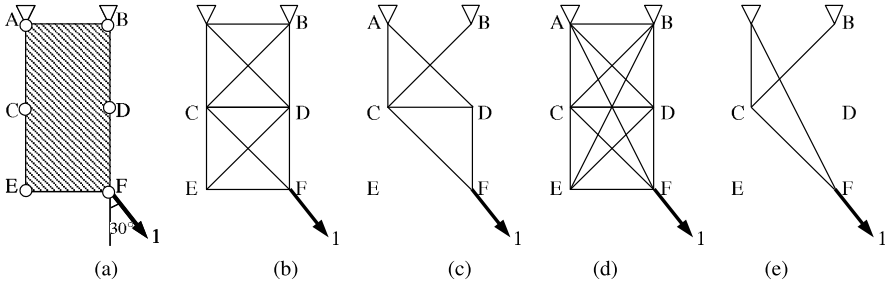

Fig. 5 Simple truss layout optimization problem (after [7]): (**a**) design domain [1 unit × 2 units], loading and support conditions; (**b**) minimal connectivity ground structure containing 11 bars; (**c**) optimal solution for ground structure [b], volume = 3.36603; (**d**) full connectivity ground structure containing 15 bars, including overlapping bars; (**e**) optimal solution for ground structure [d], volume = 2.63397 (limiting compressive and tensile strengths taken as unity)

of approx. 100 million LP variables when using the formulation given in Eq. (4), which would be difficult to solve directly using a standard desktop PC.

Thus referring to the basic adaptive algorithm described in Sect. 2.1, it is desirable to commence with an initial problem which has limited initial connectivity (Step 1), and to then use violation of the dual constraint, Eq. (6), in Step 3 as a means of producing a list of additional bars likely to improve the solution (Step 4). The procedure continues (Step 4→Step 2) until the violation list is empty. The final solution is provably equal in terms of volume to that which would have been obtained had the corresponding fully connected ground structure problem been solved instead; further details are provided in [7].

3.3 Example: Point Load Between Pin/Roller Supports

To illustrate the adaptive solution scheme in the context of truss layout optimization, a problem first studied by Michell [22] was considered in [8]. The problem comprises a 2×1 design domain discretized using 30×15 nodal divisions. A fixed pin is present at the lower left corner and a pin and roller (free in the x direction) is present at the lower right corner. A unit point load is applied centrally at the bottom of the domain and the allowable stresses in compression and tension are both taken as unity. The fully connected ground structure for this domain would have over 122,760 frame bars. Instead, using the adaptive solution scheme described, the initial ground structure has only adjacent connectivity, with 1845 frame bars. At each iteration the number of bars which can be added is for efficiency here limited to 10 % of those present in the initial ground structure, with those most violating Eq. (6) having priority for admission during a given iteration.

Figures 6(a)–(l) show the optimal solutions for each successively expanded ground structure. The final solution, shown in Fig. 6(l) is identical to that obtained

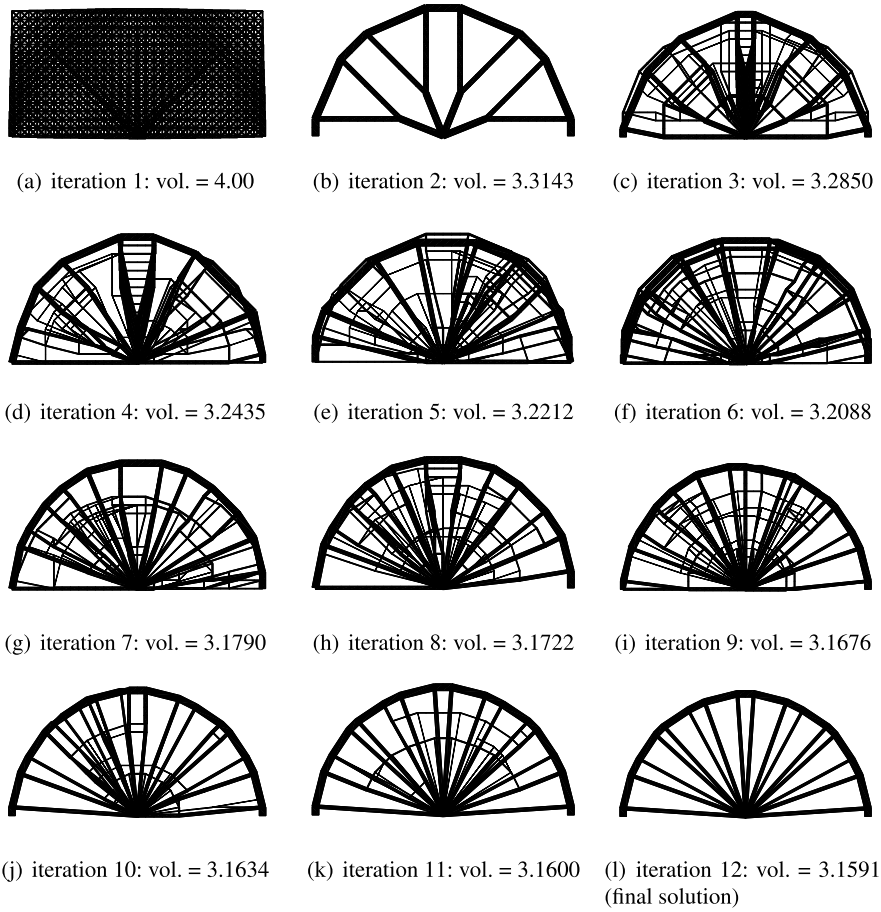

(a) iteration 1: vol. = 4.00 (b) iteration 2: vol. = 3.3143 (c) iteration 3: vol. = 3.2850

(d) iteration 4: vol. = 3.2435 (e) iteration 5: vol. = 3.2212 (f) iteration 6: vol. = 3.2088

(g) iteration 7: vol. = 3.1790 (h) iteration 8: vol. = 3.1722 (i) iteration 9: vol. = 3.1676

(j) iteration 10: vol. = 3.1634 (k) iteration 11: vol. = 3.1600 (l) iteration 12: vol. = 3.1591 (final solution)

Fig. 6 Point load between pin/roller supports example: optimal layouts at each iteration in the adaptive solution procedure (after [8])

when an initially fully connected ground structure is used but the computational effort required is considerably less. Additionally, when adaptivity was used, the peak number of LP variables present was 5766, compared with 245,520 when an initially fully connected ground structure was employed.

3.4 Example: Point Load Between Fixed Pins

Here all design parameters are identical to those in the previous example problem except that both supports are now fixed pins and the design domain has a much finer nodal discretization, using 180×180 nodal divisions, with half the nodal spacing in the y direction. This corresponds to a fully connected ground structure containing

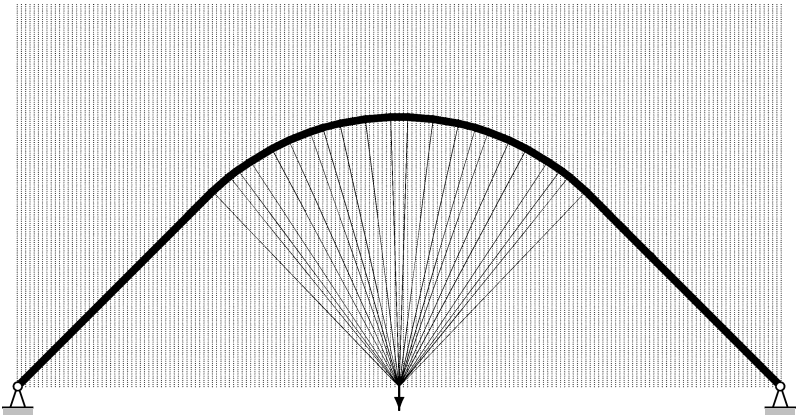

Fig. 7 Point load between fixed pins example: 180 × 180 nodal division solution (after [8])

over 526 million potential members. The reported optimal volume of 2.57176 [8] is just 0.037 % higher than the known exact value of $1 + \pi/2$. The solution is shown in Fig. 7; this problem took approximately 15 hours to solve when using hardware available in 2003 [8], and is still computationally intractable today when using a fully connected ground structure.

3.5 Example: Uniform Load Between Fixed Pins

The primary focus of researchers in the field of structural optimization over the past few decades has been on problems involving point loads. For example, cantilevers with tip loads have been especially popular (e.g. see [17]), and more recently the 'three forces problem' has attracted interest, e.g. see [28].

However, problems involving uniformly distributed loads are often of practical interest, and were considered in the 1970s by Hemp [13] and his co-workers at Oxford. A key issue is that obtaining analytical solutions for any 'Michell truss' problem is generally already difficult, but more so when uniform loads are present. Fortunately the precision of the solutions now obtainable using layout optimization is such that they can now be used to help identify new analytical solutions, or to check the range of applicability of existing ones.

Thus the uniform load between fixed pins problem originally considered by Hemp [13] has recently been revisited numerically (after Pichugin et al. [23]). Figure 8(a) shows a numerical solution for the problem (comprising 180 × 252 nodal divisions, and involving approx. 1.048×10^9 potential truss bars). By considering various ratios of limiting tensile and compressive stresses it was found that the original analytical solution proposed by Hemp, which was known not to be optimal in general, is in fact optimal when the limiting compressive and tensile stresses are *unequal*, provided the ratio of limiting tensile to compressive stresses falls below a certain threshold value (0.417785). This solution is shown in Fig. 8(b).

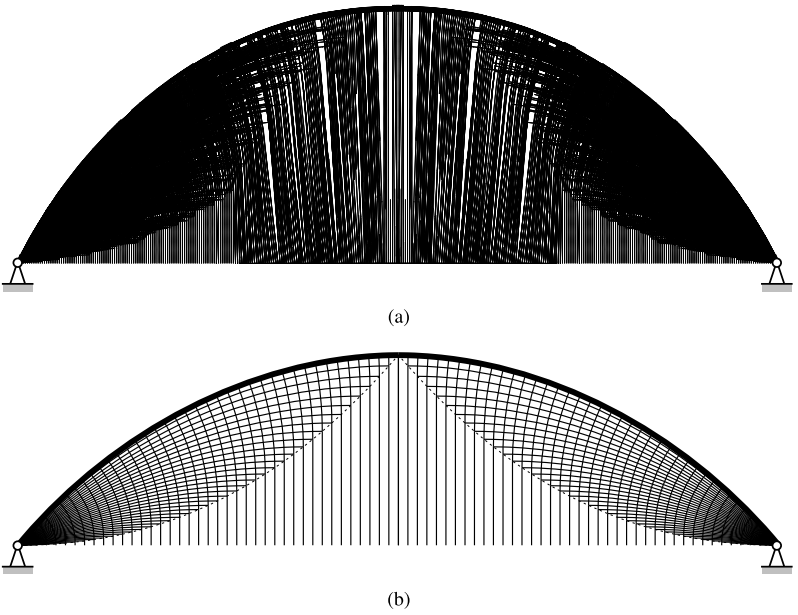

(a)

(b)

Fig. 8 Uniform load between fixed pins example: (**a**) numerical solution for $\sigma^+ = \sigma^-$ case; (**b**) exact analytical solution for $\sigma^+ = 0.417785\sigma^-$ case (limiting ratio for vertical hangers) (after [23])

3.6 Example: Uniform Transmissible Load Between Fixed Pins

The final example provides perhaps the clearest indication of the power of truss layout optimization techniques, showing that the technique can be used in 'scientific discovery'. The example is essentially identical to the preceding one except that the uniform loads are now free to migrate vertically to their optimal point of application (so-called 'transmissible' loading). Although this type of loading requires a slight change to the formulation (i.e. modification of Eq. (4)), it can still be treated using LP (see [4] for details).

When a layout optimization is performed the outcome is surprising. Whereas it might be expected that the optimal form is a parabolic arch (or suspended cable), a form first identified by Christiaan Huygens in the 17th century, in fact a more complex structure, comprising a central parabolic section and networks of truss bars in the haunch regions, is identified. The corresponding optimal volume is marginally less than that of the optimal parabolic arch (0.3425 % less when using 41,783 nodes and 530,712,246 potential bars [4]). It was subsequently found that a parabolic arch could be identified, but only when the limiting tensile stress was prescribed to be significantly less than the limiting compressive stress (the numerical solution was in this case within 0.0071 % of the volume of the optimal parabola).

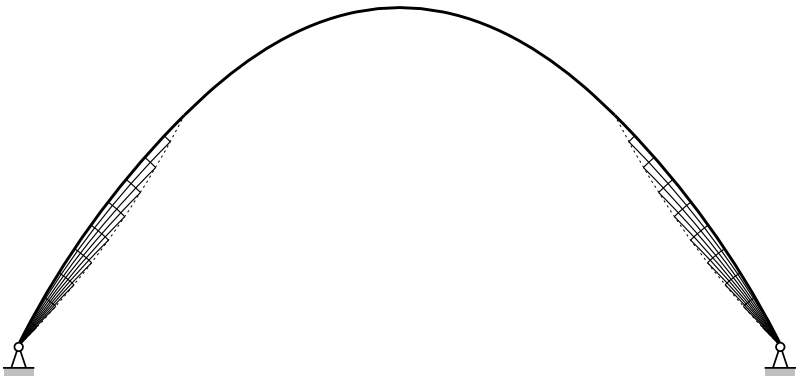

Fig. 9 Uniform transmissible load between fixed pins example: analytical solution [30]

Significantly, the numerical solution obtained provided the stimulus to explore this problem analytically. The exact analytical solution, found to be 0.3495 % lighter than the lightest parabolic arch, is shown in Fig. 9 (after [30]).

Whilst the examples of 'trusses' shown here are primarily of academic interest, in that the optimal structures are highly refined discrete versions of optimal continua, the approach offers two important practical applications. Firstly, the layout optimization approach can quickly and accurately establish an absolute minimum volume for a given problem. Secondly, it is possible, without losing the linear character of the problem, to change the formulation to include practical considerations, such as joint penalties to simplify the structure, the use of multiple load cases, or the inclusion of stability load cases to ensure that the optimal structure is not in unstable equilibrium (e.g. see [29]).

4 Discontinuity Layout Optimization

Smith and Gilbert [27] observed that there existed an analogy between the optimal layout of truss bars in a 2D truss structure and the optimal layout of slip-line discontinuities in a plane strain plastic collapse mechanism, assuming a weightless Tresca material was involved. This led to the formulation of a new limit analysis procedure, termed 'discontinuity layout optimization' (DLO) [27].

4.1 Discontinuity Layout Optimization: Kinematic Formulation

The kinematic form of the DLO equations can be presented as follows:

$$\min \lambda \mathbf{f}_{\mathrm{L}}^{T}\mathbf{d} = -\mathbf{f}_{\mathrm{D}}^{T}\mathbf{d} + \mathbf{g}^{T}\mathbf{p} \tag{7}$$

subject to:

$$\mathbf{Bd} = \mathbf{0}, \tag{8}$$

$$\mathbf{Np} - \mathbf{d} = \mathbf{0}, \tag{9}$$

$$\mathbf{f}_{\mathrm{L}}^{T}\mathbf{d} = 1, \tag{10}$$

$$\mathbf{p} \geq \mathbf{0} \tag{11}$$

where λ is the unknown load factor at collapse, $\mathbf{f}_{\mathrm{D}}$ and $\mathbf{f}_{\mathrm{L}}$ are vectors containing respectively specified dead and live loads acting at discontinuities, $\mathbf{d}$ contains displacements along the discontinuities, $\mathbf{p}$ is a vector of plastic multipliers and $\mathbf{g}$ contains the corresponding dissipation coefficients. $\mathbf{B}$ is a suitable compatibility matrix containing direction cosines and $\mathbf{N}$ is a suitable flow matrix.

Though this formulation has similarities with the corresponding truss optimization formulation, it also includes additional terms that are not directly analogous. These include live and dead loads in Eq. (7), a flow rule in Eq. (9) that permits modelling of frictional problems, and a term to exclude trivial zero solutions, Eq. (10).

For a typical translational cohesive-frictional plane-strain plastic analysis problem: $\mathbf{d}^T = \{\mathbf{d}_1^T, \mathbf{d}_2^T, \ldots, \mathbf{d}_m^T\} = \{s_1, n_1, s_2, n_2, \ldots, n_m\}$, where s_i and n_i are the relative shear and normal displacements at discontinuity i; $\mathbf{g}^T = \{c_1 l_1, c_1 l_1, c_2 l_2, \ldots, c_m l_m\}$, where l_i and c_i are respectively the length and cohesive shear strength of discontinuity i.

In the same way that force equilibrium is enforced at nodes for the truss optimization problem, kinematic compatibility is enforced at the nodes in DLO as illustrated in Figs. 10 and 11, where α_i and β_i are respectively x-axis and y-axis direction cosines for truss bar or discontinuity i. Thus the contribution of a given discontinuity i to the global compatibility constraint Eq. (8) can be written as:

$$\mathbf{B}_i\mathbf{d}_i = \begin{bmatrix} \alpha_i & -\beta_i \\ \beta_i & \alpha_i \\ -\alpha_i & \beta_i \\ -\beta_i & -\alpha_i \end{bmatrix} \begin{bmatrix} s_i \\ n_i \end{bmatrix}. \tag{12}$$

Similarly, when the Mohr-Coulomb failure criteria is used the local plastic flow constraint for discontinuity i can be written as:

$$\mathbf{N}_i\mathbf{p}_i - \mathbf{d}_i = \begin{bmatrix} 1 & -1 \\ \tan\phi_i & \tan\phi_i \end{bmatrix} \begin{bmatrix} p_i^1 \\ p_i^2 \end{bmatrix} - \begin{bmatrix} s_i \\ n_i \end{bmatrix} = 0 \tag{13}$$

where $\mathbf{N}_i$ is a local plastic flow matrix, $\mathbf{p}_i$ is a vector containing plastic multipliers p_i^1, p_i^2, where p_i^1, $p_i^2 \geq 0$, and where ϕ_i is the angle of friction of the material.

The discontinuity displacements in $\mathbf{d}$ and the plastic multipliers in $\mathbf{p}$ are the variables in the optimization problem, which can be solved using LP when the Tresca or Mohr-Coulomb failure criteria are used.

Stages in the DLO procedure are outlined diagrammatically in Fig. 12. In the kinematic formulation compatibility at nodes is *explicitly* enforced. However, when discontinuities crossover one another at non-nodal points, it can be shown that compatibility is *implicitly* enforced.

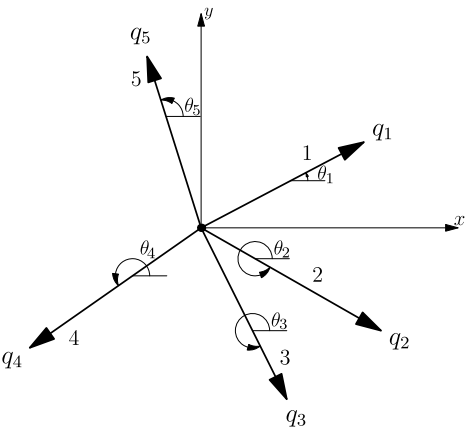

Fig. 10 Equilibrium at (unloaded) node in a truss (see Eq. (4)). $\sum_{i=1}^{5} \alpha_i q_i = 0$, $\sum_{i=1}^{5} \beta_i q_i = 0$

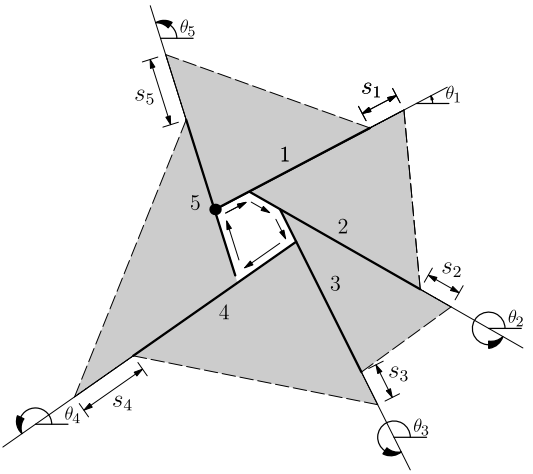

Fig. 11 Compatibility at a node in a sliding mechanism (translation only, see Eq. (8)). $\sum_{i=1}^{5} \alpha_i s_i = 0$, $\sum_{i=1}^{5} \beta_i s_i = 0$

4.2 Body Forces

Body forces that arise in plane strain limit analysis problems have no obvious analogy in truss optimization problems. However they may readily be included in the problem formulation [11, 26, 27]. For example, the body force contribution made by discontinuity (slip-line) i to the $\mathbf{f}_\mathrm{D}$ term in Eq. (7) due to horizontal and vertical accelerations a_x and a_y respectively, can be written as follows:

$$\mathbf{f}_{\mathrm{D}i}^{T}\mathbf{d}_i = \left\{ a_y m_i \begin{bmatrix} \beta_i & \alpha_i \end{bmatrix} + a_x m_i \begin{bmatrix} \alpha_i & -\beta_i \end{bmatrix} \right\} \begin{bmatrix} s_i \\ n_i \end{bmatrix} \tag{14}$$

where m_i is the total mass of material lying vertically above slip-line i. The left and right hand terms in the curly brackets represents the work done by the vertical and

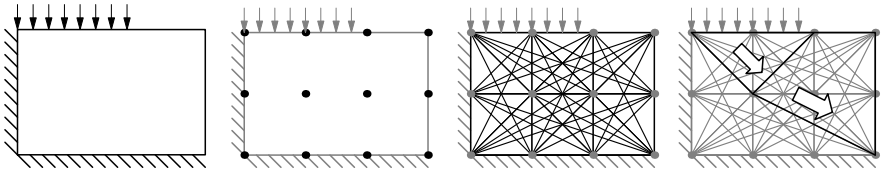

Fig. 12 Stages in DLO procedure: (**a**) starting problem (surcharge applied to block of soil close to a vertical cut); (**b**) discretization of soil using nodes; (**c**) interconnection of nodes with potential discontinuities; (**d**) identification of critical subset of potential discontinuities using optimization (giving the layout of slip-lines in the critical failure mechanism) (after [10])

horizontal movements of material lying vertically above the slip-line. (A vertical strip has been chosen arbitrarily; the actual direction does not matter as long as it is consistent throughout the problem. Also, for conventional plastic collapse problems subjected to gravity, $a_x = 0$ and $a_y = -g$, where g is the acceleration due to gravity.)

4.3 Discontinuity Layout Optimization: Equilibrium *Formulation*

Duality principles can be used to derive the dual of Eqs. (7) to (11), which is an *equilibrium* formulation. Thus for a planar body discretized using m nodal connections (slip-line discontinuities) and n nodes this may be stated as follows [27]:

$$\max \lambda \tag{15}$$

subject to:

$$\mathbf{B}^T\mathbf{t} + \lambda\mathbf{f}_\mathrm{L} - \mathbf{q} = -\mathbf{f}_\mathrm{D}, \tag{16}$$

$$\mathbf{N}^T\mathbf{q} \leq \mathbf{g} \tag{17}$$

where $\mathbf{t}^T = \{t_1^x, t_1^y, t_2^x, t_2^y, \ldots, t_n^y\}$ and where t_j^x and t_j^y can be interpreted as x and y direction equivalent nodal forces acting at node j ($j = 1 \ldots n$), corresponding in a work sense to u_j^x and u_j^y respectively, and where $\mathbf{q}$ is here a vector of shear and normal forces acting on discontinuities, i.e. $\mathbf{q}^T = \{S_1, N_1, S_2, N_2, \ldots, N_m\}$, where S_i and N_i represent respectively the shear and normal force acting on discontinuity i ($i = 1 \ldots m$). The LP variables are therefore t_j^x, t_j^y, S_i, N_i and the live load factor λ. The objective is thus to maximize λ whilst ensuring that the yield condition is not violated along any potential discontinuity.

The required equilibrium constraint can alternatively be written for a potential discontinuity i interconnecting nodes A and B as follows:

$$\mathbf{B}_i^T\mathbf{t}_i + \lambda\mathbf{f}_{\mathrm{L}i} - \mathbf{q}_i = -\mathbf{f}_{\mathrm{D}i} \tag{18}$$

or, in expanded form as:

$$\begin{bmatrix} \alpha_i & \beta_i & -\alpha_i & -\beta_i \\ -\beta_i & \alpha_i & \beta_i & -\alpha_i \end{bmatrix} \begin{bmatrix} t_A^x \\ t_A^y \\ t_B^x \\ t_B^y \end{bmatrix} + \lambda \begin{bmatrix} f_{\mathrm{L}i}^{\mathrm{s}} \\ f_{\mathrm{L}i}^{\mathrm{n}} \end{bmatrix} - \begin{bmatrix} S_i \\ N_i \end{bmatrix} = - \begin{bmatrix} f_{\mathrm{D}i}^{\mathrm{s}} \\ f_{\mathrm{D}i}^{\mathrm{n}} \end{bmatrix}. \tag{19}$$

The required yield constraint can also be written for a potential discontinuity i as follows:

$$\mathbf{N}_i^T \mathbf{q}_i \leq \mathbf{g}_i \tag{20}$$

or, in expanded form for the Mohr-Coulomb yield condition as:

$$\begin{bmatrix} 1 & \tan\phi_i \\ -1 & \tan\phi_i \end{bmatrix} \begin{bmatrix} S_i \\ N_i \end{bmatrix} \leq \begin{bmatrix} c_i l_i \\ c_i l_i \end{bmatrix} \tag{21}$$

where here tensile forces are taken as positive.

Duality principles mean that values for t_j^x, t_j^y, S_i and N_i are available even if the primal problem is actually formulated and solved. Thus the required yield constraint Eq. (21) can easily be checked for a potential discontinuity i which is not presently represented in the current LP problem. The yield constraint is checked by firstly rearranging Eq. (19) so that the shear and normal force acting on the potential discontinuity between nodes A and B can be obtained from the solution of the last LP problem, using values of the internal nodal forces t_A^x, t_A^y, t_B^x, t_B^y and load factor λ:

$$\begin{bmatrix} \tilde{S}_i \\ \tilde{N}_i \end{bmatrix} = \begin{bmatrix} \alpha_i & \beta_i & -\alpha_i & -\beta_i \\ -\beta_i & \alpha_i & \beta_i & -\alpha_i \end{bmatrix} \begin{bmatrix} t_A^x \\ t_A^y \\ t_B^x \\ t_B^y \end{bmatrix} + \lambda \begin{bmatrix} f_{\mathrm{L}i}^{\mathrm{s}} \\ f_{\mathrm{L}i}^{\mathrm{n}} \end{bmatrix} + \begin{bmatrix} f_{\mathrm{D}i}^{\mathrm{s}} \\ f_{\mathrm{D}i}^{\mathrm{n}} \end{bmatrix} \tag{22}$$

where $\tilde{S}_i$ and $\tilde{N}_i$ are identical to S_i and N_i respectively, except that they are not LP variables. Using the newly computed values of $\tilde{S}_i$ and $\tilde{N}_i$, the yield constraint Eq. (21) can be checked for violation for the potential discontinuity. When using an adaptive solution scheme, this checking process can be repeated at each iteration for all potential discontinuities, with any violating discontinuities becoming candidates for admission to the expanded LP problem at the next iteration (i.e. in step 3 of the adaptive solution scheme presented in Sect. 2.1).

4.4 Example Problems

To illustrate the accuracy and range of applicability of the DLO procedure, this will now be applied to various example problems.

4.4.1 Punch Indentation of a Block of Finite Depth

Consider a block of Tresca material of depth h and strength k resting on smooth base and indented by a flat punch of width $2a$, where the block has a finite width $\gg 2a$. Chakrabarty [3] has solved this problem over a range of h/a ratios using slip-line fields. For $h/a < 4.77$, Chakrabarty's slip-line solutions are of the form presented in Fig. 13(a) (also showing the problem geometry). For $h/a > 8.77$, the Prandtl mechanism becomes critical and the average bearing pressure q remains at $k(2+\pi)$ with increasing h/a. A comparative study over the full range of h/a ratios considered by [3] has been undertaken using a commercial software implementation of DLO, LimitState:GEO [19]. A number of models with different h/a ratios have been constructed and solved. Taking advantage of symmetry only the righthand side of the problem domain was considered and the target number of nodes in these models was set at 2000.

For $h/a < 4.77$, good agreement was found between the slip-line fields of [3] and the mechanisms obtained using DLO (see Figs. 13(a) and (b)). For $4.77 < h/a < 8.77$, values of $q/2k$ still compare favourably, but the slip-line fields of [3] and the mechanisms from DLO no longer agree. For $h/a > 8.77$, DLO also identifies the Prandtl mechanism, considered in more detail in the next section. Values of $q/2k$ obtained using DLO also compare favourably with [3] across the full range of h/a ratios, as demonstrated by Fig. 13(c).

4.4.2 Punch Indentation of a Block of infinite Depth

Now consider a block of Tresca material of strength k and infinite depth and indented by a flat punch of width $2a$, where the block is constrained by rigid supports along the left, right and bottom edges. Providing the rigid supports are not too close to the punch, this leads to the well known Prandtl problem. Two scenarios are considered here, the first involving the standard case of a punch applied remote from the rigid supports, the second involving a punch applied adjacent to one of the rigid supports. The latter case is of interest since the problem can be shown to be directly analogous to the truss optimization problem considered in Sect. 3.4. Results for a variety of nodal discretizations are shown in Table 1.

As expected, the results for the punch applied close to the edge of block are identical to those for the centrally applied punch. It is also notable that, even for relatively coarse nodal discretizations, highly accurate results can be obtained (within 1 % of the known analytical solution of $2+\pi$), with the singularities at the edge of the punch automatically identified. Figure 14 shows a sample predicted collapse mechanism, with the rigid blocks of material lying between slip-line discontinuities identified and then displaced to aid interpretation.

4.4.3 Combined End and Side Extrusion

Consider the combined end and side extrusion problem shown in Fig. 15. In this problem, the plate on the right hand side moves into a block of Tresca material of

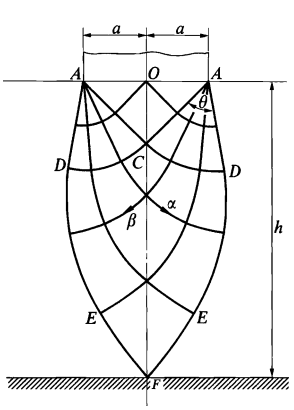

(a) Slip-line field from [3] for $h/a < 4.77$. Also showing relative block and indenter dimensions (from [3])

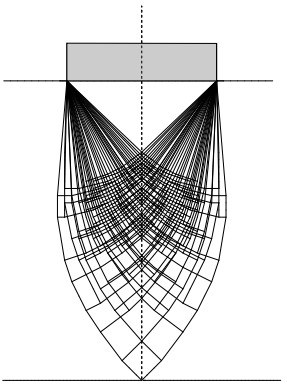

(b) Mechanism from DLO for $h/a = 4$

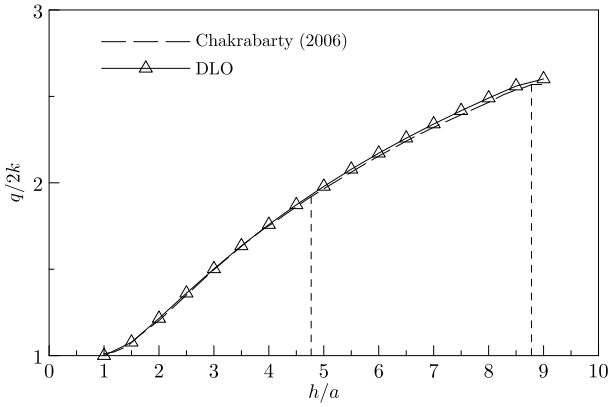

(c) Comparison of results from Chakrabarty [3] and DLO

Fig. 13 Punch indentation of a block of finite depth example

strength k, resulting in an average pressure p on the plate. In order to satisfy the incompressibility condition, material must escape from the vessel via the single end hole and two side holes shown. Johnson et. al. [16] solved this problem, assuming equal widths for all three holes, using slip-line theory. (Note that Johnson's results [16] are reproduced in Chakrabarty's well-known textbook [3].) The assumed slip-line field limits the geometries that can be considered. The geometries considered in [3] can be identified in Fig. 16 by reading of the relevant d/h ratio for a given H/h ratio. A comparative study was undertaken for a number of H/h ratios using the appropriate d/h value from Fig. 16. In the DLO analysis, the number of nodes was fixed to be approximately 1000. Taking advantage of symmetry only the top half was considered.

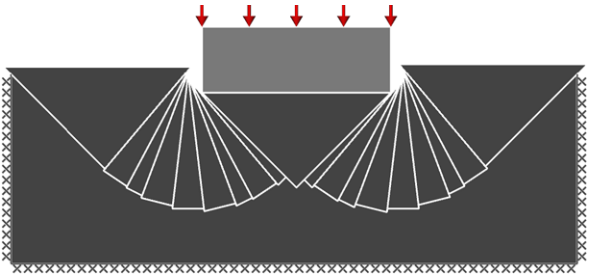

Fig. 14 Punch indentation of a block of infinite depth (90×30 nodal division DLO solution), showing predicted mode of deformation

Table 1 Punch indentation of a block of infinite depth: DLO results

Punch position	Nodal divisions	DLO (q/k)	Diff (%)
Central	45 × 15	5.17344	0.425
	90 × 30	5.15408	0.243
	180 × 60	5.14719	0.109
Edge	30 × 15	5.17344	0.425
	60 × 30	5.15408	0.243
	120 × 60	5.14719	0.109
	180 × 180[a]	5.14352[a]	0.037[a]

[a]solution from Sect. 3.4, taking $q = 2V$

In Fig. 15, a representative mechanism obtained using DLO is presented. As demonstrated in Fig. 16, extremely good agreement was found between the $p/2k$ values obtained from the slip-line analysis [16] and DLO. However, unlike standard slip-line analysis theory, DLO is able to handle arbitrary geometries and is thus much more flexible.

4.4.4 Bearing Capacity of Sand Layer over Clay

The case of a strip footing of width B resting on a sand layer of thickness D, internal friction angle ϕ, unit weight γ, which in turn is underlain by a deep bed of clay of undrained shear strength c_u is used to illustrate the capability of the DLO method to model combined cohesive-frictional problems. It is required that the short-term stability of the footing is assessed, with the sand layer assumed to be fully drained and the clay bed undrained.

Shia et al. [24] have investigated this problem over a range of the problem parameters using finite element limit analysis (FELA). An illustrative example for the case of $\phi = 40°$, $D = B$, and $c_u/\gamma B = 5$ is presented in Fig. 17. A DLO analysis was undertaken using a nodal spacing of $B/40$. This gave a predicted collapse load $V/\gamma B^2 = 29.19$, which compares well with the lower and upper bounds of 26.59 and 30.54 respectively obtained by Shia et al. [24]. (For clarity the mechanism presented in Fig. 17 was obtained with a nodal spacing of $B/20$.)

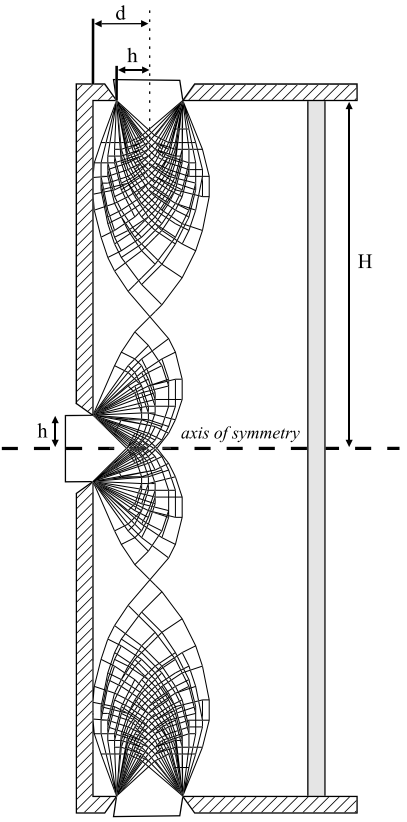

Fig. 15 Combined end and side extrusion example: DLO mechanism for $d/h = 1.712$ and $H/h = 10.50$

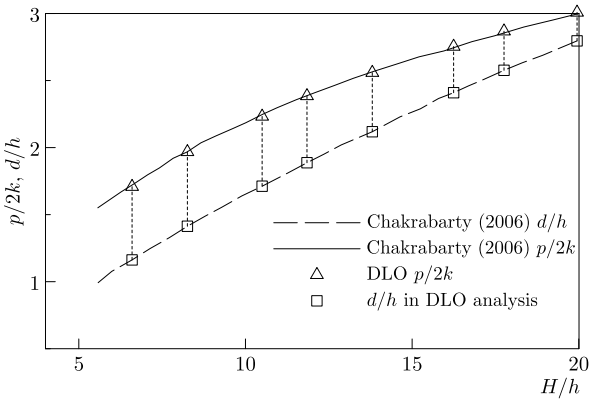

Fig. 16 Combined end and side extrusion example: comparison of results from [3] and DLO

5 Future Research Directions

Although layout optimization techniques were first developed almost half a century ago [5], there appears to have been comparatively little research in the field until

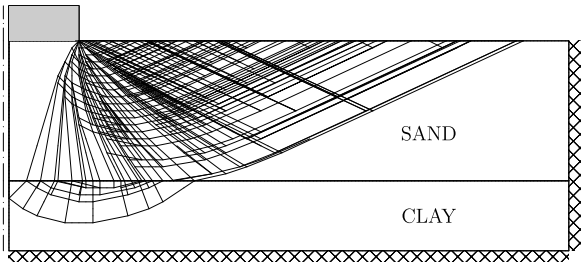

Fig. 17 Bearing capacity of sand layer over clay example: a rigid footing of width B founded on a sand layer of depth $D = B$, angle of shearing resistance $\phi = 40°$, unit weight γ overlying clay of strength $c_u/\gamma B = 5$ (symmetrical half space model)

relatively recently. This means that there are still many potentially fruitful avenues to explore. For example, the problems described in this chapter all assume the presence of straight-line connections (e.g. truss bars or slip-line discontinuities) between nodes. However, different kinds of connections can potentially be used. Thus in two-dimensions curved connections could instead be used, perhaps to model truss bars optimally shaped to carry their own self-weight, or to model the curved slip-lines associated with rotational collapse mechanisms. Another possibility is to consider surface connections, which may represent shell elements in a design context, or potential surface discontinuities in a three-dimensional limit analysis context. Initial investigations into the latter have already begun and this will therefore be considered further in the next section.

5.1 3D Discontinuity Layout Optimization

In plane strain, DLO is capable of obtaining accurate solutions for problems involving arbitrary, often complex, geometry and boundary conditions as has been demonstrated in the previous section. Adaptive techniques allow highly accurate solutions to be obtained at moderate computational expense. A natural progression is to apply the technique to more challenging and computationally expensive three-dimensional problems. In three-dimensions, the analogy with truss optimization breaks down (i.e. truss elements remain linear but discontinuities are now planar). However, a three-dimensional formulation is still possible. This three-dimensional formulation can be viewed as analogous to an optimization problem involving seeking an optimum structure comprising intersecting shell elements (e.g. a honeycomb). The changes necessary to the plane strain formulation for three-dimensional analysis can be summarized as follows (after [12]):

1. Potential discontinuities must now be polygonal rather than linear in form.
2. Three variables per potential discontinuity are now necessary to fully specify the change in velocity at each potential discontinuity (one normal and two shear components). $\mathbf{d}^{\mathbf{T}}$ now becomes $\{s_{11}, s_{12}, n_1, s_{21}, s_{22}, n_2, \ldots, n_m\}$, where s_{i1} and s_{i2} are the two shear components of change in velocity across discontinuity i.
3. The resultant of the shear components at each discontinuity must now be calculated in order to find the energy dissipated. This can be done using a conic

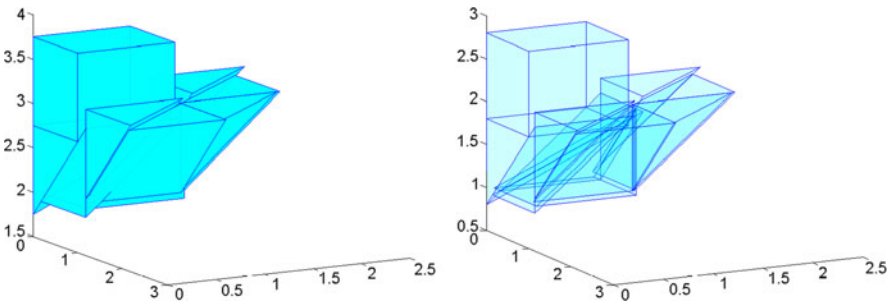

(a) Opaque blocks (b) Translucent blocks

Fig. 18 Deformed mechanism, obtained using DLO, for rough based square punch (showing a quarter of the square punch)

constraint, $s_{ir} \geq \sqrt{s_{i1}^2 + s_{i2}^2}$; where s_{ir} is the resultant shear change in velocity across discontinuity i. $\mathbf{p}^{\mathbf{T}}$ now becomes $\{s_{1r}, s_{2r}, \ldots, s_{rm}\}$.

4. $\mathbf{g}^{\mathbf{T}}$ now equals $\{c_1 a_1, c_2 a_2, \ldots, c_m a_m\}$, where a_i is the area of discontinuity i.
5. Compatibility is now conveniently enforced along each edge rather than at each node.
6. A cone programming solver can now be conveniently used to obtain the minimum.

An initial investigation [12] using a non-adaptive formulation considered the indentation of a semi-infinite Tresca continuum by a square perfectly rough punch (see Fig. 18). Despite the use of relatively coarse nodal discretizations, a bearing capacity factor equal to 6.102 could be obtained, which compares well with the best upper bound solution in the literature of 6.051, obtained by [25] using FELA. Future work will concentrate on developing a suitable adaptive solution scheme, allowing finer nodal discretizations to be considered.

6 Conclusions

Layout optimization techniques were developed almost half a century ago, but are now the subject of renewed interest. When suitable adaptive solution schemes are employed, layout optimization techniques can be applied to large-scale problems. This means that very accurate solutions can be obtained relatively rapidly, potentially allowing new-insights into the optimal forms of structures to be obtained. The inherent similarities between limit analysis and limit design problem formulations also means that methods originally developed for the design of trusses can be adapted to identify the critical layout of discontinuities in solids (discontinuity layout optimization, DLO). DLO is a powerful and flexible technique which is now finding use in industry, clearly demonstrating its practical usefulness.

Acknowledgements The authors acknowledge the assistance provided by Dr Wael Darwich, Dr Thomas Pritchard and Dr Iain Haslam, who assisted with the development of the software used in this Chapter. Also acknowledged are the mathematical insights provided by Dr Aleksey Pichugin of Brunel University. Finally the financial support provided by EPSRC (Advanced Research Fellowship grant ref: GR/S53329/01) is gratefully acknowledged.

References

1. Andersen KD, Christiansen E, Overton ML (1998) Computing limit loads by minimizing a sum of norms. SIAM J Sci Comput 19(3):1046–1062
2. Bazaraa MS, Jarvis JJ, Sherali HD (2009) Linear programming and network flows, 4th edn. Wiley, New York
3. Chakrabarty J (2006) Theory of plasticity, 3rd edn. Butterworth-Heinemann, Oxford
4. Darwich W, Gilbert M, Tyas A (2010) Optimum structure to carry a uniform load between pinned supports. Struct Multidiscip Optim 42(1):33–42
5. Dorn WS, Gomory RE, Greenberg HJ (1964) Automatic design of optimal structures. J Mech 3:25–52
6. Gilbert M, Smith CC (2010) Soil structure revolution. Struct Eng 88(3):18–22
7. Gilbert M, Tyas A (2003) Layout optimisation of large-scale pin-jointed frames. Eng Comput 20(8):1044–1064
8. Gilbert M, Tyas A, Pritchard T (2003) An efficient linear programming based layout optimization method for pin-jointed frames. In: Proceedings of the 5th world congress on structural and multidisciplinary optimization, Venice. CD-ROM proceedings paper no 67
9. Gilbert M, Casapulla C, Ahmed HM (2006) Limit analysis of masonry block structures with non-associative frictional joints using linear programming. Comput Struct 84(13):873–887
10. Gilbert M, Smith CC, Haslam IW, Pritchard TJ (2010) Application of discontinuity layout optimization to geotechnical limit analysis problems. In: Proceedings of the 7th European conference on numerical methods in geotechnical engineering, Trondheim, Norway, pp 169–174
11. Gilbert M, Smith CC, Pritchard TJ (2010) Masonry arch analysis using discontinuity layout optimisation. Proc Inst Civ Eng, Eng Comput Mech 163(3):155–166
12. Hawksbee SJ, Smith CC, Gilbert M (2013) Application of discontinuity layout optimization to three-dimensional plasticity problems. Proc R Soc A 469(2155):20130009
13. Hemp WS (1974) Michell framework for uniform load between fixed supports. Eng Optim 1(1):61–69
14. Heyman J (1966) The stone skeleton. Int J Solids Struct 2(2):249–279
15. Heyman J (1972) Coulomb's memoir on statics. Cambridge University Press, Cambridge
16. Johnson W, Mellor PB, Woo DM (1958) Extrusion through single hole staggered and unequal dies. J Mech Phys Solids 6:203–222
17. Lewinski T, Zhou M, Rozvany GIN (1994) Extended exact solutions for least-weight truss layouts, part I: cantilever with a horizontal axis of symmetry. Int J Mech Sci 36:375–398
18. LimitState (2011) In: LimitState:RING masonry arch bridge analysis software. http://www.limitstate.com/ring
19. LimitState (2012) In: LimitState:GEO geotechnical analysis software. http://www.limitstate.com/geo
20. Livesley RK (1978) Limit analysis of structures formed from rigid blocks. Int J Numer Methods Eng 12(12):1853–1871
21. Makrodimopoulos A, Martin CM (2006) Lower bound limit analysis of cohesive-frictional materials using second-order cone programming. Int J Numer Methods Eng 66(4):604–634
22. Michell AGM (1904) The limits of economy of material in frame-structures. Philos Mag 8(47):589–597

23. Pichugin AV, Tyas A, Gilbert M (2012) On the optimality of Hemp's arch with vertical hangers. Struct Multidiscip Optim 46(1):17–25
24. Shiau JS, Lyamin AV, Sloan SW (2003) Bearing capacity of a sand layer on clay by finite element limit analysis. Can Geotech J 40:900915
25. Vicente da Silva M, Antão AN (2007) A non-linear programming method approach for upper bound limit analysis. Int J Numer Methods Eng 72:1192–1218
26. Smith CC, Cubrinovskii M (2011) Pseudo-static limit analysis by discontinuity layout optimization: application to seismic analysis of retaining walls. Soil Dyn Earthq Eng 31(10):1311–1323
27. Smith C, Gilbert M (2007) Application of discontinuity layout optimization to plane plasticity problems. Proc R Soc A 463(2086):2461–2484
28. Sokół T, Lewiński T (2010) On the solution of the three forces problem and its application in optimal designing of a class of symmetric plane frameworks of least weight. Struct Multidiscip Optim 42(6):835–853
29. Tyas A, Gilbert M, Pritchard TJ (2006) Practical plastic layout optimization of trusses incorporating stability considerations. Comput Struct 84(3):115–126
30. Tyas A, Pichugin A, Gilbert M (2011) Optimum structure to carry a uniform load between pinned supports: exact analytical solution. Proc R Soc A 467(2128):1101–1120
31. Wright SJ (1987) Primal-dual interior-point methods, vol 54. SIAM, Philadelphia

Macroscopic Modeling of Porous Nonassociated Frictional Materials

Long Cheng, Géry de Saxcé, and Djimedo Kondo

Abstract The aim of this work is to propose a macroscopic plastic model for "Porous nonassociated Drucker-Prager"-type materials, using homogenization techniques and the hollow sphere model proposed by Gurson (J Eng Mater Technol 99:2–15, 1977) for von Mises solid matrix. In the first part, we determine analytically the plastic limit state of a hollow sphere with a Drucker-Prager matrix and subjected to hydrostatic loading. For the associated case, the collapse is complete with a unique regime. For the nonassociated cases, we consider weaker solutions (partial collapse and regime change). Nevertheless, we show that the collapse is complete and exhibits a single regime. Consequently, the collapse stress field and the limit load do not depend on the value of the dilation angle, as confirmed by numerical simulations. This result has been already obtained by Maghous et al. (Eur J Mech A, Solids 28:179–188, 2009) by means of a modified second moduli approach. In Gurson's footsteps, Guo et al. (J Mech Phys Solids 56:2188–2212, 2008) proposed a macroscopic model for porous solid with pressure-sensitive dilatant matrix obeying to the normality law (associated material). The second part of the paper is a first attempt to extend Guo's model to the nonassociated materials. Using the concept of bipotential, we proposed a two-fields variational approach to deduce a macroscopic model.

L. Cheng · G. de Saxcé (✉)
Laboratoire de Mécanique de Lille (UMR CNRS 8107), Université de Lille 1, cité scientifique, 59655 Villeneuve d'Ascq, France
e-mail: gery.desaxce@univ-lille1.fr

L. Cheng
e-mail: long.cheng@ed.univ-lille1.fr

D. Kondo
Institut Jean Le Rond d'Alembert (UMR CNRS 7190), Université Pierre et marie Curie, 4 place Jussieu, 75005 Paris, France
e-mail: djimedo.kondo@upmc.fr

K. Spiliopoulos, D. Weichert (eds.), *Direct Methods for Limit States in Structures and Materials*, DOI 10.1007/978-94-007-6827-7_9,

1 Introduction

The present work must be considered as a first attempt to propose a macroscopic plastic model for "Porous nonassociated Drucker-Prager"-type materials, using homogenization techniques. In a famous paper [35], Gurson derived an upper bound limit analysis approach of a hollow sphere and a hollow cylinder having a von Mises solid matrix. Several extensions of Gurson's model have been further proposed in the literature, the probably most important developments being those accounting for void shape effects [32, 33, 54]. Other extensions are concerned by the plastic anisotropy [2, 55] or take into account the plastic compressibility of the matrix through associated Drucker-Prager model in the perspective of applications to polymer and cohesive geomaterials [1, 41, 42, 52].

In the first part (Sect. 2), we consider the hollow sphere subjected to the particular case of hydrostatic loading. This part is a direct extension of a recent paper [60] dedicated to the same problem but here with the nonassociated flow rule. Classical bound limit analysis theorems have been generalized to the class of implicit standard materials, *i.e.* with a nonassociated flow rule represented with a bipotential [9, 24]. In the spirit of Gurson's paper, a trial velocity field is built by adding linear terms to the exact one for hydrostatic loading. The goal of this part is to determine such an exact field. In limit analysis, the most simple solutions are smooth with a single plastic regime covering the whole body but, generally speaking, it is *a priori* expected that limit state solutions may involve some field discontinuities compatible with the continuum mechanics principles [17, 58]. In particular, the collapse may be incomplete and/or exhibits distinct regimes in subdomains. For nonassociated Drucker-Prager model, the collapse stress field is statically and plastically admissible. Then the limit load for the nonassociated model is *a priori* less than the limit load for the corresponding associated model (*i.e.* with the normality rule and the same friction angle). As a matter of fact, although exact solutions do not exist up to now for such class of problems, numerical simulations show that for classical soil mechanics applications (bearing capacity of a strip footing, stability of foundations and tunnels), the limit load of the nonassociated case is really strictly less than the one of the corresponding associated case [3, 18, 39]. In the hollow sphere problem, we consider the event of such weaker solutions but we conclude to the impossibility of incomplete collapse and more than one plastic regime. The paradoxical consequence is the nonsensitivity of the limit load to the dilatancy angle. This theoretical result which has been already obtained by [52] through a non-linear homogenization technique is confirmed by numerical simulations.

In the second part, we tackle the general case of combined hydrostatic and deviatoric loadings. Roughly speaking, a constitutive law in Mechanics is a relationship between dual variables. The constitutive laws of the materials can be represented, as in Elasticity, by a univalued mapping or, as in Plasticity, can be generalized in the form of a multivalued mapping. But this representation is not necessarily convenient. When the graph is maximal and cyclically monotone, we can model it thanks to a convex and lower semi-continuous function ϕ, called a superpotential (or

pseudo-potential), such that the graph is the one of its subdifferential $\partial\phi$. The function ϕ and its Fenchel conjugate one ϕ^* verifies for any couple of dual variables Fenchel's inequality. The dissipative materials admitting a superpotential of dissipation are often qualified as standard [36] and the law is said to be a normality law, a subnormality law or an associated law.

However, several models proposed these last decades, particularly in Plasticity, are nonassociated. For such laws, the second author introduced in [20, 21] a suitable modelization based on the bipotential, a function b of both dual variables, convex and lower semicontinuous in each argument and satisfying a cornerstone inequality saying that for any couple of dual variables the value of the bipotential is greater than or equal to their duality pairing. When equality holds, the couple is said extremal. In a mechanical view point, the extremal couples are the ones satisfying the constitutive law. Materials admitting a bipotential are called implicit standard materials (ISM) because the constitutive law is a subnormality law but the relation between the dual variables is implicit. The classical standard materials correspond to the particular event of the bipotential being separated as the sum of a superpotential and its conjugate one. In this sense, the cornerstone inequality of the bipotential generalizes Fenchel's one. The existence and construction of a bipotential for a given constitutive law is discussed in [11, 12, 14].

Linked to the structural mechanics and in particular with the Calculus of Variation, the bipotential theory offers an elegant framework to model a broad spectrum of nonassociated laws. Examples of such nonassociated constitutive laws are:

- in soil mechanics, non-associated Drucker-Prager [3, 8, 22, 24, 39] and Cam-Clay models [23, 62],
- the nonlinear kinematical hardening rule for cyclic Plasticity [5–7, 21, 53] and Viscoplasticity [37],
- Lemaitre's coupled damage law [4],
- the coaxial laws [26, 61],
- Coulomb's friction law [9, 21, 22, 24, 25, 28–31, 38, 40, 44],
- the blurred constitutive laws [13, 15].

A complete survey can be found in [26]. In the previous works, robust numerical algorithms were proposed to solve structural mechanics problems.

The limit analysis is a general method to determine the plastic collapse of structures under proportional loading [58], particularly in soil mechanics [17, 18], but it is restricted to associated plasticity (with normality law). The classical presentation of the nonassociated plasticity is based on a yield function and a plastic potential. The bipotential offers an alternative formulation opening naturally into a variational formulation, paving the way to an extension of limit analysis techniques to nonassociated laws [8, 9, 16, 24, 62]. Extension of this method to the repeated variable loading is called shakedown theory and its extension to the ISM by the bipotential approach was also considered in [6–8, 10, 26].

2 First Part: The Exact Analytical Solution for the Pure Hydrostatic Loading

2.1 Problem Formulation

We consider a hollow sphere made up of a spherical cavity embedded in a homothetic cell of a rigid-plastic isotropic and homogeneous material with nonassociated Drucker-Prager model. The inner and outer radii are respectively denoted a and b, giving the void volume fraction $f = (a/b)^3 < 1$. The hollow sphere is subjected to a uniform hydrostatic stress q upon its external boundary and a uniform pressure p upon the cavity boundary. Accounting for the central symmetry of the problem, the spherical coordinate (r, θ, φ) are used, r being the radius, θ the inclination angle, φ the azimuth one, and all the fields are depending only on r.

The velocity components v_θ and v_φ are null. The strain rate tensor $\boldsymbol{d}$ has three non-vanishing components given with respect to the radial velocity v_r by:

$$d_{rr} = \frac{dv_r}{dr}, \qquad d_{\theta\theta} = d_{\varphi\varphi} = \frac{v_r}{r}. \tag{1}$$

There is no kinematic boundary conditions but the velocity field $v_r(r)$ must be continuous anywhere.

The stress tensor $\boldsymbol{\sigma}$ has three nonvanishing components, σ_{rr}, $\sigma_{\theta\theta} = \sigma_{\varphi\varphi}$ and, in absence of body forces, satisfies the radial equilibrium equation:

$$\frac{d\sigma_{rr}}{dr} + 2\frac{\sigma_{rr} - \sigma_{\theta\theta}}{r} = 0, \tag{2}$$

with static boundary conditions:

$$\sigma_{rr}(a) = -p, \qquad \sigma_{rr}(b) = q. \tag{3}$$

According to the mechanics of continua, some discontinuities of $\sigma_{\theta\theta}$ and $\sigma_{\varphi\varphi}$ may occur when r varies but the radial stress $\sigma_{rr}(r)$ must be continuous anywhere.

Drucker-Prager model is considered with the yield criterion:

$$F(\boldsymbol{\sigma}) = \sigma_e + 3\alpha\sigma_m - \sigma_0 = 0, \tag{4}$$

where σ_e is the equivalent stress of Von Mises, σ_m the mean stress, $\sigma_0 > 0$ the cohesion stress of the material and α the pressure sensitivity factor related to the friction angle ϕ by:

$$\tan\phi = 3\alpha.$$

The nonassociated flow rule:

$$\boldsymbol{d} = \lambda\frac{\partial G}{\partial \boldsymbol{\sigma}}, \tag{5}$$

is given by the plastic potential:

$$G(\boldsymbol{\sigma}) = \sigma_e + 3\beta\sigma_m - \sigma_0,$$

where β depends on the dilatancy angle ψ through:

$$\tan\psi = 3\beta.$$

Moreover, the plastic multiplier must be nonnegative:

$$\lambda \geq 0. \tag{6}$$

Of course, for the particular event $\psi = \phi$ hence $F = G$, the normality rule is recovered and the plasticity model is associated. Without loss of generality, we can assume that:

$$0 \leq \beta \leq \alpha < \frac{1}{2}, \tag{7}$$

or equivalently $0 \leq \psi \leq \phi < 56°18'$. In practice, these conditions are fulfilled by the geomaterials and other pressure sensitive dilatant materials. Experimental data can be found for polymers, high strength steels and aluminium in [34].

2.2 Plastic Limit State

The equivalent stress reads:

$$\sigma_e = \frac{1}{\sqrt{2}}\sqrt{(\sigma_{rr}-\sigma_{\theta\theta})^2 + (\sigma_{\theta\theta}-\sigma_{\varphi\varphi})^2 + (\sigma_{\varphi\varphi}-\sigma_{rr})^2}.$$

The mean stress is:

$$\sigma_m = \frac{1}{3}(\sigma_{rr} + \sigma_{\theta\theta} + \sigma_{\varphi\varphi}). \tag{8}$$

The flow rule (5) takes the form:

$$d_{rr} = \lambda\left(\beta + \frac{1}{2\sigma_e}(2\sigma_{rr} - \sigma_{\theta\theta} - \sigma_{\varphi\varphi})\right),$$

$$d_{\theta\theta} = \lambda\left(\beta + \frac{1}{2\sigma_e}(2\sigma_{\theta\theta} - \sigma_{\varphi\varphi} - \sigma_{rr})\right).$$

Owing to $\sigma_{\theta\theta} = \sigma_{\varphi\varphi}$, the equivalent stress is reduced to:

$$\sigma_e = |\sigma_{rr} - \sigma_{\theta\theta}| = \varepsilon(\sigma_{\theta\theta} - \sigma_{rr}), \tag{9}$$

with the following convention to distinguish the plastic regimes:

- $\varepsilon = +1$ if $\sigma_{rr} \leq \sigma_{\theta\theta}$,
- $\varepsilon = -1$ if $\sigma_{\theta\theta} \leq \sigma_{rr}$.

Considering (9) and once again $\sigma_{\theta\theta} = \sigma_{\varphi\varphi}$, one obtains:

$$d_{rr} = \lambda(\beta - \varepsilon), \qquad d_{\theta\theta} = d_{\varphi\varphi} = \lambda\left(\beta + \frac{\varepsilon}{2}\right). \tag{10}$$

Eliminating the velocity between the two equations (1), one obtains:

$$d_{rr} = \frac{d}{dr}(r d_{\theta\theta}).$$

Eliminating the strain rate components between the previous relations leads to:

$$\frac{d\lambda}{dr} + \frac{3\lambda}{s_\varepsilon r} = 0,$$

where we put for convenience $s_\varepsilon = 1 + 2\varepsilon\beta$. The general solution is:

$$\lambda(r) = \lambda_\varepsilon r^{-\frac{3}{s_\varepsilon}}. \tag{11}$$

Combining (10) with (1) leads to:

$$v_r(r) = K_\varepsilon r^{1-\frac{3}{s_\varepsilon}}, \tag{12}$$

where

$$K_\varepsilon = \left(\beta + \frac{\varepsilon}{2}\right)\lambda_\varepsilon. \tag{13}$$

As usual, due to the nature of the limit load problem, the kinematical fields are defined up to a positive factor.

Let us now discuss the existence of solutions with discontinuities:

- Suppose that there exist adjoining spherical shells which have distinct plastic regimes corresponding respectively to ε and $-\varepsilon$. The continuity of the velocity field at the interface of radius r_0 entails:

  $$K_{-\varepsilon} = K_\varepsilon r_0^{-3(\frac{1}{s_\varepsilon} - \frac{1}{s_{-\varepsilon}})}.$$

  Assuming that K_ε and $K_{-\varepsilon}$ do not vanish, they should have the same sign, and the plastic multiplier should be positive. However, under the condition (7), $\lambda_\varepsilon = K_\varepsilon/(\beta + \frac{\varepsilon}{2})$ and $\lambda_{-\varepsilon} = K_{-\varepsilon}/(\beta - \frac{\varepsilon}{2})$ have opposite signs, which is absurd because, accounting for (11), condition (6) would be violated in one of these regimes. Thus no change of regime is allowed at the limit state.
- Finally, let us suppose that the collapse is not complete. The plastic multiplier field is identically null in a nonplastified spherical shell, hence so is the velocity field because of (11), (12) and (13). It is absurd to assume the existence of a plastic yielding adjoining shell because the continuity of the velocity field at the interface would force the velocity field to vanish in the yielding shell. Hence the collapsed must be complete.

Next, the corresponding statical solution is presented. Considering (8), (9) and once again $\sigma_{\theta\theta} = \sigma_{\varphi\varphi}$, the yield function reads:

$$F(\boldsymbol{\sigma}) = \varepsilon(\sigma_{\theta\theta} - \sigma_{rr}) + \alpha(\sigma_{rr} + 2\sigma_{\theta\theta}) - \sigma_0 = 0.$$

It follows:

$$2(\sigma_{\theta\theta} - \sigma_{rr}) = 3\gamma_\varepsilon(H - \sigma_{rr}), \tag{14}$$

where $\gamma_\varepsilon = 2\alpha/(2\alpha+\varepsilon)$ and $H = \sigma_0/3\alpha = \sigma_0/\tan\phi > 0$. Due to the condition (7), the sign of γ_ε coincides with that of ε. Combining with the equilibrium equation (2) gives:

$$\frac{d\sigma_{rr}}{dr} + \frac{3\gamma_\varepsilon(\sigma_{rr}-H)}{r} = 0.$$

The solution satisfying the boundary condition $(3)_1$ is:

$$\frac{\sigma_{rr}(r)+p}{H+p} = 1 - f^{\gamma_\varepsilon}\left(\frac{b}{r}\right)^{3\gamma_\varepsilon}. \tag{15}$$

The limit hydrostatic stress is given by $(3)_2$ as function of the porosity:

$$\frac{q+p}{H+p} = 1 - f^{\gamma_\varepsilon}. \tag{16}$$

It can be verified that γ_ε, σ_{rr} and $(q+p)$ have the same sign ε . In short, the solution is defined by the limit load (16) and, in the interval $a \le r \le b$, by the collapse fields of plastic multiplier (11), velocity (12) and radial stress (15). The stress field and limit loads do not depend on the dilatancy angle and they are identical to the ones of the associated case with same friction angle, previously obtained in [60] when the pressure vanishes. Only the collapse mechanism is dilatancy angle dependent. This insensitivity of the limit load to the dilatancy angle agrees with the model recently proposed by [52].

For the variational model that will be presented in the second part, it is convenient to determine also the mean stress field (8). From (14), we obtain:

$$2\sigma_{\theta\theta} = (2-3\gamma_\varepsilon)\sigma_{rr} + 3\gamma_\varepsilon H.$$

Taking into account this last relation, $\sigma_{\theta\theta} = \sigma_{\varphi\varphi}$ and (15), it comes:

$$\sigma_m(r) = \frac{1}{3\alpha}\left[\sigma_0 - (\sigma_0+3\alpha p)\frac{f^{\gamma_\varepsilon}}{s_\varepsilon}\left(\frac{b}{r}\right)^{3\gamma_\varepsilon}\right]. \tag{17}$$

In the second part, to lighten the notations, the subscript ε will be erased.

2.3 Numerical Results

In this section, the previous analytical solution is compared to numerical data obtained from Finite Element Method (FEM) results. An axisymmetric model of the spherical shell, as shown in Fig. 1, is considered and 1500 quadratic axisymmetric elements are used. Hence, the numerical analysis will be carried out by means of the 2D-FEM code [43, 59] developed in LML (*Mechanics Laboratory of Lille, France*) for incremental analysis of elastoplatic materials with nonassociated flow rule and in small deformations. The radial displacement is fixed on the plans $ABCD$ of symmetry, the vertical and horizontal displacements of the lateral boundaries AB and CD are also fixed, and a uniform radial displacement is imposed upon the external boundary BC, while the internal boundary DA is free of stress.

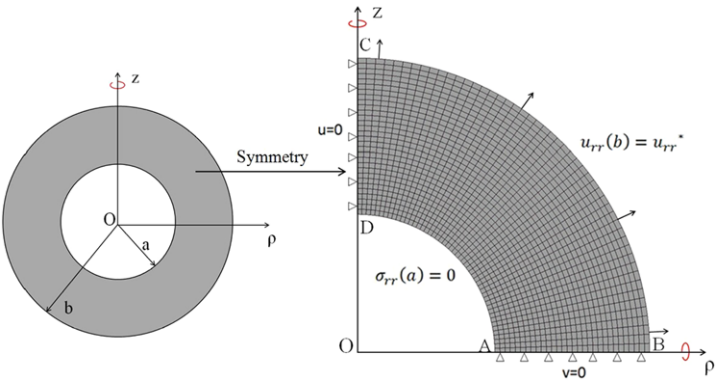

Fig. 1 Hollow sphere model: Geometry of the elementary cell and boundary conditions

A reference case, denoted Case 1, is firstly defined in which the associated flow rule is applied with the following parameters: $a = 0.585$ m, $b = 1$ m ($f \approx 0.2002$), $\phi = \psi = 30°$, $E = 500$ MPa, $\nu = 0.2$ and $\sigma_0 = 1$ MPa. Then, in order to verify the precision of the proposed model in nonassociated cases, two other simulations (denoted Cases 2 and 3) are performed with two different values of ψ (15° and 0°), both under compression and traction conditions.

Figure 2 displays the FEM results of Cases 1 to 3, where the materials possess the same porosity ($f \approx 0.2002$) but different dilation angles. $\xi(r)$ denotes the radial displacement and the limit stress is the asymptotic value. The limit loads of associated case ($\psi = \phi = 30°$) and nonassociated ones ($\phi = 30°$, $\psi = 15°$ and 0°), as expected, have almost the same value with very small differences of the order 1 %. The differences between the reference analytical solution and the finite element ones are rather small and can be attributed to numerical errors due to the discretization. However, the FEM points of these three lines in this figure do not coincide entirely. In other words, as the displacements imposed upon the external boundary being the same, the ones at the internal boundary are not. Therefore, the limit load of nonassociated Drucker-Prager porous material does not depend on the dilation angle, whereas the collapse mechanism does. More details can be found in [19] concerning the sensitivity of the proposed model with respect to the porosity and Young's modulus.

3 Second Part: Variational Formulation for Combined Hydrostatic and Deviatoric Loadings

3.1 More About the Nonassociated Drucker-Prager Model

Excepted for the apex of Drucker-Prager cone ($\sigma_e = 0$, $\sigma_m = \sigma_0/3\alpha$) where σ_e is not differentiable, the plastic strain rate is given by the nonassociated flow rule:

$$\boldsymbol{d} = \dot{\varepsilon}^p \frac{\partial G}{\partial \boldsymbol{\sigma}} = \dot{\varepsilon}^p \left(\frac{3\boldsymbol{s}}{2\sigma_e} + \beta \mathbf{1} \right), \tag{18}$$

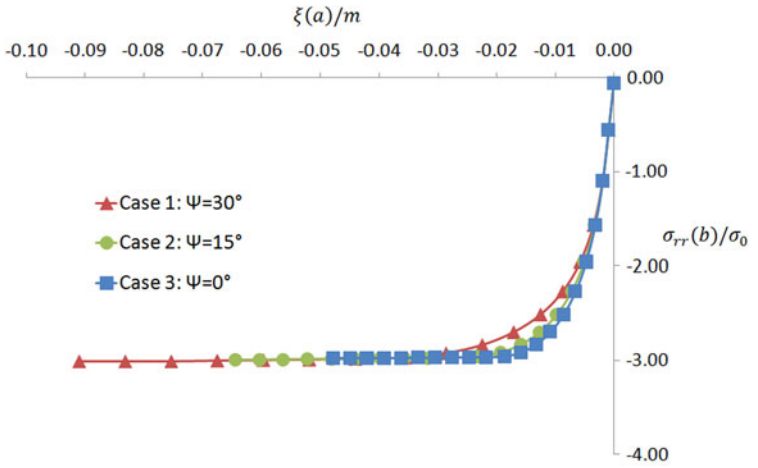

(a) Compression

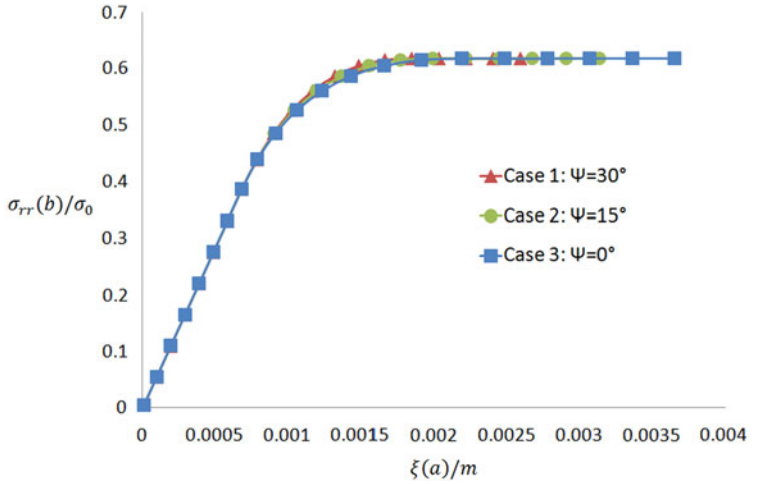

(b) Traction

Fig. 2 Comparison of numerical limit loads between associated ($\psi = 30°$) and nonassociated cases ($\psi = 15°$ and $0°$) with fixed friction angle ($\phi = 30°$) and porosity ($f \approx 0.2002$)

where $\boldsymbol{\sigma}$ is Cauchy stress tensor, $\boldsymbol{s}$ the deviatoric stress, $\mathbf{1}$ the unit tensor. the scalar $\dot{\varepsilon}^p$ is defined as:

$$\dot{\varepsilon}^p = \left| \frac{2}{3} \boldsymbol{e} : \boldsymbol{e} \right|^{1/2}$$

with $\boldsymbol{e}$ the deviatoric part of $\boldsymbol{d}$. The plastic dilatancy is given by:

$$\operatorname{tr} \boldsymbol{d} = 3\beta \dot{\varepsilon}^p. \tag{19}$$

This suggests introducing:

$$H(\boldsymbol{d}) = \beta\dot{\varepsilon}^p - d_m.$$

The plastic flow rule (18) is completed at the apex by the condition:

$$H(\boldsymbol{d}) \leq 0$$

while, because of (19), $H(\boldsymbol{d}) = 0$ at the other points of the yielding surface (called regular points).

3.2 Bipotential Formulation

In previous papers, the second author proposed a new modeling of the nonassociated constitutive laws based on the concept of bipotential [20, 21]. With the previous notations, the bipotential of nonassociated Drucker-Prager model is equal to:

$$b(\boldsymbol{d}, \boldsymbol{\sigma}) = \frac{\sigma_0}{\alpha} d_m + (\beta - \alpha)\left(3\sigma_m - \frac{\sigma_0}{\alpha}\right)\dot{\varepsilon}^p, \tag{20}$$

when $F(\boldsymbol{\sigma}) \leq 0$ and $H(\boldsymbol{d}) \leq 0$, equal to $+\infty$ otherwise. First of all, let us recall a basic concept of convex analysis, the subdifferential of a function ϕ in a point $\boldsymbol{x}$ which is the (possibly empty) set:

$$\partial\phi(\boldsymbol{x}) = \left\{\boldsymbol{y} \mid \forall \boldsymbol{x}', \phi\left(\boldsymbol{x}'\right) - \phi(\boldsymbol{x}) \geq \left(\boldsymbol{x}' - \boldsymbol{x}\right) : \boldsymbol{y}\right\}. \tag{21}$$

For more details on convex analysis, the reader is referred for instance to [27, 56, 57]. The main properties of the bipotential are:

(a) b is convex and lower semicontinuous in each argument.
(b) For any $\boldsymbol{d}'$ and $\boldsymbol{\sigma}'$ we have

$$b\left(\boldsymbol{d}', \boldsymbol{\sigma}'\right) \geq \boldsymbol{d}' : \boldsymbol{\sigma}'. \tag{22}$$

(c) For $\boldsymbol{d}$ and $\boldsymbol{\sigma}$ we have the equivalences:

$$\boldsymbol{\sigma} \in \partial b(\cdot, \boldsymbol{\sigma})(\boldsymbol{d}) \Longleftrightarrow \boldsymbol{d} \in \partial b(\boldsymbol{d}, \cdot)(\boldsymbol{\sigma}) \Longleftrightarrow b(\boldsymbol{d}, \boldsymbol{\sigma}) = \boldsymbol{d} : \boldsymbol{\sigma}. \tag{23}$$

In a mechanical point of view, the bipotential represents the plastic dissipation power (by volume unit) and (23) is the constitutive law. The couples $(\boldsymbol{d}, \boldsymbol{\sigma})$ for which ones equivalence (23) holds are called extremal couples. For the prove of the equivalence in the case of the nonassociated Drucker-Prager model, the reader is referred to [24]. Materials admitting a bipotential are called implicit standard materials (ISM). Accounting for the definition (21) of the subdifferential and the cornerstone inequality (22), the constitutive law (23) reads [12, 14, 15, 44]:

$$\min_{\boldsymbol{d}'}\left(b\left(\boldsymbol{d}', \boldsymbol{\sigma}\right) - \boldsymbol{d}' : \boldsymbol{\sigma}\right) = \min_{\boldsymbol{\sigma}'}\left(b\left(\boldsymbol{d}, \boldsymbol{\sigma}'\right) - \boldsymbol{d} : \boldsymbol{\sigma}'\right) = 0. \tag{24}$$

It is worth remarking that, with respect to the previous minimization problems, the bipotential has the required convexity properties. Let us show how to recover simply the plastic yielding condition $F(\boldsymbol{\sigma}) = 0$ by the bipotential formalism. The first minimization problem becomes:

$$\min_{H(\boldsymbol{d})\leq 0} \big(b_0(\boldsymbol{d},\boldsymbol{\sigma}) - \boldsymbol{d}:\boldsymbol{\sigma}\big) = 0,$$

where b_0 is the finite part of the bipotential, given by (20). Relaxing the kinematical condition $H(\boldsymbol{d}) \leq 0$ by use of Lagrange's multiplier λ, this constrained minimization problem is transformed into an equivalent saddle-point problem

$$\max_{\lambda\geq 0}\min_{\boldsymbol{d}}\big(L(\boldsymbol{d},\boldsymbol{\sigma},\lambda) = b_0(\boldsymbol{d},\boldsymbol{\sigma}) - \boldsymbol{d}:\boldsymbol{\sigma} + \lambda H(\boldsymbol{d})\big) = 0,$$

where the Lagrangian is:

$$L(\boldsymbol{d},\boldsymbol{\sigma},\lambda) = \frac{\sigma_0}{\alpha}d_m + (\beta-\alpha)\left(3\sigma_m - \frac{\sigma_0}{\alpha}\right)\dot{\varepsilon}^p - \big(\sigma_e\dot{\varepsilon}^p + 3d_m\sigma_m\big) + \lambda\big(\beta\dot{\varepsilon}^p - d_m\big).$$

Its stationarity with respect to $\dot{\varepsilon}^p$ and d_m gives:

$$\sigma_e = (\beta-\alpha)\left(3\sigma_m - \frac{\sigma_0}{\alpha}\right) + \beta\lambda,$$

$$3\sigma_m = \frac{\sigma_0}{\alpha} - \lambda.$$

Eliminating λ between these relations leads to the plastic criterion:

$$F(\boldsymbol{\sigma}) = \sigma_e + 3\alpha\sigma_m - \sigma_0 = 0.$$

In a similar way, it is possible to recover the plastic flow rule (18) at a regular point. The second minimization problem in (24) becomes:

$$\min_{F(\boldsymbol{\sigma})\leq 0} \big(b_0(\boldsymbol{d},\boldsymbol{\sigma}) - \boldsymbol{d}:\boldsymbol{\sigma}\big) = 0.$$

Relaxing the plastic yielding condition $F(\boldsymbol{\sigma}) \leq 0$ by use of Lagrange's multiplier λ^*, this problem is transformed into an equivalent saddle-point problem

$$\max_{\lambda^*\geq 0}\min_{\boldsymbol{\sigma}}\big(L^*\big(\boldsymbol{d},\boldsymbol{\sigma},\lambda^*\big) = b_0(\boldsymbol{d},\boldsymbol{\sigma}) - \boldsymbol{d}:\boldsymbol{\sigma} + \lambda^* F(\boldsymbol{\sigma})\big) = 0,$$

where the Lagrangian is:

$$L^*\big(\boldsymbol{d},\boldsymbol{\sigma},\lambda^*\big) = \frac{\sigma_0}{\alpha}d_m + (\beta-\alpha)\left(3\sigma_m - \frac{\sigma_0}{\alpha}\right)\dot{\varepsilon}^p - (\boldsymbol{e}:\boldsymbol{s} + 3d_m\sigma_m) + \lambda^*(\sigma_e + 3\alpha\sigma_m - \sigma_0).$$

Its stationarity with respect to $\boldsymbol{s}$ and σ_m gives:

$$\boldsymbol{e} = \lambda^*\frac{3\boldsymbol{s}}{2\sigma_e}, \tag{25}$$

$$(\beta-\alpha)\dot{\varepsilon}^p - d_m + \alpha\lambda^* = 0. \tag{26}$$

From (25) we obtain $\lambda^* = \dot{\varepsilon}^p$. Eliminating λ^* in (26) leads to the kinematical condition:

$$H(\boldsymbol{d}) = \beta\dot{\varepsilon}^p - d_m = 0,$$

that allows recovering the nonassociated flow rule (5):

$$\boldsymbol{d} = \boldsymbol{e} + d_m\mathbf{1} = \dot{\varepsilon}^p\left(\frac{3\boldsymbol{s}}{2\sigma_e} + \beta\mathbf{1}\right).$$

For the treatment of the apex, the reader is referred to [39].

3.3 Variational Formulation and Limit Analysis

Unlike the classical presentation of the nonassociated constitutive laws by means of the yield function and the plastic potential, the bipotential formulation naturally opens into a variational formulation, paving the way to an extension of limit analysis techniques to nonassociated laws. We present it directly in the framework of homogenization of porous material, considering a reference elementary volume or macro-element V composed of a matrix V_M made of an ISM and a void V_f subjected to a uniform hydrostatic pressure p. The macro-element V is enclosed by surface S and the void V_f by S_f. The macroscopic stress $\boldsymbol{\Sigma}$ and strain rate $\boldsymbol{D}$ are defined as volume averages of their microscopic counterpart $\boldsymbol{\sigma}$ and $\boldsymbol{d}$:

$$\boldsymbol{\Sigma} = V^{-1}\int_V \boldsymbol{\sigma}\,dV, \qquad \boldsymbol{D} = V^{-1}\int_V \boldsymbol{d}\,dV.$$

The set of kinematical admissible velocity fields is defined in the following sense:

$$\mathscr{K}_a = \left\{\boldsymbol{v} \text{ s.t. } \boldsymbol{v}(\boldsymbol{x}) = \boldsymbol{D}.\boldsymbol{x} \text{ on } S\right\}.$$

The associated strain rate field is $\boldsymbol{d}(\boldsymbol{v}) = \text{grad}_s\,\boldsymbol{v}$. The set of statically admissible stress fields is:

$$\mathscr{S}_a = \{\boldsymbol{\sigma} \text{ s.t. } \text{div}\,\boldsymbol{\sigma} = 0 \text{ in } V_M \text{ and } \boldsymbol{\sigma} = -p\mathbf{1} \text{ in } V_f\}.$$

The set of admissible couples is the product $\mathscr{A} = \mathscr{K}_a \times \mathscr{S}_a$ and the set of extremal ones is:

$$\mathscr{E} = \left\{(\boldsymbol{v}, \boldsymbol{\sigma}) \text{ s.t. } \left(\boldsymbol{d}(\boldsymbol{v}), \boldsymbol{\sigma}\right) \text{ is extremal in } V_M\right\}.$$

The homogenization problem consists in determining the set $\mathscr{A} \times \mathscr{E}$ of admissible and extremal fields. Accounting for its strong nonlinear nature, this problem has in general no closed analytical solution. We present now an equivalent variational formulation, more appropriate for simple approximations, thanks to relevant choice of trial fields and minimization procedure. Let us consider an admissible couple $(\boldsymbol{v}, \boldsymbol{\sigma})$. Thus, by Hill's lemma, one has:

$$\boldsymbol{D} : \boldsymbol{\Sigma} = V^{-1}\int_V \boldsymbol{d}(\boldsymbol{v}) : \boldsymbol{\sigma}\,dV = -V^{-1}\int_{V_f} \boldsymbol{d}(\boldsymbol{v})dV : p\mathbf{1} + V^{-1}\int_{V_M} \boldsymbol{d}(\boldsymbol{v}) : \boldsymbol{\sigma}\,dV,$$

$$\boldsymbol{D} : \boldsymbol{\Sigma} = -V^{-1} \int_V \boldsymbol{d}(\boldsymbol{v}) dV : p\mathbf{1} + V^{-1} \int_{V_M} \boldsymbol{d}(\boldsymbol{v}) : (\boldsymbol{\sigma} + p\mathbf{1}) dV.$$

Then, for any admissible couple, it holds:

$$\boldsymbol{D} : (\boldsymbol{\Sigma} + p\mathbf{1}) = V^{-1} \int_{V_M} \boldsymbol{d}(\boldsymbol{v}) : (\boldsymbol{\sigma} + p\mathbf{1}) dV. \tag{27}$$

This suggests introducing the following two field functional:

$$B\big(\boldsymbol{v}', \boldsymbol{\sigma}'\big) = V^{-1} \int_{V_M} \big(b\big(\boldsymbol{d}\big(\boldsymbol{v}'\big), \boldsymbol{\sigma}'\big) + \boldsymbol{d}\big(\boldsymbol{v}'\big) : p\mathbf{1}\big) dV - \boldsymbol{D} : (\boldsymbol{\Sigma} + p\mathbf{1}),$$

called the bifunctional. As previously said, we are interested for homogenization purpose in finding the admissible and extremal couples $(\boldsymbol{v}, \boldsymbol{\sigma})$. In fact, they are solutions of the simultaneous minimization problems:

$$B(\boldsymbol{v}, \boldsymbol{\sigma}) = \min_{\boldsymbol{v}' \in \mathscr{K}_a} B\big(\boldsymbol{v}', \boldsymbol{\sigma}\big) = \min_{\boldsymbol{\sigma}' \in \mathscr{S}_a} B\big(\boldsymbol{v}, \boldsymbol{\sigma}'\big) = 0. \tag{28}$$

Indeed, if $(\boldsymbol{v}', \boldsymbol{\sigma}')$ is admissible, relation (27) and (22) entail:

$$B\big(\boldsymbol{v}', \boldsymbol{\sigma}'\big) = V^{-1} \int_{V_M} \big(b\big(\boldsymbol{d}\big(\boldsymbol{v}'\big), \boldsymbol{\sigma}'\big) - \boldsymbol{d}\big(\boldsymbol{v}'\big) : \boldsymbol{\sigma}'\big) dV \geq 0.$$

In particular, this occurs for admissible couples $(\boldsymbol{v}', \boldsymbol{\sigma})$, $(\boldsymbol{v}, \boldsymbol{\sigma}')$, $(\boldsymbol{v}, \boldsymbol{\sigma})$ and moreover, in the last case, because of (23):

$$B(\boldsymbol{v}, \boldsymbol{\sigma}) = 0.$$

In short, one has for all admissible fields $\boldsymbol{v}' \in \mathscr{K}_a$ and $\boldsymbol{\sigma}' \in \mathscr{S}_a$:

$$B\big(\boldsymbol{v}', \boldsymbol{\sigma}\big) \geq B(\boldsymbol{v}, \boldsymbol{\sigma}) = 0 \quad \text{and} \quad B\big(\boldsymbol{v}, \boldsymbol{\sigma}'\big) \geq B(\boldsymbol{v}, \boldsymbol{\sigma}) = 0,$$

which proves (28).

Now, let us discuss some relevant aspects of the variational principles for rigid perfectly plastic materials such as the one described in the previous sections. The set of plastically admissible velocity and stress fields are respectively defined as:

$$\mathscr{K}_p = \big\{\boldsymbol{v} \text{ s.t. } H\big(\boldsymbol{d}(\boldsymbol{v})\big) \leq 0 \text{ in } V_M\big\},$$
$$\mathscr{S}_p = \big\{\boldsymbol{\sigma} \text{ s.t. } F(\boldsymbol{\sigma}) \leq 0 \text{ in } V_M\big\}.$$

The sets of licit velocity and stress fields are respectively $\mathscr{K}_l = \mathscr{K}_a \cap \mathscr{K}_p$ and $\mathscr{S}_l = \mathscr{S}_a \cap \mathscr{S}_p$ while we considered the finite valued functional:

$$B_0\big(\boldsymbol{v}', \boldsymbol{\sigma}'\big) = V^{-1} \int_{V_M} \big(b_0\big(\boldsymbol{d}\big(\boldsymbol{v}'\big), \boldsymbol{\sigma}'\big) + \boldsymbol{d}\big(\boldsymbol{v}'\big) : p\mathbf{1}\big) dV - \boldsymbol{D} : (\boldsymbol{\Sigma} + p\mathbf{1}).$$

Hence, the variational homogenization problem becomes:

$$B_0(\boldsymbol{v}, \boldsymbol{\sigma}) = \min_{\boldsymbol{v}' \in \mathscr{K}_l} B_0\big(\boldsymbol{v}', \boldsymbol{\sigma}\big) = \min_{\boldsymbol{\sigma}' \in \mathscr{S}_l} B_0\big(\boldsymbol{v}, \boldsymbol{\sigma}'\big) = 0. \tag{29}$$

For rigid perfectly plastic, because b_0 is positively homogeneous of order one in $\boldsymbol{d}$, there is a trivial kinematical solution to the previous problem where $\boldsymbol{v}$ and $\boldsymbol{D}$ vanish.

The limit analysis approach consists in finding nontrivial solutions qualified as collapse mechanisms. It is expected that there exist only under an equality condition on $\boldsymbol{\Sigma}$ that can be interpreted as the equation of the yielding surface in the macroscopic model.

It is worth noting that if both $\boldsymbol{D}$ and $\boldsymbol{\Sigma}$ are chosen arbitrarily, there is in general no solution to the problem (29). In a practical point of view, it is more convenient for instance to fix only $\boldsymbol{\Sigma}$ and to find $\boldsymbol{D}$ and $\boldsymbol{v}$ satisfying the first minimization problem in (29). Introducing Lagrange's multiplier field $\boldsymbol{x} \mapsto \lambda(\boldsymbol{x})$, this constrained minimization problem is transformed into an equivalent saddle-point problem

$$\max_{\lambda \geq 0} \min_{\boldsymbol{v} \in \mathscr{K}_a} \left(\mathscr{L}(\boldsymbol{v}, \boldsymbol{\sigma}, \lambda) = B_0(\boldsymbol{v}, \boldsymbol{\sigma}) + V^{-1} \int_{V_M} \lambda H(\boldsymbol{d}) dV \right).$$

Following [34], we perform a first approximation by imposing Lagrange's multiplier field to be uniform in V_M:

$$\max_{\lambda \geq 0} \min_{\boldsymbol{v} \in \mathscr{K}_a} \left(\mathscr{L}(\boldsymbol{v}, \boldsymbol{\sigma}, \lambda) = B_0(\boldsymbol{v}, \boldsymbol{\sigma}) + \lambda V^{-1} \int_{V_M} H(\boldsymbol{d}) dV \right),$$

that is equivalent to minimize the bifunctional B_0 under the relaxed kinematical condition:

$$V^{-1} \int_{V_M} H(\boldsymbol{d}) dV = 0. \tag{30}$$

Satisfying the kinematical condition only in an average sense but not locally anywhere in V_M is a strong approximation but leading to easier calculations. As consequence of the approximation, it is crucial to remark that the minimum of B_0 may not be expected to be zero. Nevertheless, in the spirit of Ladevèze's method of the error on the constitutive law [45–51], its value for the minimizer can be used as a variational error estimator [30]. The minimum principle allows obtaining the "better"solution within the framework imposed by the approximations.

Introducing the macroscopic strain rate of the void and equivalent strain rate, respectively defined by:

$$\boldsymbol{D}_{void} = V^{-1} \int_{V_f} \boldsymbol{d} dV, \qquad \digamma(\boldsymbol{v}) = V^{-1} \int_{V_M} \dot{\varepsilon}^p dV,$$

condition (30) reads:

$$\beta \digamma(\boldsymbol{v}) - \frac{1}{3} \operatorname{tr}(\boldsymbol{D} - \boldsymbol{D}_{void}) = 0.$$

Introducing, as in [34], the normalized macro-stress tensor:

$$\boldsymbol{T} = \frac{\boldsymbol{\Sigma} + p\boldsymbol{1}}{\sigma_0 + 3\alpha p},$$

and accounting for (20), the normalized bifunctional is:

$$\bar{B}_0(\boldsymbol{v}, \boldsymbol{\sigma}) = \frac{B_0(\boldsymbol{v}, \boldsymbol{\sigma})}{\sigma_0 + 3\alpha p} = \frac{1}{3\alpha} \operatorname{tr}(\boldsymbol{D} - \boldsymbol{D}_{void}) + \left(1 - \frac{\beta}{\alpha}\right) \hat{\digamma}(\boldsymbol{v}, \boldsymbol{\sigma}) - \boldsymbol{D} : \boldsymbol{T},$$

where:

$$\hat{F}(\boldsymbol{v},\boldsymbol{\sigma}) = V^{-1}\int_{V_M}\frac{\sigma_0 - 3\alpha\sigma_m}{\sigma_0 + 3\alpha p}\dot{\varepsilon}^p dV. \tag{31}$$

Introducing the normalized multiplier $\bar{\lambda} = \lambda/(\sigma_0 + 3\alpha p)$, the normalized Lagrangian is:

$$\bar{\mathscr{L}}(\boldsymbol{v},\boldsymbol{\sigma},\bar{\lambda}) = \frac{\mathscr{L}(\boldsymbol{v},\boldsymbol{\sigma},\lambda)}{\sigma_0 + 3\alpha p},$$

$$\bar{\mathscr{L}}(\boldsymbol{v},\boldsymbol{\sigma},\bar{\lambda}) = \left(\frac{1}{\alpha} - \bar{\lambda}\right)\frac{1}{3}\operatorname{tr}(\boldsymbol{D} - \boldsymbol{D}_{void}) + \bar{\lambda}\beta F(\boldsymbol{v}) + \left(1 - \frac{\beta}{\alpha}\right)\hat{F}(\boldsymbol{v},\boldsymbol{\sigma}) - \boldsymbol{D}:\boldsymbol{T}. \tag{32}$$

3.4 Hollow Sphere Model with Nonassociated Drucker-Prager Type Matrix

We consider a hollow sphere made up of a spherical void embedded in a homothetic cell of a rigid-plastic isotropic and homogeneous material with nonassociated Drucker-Prager model. The inner and outer radii are respectively denoted a and b, giving the porosity $f = (a/b)^3 < 1$. Accounting for the central symmetry of the problem, the cylindrical coordinates (ρ, ϕ, z) are used, ρ and ϕ being the polar radius and angle, z the height with respect to the Oxy plane.

In order to limit the errors due to approximations, we hope the macroscopic model to be exact at least for the pure hydrostatic case. Taking into account the expression (12) of the velocity field obtained in the first part for the pure hydrostatic loading, the following trial velocity field is chosen:

$$\boldsymbol{v} = C_0\left(\frac{b}{r}\right)^{3/\tilde{s}}(\rho\boldsymbol{e}_\rho + z\boldsymbol{e}_z) + C_1\rho\boldsymbol{e}_\rho + C_2 z\boldsymbol{e}_z,$$

with $r = \sqrt{\rho^2 + z^2}$, $\tilde{s} = 1 + 2\varepsilon\beta$ where ε is the sign of C_0. The first term is the solution (12) of the pure hydrostatic case. As in Gurson's model [35] and its extension to pressure sensitive dilatant materials [34], it is completed by two linear terms to capture the shear effects. In this last paper, the macro-strain rate is shown to be:

$$\boldsymbol{D} = C_0\mathbf{1} + C_1(\boldsymbol{e}_\rho\otimes\boldsymbol{e}_\rho + \boldsymbol{e}_\phi\otimes\boldsymbol{e}_\phi) + C_2\boldsymbol{e}_z\otimes\boldsymbol{e}_z, \tag{33}$$

$$\boldsymbol{D}_{void} = C_0 f^{\tilde{\gamma}}\mathbf{1} + f\left[C_1(\boldsymbol{e}_\rho\otimes\boldsymbol{e}_\rho + \boldsymbol{e}_\phi\otimes\boldsymbol{e}_\phi) + C_2\boldsymbol{e}_z\otimes\boldsymbol{e}_z\right], \tag{34}$$

with $\tilde{\gamma} = 1 - \tilde{s}^{-1}$. Introducing the ratio:

$$\tilde{\omega} = \frac{2C_0}{\tilde{s}D_e},$$

the macroscopic equivalent strain rate is [34]:

$$F(\boldsymbol{v}) = D_e \int_f^1 \mathscr{J}(\zeta)\sqrt{1+\tilde{\omega}^2 x^{-2/\tilde{s}}}dx,$$

with

$$\mathscr{J}(\zeta) = \frac{1}{2}\int_0^\pi \sqrt{1+\frac{1}{2}\left(3\cos^2\theta - 1\right)\zeta}\,\sin\theta d\theta,$$

where

$$\zeta = \frac{2\tilde{\omega}x^{-1/\tilde{s}}}{1+\tilde{\omega}^2 x^{-2/\tilde{s}}}\,\mathrm{sign}(C_1 - C_2), \quad |\,\zeta\,| \leq 1.$$

On the other hand, the bifunctional depends on the stress field only through σ_m. Under condition (7), the following trial stress field is chosen as the solution (17) of the pure hydrostatic case, without additional terms:

$$\sigma_m(r) = \frac{1}{3\alpha}\left[\sigma_0 - (\sigma_0 + 3\alpha p)\frac{f^\gamma}{s}\left(\frac{b}{r}\right)^{3\gamma}\right],$$

where $s = 1 + 2\varepsilon\alpha$ and $\gamma = 1 - s^{-1}$. Introducing this expression into (31) gives:

$$\hat{F}(\boldsymbol{v},\boldsymbol{\sigma}) = V^{-1}\frac{f^\gamma}{s}\int_{V_M}\left(\frac{b}{r}\right)^{3\gamma}\dot{\varepsilon}^p dV = \frac{f^\gamma}{s}I(\gamma),$$

where

$$I(\gamma) = D_e\int_f^1 x^{-\gamma}\,\mathscr{J}(\zeta)\sqrt{1+\tilde{\omega}^2 x^{-2/\tilde{s}}}dx. \tag{35}$$

It is worth noting the particular case:

$$F(\boldsymbol{v}) = I(0).$$

The function $\mathscr{J}(\zeta)$ is smooth over the compactly supported domain with extreme values $\mathscr{J}_{max} = \mathscr{J}(0) = 1$ and $\mathscr{J}_{min} = \mathscr{J}(-1) = 0.962$. Following [35], this function is taken to be equal to unity, that reduces (35) to:

$$I(\gamma) = D_e\int_f^1 x^{-\gamma}\sqrt{1+\tilde{\omega}^2 x^{-2/\tilde{s}}}dx. \tag{36}$$

Accounting of (33) and (34), the normalized Lagrangian is:

$$\begin{aligned}\bar{\mathscr{L}}(\boldsymbol{v},\boldsymbol{\sigma},\bar{\lambda}) = &\left(\frac{1}{\alpha} - \bar{\lambda}\right)\left[(1-f)D_m - \left(f^{\tilde{\gamma}} - f\right)C_0\right]\\ &+ \bar{\lambda}\beta F(\boldsymbol{v}) + \left(1 - \frac{\beta}{\alpha}\right)\hat{F}(\boldsymbol{v},\boldsymbol{\sigma}) - (D_e T_e + 3D_m T_m),\end{aligned}$$

where F and $\hat{F}$ depends on C_0 and D_e. With simplified notations for partial derivatives, its stationarity with respect to D_e, D_m and C_0 gives:

$$T_e = \bar{\lambda}\beta F_{,D_e} + \left(1 - \frac{\beta}{\alpha}\right)\hat{F}_{,D_e}, \tag{37}$$

$$3T_m = \left(\frac{1}{\alpha} - \bar{\lambda}\right)(1-f), \tag{38}$$

$$\bar{\lambda}\beta F_{,C_0} + \left(1 - \frac{\beta}{\alpha}\right)\hat{F}_{,C_0} - \left(\frac{1}{\alpha} - \bar{\lambda}\right)\left(f^{\tilde{\gamma}} - f\right) = 0. \tag{39}$$

From (39), we deduce the expression of the multiplier:

$$\bar{\lambda} = \frac{\frac{1}{\alpha}(f^{\tilde{\gamma}} - f) + (\frac{\beta}{\alpha} - 1)\hat{F}_{,C_0}}{f^{\tilde{\gamma}} - f + \beta F_{,C_0}}.$$

Eliminating it in (37) and (38) leads to:

$$T_e = \frac{(f^{\tilde{\gamma}} - f)[\frac{\beta}{\alpha}F_{,D_e} + (1 - \frac{\beta}{\alpha})\hat{F}_{,D_e}] + (1 - \frac{\beta}{\alpha})\beta(F_{,C_0}\hat{F}_{,D_e} - F_{,D_e}\hat{F}_{,C_0})}{f^{\tilde{\gamma}} - f + \beta F_{,C_0}}, \tag{40}$$

$$3T_m = (1-f)\frac{\frac{\beta}{\alpha}F_{,C_0} + (1 - \frac{\beta}{\alpha})\hat{F}_{,C_0}}{f^{\tilde{\gamma}} - f + \beta F_{,C_0}}. \tag{41}$$

3.5 Limit Cases

Let us examine the particular cases of pure hydrostatic and deviatoric loadings.

- **Purely hydrostatic case:** $|\tilde{\omega}| = +\infty \implies D_e = 0$. The integral (36) is:

$$I(\gamma) = |\tilde{\omega}| D_e \int_f^1 x^{-\gamma - \tilde{s}^{-1}} dx = \frac{2|C_0|}{\tilde{s}} \frac{1 - f^{\tilde{\gamma}-\gamma}}{\tilde{\gamma} - \gamma}.$$

  Then, it holds:

$$F(\boldsymbol{v}) = I(0) = \frac{C_0}{\beta}\left(1 - f^{\tilde{\gamma}}\right), \qquad \hat{F}(\boldsymbol{v}, \boldsymbol{\sigma}) = \frac{C_0}{\beta - \alpha}\left(f^{\gamma} - f^{\tilde{\gamma}}\right),$$

$$f^{\tilde{\gamma}} - f + \beta F_{,C_0} = 1 - f.$$

  Finally, the macro-stress is given by (40) and (41):

$$T_e = 0, \qquad 3T_m = \frac{1}{\alpha}\left(1 - f^{\gamma}\right), \tag{42}$$

  that was expected with respect to the exact result (16) determined in the first part. The solution is the same as for the corresponding associated case [34].

- **Purely deviatoric case:** $\tilde{\omega} = 0 \Longrightarrow C_0 = 0$. The integral (36) is:

$$I(\gamma) = D_e \int_f^1 x^{-\gamma} dx = D_e \frac{1 - f^{1-\gamma}}{1 - \gamma}.$$

  Then, it holds:

$$F(\boldsymbol{v}) = I(0) = D_e(1-f), \qquad \hat{F}(\boldsymbol{v}, \boldsymbol{\sigma}) = D_e\left(f^{\gamma} - f\right),$$

$$f^{\tilde{\gamma}} - f + \beta \Gamma_{,C_0} = f^{\tilde{\gamma}} - f.$$

Finally, the macro-stress is given by (40) and (41):

$$T_e = 1 - f + \left(1 - \frac{\beta}{\alpha}\right)\left(f^{\gamma} - f\right), \quad T_m = 0. \tag{43}$$

When the flow rule is associated, we recover the result obtained in [34]. Nevertheless, the accuracy of (43) is poor for strong lack of associativity. The weakness of this model is that we use the expression (17) of the mean stress deriving from the solution in the pure hydrostatic case. We are currently working to improve the trial stress field by introducing additional terms into (17) and working on the stress principle.

4 Conclusion

Unlike currently observed in other problems, in the one of the hydrostatically loaded hollow sphere the limit load and collapse stress field for the nonassociated cases are the same as for the corresponding associated case. This event may appear at first glance paradoxical. The key point is the strong condition of central symmetry which is very restrictive and prevents field discontinuities generally allowed by the continuum mechanics. Thus only complete solution with a unique plastic regime is considered and it is necessarily identical to the one of the associated case. The general case of combined hydrostatic and deviatoric loadings is in progress. The first elements of the corresponding theory are exposed in Sect. 3.

References

1. Barthélémy JF, Dormieux L (2003) Détermination du critère de rupture macroscopique d'un milieux poreux par homogénéisation nonlinéaire. C R, Méc 331:271–276
2. Benzerga AA, Besson J (2001) Plastic potentials for anisotropic porous solids. Eur J Mech A, Solids 20:397–434
3. Berga A, de Saxcé G (1994) Elastoplastic finite element analysis of soil problems with implicit standard material constitutive laws. Rev Eur Éléments Finis 3:411–456
4. Bodovillé G (1999) On damage and implicit standard materials. C R Acad Sci Paris, Sér II, Fasc B, Méc Phys Astron 327:715–720
5. Bodovillé G, de Saxcé G (2001) Plasticity with nonlinear kinematic hardening: modelling and shakedown analysis by the bipotential approach. Eur J Mech A, Solids 20:99–112
6. Bouby C, de Saxcé G, Tritsch JB (2006) A comparison between analytical calculations of the shakedown load by the bipotential approach and step-by-step computations for elastoplastic materials with nonlinear kinematic hardening. Int J Solids Struct 43:2670–2692
7. Bouby C, de Saxcé G, Tritsch JB (2009) Shakedown analysis: comparison between models with the linear unlimited, linear limited and nonlinear kinematic hardening. Mech Res Commun 36:556–562
8. Bousshine L, Chaaba A, de Saxcé G (2001) Softening in stress-strain curve for Drucker-Prager non-associated plasticity. Int J Plast 17:21–46

9. Bousshine L, Chaaba A, de Saxcé G (2002) Plastic limit load of plane frames with frictional contact supports. Int J Mech Sci 44:2189–2216
10. Bousshine L, Chaaba A, de Saxcé G (2003) A new approach to shakedown analysis for non-standard elastoplastic material by the bipotential. Int J Plast 19:583–598
11. Buliga M, de Saxcé G, Vallée C (2008) Existence and construction of bipotential for graphs of multivalued laws. J Convex Anal 15:87–104
12. Buliga M, de Saxcé G, Vallée C (2009) Bipotentials for non-monotone multivalued operators: fundamental results and applications. Acta Appl Math 110:955–972
13. Buliga M, de Saxcé G, Vallée C (2011) Blurred constitutive laws and bipotential convex covers. Math Mech Solids 16:161–171
14. Buliga M, de Saxcé G, Vallée C (2010) Nonmaximal cyclically monotone graphs and construction of a bipotential for the Coulomb's dry friction law. J Convex Anal 17:81–94
15. Buliga M, de Saxcé G, Vallée C (2010) Blurred maximal cyclically monotone sets and bipotentials. Anal Appl 8:323–336
16. Chaaba A, Bousshine L, de Saxcé G (2010) Kinematic limit analysis of nonassociated perfectly plastic material by the bipotential approach and finite element method. J Appl Mech 77:16–31
17. Chen WF (1975) Limit analysis and soil plasticity. Elsevier, New York
18. Chen WF, Liu XL (1990) Limit analysis in soil mechanics. Developments in geotechnical engineering, vol 52
19. Cheng L, Jia Y, Oueslati A, de Saxce G, Kondo D (2012) Plastic limit state of the hollow sphere model with nonassociated Drucker-Prager material under isotropic loading. Comput Mater Sci 62:210–215
20. de Saxcé G, Feng ZQ (1991) New inequality and functional for contact friction: the implicit standard material approach. Mech Struct Mach 19:301–325
21. de Saxcé G (1992) Une généralisation de l'inégalité de Fenchel et ses applications aux lois constitutives. C R Acad Sci Paris, Sér II 314:125–129
22. de Saxcé G, Bousshine L (1993) On the extension of limit analysis theorems to the nonassociated flow rules in soils and to the contact with Coulomb's friction. In: XI Polish conference on computer methods in mechanics, Kielce, Poland, pp 815–822
23. de Saxcé G (1995) The bipotential method, a new variational and numerical treatment of the dissipative laws of materials. In: Proceedings of the 10th international conference on mathematical and computer modelling and scientific computing, Boston, Massachusetts
24. de Saxcé G, Bousshine L (1998) Limit analysis theorems for the implicit standard materials: application to the unilateral contact with dry friction and the non-associated flow rules in soils and rocks. Int J Mech Sci 40:387–398
25. de Saxcé G, Feng ZQ (1998) The bi-potential method: a constructive approach to design the complete contact law with friction and improved numerical algorithms. Math Comput Model 6:225–245
26. de Saxcé G, Bousshine L (2002) Implicit standard materials. In: Weichert D, Maier G (eds) Inelastic behaviour of structures under variable repeated loads. CISM courses and lectures, vol 432. Springer, Wien
27. Ekeland I, Temam R (1975) Convex analysis and variational problems. North Holland, Amsterdam
28. Feng ZQ, Hjiaj M, de Saxcé G, Mróz Z (2006) Effect of frictional anisotropy on the quasistatic motion of a deformable solid sliding on a planar surface. Comput Mech 37:349–361
29. Feng ZQ, Hjiaj M, de Saxcé G, Mróz Z (2006) Influence of frictional anisotropy on contacting surfaces during loading/unloading cycles. Int J Non-Linear Mech 41:936–948
30. Fortin J, de Saxcé G (1999) Modélisation numérique des milieux granulaires par l'approche du bipotentiel. C R Acad Sci, Sér IIb 327:721–724
31. Fortin J, Hjiaj M, de Saxcé G (2002) An improved discrete element method based on a variational formulation of the frictional contact law. Comput Geotech 29:609–640
32. Garajeu M, Suquet P (1997) Effective properties of porous ideally plastic or viscoplastic materials containing rigid particles. J Mech Phys Solids 45:873–902

33. Gologanu M, Leblond JB, Perrin G, Devaux J (1997) Recent extensions of Gurson's model for porous ductile metals. In: Suquet P (ed) Continuum micromechanics. Springer, Berlin
34. Guo TF, Faleskog J, Shih CF (2008) Continuum modeling of a porous solid with pressure-sensitive dilatant matrix. J Mech Phys Solids 56:2188–2212
35. Gurson AL (1977) Continuum theory of ductile rupture by void nucleation and growth, part I: yield criteria and flow rules for porous ductile media. J Eng Mater Technol 99:2–15
36. Halphen B, Nguyen Quoc S (1975) Sur les matériaux standard généralisés. C R Acad Sci Paris 14:39–63
37. Hjiaj M, Bodovillé G, de Saxcé G (2000) Matériaux viscoplastiques et loi de normalité implicites. C R Acad Sci Paris, Sér II, Fasc B, Méc Phys Astron 328:519–524
38. Hjiaj M, de Saxcé G, Mróz Z (2002) A variational-inequality based formulation of the frictional contact law with a non-associated sliding rule. Eur J Mech A, Solids 21:49–59
39. Hjiaj M, Fortin J, de Saxcé G (2003) A complete stress update algorithm for the non-associated Drucker-Prager model including treatment of the apex. Int J Eng Sci 41:1109–1143
40. Hjiaj M, Feng ZQ, de Saxcé G, Mróz Z (2004) Three dimensional finite element computations for frictional contact problems with on-associated sliding rule. Int J Numer Methods Eng 60:2045–2076
41. Jeong HY, Pan J (1995) A macroscopic constitutive law for porous solids with pressure-sensitive matrices and its applications to plastic flow localization. J Mech Phys Solids 39:1385–1403
42. Jeong HY (2002) A new yield function and a hydrostatic stress-controlled model for porous solids with pressure-sensitive matrices. J Mech Phys Solids 32:3669–3691
43. Jia Y (2006) Contribution à la modélisation thermo-hydro-mécanique des roches partiellement saturées: application au stockage des déchets radioactifs. Thesis of University of Lille 1
44. Laborde P, Renard Y (2008) Fixed points strategies for elastostatic frictional contact problems. Math Methods Appl Sci 31:415–441
45. Ladevèze P (1975) Comparaisons de modèles de milieux continus. Thèse d'Etat, Université Pierre et Marie Curie, Paris
46. Ladevèze P, Coffignal G, Pelle JP (1986) Accuracy of elastoplastic and dynamic analysis. In: Babuska I, Gago J, Oliveira E, Zienkiewicz OC (eds) Accuracy estimates and adaptive refinements in finite element computations. Wiley, New York, pp 181–203
47. Ladevèze P, Pelle JP, Rougeot P (1991) Error estimation and mesh optimization for classical finite element. Eng Comput 8:69–80
48. Ladevèze P, Moes N (1997) A new a posteriori error estimation for nonlinear time-dependent finite element analysis. Comput Methods Appl Mech Eng 157:45–68
49. Ladevèze P, Pelle JP (2001) La maîtrise du calcul en mécanique linéaire et non linéaire. Hermes Science, Paris
50. Ladevèze P, Florentin E (2006) Verification of stochastic models in uncertain environments using the constitutive relation error method. Comput Methods Appl Mech Eng 196:224–225
51. Ladevèze P, Puel G, Deraemaeker A, Romeuf T (2006) Validation of structural dynamics models containing uncertainties. Comput Methods Appl Mech Eng 195:373–393
52. Maghous S, Dormieux L, Barthélémy JF (2009) Micromechanical approach to the strength properties of frictional geomaterials. Eur J Mech A, Solids 28:179–188
53. Magnier V, Charkaluk E, Bouby C, de Saxcé G (2006) Bipotential versus return mapping algorithms: implementation of non-associated flow rules. In: Topping BHV, Montero G, Montenegro R (eds) Proceedings of the eighth international conference on computational structures technology, Las Palmas de Gran Canaria, September 12–15, 2006. Civil-Comp Press, Stirlingshire, paper 68
54. Monchiet V, Charkaluk E, Kondo D (2007) An improvement of Gurson-type models of porous materials by Eshelby-like trial velocity fields. C R, Méc 335:32–41
55. Monchiet V, Cazacu O, Kondo D (2008) Macroscopic yield criteria for plastic anisotropic materials containing spheroidal voids. Int J Plast 24:1158–1189
56. Moreau JJ (2003) Fonctionnelles convexes. Istituto Poligrafico e Zecca dello Stato, Rome
57. Rockafellar RT (1970) Convex analysis. Princeton University Press, Princeton

58. Save MA, Massonnet CE, de Saxcé G (1997) Plastic limit analysis of plates, shells and disks. Elsevier, New York
59. Shao JF, Jia Y, Kondo D, Chiarelli AS (2006) A coupled elastoplastic damage model for semi-brittle materials and extension to unsaturated conditions. Mech Mater 38:218–232
60. Thoré P, Pastor F, Pastor J, Kondo D (2009) Closed-form solutions for the hollow sphere model with Coulomb and Drucker-Prager materials under isotropic loadings. C R, Méc 337:260–267
61. Vallée C, Lerintiu C, Fortuné D, Ban M, de Saxcé G (2005) Hill's bipotential. In: Mihailescu-Suliciu M (ed) New trends in continuum mechanics. Theta series in advanced mathematics. Theta Foundation, Bucharest, pp 339–351
62. Zouain N, Pontes Filho I, Borges L, Mouta da Costa L (2007) Plastic collapse in non-associated hardening materials with application to Cam-clay. Int J Solids Struct 44:4382–4398

Direct Evaluation of the Post-Buckling Behavior of Slender Structures Through a Numerical Asymptotic Formulation

Giovanni Garcea, Antonio Bilotta, Antonio Madeo, and Raffaele Casciaro

Abstract The analysis of slender structures, characterized by complex buckling and postbuckling phenomena and by a strong imperfection sensitivity, is heavily penalized by the lack of adequate computational tools. Standard incremental iterative approaches are computationally expensive and unaffordable, while FEM implementation of the Koiter method is a convenient alternative. The analysis is very fast, its computational burden is of the same order as a linearized buckling load evaluation and the simulation of different imperfections costs only a fraction of that needed to characterize the perfect structure. In this respect it can be considered as a direct method for the evaluation of the critical and post-critical behaviour of geometrically nonlinear elastic structures. The main objective of the present work is to show that finite element implementations of the Koiter method can be both accurate and reliable and to highlight the aspects that require further investigation.

1 Introduction

A global evaluation of the structural collapse safety of slender elastic structures should consider all possible loadings, including the deviations due to load imperfections and geometrical defects. Standard path-following approaches, aimed at recovering the equilibrium path for a single loading case and assigned imperfections, are not suitable for this purpose. In fact in order to perform a reliable structural safety assessment the nonlinear analysis should be performed with respect to all possible imperfection shapes. The consequent computational burden can be very

G. Garcea (✉) · A. Bilotta · A. Madeo · R. Casciaro
Dipartimento di Modellistica per l'Ingegneria, Università della Calabria, Rende, Italy
e-mail: giovanni.garcea@unical.it

A. Bilotta
e-mail: antonio.bilotta@unical.it

A. Madeo
e-mail: antonio.madeo81@unical.it

R. Casciaro
e-mail: raffaele.casciaro@unical.it

K. Spiliopoulos, D. Weichert (eds.), *Direct Methods for Limit States in Structures and Materials*, DOI 10.1007/978-94-007-6827-7_10,

high particularly if no reliable information about the worst imperfection shapes is available.

The asymptotic approach, derived as a finite element implementation [1–5, 7, 11, 12, 21, 22, 29, 30, 32–36] of the Koiter nonlinear theory of elastic stability [25], can be a convenient alternative as it provides an effective and reliable strategy for predicting the initial post-critical behavior in both cases of limit or bifurcation points [8, 27, 28]. The implementation of the asymptotic approach as a computational tool, as will be shown, is quite easy and its total computational burden remains of the order as that required by a standard linearized stability analysis. It provides the initial post-buckling behavior of the structure, including *modal interactions* and *jumping-after-bifurcation* phenomena. Moreover, once the analysis has been performed, the presence of small loading imperfections or geometrical defects can be taken into account in a postprocessing phase with a negligible computational extra–cost, so allowing an inexpensive imperfection sensitivity analysis (e.g. see [9, 27]). It is also possible to extract information about the worst imperfection shapes [10, 31], and it can be used to improve the imperfection sensitivity analysis or for driving more detailed investigations through specialized path-following analysis (see [8, 10] and references therein). From this point of view we can affirm that in the field of geometrically nonlinear elastic structures, the Koiter asymptotic method works as a direct method suitable to evaluate the critical and post-critical behaviour of structures and in this sense it is similar to direct methods for limit and shakedown analysis.

The asymptotic analysis can provide a very accurate recovery of the equilibrium path, as it is confirmed by numerical testings and theoretical investigations [6] but requires great care in both the mechanical modeling [15, 16] and its finite element implementation. As will be shown in the paper accuracy cannot be obtained by an inappropriate finite element interpolation due to the occurrence of *interpolation locking* phenomena in the evaluation of the energy variation terms used to reconstruct the post-critical behaviour [8, 28]; by an inappropriate format used in the control variables that can produce *extrapolation locking* phenomena [13, 18]) or by the use of non objective structural models [15, 16].

The paper is organized as follows: Sect. 2 presents the local analysis and some definitions, Sect. 3 presents the asymptotic method and its finite element implementation, Sect. 4 discusses all the aspects regarding the FEM implementation and the accuracy, Sect. 5 gives some numerical results show the potential of the method and finally Sect. 6 summarizes the discussion and suggests possible extensions.

2 Local Analysis

Adopting the same functional notation as the paper of Budiansky [7] we consider a hyperelastic structure subjected to an assigned load, $p[\lambda]$, which is linear with a λ parameter ($p[\lambda] = \lambda \hat{p}$) and described by its potential energy $\Pi[u]$ in terms of *stress and displacement* here denoted by u. Equilibrium implies the condition

$$\Pi' \delta u := \Phi'[u]\delta u - \lambda \hat{p} \delta u = 0, \quad \forall \delta u \in \mathscr{T} \tag{1}$$

where $\Phi[u]$ is the strain energy, $p[\lambda]u$ the external work, $\mathscr{U}$ the manifold of the admissible configurations and $\mathscr{T}$ its tangent space (the prime stands for the Frechèt's differentiation with respect to u). Usually (and conveniently) the configuration is described making $\mathscr{U}$ a linear manifold, so $\mathscr{T}$ becomes independent from u.

Equation (1) defines a curve (it may be composed of several separate branches) in the space (u, λ), called *equilibrium path* that can be expressed in a parametric form in terms of a suitable abscissa $\xi = g[u, \lambda]$

$$\begin{cases} u = u[\xi], \\ \lambda = \lambda[\xi] \end{cases} \tag{2}$$

selected so that $\xi = 0$ gives the known equilibrium point (u_0, λ_0). The aim of the asymptotic analysis is the evaluation of the equilibrium path starting from this known configuration usually assumed corresponding to $\lambda_0 = 0$, exploiting an implementation of the Koiter approach to elastic stability [25] in a FEM context.

2.1 Asymptotic Expansion in a Regular Point

The solution process, based on a fourth-order expansion of the potential energy in terms of λ and ξ, is briefly summarized in the following (more details can be found in [8, 13, 18, 27, 28] and references therein).

Denoting by a dot the derivative with respect to ξ and assuming the equilibrium path is analytical in the vicinity of $\xi = 0$ (see [8]), the Taylor expansion of Eq. (2) is

$$\begin{cases} u[\xi] = u_0 + \dot{u}_0\xi + \frac{1}{2}\ddot{u}_0\xi^2 + \frac{1}{6}\dddot{u}_0\xi^3 + \cdots, \\ \lambda[\xi] = \lambda_0 + \dot{\lambda}_0\xi + \frac{1}{2}\ddot{\lambda}_0\xi^2 + \frac{1}{6}\dddot{\lambda}_0\xi^3 + \cdots \end{cases} \tag{3}$$

where a subscript denotes the point in which the quantities are evaluated and $(\dot{u}_0, \dot{\lambda}_0)$, $(\ddot{u}_0, \ddot{\lambda}_0)$, etc are the tangent, curvature etc. of the equilibrium path in $\xi = 0$. Expressing Eq. (1) using the parametrization in Eq. (2) we obtain a function of the real variable ξ, its Taylor expansion in $\xi = 0$ furnishing

$$\begin{aligned} \big(\Phi'\big[u[\xi]\big] - \lambda[\xi]\hat{p}\big)\delta u = {} & \big(\Phi_0' - \lambda_0\hat{p}\big)\delta u \\ & + \xi\big(\Phi_0''\dot{u}_0 - \dot{\lambda}_0\hat{p}\big)\delta u \\ & + \frac{1}{2}\xi^2\big(\Phi_0''\ddot{u}_0 + \Phi_0'''\dot{u}_0^2 - \ddot{\lambda}_0\hat{p}\big)\delta u \\ & + \frac{1}{6}\xi^3\big(\Phi_0''\dddot{u}_0 + 3\Phi_0'''\dot{u}_0\ddot{u}_0 + \Phi_0''''\dot{u}_0^3 - \dddot{\lambda}_0\hat{p}\big)\delta u + \cdots \end{aligned} \tag{4}$$

where $\Phi_0' \equiv \Phi'[u_0]$, $\Phi_0'' \equiv \Phi''[u_0]$, etc.

Equation (4) is a polynomial that has to be zero for each value of ξ, this means that all the coefficients, i.e. the derivative of Eq. (4) with respect to ξ to a given order, has to be zero. We obtain, in this way, the *perturbation equation* at each order

$$\left.\begin{aligned}
&\big(\Phi_0''\dot{u}_0 - \dot{\lambda}_0\hat{p}\big)\delta u = 0,\\
&\big(\Phi_0''\ddot{u}_0 - \ddot{\lambda}_0\hat{p}\big)\delta u = -\Phi_0'''\dot{u}_0^2\delta u,\\
&\big(\Phi_0''\dddot{u}_0 - \dddot{\lambda}_0\hat{p}\big)\delta u = -\big(3\Phi_0'''\dot{u}_0\ddot{u}_0 + \Phi_0''''\dot{u}_0^3\big)\delta u,\\
&\ldots = \ldots
\end{aligned}\right\} \quad \forall \delta u \in \mathscr{T} \tag{5}$$

with the perturbation equation of order zero not reported because it is verified "a priori" by the equilibrium point (u_0, λ_0).

In order to solve (5) in a point where the operator $\Phi''[u_0]$ is not singular, i.e. a *regular point*, we have to add to Eqs. (5) the *normalization condition*, that is the definition of the abscissa introduced to parametrize the equilibrium curve, $\xi := g[u, \lambda]$, whose asymptotic expansion gives

$$\left\{\begin{aligned}
&g_0'\dot{u}_0 + \hat{g}_0\dot{\lambda}_0 = 1,\\
&g_0'\ddot{u}_0 + \hat{g}_0\ddot{\lambda}_0 = -g_0''\dot{u}_0^2 - \hat{\hat{g}}_0\dot{\lambda}_0^2 - 2\hat{g}_0'\dot{\lambda}_0\dot{u}_0,\\
&g_0'\dddot{u}_0 + \hat{g}_0\dddot{\lambda}_0 = -g_0'''\dot{u}_0^3 - \hat{\hat{\hat{g}}}_0\dot{\lambda}_0^3 - 3g_0''\dot{u}_0\ddot{u}_0 - 3\hat{g}_0'\ddot{u}_0\dot{\lambda}_0,\\
&\qquad\qquad - 3\hat{g}_0'\dot{u}_0\ddot{\lambda}_0 - 3\hat{\hat{g}}_0\dot{\lambda}_0\ddot{\lambda}_0 - 3\hat{\hat{g}}_0'\dot{u}_0\dot{\lambda}_0^2 - 3\hat{g}_0''\dot{u}_0^2\dot{\lambda}_0
\end{aligned}\right. \tag{6}$$

where a hat denotes the derivative with respect to λ. Equations (5) and (6) allow us to define the necessary asymptotic quantities unequivocally.

The solution of the initial nonlinear problem is then reduced to the solution of a sequence of linear problems that define, at each order, the asymptotic terms of that order

$$\begin{aligned}
(\dot{u}_0, \dot{\lambda}_0) \rightarrow &\begin{cases} \Phi_0''\dot{u}_0\delta u - \dot{\lambda}_0\hat{p}\delta u = 0, \quad \forall \delta u,\\ g_0'\dot{u}_0 + \hat{g}_0\dot{\lambda}_0 = 1, \end{cases}\\
(\ddot{u}_0, \ddot{\lambda}_0) \rightarrow &\begin{cases} \Phi_0''\ddot{u}_0\delta u + \Phi_0'''\dot{u}_0^2\delta u - \ddot{\lambda}_0\hat{p}\delta u = 0, \quad \forall \delta u,\\ g_0'\ddot{u}_0 + \hat{g}_0\ddot{\lambda}_0 = -g_0''\dot{u}_0^2 - \hat{\hat{g}}_0\dot{\lambda}_0^2 - 2\hat{g}_0'\dot{\lambda}_0\dot{u}_0 \end{cases}\\
&\ldots
\end{aligned} \tag{7}$$

This is an important feature of the method which decouples each order from the next one and allows the asymptotic expansion to be stopped at the desired order.

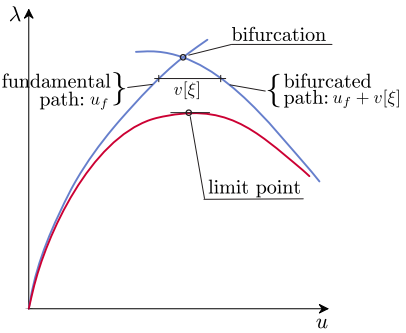

Fig. 1 Limit and bifurcation points of the equilibrium path

2.2 Asymptotic Expansion in a Critical Point

The equilibrium path can present either *limit points* or *bifurcations*, both types being *critical points* because the second variation of the strain energy, i.e. the tangent to the equilibrium path, is singular. Denoting a critical point by (u_c, λ_c), there exists at least one *critical mode* $\dot{v}_c$ such that

$$\Phi_c'' \dot{v}_c \delta u = 0, \quad \forall \delta u \in \mathscr{T}. \tag{8}$$

Let us now consider the single mode case, i.e. $\dim(\ker(\Phi_c'')) = 1$. The perturbation equations (7) with respect to the critical point can be written, as well as the regular point case. Due to the singularity of Φ_c'' in order to verify the first of Eq. (7) for $\delta u = \dot{v}_c$, the satisfaction of the following *Fredholm orthogonality* condition on the first order perturbation equation is required:

$$\dot{\lambda}_c \hat{p} \dot{v}_c = 0. \tag{9}$$

Equation (9) is verified in both cases of $\dot{\lambda}_c = 0$, i.e. a *limit point* for the loads, and of $\hat{p}\dot{v}_c = 0$ i.e. a *bifurcation point* (see Fig. 1).

2.2.1 Limit Point

In this case the tangent to the equilibrium path, $(\dot{u}_c, \dot{\lambda}_c)$, is unequivocally defined from the first condition (7). In particular the solution assumes the following expression

$$\dot{u}_c = \beta \dot{v}_c, \qquad \dot{\lambda}_c = 0 \tag{10}$$

where the values of β are defined by the normalization condition

$$\beta\left(g_c' \dot{v}_c\right) = 1.$$

With a similar procedure it is also possible to show how the curvature $(\ddot{u}_c, \ddot{\lambda}_c)$ is unequivocally defined. This means that a limit point behaves, with respect to the asymptotic expansion, like a regular point.

2.2.2 Bifurcation Point

When $p\dot{v}_c \neq 0$ using the first of Eqs. (7) and due to the singularity of Φ_c'', the tangent has the following expression

$$\dot{u}_c = \dot{\lambda}_c \hat{u}_c + \beta \dot{v}_c \tag{11}$$

where $\hat{u}_c$ is a particular solution of the equation

$$\Phi_c'' \hat{u}_c \delta u - \hat{p}\delta u = 0, \quad \forall \delta u \in \mathscr{T} \tag{12}$$

and $\beta \dot{v}_c$ is the solution of the homogenous equation (8).

Now the normalization condition is no longer sufficient to evaluate the solution because we need to evaluate both β and $\dot{\lambda}_c$. Also in this case we can use the Fredholm condition applied to the perturbation equation of the second order, evaluated for $\delta u = \dot{v}_c$, that is

$$\overbrace{\Phi_c'' \ddot{u}_c \dot{v}_c}^{0} + \Phi_c''' \dot{u}_c^2 \dot{v}_c - \ddot{\lambda}_c \overbrace{\hat{p}\dot{v}_c}^{0} = 0 \quad \Rightarrow \quad \Phi_c''' \dot{u}_c^2 \dot{v}_c = 0. \tag{13}$$

After substitution of $\dot{u}_c$ from (11) we have the second order polynomial equation

$$\dot{\lambda}_c^2 \Phi_c''' \hat{u}_c^2 \dot{v}_c + 2\dot{\lambda}_c \beta \Phi_c''' \hat{u}_c \dot{v}_c^2 + \beta^2 \Phi_c''' \dot{v}_c^3 = 0 \tag{14}$$

that, together with the normalization condition linear in $\dot{\lambda}_c$ and β

$$\dot{\lambda}_c \left(g_c' \hat{u}_c + \hat{g}_c \right) + \beta g_c' \dot{v}_c = 1, \tag{15}$$

gives the two values of the tangent. The condition $p\dot{v}_c = 0$ then detects a bifurcation point characterized by two different equilibrium paths with two different tangents.

For a given value of β we can define, from Eq. (14) two values of $\dot{\lambda}_c$. A particular case occurs when, with an appropriate selection of the parametrization, one of the tangents is characterized by the value $\beta = 0$. In this case Eq. (14) and condition $\dot{\lambda}_c \neq 0$, require that:

$$\Phi_c''' \hat{u}_c^2 \dot{v}_c = 0.$$

The two tangents are then

$$\begin{cases} \dot{u}_c^{(1)} = \hat{u}_c, \\ \dot{\lambda}_c^{(1)} = 1, \end{cases} \qquad \begin{cases} \dot{u}_c^{(2)} = \dot{\lambda}_c^{(2)} \hat{u}_c + \beta \dot{v}_c, \\ \dot{\lambda}_c^{(2)} = -\dfrac{1}{2}\beta \dfrac{\Phi_c''' \dot{v}_c^3}{\Phi_c''' \hat{u}_c \dot{v}_c} \end{cases}$$

with β defined by the normalization condition. For the first tangent we have

$$\dot{\lambda}_c = \left. \frac{\partial \lambda[\xi]}{\partial \xi} \right|_{\xi=0} = 1 \tag{16}$$

that is a path parameterized with $\xi = \lambda$ and for which all the higher order derivatives of λ with respect to ξ are zero. The discussion can be easily extended to the curvature (see [8]).

2.2.3 Path Representation on a Bifurcation Point

The previous discussion allows a different rewriting of the two paths passing through a simple bifurcation point. From a simple extension of the first order asymptotic expansion we use, the two solutions can be expressed as

$$\begin{cases} \lambda[\xi] = \lambda_c + \xi\dot{\lambda}_c + \cdots, \\ u[\xi, \lambda] = u^f[\lambda] + v[\xi] \end{cases} \tag{17}$$

with the *fundamental path*, that is the initial path followed by the structure starting from $\lambda = 0$, defined as

$$u^f[\lambda] = u_c + (\lambda - \lambda_c)\hat{u}_c$$

parameterized in λ and obtained from (17) by setting $\xi = 0$ while the *bifurcated path*,

$$v[\xi] = \xi\dot{v}_c + \frac{1}{2}\xi^2\ddot{v}_c + \cdots$$

intersects u^f in the bifurcation point. With this choice ξ measures the distance between u and u_f and can be selected as

$$\xi = \langle u - u_f, \dot{v}_c \rangle \approx \xi\langle \dot{v}_c, \dot{v}_c \rangle + \frac{1}{2}\xi^2\langle \dot{v}_c, \ddot{v}_c \rangle + \cdots \tag{18}$$

where $\langle \cdot, \cdot \rangle$ represents a given scalar product. Equation (18) at the first order furnishes a normalization condition for $\dot{v}_c$ while at the second order an orthogonality condition between $\dot{v}_c$ and $\ddot{v}_c$.

3 The Asymptotic Method

In this section an asymptotic algorithm capable of treating single or multiple, also not coincident, bifurcations and of considering the effects of a nonlinear precritical behaviour is presented. Further details can be found in [16–28].

3.1 The Fundamental Path

Let us start by considering a structure without external imperfections, for which $u^f[\lambda]$ can be evaluated using the asymptotic equations (5) in a regular point assuming $\xi = \lambda$. To simplify the exposition, the reference equilibrium point (u_0, λ_0) is

assumed to be coincident with the origin

$$u^f[\lambda] = \lambda\hat{u} + \frac{1}{2}\lambda^2\hat{\hat{u}} + \frac{1}{6}\lambda^3\hat{\hat{\hat{u}}} + \cdots .$$

The perturbation equations which allow the evaluation of $\hat{u}$, $\hat{\hat{u}}$ ect., are

$$\begin{cases} \left(\Phi_0''\hat{u} - \hat{p}\right)\delta u = 0, \\ \left(\Phi_0''\hat{\hat{u}} + \Phi_0'''\hat{u}^2\right)\delta u = 0, \\ \left(\Phi_0''\hat{\hat{\hat{u}}} + 3\Phi_0'''\hat{u}\hat{\hat{u}} + \Phi_0''''\hat{u}^3\right)\delta u = 0, \end{cases} \qquad \forall \delta u \in \mathscr{T}. \tag{19}$$

As $\xi = \lambda$, Eq. (16) holds and a critical point on u^f will be a bifurcation point. Following Koiter a structure that has an analytic path in λ will be called *perfect*.

3.2 The Bucklings Loads and Modes

Along the fundamental path $u^f[\lambda]$ we search for the buckling condition (8), i.e.

$$\Phi''\left[u^f[\lambda_i]\right]\dot{v}_i\delta u = 0 \quad \forall \delta u \in \mathscr{T},\ i = 1 \ldots m. \tag{20}$$

Equation (20) can be linearized near a suitable reference point $u_c = u^f[\lambda_c]$ not necessarily coincident with a bifurcation point to give the m buckling loads and modes

$$\Phi''\left[u^f[\lambda]\right] \equiv \left\{\Phi_c'' + (\lambda - \lambda_c)\Phi_c'''\hat{u}_c^f\right\}\dot{v}_i\delta u = 0 \quad \forall \delta u \in \mathscr{T}. \tag{21}$$

Equation (21) also furnishes the following natural orthogonality condition for modes $\dot{v}_i$

$$\Phi_c'''\hat{u}_c^f\dot{v}_i\dot{v}_j = 0 \quad \forall i, j = 1 \ldots m. \tag{22}$$

3.3 The Complete Equilibrium Path

The space of admissible displacements $\mathscr{T}$ is decomposed into a subspace $\mathscr{V}$ which is spanned by a finite number of modes $\dot{v}_i$ and in a complementary (usually the orthogonal complement) space $\mathscr{W}$ such that

$$\mathscr{T} = \mathscr{V} \oplus \mathscr{W}, \quad \mathscr{V} \cap \mathscr{W} = \{0\} \tag{23a}$$

where $\oplus$ denotes the direct sum and we select $\mathscr{V}$ so that Φ_c'' is definite positive on $\mathscr{W}$. This means that $\mathscr{V}$ could be generically selected but it is necessary to include

all the directions of singularity of Φ_c''. The natural choice for $\mathscr{V}$ is to use all the buckling modes $\dot{v}_i$ obtained by means of Eq. (21)

$$\mathscr{V} := \left\{ v : v = \sum_{i=1}^{n} \xi_i \dot{v}_i, \xi_i \in \mathbb{R} \right\} \tag{23b}$$

where ξ_i are scalar coefficients. From now on we also assume the following definition for $\mathscr{W}$

$$\mathscr{W} = \left\{ w : \Phi_c''' \hat{u}_c^f \dot{v}_i \, w = 0, \forall \dot{v}_i \right\}. \tag{23c}$$

Equations (23a) ensure that any $\delta u \in \mathscr{T}$ can be decomposed as

$$\delta u = \delta v + \delta w \quad \text{with } \delta v \in \mathscr{V}, \delta w \in \mathscr{V}. \tag{23d}$$

The equilibrium path is obtained by adding the fundamental path and the bifurcated one. Using the decomposition in Eqs. (23a)–(23d) we obtain

$$u[\xi_k, \lambda] = u^f[\lambda] + v[\xi_k] + w[\xi_k, \lambda] \quad \text{with } w \in \mathscr{W}, v \in \mathscr{V} \tag{24}$$

where the *orthogonal correctives* w are functions of λ and ξ_k. We also assume that in $u^f[\lambda_c]$ we have $\xi_k = 0$.

Introducing the admissible configurations (24) into the equilibrium equation we obtain a scalar function of ξ_k and λ

$$r[\xi_k, \lambda] := \left(\Phi'\left[u[\xi_k, \lambda]\right] - \lambda \hat{p}\right)\delta u \tag{25}$$

that using the decomposition in Eqs. (23a)–(23d) becomes

$$r^{(\alpha)}[\xi_k, \lambda] \equiv \left(\Phi'\left[u[\xi_k, \lambda]\right] - \lambda \hat{p}\right)\delta u_\alpha = 0 \quad \begin{cases} \delta u_0 \in \mathscr{W}, \\ \delta u_k = \dot{v}_k, \quad k = 1 \ldots m \end{cases} \tag{26}$$

where from now on Greek indexes go from 0 to m while the Roman ones from 1 to m and the index zero denotes quantities in $\mathscr{W}$. The residual equation for $\alpha = 0$, expressed in asymptotic form, will be used to evaluate a polynomial expression for $w[\lambda, \xi_i]$ that is then substituted in the remaining equations for $\alpha = 1 \ldots m$, these ones also being expressed in asymptotic form, to obtain the equilibrium equations.

3.3.1 Asymptotic Expansion from an Equilibrium Point

Let $u^f[\lambda]$ be a true equilibrium path. Equations (26) could be expanded from $\xi_i = 0$ and $\lambda = \lambda_c$, i.e. from $u_c = u^f[\lambda_c]$

$$r^{(\alpha)}[\xi_k, \lambda] = r_c^{(\alpha)} + \left.\frac{\partial r^{(\alpha)}}{\partial \xi_i}\right|_c \xi_i + \left.\frac{\partial r^{(\alpha)}}{\partial \lambda}\right|_c (\lambda - \lambda_c) + \left.\frac{\partial^2 r^{(\alpha)}}{\partial \xi_i \partial \lambda}\right|_c \xi_i (\lambda - \lambda_c)$$

$$+\frac{1}{2}\frac{\partial^2 r^{(\alpha)}}{\partial\lambda^2}\bigg|_c(\lambda-\lambda_c)^2+\frac{1}{2}\frac{\partial^2 r^{(\alpha)}}{\partial\xi_i\partial\xi_j}\bigg|_c\xi_i\xi_j+\cdots=0 \tag{27}$$

where $r_c^\alpha = r^\alpha[u^f[\lambda_c]] = 0$.

Denoting with a pedex k the derivative with respect to ξ_k we have

$$\begin{cases}
\dfrac{\partial r^{(\alpha)}}{\partial\xi_i} = \Phi_c''(\dot v_i+\dot w_i)\delta u_\alpha,\\
\dfrac{\partial r^{(\alpha)}}{\partial\lambda} = \big(\Phi_c''\big(\hat u_c^f+\hat w_c\big)-\hat p\big)\delta u_\alpha,\\
\dfrac{\partial^2 r^{(\alpha)}}{\partial\lambda\partial\xi_i} = \big(\Phi_c''\hat{\dot w}_i+\Phi_c'''\big(\hat u_c^f+\hat w_c\big)(\dot v_i+\dot w_i)\big)\delta u_\alpha,\\
\dfrac{\partial^2 r^{(\alpha)}}{\partial\lambda^2} = \big(\Phi_c''\big(\hat{\dot w}_c+\hat{\dot u}_c^f\big)+\Phi_c'''\big(\hat u_c^f+\hat w_c\big)^2\big)\delta u_\alpha,\\
\dfrac{\partial^2 r^{(\alpha)}}{\partial\xi_i\partial\xi_j} = \big(\Phi_c''\ddot w_{ij}+\Phi_c'''(\dot v_i+\dot w_i)(\dot v_j+\dot w_j)\big)\delta u_\alpha.
\end{cases} \tag{28}$$

Due to Eqs. (19) we obtain from the second and the fourth equation of (28) for $\alpha = 0$ that

$$\forall\dot v_0\in\mathscr{W}\quad\begin{cases}\Phi_c''\hat w\delta u_0=0 \quad\Rightarrow\quad \hat w=0,\\ \Phi_c''\hat{\dot w}\delta u_0=0 \quad\Rightarrow\quad \hat{\dot w}=0\end{cases}$$

that is all the derivatives of $w[\xi,\lambda]$ with respect to λ are zero.

The first of equations (28), using the bifurcation condition (21) becomes

$$\Phi_c''\dot v_k\delta u_0=(\lambda_k-\lambda_c)\Phi_c'''\hat u_c^f\dot v_k\delta u_0 \tag{29}$$

that furnishes $\dot w_k = 0$ due to the definition of $\mathscr{W}$. The same occurs for $\hat{\dot w}_c = 0$ while we obtain

$$\big(\Phi_c''\ddot w_{ij}+\Phi_c'''\dot v_i\dot v_j\big)\delta u_0=0\quad\forall\dot v_0\in\mathscr{W}. \tag{30}$$

We obtain then

$$w[\lambda,\xi_k]=\frac{1}{2}\sum_{i,j}\xi_i\xi_j\ddot w_{ij}$$

that can be introduced in Eq. (27) for $\alpha = 1\ldots m$ to evaluate the equilibrium path.

3.4 Asymptotic Expression from an Extrapolated Path

Now we consider the case in which $u^f[\lambda]$ is known in asymptotic fashion using Eq. (19) evaluated in the origin and retaining the linear term only

$$u^f[\lambda] = \lambda \hat{u}$$

this means that for our treatments $u_c = \lambda_c \hat{u}$ and $\hat{u}_c^f = \hat{u}$. Equilibrium equation (25) can be expressed in Taylor series starting from $u^f[\lambda]$ as follows

$$\begin{aligned}\big(\Phi'\big[u[\xi_k,\lambda]\big]-\lambda\hat{p}\big)\delta u_\alpha \approx \big(\Phi'\big[u^f[\lambda]\big]-\lambda\hat{p}\big)\delta u_\alpha \\ +\big(\Phi''\big[u^f[\lambda]\big]\big(v[\xi_k]+w[\xi_k,\lambda]\big)\big)\delta u_\alpha \\ +\frac{1}{2}\big(\Phi'''\big[u^f[\lambda]\big]\big(v[\xi_k]+w[\xi_k,\lambda]\big)^2\big)\delta u_\alpha \\ +\frac{1}{6}\big(\Phi''''\big[u^f[\lambda]\big]\big(v[\xi_k]+w[\xi_k,\lambda]\big)^3\big)\delta u_\alpha. \quad (31)\end{aligned}$$

Letting

$$\tilde{p}[\lambda]\delta u_\alpha = \big(\Phi'[u_f]-\lambda\hat{p}\big)\delta u_\alpha \approx \left(\frac{1}{2}\lambda^2\Phi_b'''\hat{u}^2\dot{v}_b+\frac{1}{6}\lambda^2(\lambda-3\lambda_b)\Phi_b''''\hat{u}^3\right)\delta u_\alpha \quad (32)$$

be the equilibrium residual along the fundamental path and performing again an asymptotic expansion of the remaining terms of (31) starting now from u_c we obtain the following function of λ and ξ_k

$$\begin{aligned}r^{(\alpha)}[\xi_k,\lambda] = \Bigg(\tilde{p}[\lambda]+\xi_i\Phi_b''\dot{v}_i+\Phi_b''w[\xi_k,\lambda]+(\lambda-\lambda_b)\xi_i\Phi_b'''\hat{u}\dot{v}_i \\ +(\lambda-\lambda_b)\Phi_b'''\hat{u}w[\xi_k,\lambda]+\frac{1}{2}\xi_i(\lambda-\lambda_b)^2\Phi_b''''\hat{u}^2\dot{v}_i \\ +\frac{1}{2}(\lambda-\lambda_b)^2\Phi_b''''\hat{u}^2w[\xi_k,\lambda] \\ +\frac{1}{2}\Phi_b'''\big(\xi_i\xi_j\dot{v}_i\dot{v}_j+w[\xi_k,\lambda]^2+2\xi_i\dot{v}_iw[\xi_k,\lambda]\big) \\ +\frac{1}{2}(\lambda-\lambda_b)\Phi_b''''\hat{u}\big(\xi_i\xi_j\dot{v}_i\dot{v}_j+w[\xi_k,\lambda]^2+2\xi_i\dot{v}_iw[\xi_k,\lambda]\big) \\ +\frac{1}{6}\Phi_b''''\big(\xi_i\dot{v}_i+w[\xi_k,\lambda]\big)^3+\cdots\Bigg)\delta u_\alpha = 0 \quad (33)\end{aligned}$$

where the convention of summing on the repeated index has been used.

From the condition $r^{(0)}[\xi_k, \lambda] = 0$ and deleting high order terms in the expansion we obtain the following expression for $w[\lambda, \xi_k]$

$$w[\xi_k, \lambda] = \frac{1}{2}\left(\lambda^2 \hat{\hat{w}} + \sum_{i,j=1}^{m} \xi_i \xi_k \ddot{w}_{ij}\right) \tag{34}$$

where

$$\begin{cases} \left(\Phi_c'' \hat{\hat{w}} + \Phi_c''' \hat{u}^2\right)\delta u_0 = 0, \\ \left(\Phi_c'' \ddot{w}_{ij} + \Phi_c''' \dot{v}_i \dot{v}_j\right)\delta u_0 = 0, \end{cases} \quad \forall \delta u_0 \in \mathscr{W}. \tag{35}$$

Substituting the definition in Eq. (34) in Eqs. (33) and recalling Eq. (21) we obtain the asymptotic expression for the equilibrium equations for $\alpha = 1 \dots m$

$$\begin{aligned} &\mu_k[\lambda] + (\lambda_k - \lambda)\xi_k - \lambda_b\left(\lambda - \frac{\lambda_b}{2}\right)\sum_{i=1}^{m} \xi_i \mathscr{C}_{ik} + \frac{1}{2}\sum_{i,j=1}^{m} \xi_i \xi_j \mathscr{A}_{ijk} \\ &+ \frac{1}{2}(\lambda - \lambda_b)^2 \sum_{i=1}^{m} \xi_i \mathscr{B}_{00ik} \\ &+ \frac{1}{2}(\lambda - \lambda_b) \sum_{i,j=1}^{m} \xi_i \xi_j \mathscr{B}_{0ijk} + \frac{1}{6}\sum_{i,j,h=1}^{m} \xi_i \xi_j \xi_h \mathscr{B}_{ijhk} = 0, \quad k = 1 \dots m \end{aligned} \tag{36}$$

where the following scalar quantities have been defined

$$\begin{cases} \mu_k[\lambda] = \frac{1}{2}\lambda^2 \Phi_b''' \hat{u}^2 \dot{v}_k + \frac{1}{6}\lambda^2(\lambda - 3\lambda_b)\Phi_b'''' \hat{u}^3 \dot{v}_k, \\ \mathscr{A}_{ijk} = \Phi_b''' \dot{v}_i \dot{v}_j \dot{v}_k, \\ \mathscr{B}_{ijhk} = \Phi_b'''' \dot{v}_i \dot{v}_j \dot{v}_h \dot{v}_k - \Phi_b''(\ddot{w}_{ij}\ddot{w}_{hk} + \ddot{w}_{ih}\ddot{w}_{jk} + \ddot{w}_{ik}\ddot{w}_{jh}), \\ \mathscr{B}_{00ik} = \Phi_b'''' \hat{u}^2 \dot{v}_i \dot{v}_k - \Phi_b'' w_{00} \ddot{w}_{ik}, \\ \mathscr{B}_{0ijk} = \Phi_b'''' \hat{u} \dot{v}_i \dot{v}_j \dot{v}_k, \\ \mathscr{C}_{ik} = \Phi_b'' \hat{\hat{w}} \ddot{w}_{ik} \end{cases} \tag{37}$$

where the *implicit imperfection factors* μ_k correspond to a consistent 4th-order expansion of the unbalanced work on the fundamental path (i.e. $\mu_k[\lambda] := (\lambda \hat{p} - \Phi'[\lambda \hat{u}])\dot{v}_k$).

3.4.1 External Imperfections

When analyzing a structure, it is difficult to characterize its geometry and loads exactly it being affected by a random distribution of small *external imperfections*. The

presence of these, while preserving the general behaviour of the structure, changes some aspects of its response and often causes a reduction in the carrying capacity (imperfection sensitivity).

The presence of small additional imperfections expressed by a load $\varepsilon_q \tilde{q}[\lambda]$ and/or an initial displacement $\varepsilon_u \tilde{u}$ can be easily considered in the asymptotic analysis. Once introduced in the equilibrium equation (26) and performing the expansion they only affect Eq. (36). In particular we only need to add the additional terms (see [8, 27, 28])

$$\mu_k^l[\lambda] := -\varepsilon \tilde{q}[\lambda] \dot{v}_k, \qquad \mu_k^g[\lambda] := \lambda \Phi_c''' \hat{u} \tilde{u} \dot{v}_k \tag{38}$$

that is, the imperfection term $\mu_k[\lambda]$ is modified to:

$$\mu_k[\lambda] = \frac{1}{2}\lambda^2 \Phi_c''' \hat{u}^2 \dot{v}_k + \frac{1}{6}\lambda^2(\lambda - 3\lambda_c)\Phi_c'''' \hat{u}^3 \dot{v}_k + \mu_k^l[\lambda] + \mu_k^g[\lambda]. \tag{39}$$

3.5 Attractive Path Theory and Imperfection Sensitivity Analysis

The aim of the *imperfection sensitivity analysis* is to link the presence of geometrical and load imperfections to the reduction in the limit load. For structures presenting coupled buckling even a small imperfection in loading or geometry can mean a marked reduction in collapse load with respect to the bifurcation load. So an effective safety analysis should include an investigation of all possible imperfection shapes and sizes to recover (albeit in a statistical sense) the worst case.

The asymptotic approach provides a powerful tool for performing this extensive investigation. In fact, the analysis for a different imperfection only needs to update the imperfection factors $\mu_k^g[\lambda]$ and $\mu_k^l[\lambda]$ through Eq. (38) and solve once more the nonlinear system (36). Even if this system, collecting all the nonlinear parts of the original problem, proves to be highly nonlinear and some care has to be taken in treating the occurrence of multiple singularities, its solution through a path-following process is relatively easy because of the small number of unknowns involved.

However, exhaustive results can only be obtained in a statistical context linking the distribution probability of the imperfection to that of the load. An effective imperfection sensitivity analysis can be performed by a Monte-Carlo statistical technique, where both the magnitude and the form of the imperfections are treated as random variables. The analysis is then performed by taking the additional imperfection factors in the form

$$\mu_k^l[\lambda] + \mu_k^g[\lambda] = \lambda\left(\tilde{q}[\lambda] - \Phi_c''' \hat{u} \tilde{u} \dot{v}_k\right) := \lambda \bar{\mu}_k, \tag{40}$$

and producing a random sequence of imperfection vectors $\bar{\boldsymbol{\mu}} = \{\bar{\mu}_1, \bar{\mu}_2, \ldots, \bar{\mu}_m\}$, modeling possible small deviations in the loads and in the geometry of the structure, and repeating a path-following solution of (36) for each of these. By a statistical treatment of the obtained results we obtain the probability distribution function

for the limit load multiplier and all the other useful statistical information. This solution process, we call *full analysis*, can be considered as a standard approach for imperfection sensitivity analysis (see [10]). The number of repetitions needed to obtain statistically reliable results increases (quite) exponentially with the number m of the buckling modes and for large m can become very expensive. The imperfection sensitivity analysis can however be performed in a simple and efficient way when a criterion for defining the (few) "significant" imperfection forms exists.

3.5.1 The Radial Path Directions

A large number of different imperfections (up to several thousands) has to be considered to obtain statistically significant results, so, while the analysis for a single imperfection can be considered an easy task, the entire solution process performed proves to be computationally expensive, especially when a large number of coupled buckling modes have to be considered. We can, however, noticeably reduce the computational effort by exploiting information given by the knowledge of the complete set of attractive radial paths

$$\xi_i = t\xi_i^*, \quad i = 1 \dots m, \ t \in \mathbb{R} \tag{41}$$

which are local minimizers for the cubic form

$$\dot{\lambda}_b := \frac{1}{2} \sum_{i,j,h=1}^{m} \mathscr{A}_{ijh} \xi_i^* \xi_i^* \xi_h^* = \min_{(\xi_k^*)}, \quad \sum_{i=1}^{m} \xi_i^* \xi_i^* = 1 \tag{42}$$

or for the quartic form

$$\ddot{\lambda}_b := \frac{1}{3} \sum_{i,j=1}^{m} \mathscr{B}_{ijhk} \xi_i^* \xi_j^* \xi_h^* \xi_k^* = \min_{(\xi_k^*)}, \quad \sum_{i=1}^{m} \xi_i^* \xi_i^* = 1 \tag{43}$$

on the unit hypersphere.

Attractive paths theory [10, 23, 24, 26, 31] can actually provide a helpful tool for driving the analysis and reducing its total cost. In fact, it suggests that each imperfect path obtained from the solution of (36) will be attracted by one of the minimizing radial directions $\boldsymbol{\xi}^*$ (see Fig. 10 in the numerical results section). Then, an evaluation for the limit load associated to the single imperfection vector $\bar{\boldsymbol{\mu}}$ can be obtained by performing a series of different monomodal analyses, one for each minimum radial path (41), and then taking the smallest value obtained for the limit load within all directions. The single monomodal analysis is quite quick, so a large number of different imperfections can be investigated rapidly with results, in terms of limit load distribution, equivalent to that provided by a full analysis [10].

Furthermore, it is worth mentioning that, once the worst imperfection shapes have already been obtained from an imperfection sensitivity analysis, a detailed investigation can be performed through a specialized path-following analysis, taking into account these imperfections.

4 Accuracy and Efficiency in Finite Element Implementation of the Asymptotic Analysis

In the following we present a numerical formulation of the method suitable for numerical implementation using finite elements and discuss some aspects that are crucial to achieve accuracy and efficiency.

4.1 FE Implementation of Asymptotic Method

Applying a FE interpolation $u := \mathscr{L}\mathbf{u}$, $\mathscr{L}$ being the interpolation operator and $\mathbf{u}$ the vector collecting the discrete displacement and stress parameters, the asymptotic analysis requires the following steps:

(i) The *fundamental path* is obtained introducing the linear extrapolation

$$\mathbf{u}^f[\lambda] := \mathbf{u}_0 + \lambda\hat{\mathbf{u}} \tag{44}$$

where $\hat{\mathbf{u}}$ is the initial path tangent, solution of the linear vectorial equation

$$\mathbf{K}_0\hat{\mathbf{u}} = \hat{\mathbf{p}} \tag{45}$$

$\mathbf{K}_0$ being the stiffness matrix evaluated for $\mathbf{u} = \mathbf{u}_0$ and $\hat{\mathbf{p}}$ the *unitary load vector*, defined by the energy equivalencies

$$\delta\mathbf{u}^T\mathbf{K}[\mathbf{u}]\dot{\mathbf{u}} = \Phi''[u]\dot{u}\delta u, \quad \delta\mathbf{u}^T\hat{\mathbf{p}} = \hat{p}\delta u.$$

The solution of linear system (45) requires a standard factorization of $\mathbf{K}_0$.

(ii) A cluster of *buckling loads* λ_i, $i = 1\ldots m$, and associated *buckling modes* $\dot{\mathbf{v}}_i$ are obtained along $\mathbf{u}^f[\lambda]$ exploiting the critical condition

$$\mathbf{K}[\lambda_i]\dot{\mathbf{v}}_i = \mathbf{0}, \quad \mathbf{K}[\lambda] := \mathbf{K}[\mathbf{u}_0 + \lambda\hat{\mathbf{u}}] \tag{46}$$

This corresponds to a nonlinear eigenvalue problem which can be linearized and solved using standard algorithms and exploiting matrix $\mathbf{K}_0^{-1}$, already available from the previous step, to perform the iterations [9].

(iii) Letting λ_c be an appropriate reference value for the cluster, e.g. the smallest of λ_i or their mean value, the asymptotic approximation for the

required path is defined by the expansion

$$\mathbf{u}[\lambda, \xi_k] := \mathbf{u}_b + \sum_{i=0}^{m} \xi_i \dot{\mathbf{v}}_i + \frac{1}{2} \sum_{i,j=0}^{m} \xi_i \xi_j \mathbf{w}_{ij} \tag{47}$$

where the quadratic corrections $\mathbf{w}_{ij} \in \mathscr{W}$ are obtained by the linear *orthogonal equations*

$$\delta \mathbf{w}^T (\mathbf{K}_c \mathbf{w}_{ij} + \mathbf{p}_{ij}) = 0, \quad \forall \mathbf{w} \in \mathscr{W} \tag{48}$$

with $\mathbf{K}_c := \mathbf{K}[\mathbf{u}^f[\lambda_c]]$ and vectors $\mathbf{p}_{ij}$ defined as a function of modes $\dot{\mathbf{v}}_i$ and $i = 0 \ldots m$ obtained by an element-by-element assembling process using the energy equivalence

$$\delta \mathbf{w}^T \mathbf{p}_{ij} = \Phi_c''' \delta w \dot{v}_j \dot{v}_j.$$

The solution of linear system (48) can be conveniently obtained, as described in [8, 9], through a Modified Newton-like iteration scheme exploiting $\mathbf{K}_0^{-1}$ as iteration matrix.

(iv) The *energy terms* in (37) being scalar quantities are evaluated as a sum, at the element level, of the integrals of known functions.

(v) The equilibrium path is obtained by solving the algebraic nonlinear system of m equations in the $m + 1$ variables $\xi_0, \xi_1, \ldots, \xi_m$ defined in Eq. (36) using a path-following algorithm. Because of the small dimensions of the system, this can be obtained very quickly using standard or even specialized variants of the arc-length scheme.

The actual implementation of the asymptotic approach as a computational tool is therefore quite easy in practice and its total computational burden, which is mainly involved in the factorization of matrix $\mathbf{K}_0$, remains of the order of that required by a standard linearized stability analysis. It provides the initial post-buckling behavior of the structure, including *modal interactions* and *jumping-after-bifurcation* phenomena. Moreover, once the preprocessor phase of the analysis has been performed (steps i to iv), the presence of small loading imperfections or geometrical defects can be taken into account in the postprocessing phase (step v), by adding some, easily computed, additional imperfection terms in the expression of $\mu_k[\lambda]$, with a negligible computational extra-cost, so allowing an inexpensive imperfection sensitivity analysis (e.g. see [13, 27]).

Imperfection sensitivity analysis can be simplified by evaluating all the minimum directions of the cubic (42) and quartic forms (42) to obtain the worst imperfection directions as discussed in Sect. 3.5.1. Today this is not a completely solved problem and it can also be expensive. Nevertheless, relative minimum solutions can be (quite easily) obtained by using the iterative scheme suggested in [31]. Furthermore for

the case of symmetric buckling, problem (43) can be transformed into a non-convex Quadratic Problem subject to linear constraints and solved using the strategy presented in [10].

4.2 On the Accuracy of the Asymptotic Formulation

The method, as will be shown in the numerical results section, is potentially capable of furnishing accurate results if a series of modelling and implementation aspects are carefully tuned. In the following we quickly present some of the sources of inaccuracy referring readers to the references for a deeper discussion.

4.2.1 Interpolation Locking

In the asymptotic algorithm a locking phenomenon related to the discretization process can arise from the evaluation of the fourth-order term

$$\mathscr{B}_{ijhk} = \Phi_c''''\dot{v}_i\dot{v}_j\dot{v}_h\dot{v}_k - \Phi_c''(\ddot{w}_{ij}\ddot{w}_{hk} + \ddot{w}_{ih}\ddot{w}_{jk} + \ddot{w}_{ik}\ddot{w}_{jh})$$

that defines the initial curvature of the post-buckling path. The coefficients $\mathscr{B}_{ijhk}$ are obtained as the difference between two quantities derived from the fourth and second variations. In compatible formulations the single term of this difference is, usually, very large while the difference is small. The discretization error on the single term could in this case be greater than the small results in their difference. Obviously, the numerical response given by the asymptotic algorithm in this case is completely unreliable.

The size of the error produced by this locking pathology depends on the finite element interpolation functions and decreases for an appropriate balancing of the polynomial functions used to describe each displacement component. The phenomenon is particular evident for beam and plate structures where the buckling modes $\dot{v}_i$ usually contain only flexural displacement components while $\ddot{w}_{ij}$ only in plane or axial ones. The locking is sanitized when a mixed finite element is used [8, 28].

Figure 2, which refers to a planar Euler rod case reports numerical results for the post-buckling factor $\ddot{\lambda}_b = \mathscr{B}_{1111}$ obtained for different values of the ratio EAL^2/EJ between the axial and the flexural stiffness, by using an element called HC [28] that uses the same quadratic spline functions for both the transversal and the axial components and standard beam elements (linear and cubic interpolation for the axial and transversal displacements, respectively).

Note that, for $EAL^2/EJ = 1.2 \times 10^5$, 20 HC elements are sufficient to contain the error in $\ddot{\lambda}_b$ at under 1 % while standard discretizations do not yield reliable results even using a large number of elements. A mixed finite element completely sanitizes this pathological phenomenon.

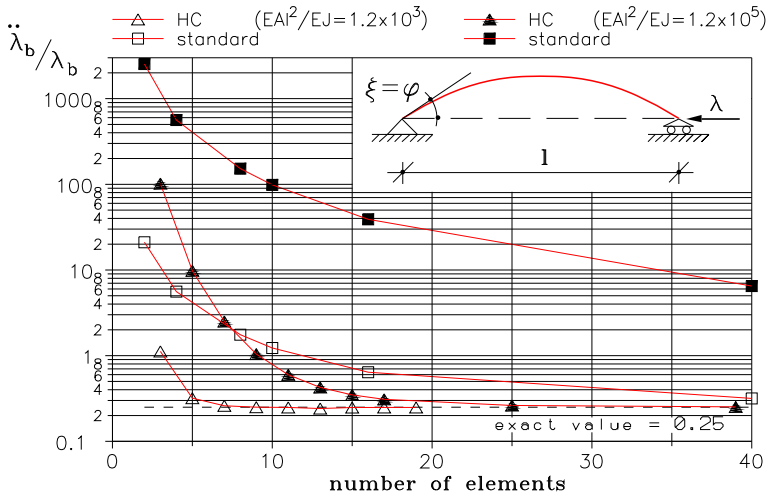

Fig. 2 Locking in Euler rod case

4.2.2 Extrapolation Locking

Mixed or compatible formats, while completely equivalent in principle, behave very differently when implemented in asymptotic but also in path-following solution strategies. This is an important, even if frequently misunderstood, point in practical computations which has been widely discussed in [8, 13, 14, 18, 19]. By referring readers to these papers for more details, we only recall here that both numerical strategies need function Φ and its Hessian $\mathbf{K}[\mathbf{u}]$ to be appropriately smooth in its controlling variables. In path-following analysis, this ensures a fast convergence of the Newton iterative process; in asymptotic analysis, it implies that the higher-order energy term neglected in expansion (33) be really irrelevant, allowing an accurate recovery of the equilibrium path. We know that the smoothness of a nonlinear function strictly depends on the choice of the set of its control variables, that is on the format of its description, and can change noticeably when referring to another, even corresponding, set. As a consequence, the mixed and compatible format, even if referring to the same problem, can be characterized by a different smoothness and so they behave differently in practice, when used within a numerical solution process. Actually, the compatible format is particularly sensitive to what we call *extrapolation locking* in [13, 18] which can produce a loss in convergence when used in path-following analyses, or unacceptable errors in the path recovery in the asymptotic case. These inconveniences are easily avoided by changing to a mixed format.

4.2.3 Objective Structural Model

The asymptotic analysis makes great use of information attained from a fourth-order expansion of the strain energy and then requires a fourth-order accuracy be

guaranteed in the structural modeling. Small inaccuracies, deriving from geometrical incoherencies in the higher-order terms of the expansion of the kinematical laws or in its finite element representation, significantly affect the accuracy of the solution and can make it unreliable. Structural models not affected by rigid body motions or by changes in observer are then required. This aspect is more important with respect to the path-following case where only the first variation needs to be correctly evaluated.

With this aim the *Implicit Corotational Method (ICM)* has been proposed as a tool to obtain geometrically exact nonlinear models for structural elements, such as beams or shells, undergoing finite rotations and small strains starting from the solutions for the 3D Cauchy continuum used in the corresponding linear modelings (see [15, 16]). The main idea is to associate a corotational frame to each point of the 3D continuum so allowing the motion in the neighbor of the point to be split in a pure stretch followed by a pure rotation, according to the decomposition theorem. It is possible to show how, using the small strain hypothesis and rotation algebra, the linear stress and linear strain fields, when viewed in this corotational frame, can provide accurate approximations for the Biot nonlinear stress and strain fields. Once the corotational rotation is appropriately defined, the local statics and kinematics of the model are recovered from the linear solution as a function of the stress/displacement resultants. Stress and strain fields are then introduced within a mixed variational principle in order to obtain the constitutive laws directly in terms of stress/strain resultants. This completes the ICM definition of the nonlinear model.

The nonlinear model so obtained retains all the details of the 3D linear solution, including torsion/shear warping, while its objectivity is ensured implicitly. Furthermore, the use of the mixed formulation and the greater accuracy with which the ICM recovers the stress field, allows an accurate description of the constitutive laws in terms of resultants. ICM does not require any ad-hoc assumption about the structural model at hand, nor depends on any particular parametrization of the rotation tensor, but actually behaves as a black-box tool able to translate known linear models into the corresponding nonlinear ones. Moreover, the direct use of a mixed (stress/strain) description provides an automatic and implicitly coherent methodology for generating models free of the nonlinear locking effects previously discussed, in a format directly suitable for use in FEM implementations.

The method was applied in [15] to derive 3D beam and plate nonlinear models starting from the Saint Venànt rod and Kirchhoff and Mindlin-Reissner plate linear theories, respectively. Some results obtained in [16] will be also given.

5 Numerical Results

Some results regarding the analysis of both 3D beams and plates are reported and compared with particular reference to accuracy as previously discussed. In the monomodal buckling tests, to compare the accuracy with known solutions, the following quantities, defining the postcritical tangent and curvature to the bifurcated

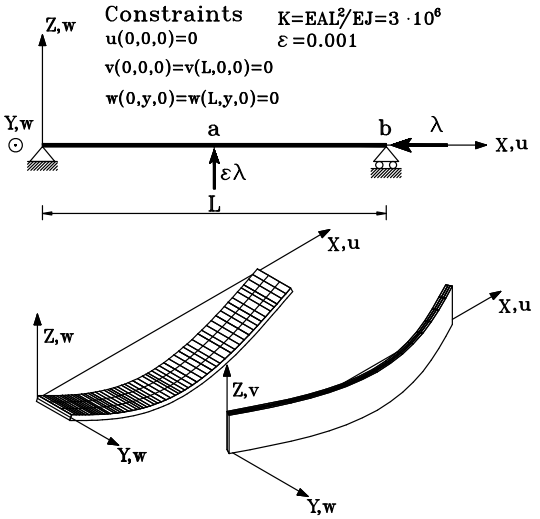

	N.elem.	Out plane			In plane			2D Beam(*)
		LC	*LS*	*PM*	*LC*	*LS*	*PM*	
λ_b	16	9.901	9.901	9.901	9.918	9.918	9.918	9.870
	32	9.877	9.877	9.877	9.870	9.870	9.870	
	64	9.872	9.872	9.871	9.867	9.870	9.870	
$\frac{\ddot{\lambda}_b}{2\dot{\lambda}_b}$	16	−0.354	0.020	0.145	0.166	1.03	0.166	0.125
	32	−0.375	0.000	0.125	0.126	1.00	0.126	
	64	−0.375	0.000	0.125	0.125	1.00	0.125	

Fig. 3 Euler beam: problem description and buckling and post-buckling parameters

path, have been introduced

$$\dot{\lambda}_b = -\frac{1}{2}\frac{\mathscr{A}_{111}}{\mathscr{A}_{011}}, \qquad \ddot{\lambda}_b = -\frac{\mathscr{B}_{1111} + 3\dot{\lambda}_b\mathscr{B}_{0111} + 3\dot{\lambda}_b^2\mathscr{B}_{0011}}{3\mathscr{A}_{011}}.$$

The results are compared with known analytical solutions and with the ones obtained using the *LC* (Complete Lagrangian) and *LS* (Simplified Lagrangian) technical plate models already implemented in the code named KASP [13, 20]. An independent analysis has also been made using the commercial code ABAQUS.

5.1 The Influence of the Structural Model

The test refers to the Euler beam shown in Fig. 3. The beam is analyzed forcing the buckling to have in-plane or out-of-plane components only.

Despite its simplicity, when analyzed with an asymptotic approach, the problem is taxing with regard to the accuracy of the structural model and its FEM discretiza-

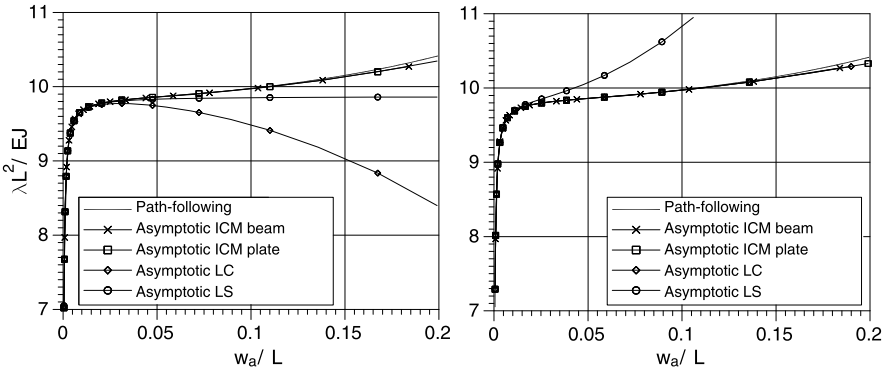

Fig. 4 Euler beam: out-plane and in-plane equilibrium paths

tion [16]. In Fig. 3 the values of the buckling loads and post-critical curvatures are compared with the values obtained by using the Antman beam model and exact interpolation functions. The ICM model recovers the analytical solution for sufficiently fine grids exactly. The *LC* and *LS* models provide a correct answer for the buckling load, but have a different post-buckling behavior in the in-plane or out-of-plane analysis: *LC* agrees perfectly with the exact solution in the in-plane case, whereas *LS* provides the wrong result $\ddot{\lambda}/\lambda_b = 2$, which is eight times greater; conversely, *LS* behaves better in the out-of-plane case, by providing the approximation $\ddot{\lambda}_b/\lambda_b = 0$, while *LC* gives a completely erroneous unstable postbuckling curvature $\ddot{\lambda}/\lambda_b = -0.75$. The resulting paths in Fig. 4 show a good agreement with those computed by path-following analyses.

5.2 Tests with a Nonlinear Precritical Behaviour

The tests shown in Figs. 5 and 6 are relative to structures characterized by a highly nonlinear pre-critical behavior. For the shallow arch the first buckling load is obtained at $\lambda_1 = 22$ while for the hinged cylindrical shell the first two buckling loads are equal to $\lambda_1 = 4.52$ and $\lambda_2 = 7.11$ respectively. In both cases the limit load is almost a half of the minimum buckling value and is evaluated exactly as can be observed by the comparison with the asymptotic and path-following (ABAQUS) curve denoted respectively CR4 and SR8. It is worth of noting that only the implicit imperfection acts on the structure.

5.3 Multimodal Buckling and Attractive Paths

The first test, whose geometry is reported in Fig. 7, deals with the multimodal analysis of space structures modelled as 3D beam assemblages. The 3D beam model

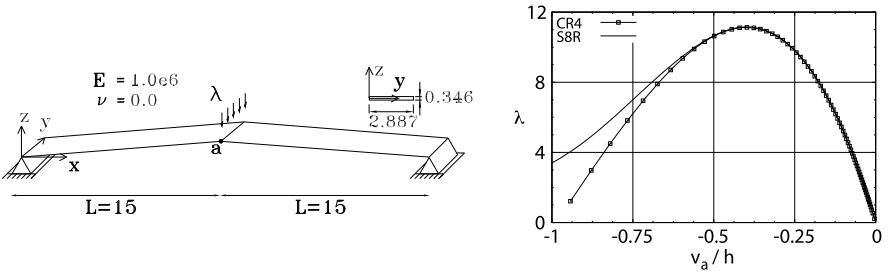

Fig. 5 Shallow arch

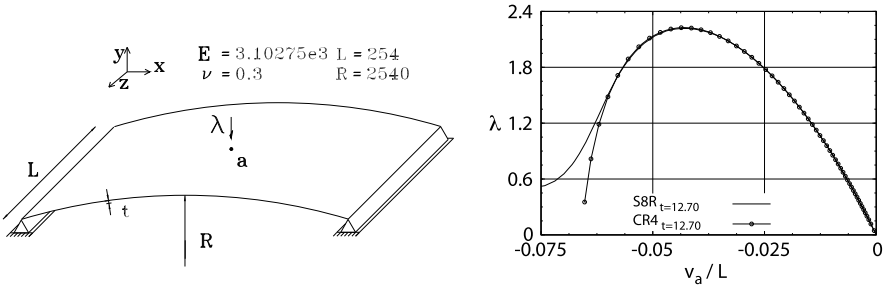

Fig. 6 Hinged cylindrical shell

used is that reported in [17]. The equilibrium paths reported in Fig. 7, compared with the results of a path-following analysis with ABAQUS, show the accuracy of the asymptotic analysis.

The second test is the thin-walled beam in Fig. 8 modelled as a plate assemblage. The model is that proposed in [15, 16] on the basis of the ICM and is denoted as MP in the results. The results are compared with those of an ABAQUS analysis using a path-following approach and of the technical plate models [13]. The greater accuracy of the objective structural model is evident in Fig. 8 where the equilibrium paths are depicted.

The third case regards a C-shaped cantilever beam subjected to a single force at the free end reported in Fig. 9. In this case the strong modal interaction between non near buckling loads also produce a highly unstable behaviour as shown by the equilibrium path.

Finally the last test regards the Geodetic Dome modelled through a 3D truss as proposed in [10]. In this case many locally coincident buckling modes interact and the structure exhibits a very marked unstable behaviour. In Fig. 10, in the modal space (ξ_k) different equilibrium paths, clearly converging along only one of the minimum directions, are reported. The test shows how it is possible to perform the sensitivity analysis in a simplified way along the predetermined quartic form minimum directions.

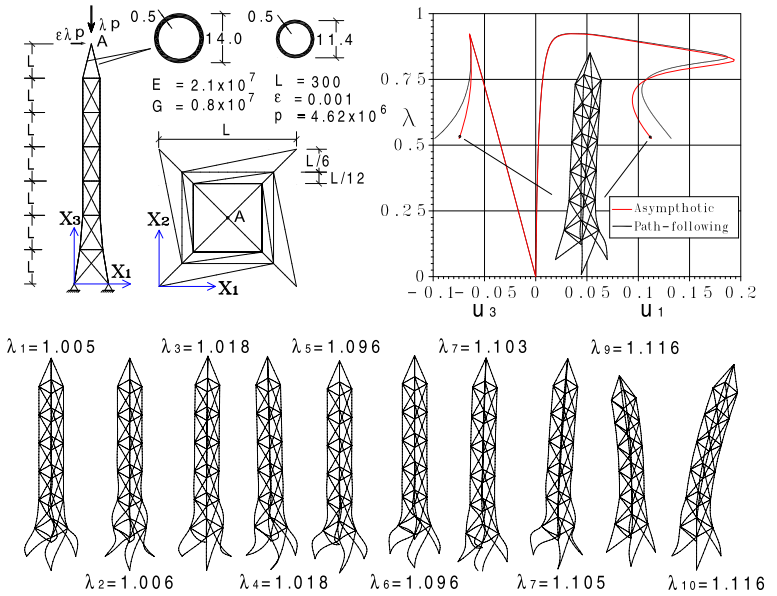

Fig. 7 3D tower: buckling modes and equilibrium paths

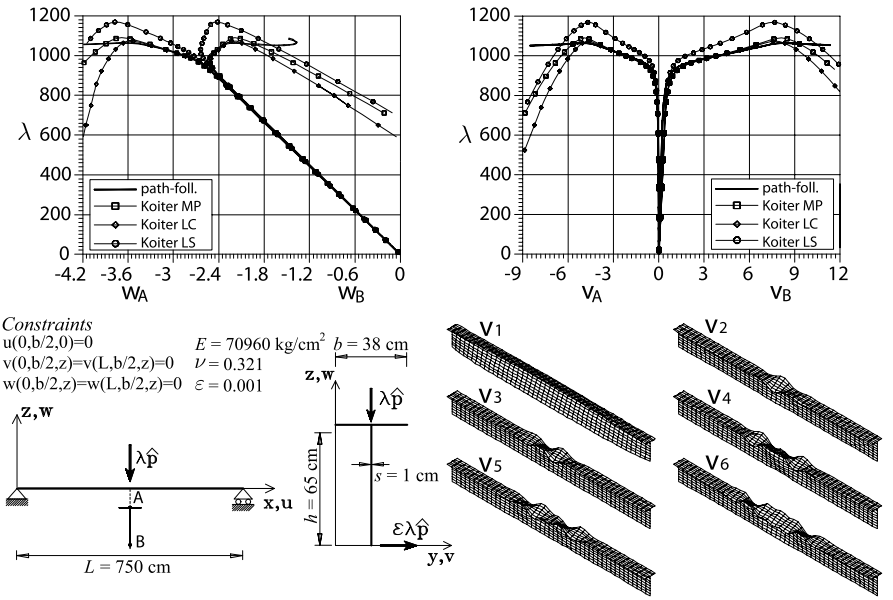

Fig. 8 T beam: buckling modes and equilibrium paths

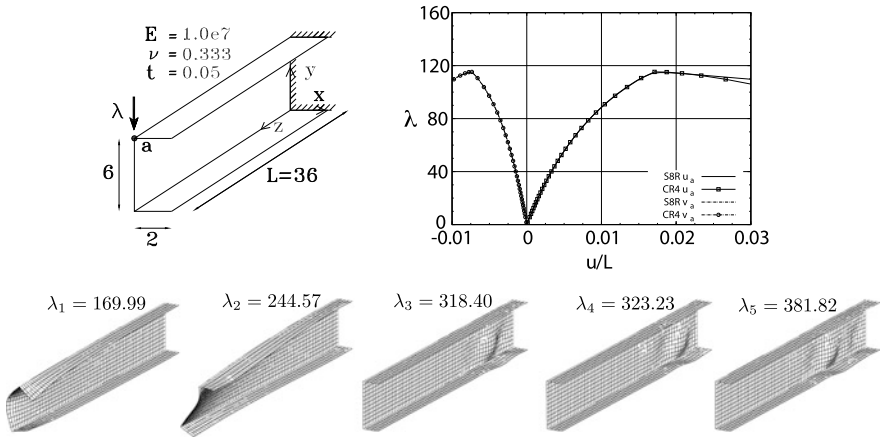

Fig. 9 C-shaped cantilever beam

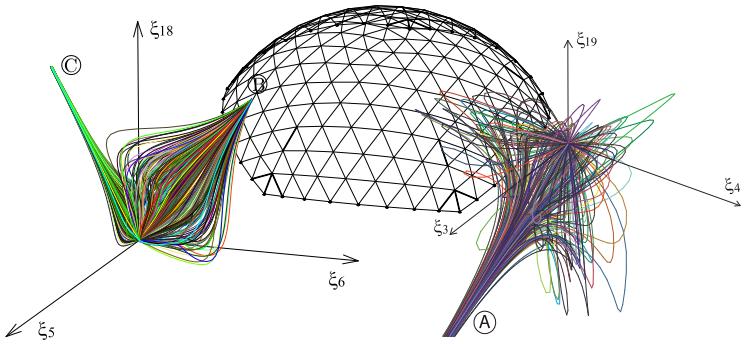

Fig. 10 Geodetic dome: modal interaction between 20 critical modes

6 Conclusions

The paper deals with the numerical implementation of the Koiter asymptotic approach to directly evaluate the buckling and postbuckling behaviour of geometrically nonlinear structures also in the case of multiple coincident buckling loads and random loading and/or geometrical imperfections. Standard techniques, based on repeated path-following analyses, are useful for a thorough investigation of the structural behaviour with a single imperfection shape, but cannot be considered effective tools to predict the safety factor for geometrically nonlinear problems. The asymptotic method, instead, appears to be an attractive alternative as it allows a reliable analysis with computational costs similar to those required by a standard load buckling prediction, while subsequent analyses for different imperfections are possible only solving a nonlinear system of m equations, m being the number of buckling loads considered. In this sense it can be considered as a direct method for predicting the safety factor of geometrically nonlinear elastic structures. The method furnishes

accurate results and also information about the worst imperfection shape if a series of modelling and implementation aspects are carefully tuned. In particular it was shown how the effects of the use of geometrically exact structural models and their coherent finite element implementation are very relevant, while a mixed formulation eliminates both interpolation and extrapolation locking phenomena.

References

1. Abichou H, Zahrouni H, Potier-Ferry M (2002) Asymptotic numerical method for problems coupling several nonlinearities. Comput Methods Appl Mech Eng 191 (51-52):5795–5810
2. Ali MA, Sridharan S (1988) A versatile model for interactive buckling of columns and beam columns. Int J Solids Struct 24:481–496
3. Arbocz J, Hol JMAM (1990) Koiter's stability theory in a computer-aided engineering (CAE) environment. Int J Solids Struct 26:945–973
4. Barbero EJ, Godoy LA, Raftoyiannis IG (1996) Finite elements for three-mode interaction in buckling analysis. Int J Numer Methods Eng 39:469–488
5. Boutyour EH, Zahrouni H, Potier-Ferry M, Boudi M (2004) Asymptotic-numerical method for buckling analysis of shell structures with large rotations. J Comput Appl Math 168(1–2):77–85
6. Brezzi F, Cornalba M, Di Carlo A (1986) How to get around a simple quadratic fold. Numer Math 48:417–427
7. Budiansky B (1974) Theory of buckling and post-buckling of elastic structures. Advances in applied mechanics, vol 14. Academic Press, New York
8. Casciaro R (2005) Computational asymptotic post-buckling analysis of slender elastic structures. CISM courses and lectures, vol 470. Springer, New York
9. Casciaro R, Garcea G, Attanasio G, Giordano F (1998) Perturbation approach to elastic post-buckling analysis. Comput Struct 66:585–595
10. Casciaro R, Mancusi G (2006) Imperfection sensitivity due to coupled local instability: a non-convex QP solution algorithm. Int J Numer Methods Eng 67:815–840
11. Chen H, Virgin LN (2006) Finite element analysis of post–buckling dynamics in plates, part I: an asymptotic approach. Int J Solids Struct 43:3983–4007
12. Flores FG, Godoy LA (1992) Elastic postbuckling analysis via finite element and perturbation techniques, part 1: formulation. Int J Numer Methods Eng 33:1775–1794
13. Garcea G (2001) Mixed formulation in Koiter analysis of thin-walled beam. Comput Methods Appl Mech Eng 190:3369–3399
14. Garcea G, Formica G, Casciaro R (2005) A numerical analysis of infinitesimal mechanisms. Int J Numer Methods Eng 62:979–1012
15. Garcea G, Madeo A, Casciaro R (2012) The implicit corotational method and its use in the derivation of nonlinear structural models for beams and plates. J Mech Mater Struct 7(6):509–538
16. Garcea G, Madeo A, Casciaro R (2012) Nonlinear FEM analysis for beams and plate assemblages based on the implicit corotational method. J Mech Mater Struct 7(6):539–574
17. Garcea G, Madeo A, Zagari G, Casciaro R (2009) Asymptotic post-buckling FEM analysis using a corotational formulation. Int J Solids Struct 46(2):523–532
18. Garcea G, Salerno G, Casciaro R (1999) Extrapolation locking and its sanitization in Koiter asymptotic analysis. Comput Methods Appl Mech Eng 180(1–2):137–167
19. Garcea G, Trunfio GA, Casciaro R (1998) Mixed formulation and locking in path-following nonlinear analysis. Comput Methods Appl Mech Eng 165(1–4):247–272
20. Garcea G, Trunfio GA, Casciaro R (2002) Path-following analysis of thin-walled structures and comparison with asymptotic post-critical solutions. Int J Numer Methods Eng 55:73–100

21. Godoy LA, Banchio EG (2001) Singular perturbations for sensitivity analysis in symmetric bifurcation buckling. Int J Numer Methods Eng 52:1465–1485
22. Goltermann P, Møllmann H (1989) Interactive buckling in thin-walled beams, I: theory. Int J Solids Struct 25:715–749
23. Ho D (1972) The influence of imperfections on systems with coincident buckling loads. Int J Non-Linear Mech 7:311–321
24. Ho D (1974) Buckling load of non-linear systems with multiple eigenvalues. Int J Solids Struct 10:1315–1330
25. Koiter WT (1945) On the stability of elastic equilibrium. Thesis, Delft. English translation: NASA TT-F10, 883 (1967) and AFFDL-TR70-25 (1970)
26. Koiter WT (1976) Some properties of (completely) symmetric multilinear forms with an application to Ho's theorem for multi-mode buckling. Technologic University of Delft, Lab Rep 587
27. Lanzo AD, Garcea G (1996) Koiter analysis of thin-walled structures by a finite element approach. Int J Numer Methods Eng 39:3007–3031
28. Lanzo AD, Garcea G, Casciaro R (1995) Koiter post-buckling analysis of elastic plates. Int J Numer Methods Eng 38:2325–2345
29. Peek R, Kheyrkhahan M (1993) Postbuckling behavior and imperfection sensitivity of elastic structures by the Lyapunov-Schmidt-Koiter approach. Comput Methods Appl Mech Eng 108(3–4):261–279
30. Poulsen PN, Damkilde L (1998) Direct determination of asymptotic structural postbuckling behaviour by the finite element method. Int J Numer Methods Eng 42(4):685–702
31. Salerno G, Casciaro R (1997) Mode jumping and attractive paths in multimode elastic buckling. Int J Numer Methods Eng 40:833–861
32. Schafer BW, Graham-Brady L (2006) Stochastic post-buckling of frames using Koiter's methods. Int J Struct Stab Dyn 6(3):333–358
33. Silvestre N, Camotim D (2005) Asymptotic-numerical method to analyze the postbuckling behavior, imperfection-sensitivity, and mode interaction in frames. J Eng Mech 131(6):617–632
34. Sridharan S (1983) Doubly symmetric interactive buckling of plate structures. Int J Solids Struct 19:625–641
35. van Erp GM, Menken CM (1991) Initial post-buckling analysis with the spline finite-strip method. Comput Struct 40:1193–1201
36. Wu B, Wang Z (1997) A perturbation method for the determination of the buckling strength of imperfection-sensitive structures. Comput Methods Appl Mech Eng 145(3–4):203–215

A Quasi-periodic Approximation Based Model Reduction for Limit Analysis of Micropile Groups

Zied Kammoun, Joseph Pastor, and Hichem Smaoui

Abstract The behavior of soils reinforced by micropile networks is still not fully understood due to the lack of accurate modelling capabilities. Particularly, the complex geometry of large soil-micropile systems makes accurate calculation of the bearing capacity of the reinforced soil a computational challenge. This complexity requires highly detailed and finely discretized models to achieve reasonable accuracy using direct numerical methods. Such models lead to large scale numerical optimization problems that are hardly tractable using a personal computer.

In the present paper a model reduction method is made capable of solving the numerical static limit analysis problem of soil reinforced by a group of micropiles according to a 2D plane strain model. The method has been successfully applied to the limit analysis problem of a soil reinforced by a large group of micropiles when resources did not permit solution of the full model.

1 Introduction

A micropile is a pile with a small diameter (generally in the range 75 to 200 mm) and high aspect ratio. Micropiles are used in soil reinforcement and foundation works beneath existing buildings. The micropile technique was developed as early as 1952 by the Fondedile company under the authority of F. Lizzi [1]. Micropiles were used for the first time in Italy in soil reinforcement of existing buildings and were then named root piles (pali radice). Within the timeframe of half a century, the technique

Z. Kammoun · H. Smaoui
Ecole Nationale d'Ingénieurs de Tunis, LR11ES16 Laboratoire de Matériaux, Optimisation et Energie pour la Durabilité, Université de Tunis El Manar, 1002, Tunis, Tunisia

Z. Kammoun
e-mail: kammounzied@yahoo.fr

H. Smaoui
e-mail: hismaoui@yahoo.fr

J. Pastor (✉)
LOCIE Laboratory, Polytech' Annecy Chambéry, University of Savoie, Chambéry, France
e-mail: joseph.pastor@univ-savoie.fr

K. Spiliopoulos, D. Weichert (eds.), *Direct Methods for Limit States in Structures and Materials*, DOI 10.1007/978-94-007-6827-7_11,

has been applied all over the world [4] with micropile groups counting as many as 1100 micropiles in a landmark example in Neuchâtel, Switzerland.

Nevertheless, the behaviour of micropile groups is still not well understood, particularly because of the complex geometry of large soil-micropile systems that challenged the development of accurate modeling methods.

Various approaches are used for predicting the bearing capacity of micropile groups. Simplified analytical methods [3] are commonly used in engineering practice whereas elastoplastic analysis ([4] and [1]) is often applied in special application and in research. Another alternative is limit analysis [7] by direct methods. The merit of Limit Analysis (LA) is the rigorous underlying theoretical basis and the high level of accuracy that may be achieved.

Because of their complex geometry, raisonably accurate prediction for micropile groups of practical size by Limit Analysis requires finely discretized finite element models leading to numerical optimization problems that are too large to be directly tractable by available algorithms [7].

In an attempt to circumvent the problem size difficulty, different techniques have been devised to reduce the size of the numerical Limit Analysis problem to be solved. Among these techniques, homogenization methods [2] have been proposed. While successful in reducing the computational effort these methods do not provide a realistic description of the stress and strain fields in the heterogeneous medium, especially near the boundaries of the reinforced zone. Domain decomposition is another approach that is developed for solving large size LA problems. It converts the original numerical LA problem into a sequence of smaller LA like subproblems that are solved iteratively. This approach has proven to be successfull in solving problems that are untractable when solved directly ([8] and [10]).

In this work, an alternative technique is presented that aims at reducing the size of the numerical LA problem for uniformly spaced micropile groups by taking advantage of the periodicity of the geometry and structure of the reinforced zone. It is inspired from the case of fiber reinforced composites which is suited to modeling using periodic homogenization [5].

In this study, a two dimensional representation of the reinforced soil will be adopted to reduce the numerical problem dimension. Extension to the three dimensional problem will be possible because it is conceptually equivalent to the two dimensional problem.

The paper begins with a brief presentation of limit analysis followed by a description of the proposed periodic reduction method. The method is then tested and assessed by applying it to examples of soil-micropile systems.

2 Limit Analysis and the Static Method

According to Salençon (see [12, 13]), a stress tensor field σ is said to be statically admissible (SA) if equilibrium equations, stress vector continuity, and stress boundary conditions are verified. It is said to be plastically admissible (PA) if $f(\sigma) \leq 0$,

where $f(\sigma)$ is the (convex) plasticity criterion of the material. A field σ that is SA and PA here will be said to be (fully) admissible.

Similarly, a strain rate tensor field v is kinematically admissible (KA) if it is derived from a continuous velocity vector field u such that the velocity boundary conditions are verified. It is said to be plastically admissible (PA) if the flow rule (1) is verified; the fields u and v, which are KA and PA, will be called admissible in the following.

$$v = \lambda \frac{\partial f}{\partial \sigma}, \quad f(\sigma) = 0,\ \lambda \geq 0. \tag{1}$$

The so-called associated flow rule (1) (or normality law) characterizes the standard material of LA. Equivalently, a standard material satisfies Hill's maximum work principle (MWP) [6], which states that:

$$\left(\sigma - \sigma^*\right) : v \geq 0 \quad \forall \text{PA } \sigma^*. \tag{2}$$

A solution to the LA problem is a pair of fields (σ, v) where σ and v are both admissible and associated by the normality law. Classically, these solutions can be found or approached using two optimization methods. The first one, involving only the stresses as variables, is the static (or lower bound) method. The second one, involving only the displacement velocities as variables, is the classical kinematical (or upper bound) method.

Let us assume that the virtual power of the external loads can be written as the scalar product of a loading vector $Q \in \mathbb{R}^n$ and a generalized velocity vector $q = q(u)$, linear in u. A loading process linearly associated with a statically admissible stress field σ, $Q = Q(\sigma)$, is said to be admissible. The set of these admissible loadings forms a convex K in $\mathbb{R}^n$ and the n components of Q are called loading parameters.

Finding the solution of the limit analysis problem consists in determining an admissible field σ together with an admissible strain rate field associated to σ by the normality law. In this case the loading $Q(\sigma)$ is a limit loading of the mechanical system. The set of the limit loadings is the boundary ∂K of the convex K: this boundary can be approached by solving the following optimization problems:

$$Q_{lim} = \left(Q_1^d, \ldots, \lambda_0 Q_i^d, \ldots, Q_n^d\right), \tag{3a}$$

$$\lambda_0 = \max\left\{\lambda,\ Q(\sigma) = \left(Q_1^d, \ldots, \lambda Q_i^d, \ldots, Q_n^d\right)\right\}, \tag{3b}$$

where σ is an admissible stress field and Q^d a given admissible loading. Then, by varying Q^d it is possible to construct various points on ∂K: the smallest convex envelope of these points gives an approximation of ∂K from inside. This is the static, or lower bound method of LA, as it will be used here.

3 Finite Element Formulation of the Static Problem

In the present work the problem is formulated in plane strain. The numerical static method is used as it was defined and detailed in [11].

Let us consider a triangular finite element discretization of the mechanical volume V in the global frame (x, y); the stress field is chosen as linearly varying in x, y coordinates in each triangular element and it can be discontinuous through any element edge. In plane strain, the von Mises or Tresca criterion is written as:

$$f(\sigma) = \sqrt{(\sigma_x - \sigma_y)^2 + (2\tau_{xy})^2} \leq 2c, \tag{4}$$

where c is the cohesion of the material. It is worth noting here that the proposed problem reduction method is valid for the Coulomb or Drucker-Prager criteria (provided the final optimization problem could be solved by efficient mathematical programming techniques).

In order to ensure static and plastic admissibility of the stress solution field, the following, briefly recalled conditions are imposed:

- In each element, the equilibrium equations $\sigma_{ij,j} + \gamma_i = 0$ expressed in the Cartesian frame, where γ is the specific weight vector.
- Continuity conditions: the stress vector is continuous across a discontinuity line: for each discontinuity segment of normal n, the continuity of the stress vector $T_i = \sigma_{ij} n_j$ is written at the apices defining this discontinuity segment.
- Boundary conditions: the stress vector verifies $\sigma_{ij} n_j = T_i^d$ at each apex of the boundary element sides where the stress vector T^d—linearly varying— is imposed.
- Definition of the functional from the power of external loads: for example, the integral of the normal stresses in the case of the footing under an imposed normal uniform velocity.
- Stress field plastic admissibility: imposed at each triangle apex. This ensures that it is verified over the total domain from the linear variation of the stress in a triangle and the convexity of the criterion (4).

By writing the criterion directly in the conic form $V = 2c \geq \sqrt{Y^2 + Z^2}$, where V is an auxiliary variable, the numerical optimization problem can be solved using the conic programming code MOSEK [9] as in [14].

4 Quasi-periodic Reduction Method

In large micropile groups the micropiles are usually arranged in a regular pattern with a periodic geometry and structure. When the loading is uniformly distributed among the reinforcements the reinforced soil tends to respond in a periodic mode, at least away from the boundaries of the reinforced zone. The proposed method takes advantage of this periodicity to reduce the size of the numerical limit analysis

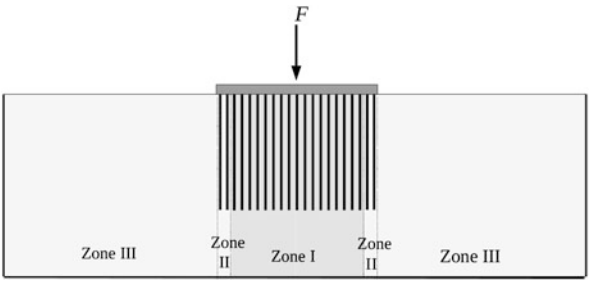

Fig. 1 The problem of the rigid footing under a central force F

problem. It is inspired from the case of fiber reinforced composites for which a successful periodic homogenization approach was developed in [5].

Figure 1 shows a typical soil-micropile group configuration with a reinforced zone supporting a rigid foundation and the natural soil extending on its sides and beneath, all the way down to a rigid substrate. To apply the reduction procedure the domain is subdivided into three parts. The first is the central reinforced zone where the behavior is assumed to be periodic, denoted zone I. The second, the edge zone, denoted zone II, is a part of the reinforced soil separating the periodic zone from the domain occupied by the natural soil. Finally, the rest of the soil represents the zone III. Although geometrically and materialwise periodic, zone II (the transition zone) is treated as non periodic.

A representative volume element (RVE) is constituted by a micropile and half the width of soil on each side in addition to the underlying volume of soil.

Regardless of the number of micropiles it includes, the periodic zone is replaced by a single periodic representative volume element (PRVE) fulfilling built-in periodicity and inter-RVE continuity constraints.

The periodicity conditions imposed on the stress field are

$$\sigma^{left}.n = \sigma^{right}.n, \tag{5}$$

where n is the normal to the right (or the left) side of the PRVE. As the n_{pp} periodic RVEs are replaced by a PRVE, the loading F_R of the reduced problem, equivalent to the original load F (Figs. 2 and 3) is given by

$$F_R = F_T + n_{pp}.F_P \tag{6}$$

where F_T is the load supported by zone II and F_P is the load supported by the PRVE in the reduced problem.

This results in a considerable reduction in problem size at the cost of an approximation error. Interestingly, the error is on the conservative side, preserving the lower bound nature of the solution of the static problem. Edge zones are defined by a few RVE's on each side. The finite element mesh corresponding to these edge zones and the natural soil (Zone III) remains unchanged. Furthermore, the detailed modeling of the soil-micropile composite at the RVE level, both in the horizontal and vertical directions, has the merit of accounting for the toe and lateral effects on the bearing

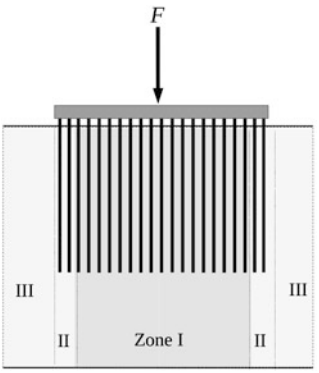

Fig. 2 Load in initial problem

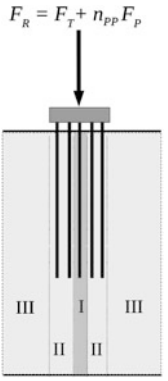

Fig. 3 Load in reduced problem

capacity. This is partly because the interaction effect between micropiles can be captured as a result of the full consideration of the soil layers underlying the reinforced zone.

5 Numerical Examples

The method is applied to some examples of soil reinforcement by groups of micropiles. The optimization problem is solved using the conic programming code MOSEK for both the direct problem, when possible, and the reduced problem, and performance is compared.

The LA problem considered (Fig. 4) is that of a Tresca soil reinforced by a group of n_p micropiles to support a weighless foundation slab of width b loaded at its middle by a force F. The soil cohesion is $C = 10$ kPa and depth is $H = 30$ m. The micropiles length is $h = 20$ m and width $d = 0.2$ m. The bearing capacity of the foundation is determined as the maximum load F that, together with a stress field σ, form a statically and plastically admissible pair. The associated numerical optimization problem is denoted P_0.

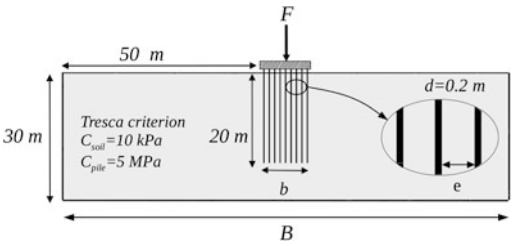

Fig. 4 Example of a soil reinforced with micropiles

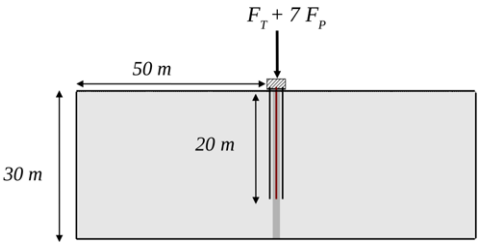

Fig. 5 Reduced problem of the considered example

In the reduced problem (Fig. 5), denoted P, Zone I is modeled using a single PRVE and the load is defined as the sum of the loads supported by the RVEs in Zone II and the load supported by the PRVE scaled up by the number of micropiles belonging to Zone I. Since the solution for the reduced problem is admissible for P_0, it provides a lower bound for the original LA problem. By limiting the number of transition micropiles to one on each side, the number of micropiles in the model decreased from n_p to only 3.

5.1 Effect of Load Transmission Mode

To illustrate the influence of the load transmission mode from the slab to the reinforced soil the problem is considered with two alternative transmission mechanisms and is modelled with the same degree of discretization. In the first, the foundation is assumed to be supported solely by the micropiles. In the second, it is supposed to rest on both the soil surface and the micropile tips. In both cases the kinematic and static bounds of the bearing capacity are first determined by solving the direct problem for a reinforcement with nine micropiles ($n_p = 9$). Furthermore, a static bound is estimated by solving the reduced problem resulting from the quasi-periodic approximation. Results are produced for a range of micropile spacings to assess the effects of spacing and surface load transmission mode.

5.1.1 Foundation Supported Solely by the Micropiles

The limit load (load-bearing capacity) F of the reinforced soil is determined in this case with the boundary conditions defined such that the load is carried only by the

Table 1 Number of elements for different values of micropile spacing

Spacing	1.8	2.8	3.8	4.8	5.8	6.8	7.8	8.8
Elements (×1000)	110	126	141	156	171	134	–	149

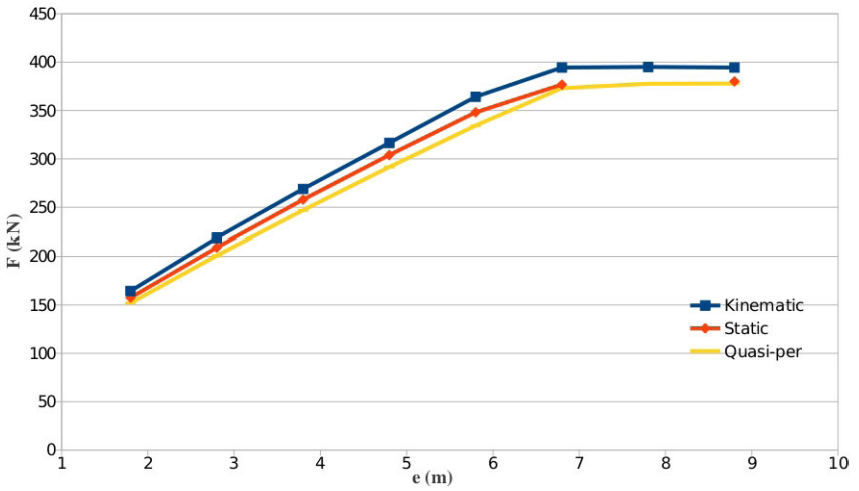

Fig. 6 Influence of spacing on bearing capacity. Direct and reduced model solutions

micropiles. The limit load is calculated for different values of micropile spacing. Figure 6 shows the limit load of the reinforced soil, calculated with different methods, as a function of spacing. The blue line represents the kinematic solution (upper bound) of the reference problem. The red line represents the static solution (lower bound) of the reference problem. The yellow line corresponds to the solution of the reduced model problem.

The results for $e < 6.8$ were all obtained with the same degree of discretization (elements size) which did not permit the direct solution beyond that spacing. Therefore, the problems with $e > 6.8$ were solved with fewer, larger elements. It should however be stated here that for the case $e = 7.8$ the results were not shown because the case was simply not treated. The reason was that it was not possible to create a regular mesh with the large element size because of the particular geometrical dimensions of the reinforced soil. The number of elements for each spacing is indicated in Table 1.

It may be noted from the results that:

– The reinforced soil bearing capacity increases with spacing for spacing under 6.8 m. Beyond this value the bearing capacity saturates and remains nearly indifferent to spacing. The saturation should reflect the vanishing of the interaction among micropiles which tend to behave as isolated inclusions.
– The error between the direct static and the reduced model solution is relatively small (less than 4.2 %).

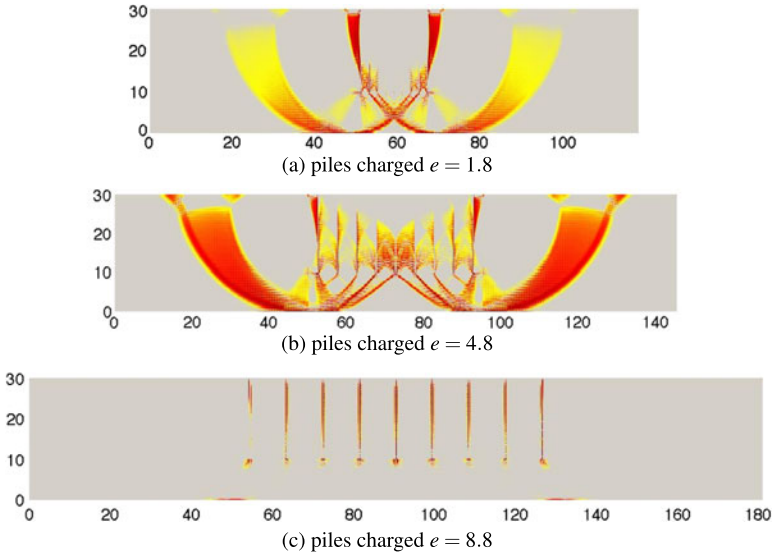

(a) piles charged $e = 1.8$

(b) piles charged $e = 4.8$

(c) piles charged $e = 8.8$

Fig. 7 Optimal stress field (direct solution)

The solution stress field is visualized in Fig. 7 for selected values of spacing. It can be seen that, for small spacing, the behavior of the reinforced area is reminiscent of a block mechanism (Fig. 7(a)). For large spacing (Fig. 7(c)), the elementary volumes tend to behave independently as if the micropiles were isolated. From the stress field in Fig. 7(c) a pattern can be seen that is characterized by a localization of the failure zone in a thin volume of soil surrounding the micropile.

5.1.2 Foundation Supported by Both the Soil and the Micropiles

The boundary conditions in this case are defined such that the load is carried at the soil surface by both the micropiles and the intersticial soil. Figure 8 shows the limit load calculated for different values of micropile spacing. It is observed that:

- The limit load always increases with spacing in contrast to the behavior observed with the loading supported solely by the micropiles. The reduced model solution increases linearly, whereas the direct static and kinematic limit load increases in a slightly bilinear pattern.
- The error increases with spacing to 9 % at $e = 8.8$ m.

The solution stress field is visualized in Fig. 9 for the same selection of spacing values. It shows that:

- For small spacing, the behavior of the reinforced zone is similar to that of a block mechanism.

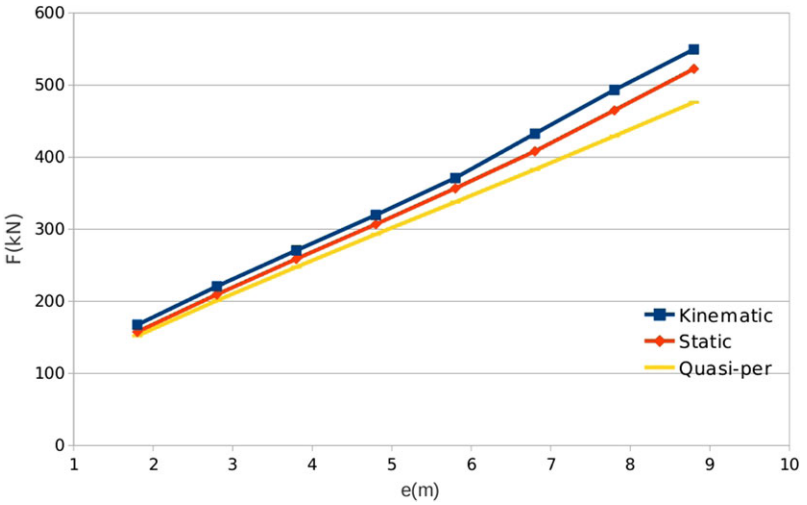

Fig. 8 Limit load for different values of spacing

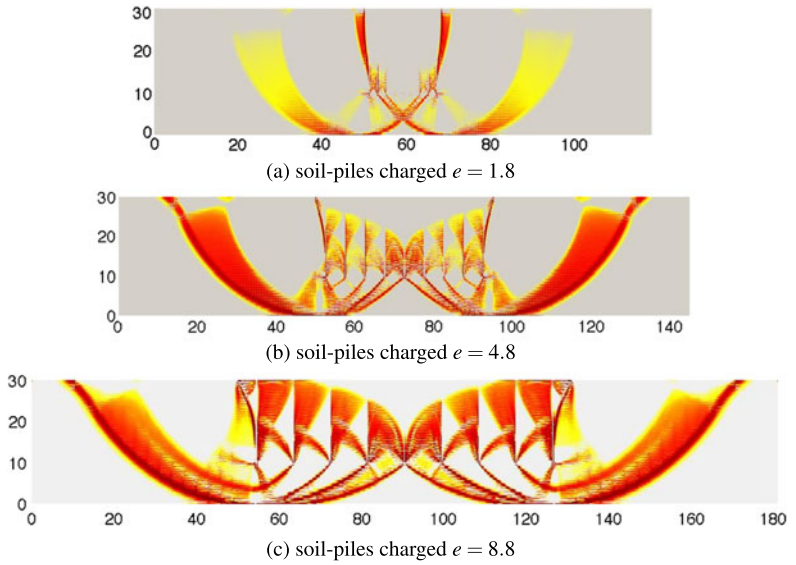

(a) soil-piles charged $e = 1.8$

(b) soil-piles charged $e = 4.8$

(c) soil-piles charged $e = 8.8$

Fig. 9 Optimal stress field (direct solution)

– For large spacing, the behavior does not clearly reflect the assumption of periodicity. The stress distribution for $e = 8.8$ in Fig. 9(c) looks more like that in Fig. 7(b) (for $e = 5$) than the nearly periodic stress field shown in Fig. 7(c), obtained for the same spacing $e = 9$ when the load is supported by the micropiles only.

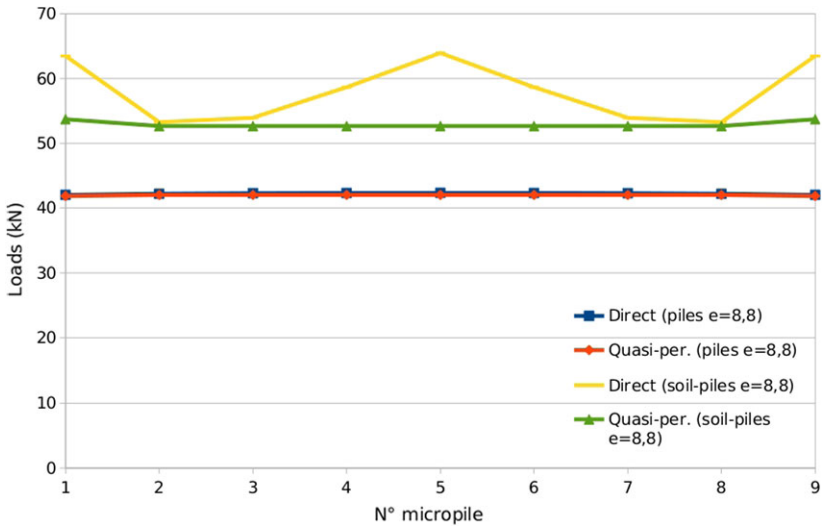

Fig. 10 Load distribution among elementary volumes

5.1.3 Results Interpretation

The details of the distribution of load among the elementary volumes are given in Fig. 10 for $e = 8.8$ m. For a load supported by both the soil and the micropiles, the distribution of the limit load obtained via the direct static solution shows significant fluctuations compared to the uniform distribution typical of the reduced model solution. The largest error on the load acting on an elementary volume is 17.65 %, it occurs at the center of the reinforced soil surface. The second largest error is found at the edge of the reinforced zone. These levels of errors are reasonable since they should be larger than the error of 9 % relative to the total load which is actually the integral of these elementary loads. For a load supported by the micropiles only, the distribution of limit load obtained by the direct static solution is almost uniform as expected since the micropiles have been shown to behave practically independently and, thus, to fulfill the periodicity assumption. When spacing is small, the failure occurs in a block mechanism mode regardless of the load transmission pattern. This explains the closeness of the limit loads evaluated using the Direct and Reduced formulations.

5.2 Effect of Micropile Number on Performance

To assess the performance gain of the reduction method for larger micropile group sizes (Fig. 11) the limit analysis problem is solved using the Direct (i) Static and (ii) Kinematic and the (iii) Reduced Model formulations with the number of micropiles varying from 1 to 31.

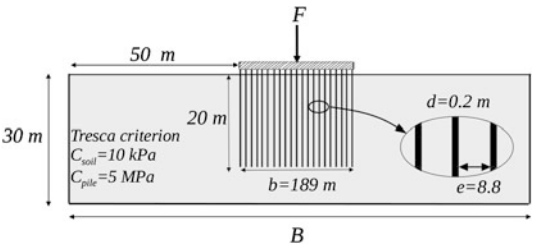

Fig. 11 Example for large number of micropiles

Table 2 Effect of micropile number

Nbr. of piles	Static			Quasi-periodic				Kinematic		
	Nbr elem.	F (kN)	CPU (s)	Nbr elem.	F (kN)	CPU (s)	Error (%)	Nbr elem.	F (kN)	CPU (s)
1	95760	419.7	249	–	–	–	–	98100	432.9	1078
3	103320	1263.4	232	–	–	–	–	114300	1304.7	1998
7	133560	2957.5	354	126000	2938.4	315	0.65	146700	3059.9	1845
9	148680	3800.3	204	126000	3779.2	273	0.56	162900	3944.1	1699
11	163800	4651.4	360	126000	4619.6	350	0.68	167160	4809.5	1948
15	194040	6342.8	402	126000	6301.0	352	0.66	197400	6580.7	1833
19	224280	8037.6	459	126000	7982.4	281	0.69	227640	8320.8	2299
21	239400	8884.6	446	126000	8822.9	257	0.69	–	–	–
31	–	–	–	126000	13026	327	–	–	–	–

The boundary conditions are such that the load is carried by the micropiles only. The same degree of discretization, i.e. in terms of size of finite elements, is used in all the models. The reduced model counts 126,000 finite elements regardless of the number of micropiles.

From the results, summarized in Table 2, it is seen that, as expected, the CPU time required by the reduced model solution has no clear tendency to increase with the number of micropiles, whereas the CPU time of the Direct solution increases with it nearly proportionally.

For a reinforcement with 21 micropiles (Table 3) the mesh of the Direct problem model amounts to 239,400 finite elements, nearly twice the number of elements in the reduced model, and the consumed CPU time is almost double the CPU of the reduced model solution for an accuracy gain of 0.7 %. This is the largest problem for which the Direct solution was possible with the Mac Pro 3 GHz machine used in this work.

For the same number of micropiles and using a finer mesh with 277200 elements in the Direct problem model, the Direct solution fails to converge whereas the reduced model solution converges in twice the CPU time and improves the "reduced" lower bound by 0.15 %.

The relative error between the Direct and the Reduced Model solutions is between 0.5 and 0.7 % and does not appear to increase with the number of micropiles.

Table 3 Reinforcement with 21 micropiles

Method	Nbr of elements	F (kN)	CPU (s)
Static	239400	8884.6	446
Quasi-periodic	126000	8822.9	257
Quasi-periodic	277200	8835.9	530

Consequently, it may be concluded that the reduction method provides a fairly accurate estimate for an unlimited number of micropiles within a nearly constant computational effort.

6 Conclusion

A model reduction method is proposed to solve the numerical static limit analysis problem of a composite medium, characterized by periodic reinforcement, embedded in a homogeneous domain, while preserving the fineness of the Finite Element description of the Representative Volume Element. The reduction method has been successfully applied to the Limit Analysis of a soil reinforced by a large group of micropiles when resources do not permit solution of the full model problem. Numerical results demonstrate that the reduction method provides a fairly accurate estimate of the limit load for an unlimited number of micropiles within a nearly constant computational time. Significant differences in behavior and bearing capacity are observed depending on the way the applied load is distributed between the soil and the micropiles. When the load is supported solely by the micropiles the reduced model results in terms of limit load of individual micropiles are very close to the reference solution (in confirmation of the periodicity assumption). When the load is supported by both the soil and the micropiles the error is larger than when only the micropiles carry the load. In a future work the reduction method will be extended to more general periodic representative volume elements by relaxing the symmetry requirement and allowing some forms of controlled variability of the stress field in the PRVEs. This will lead to more accurate solutions at the cost of a little extra computational effort. Another extension that might improve the accuracy of the reduction method, consists in limiting the length of the RVE to the height of the micropile allowing more degrees of freedom in the soil beneath the reinforced zone.

References

1. FOREVER (2004) Synthèse des résultats et recommandations du projet national sur les micropieux. Presses de l'Ecole Nationale des Ponts et Chaussées, Paris
2. Abdi R, de Buhan P, Pastor J (1994) Calculation of the critical height of a homogenized reinforced soil wall: a numerical approach. Int J Numer Anal Methods Geomech 18:485–505
3. Ministère de l'équipement, du logement et des transports (1993) Fascicule no 62. Titre v: Régles techniques de conception et de calcul des fondations des ouvrages de génie civil

4. Estephan R (2003) Contributions aux méthodes de calcul des groupes et des réseaux de micropieux. Thèse de doctorat, Ecole Nationale des Ponts et Chaussées, 25 juin
5. Turgeman S, Pastor J (1987) Comparaison des charges limites d'une structure hétérogène et homogénéisée. J Méc Théor Appl 6(1):121–143
6. Hill R (1950) The mathematical theory of plasticity. Oxford engineering science series. Clarendon, Oxford
7. Kammoun Z (2010) Prévision de la charge limite des sols renforcés par réseaux de micropieux. Thèse de doctorat, Université de Savoie et Ecole Nationale d'Ingénieurs de Tunis
8. Kammoun Z, Pastor F, Smaoui H, Pastor J (2010) Large static problem in numerical limit analysis: a decomposition approach. Int J Numer Anal Methods Geomech 34:1960–1980
9. MOSEK ApS (2002) C/O Symbion Science Park, Fruebjergvej 3, Box 16, 2100 Copenhagen ϕ, Denmark. www.mosek.com.
10. Pastor F, Loute E, Pastor J (2009) Limit analysis and convex programming: a decomposition approach of the kinematical mixed method. Int J Numer Methods Eng 78(3):213–219
11. Pastor J (1978) Analyse limite: détermination numérique de solutions statiques complètes. Application au talus vertical. J Méc Théor Appl 2:167–196
12. Salençon J (1967) Théorie des charges limites: poinçonnement d'une plaque par deux poinçons symétriques en déformation plane. C R Acad Sci Paris 265:869–872
13. Salençon J (1974) Théorie de la plasticité pour les applications à la mécanique des sols. Eyrolles, Paris
14. Trillat M, Pastor J (2005) Limit analysis and Gurson's model. Eur J Mech A, Solids 24:800–819

The Anderson-Bishop Problem—Thermal Ratchetting of a Polycrystalline Metals

A.R.S. Ponter and A.C.F. Cocks

Abstract The paper readdresses a theory of super-plastic behaviour induced by cyclic temperature for certain classes of polycrystalline metals and composite materials, originally analyses by Anderson and Bishop in the 1950's for polycrystalline alpha uranium. The background to the original analysis and its subsequent history in the literature is discussed. Two distinct phenomena are involved. The first is ratchetting due to a fluctuating residual stress field and commonly found in structural analysis. The second form of ratchetting is due to the severe kinematic constraint on the deformation of each crystal within a polycrystal. The Anderson Bishop analysis did not take into account the former. Adopting the same kinematic assumptions as these authors, new solutions are discussed for simplified polycrystalline models and an isotropic polycrystal. These new solutions provide functional forms for material behaviour that need to be taken into account in discussions of the phenomena by material scientists.

1 Introduction

During the earlier phases of development of civil nuclear power in the UK, a number of phenomena were identified that arose from the unique and extreme conditions materials and structures were required to withstand. For those with interest in Direct Methods the best known example is Bree's complete solution for a thermally cycled tube [13]. Bree's solution illustrates the nature of structural ratchetting whereas it was observed within the earliest reactors that polycrystalline uranium exhibited two interesting modes of strain growth that related to mechanisms occurring on the material micro-scale. The first was Cottrell Creep resulting from neutron irradiation and the second was cyclic strain growth due to temperature variations within the

A.R.S. Ponter (✉)
Department of Engineering, University of Leicester, Leicester, UK
e-mail: asp@le.ac.uk

A.C.F. Cocks
Department of Engineering Science, University of Oxford, Oxford, UK

K. Spiliopoulos, D. Weichert (eds.), *Direct Methods for Limit States in Structures and Materials*, DOI 10.1007/978-94-007-6827-7_12,

Fig. 1 Steel test specimen repeatedly temperature cycles through a phase change. From Greenwood [5]

temperature range from room temperature to 668 °C, the range for which uranium has the alpha crystal structure.

As the original work was carried out as part of the development of civil nuclear reactors, the resulting reports [1, 2] were subject to the UK Official Secret Act and received very limited circulation at the time. The symposium paper [3] summarised their results, but the details of the analysis were not included. Subsequent workers in the field seem to have relied predominantly on the brief appendix to Greenwood and Johnsons [4] paper on the adaptation of the theory for metals that suffer a phase change during thermal cycling.

The reports [1, 2] were declassified in the early 1980's and may now be accessed at the UK National Archive at Kew, London. The Archive has agreed to their general availability and they may be obtained from the web-site listed in the foot-note to the references.

In the following sections we discuss the two modes of behaviour discuss by Anderson and Bishop and the nature of the analysis used.

1.1 Cottrell Creep

While under neutron irradiation, if a small stress $\Delta\sigma$ was applied to the polycrystal, constant strain growth occurred in the direction of the stress. Tests on helical springs under tension confirmed that the rate of strain growth $\dot{\varepsilon}$ was given, experimentally, by a relationship of the type

$$\dot{\varepsilon} = A\frac{\Delta\sigma}{\sigma_y}\dot{I} \tag{1}$$

where $\dot{I}$ is a measure proportional to the neutron density, σ_y is the uniaxial yield stress and A a material constant. The striking feature of this equation is the linearity with stress. In modern terms, this would be regarded as a type of super-plasticity. Because of the linearity with stress, very large strains may accumulate before necking of a sample occurs, of the type illustrated in Fig. 1. The first discussion of this behaviour was first given by Alan Cottrell (see Anderson and Bishop [1]) and is hence known as Cottrell Creep.

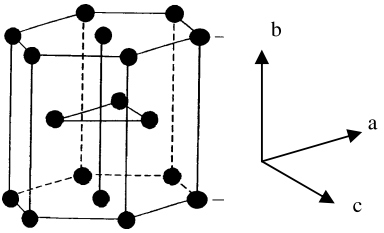

Fig. 2 Hexagonal Close Pack (HCP) crystalline structure of Alpha Uranium

Individual alpha uranium crystals have an orthorhombic hexagonal close-pack (HCP) structure, illustrated in Fig. 2. Unlike the other basic metallic crystal structures, the crystals are highly anisotropic and can show very differing properties in the b direction, compared with those in the a and c directions. Under irradiation, neutrons collisions displace atoms from their crystal position forming interstitials, atoms in a higher energy state wedged between other atoms in the regular array. These interstitials are capable of diffusing through the crystal under potential gradients. They diffuse together to form new layers of atoms, wedged into the crystal structure. The net effect on a single crystal is to cause a distortional permanent strain rate that Cottrell modeled as:

$$\dot{\varepsilon}^g_{ij} = \dot{\varepsilon}^g \begin{bmatrix} -1 & 0 & 0 \\ 0 & 1 & 0 \\ 0 & 0 & 0 \end{bmatrix} \tag{2}$$

where $\dot{\varepsilon}^g$ is proportional to $\dot{I}$ and the axis $(x, y, z) = (b, a, c)$ with respect to the crystal structure. In a polycrystal, the random orientation of adjacent crystals results in an overall strain growth of zero as there is no preferred direction, provided the b directions are completely randomly orientated. The strains resulting from Eq. (2) are offset by plastic strain rate $\dot{\varepsilon}^p_{ij}$, so that in a single crystal $\dot{\varepsilon}_{ij} = \dot{\varepsilon}^g_{ij} - \dot{\varepsilon}^p_{ij} = 0$ and there is zero overall strain growth. The polycrystal is a seething mass of plastically straining crystals. In their analysis Anderson and Bishop adopted the von Mises yield condition with the associated Prantl-Reuss flow rule, following the same assumptions as previously adoptd by Bishop and Hill [9]. Hence, with $\dot{\varepsilon}^g_{ij}$ prescribed for each crystal, the state of stress at yield is also prescribed and assumed constant within each crystal. Consider now applying an external small macro stress $\Delta\Sigma_{ij}$,

$$\Delta\Sigma_{ij} = \begin{bmatrix} 1 & 0 & 0 \\ 0 & 0 & 0 \\ 0 & 0 & 0 \end{bmatrix}_{X_i} \Delta\Sigma_X \tag{3}$$

in this case referred to fixed external axis (X, Y, Z). The resulting macro strain rate, as the polycrystal is isotropic, is given by

$$\dot{E}_{ij} = \begin{bmatrix} 1 & 0 & 0 \\ 0 & -1/2 & 0 \\ 0 & 0 & -1/2 \end{bmatrix}_{X_i} \dot{E}_X. \tag{4}$$

Anderson and Bishop assumed that all crystals experienced this same total strain rate and that the stress in each crystal was constant within each crystal but varies

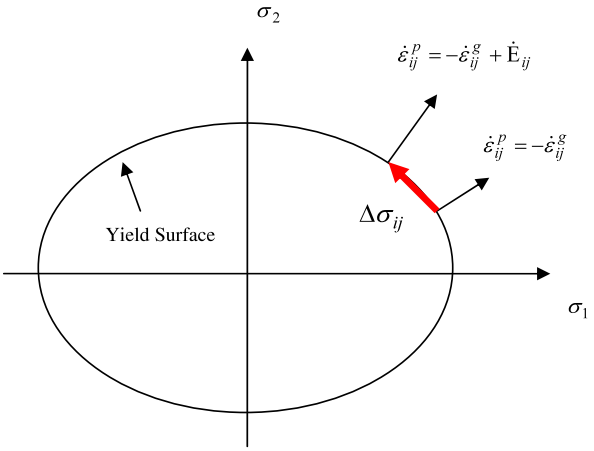

Fig. 3 Schematic representation of source of strain growth in Cottrell Creep. The imposition of the macro strain rate $\dot{E}_{ij}$ causes a movement of the yield point by stress $\Delta\sigma_{ij}$

from crystal to crystal. Hence the circumstance within an individual crystal may be understood from Fig. 3. The plastic strain $\dot{\varepsilon}_{ij}^{g}$, Eq. (2) and the strain growth Eq. (4) will not be consistent with each other when transformed to a common set of axes (X, Y, Z). The imposition of $\dot{E}_{ij}$ causes the stress at yield to move around the yield surface by an amount $\Delta\sigma_{ij}$ defined by the flow law. The analysis consists of using the Prandl-Reuss flow rule to compare the states of stress resulting from plastic strain rates $\dot{\varepsilon}_{ij}^{p} = -\dot{\varepsilon}_{ij}^{g}$ and $\dot{\varepsilon}_{ij}^{p} = -\dot{\varepsilon}_{ij}^{g} + \dot{E}_{ij}$ and then expanding the difference for small $\dot{E}_x$ compared with $\dot{\varepsilon}^{g}$ to obtain the stress difference at yield, $\Delta\sigma_{ij}$. The average of $\Delta\sigma_{ij}$ over-all crystals then gives $\Delta\Sigma_x$. Anderson and Bishop [1] complete this analysis and obtain

$$\dot{E}_x = \frac{5}{2\sqrt{3}} \frac{\Delta\Sigma_x}{\sigma_y} \dot{\varepsilon}_g \tag{5}$$

for $\Delta\Sigma_x$ small compared with σ_y. Although the authors do not consider conditions of equilibrium formally, relying entirely on the kinematics of the situation, conditions of equilibrium consistent with the kinematic assumptions may be easily applied to the analysis using the Principle of Virtual Work yielding the identical result (5) (see Ponter and Cocks [19]). Hence, within the limitations of the model, result (5) may be regarded as correct, as it has been for the last 60 years.

1.2 Temperature Cycling of Alpha-Uranium

The authors [1, 3] then turn to the second case of interest. When a uranium polycrystal is subjected to cycles of temperature change ΔT in excess of a critical value ΔT_s, in the absence of applied stress, a small amount of strain growth occurs. How-

ever, if a macro-stress $\Delta\Sigma_X$, Eq. (3), is applied, a cyclic strain growth ΔE_x per cycle occurs, given by the general form

$$\Delta E_x = B\left(\frac{\Delta\Sigma_x}{E}\right)\left(\frac{\Delta T - \Delta T_s}{\Delta T_s}\right) \tag{6}$$

where B is a numerical constant and E denotes Young's modulus. Such behaviour was also shown in test on helical springs suspended under weights. Although the correlation was by no means exact the linearity with stress and the existence of a critical temperature difference threshold was confirmed. Cottrell predicted the form of Eq. (6) in a Note, now lost, on the basis of the behaviour of a two bar structure (see below). Although the arguments he used were clearly suspect from the point of view of mechanics, Anderson and Bishop were not entirely surprised to discover that, on detailed analysis, Alan Cottrell was, again, correct.

The property of the crystal that gives rise to this phenomenon is the strongly anisotropic thermal expansion coefficients. In terms of axis $(x, y, z) = (b, a, c)$ local to the crystal, the coefficients of thermal expansion are given by

$$\alpha_a = \alpha_c = 30 \times 10^{-8}\ ^\circ\mathrm{C}^{-1}, \qquad \alpha_b = -5 \times 10^{-8}\ ^\circ\mathrm{C}^{-1}. \tag{7}$$

Alternatively these may be described by average and deviating components,

$$\bar{\alpha} = (\alpha_a + \alpha_b + \alpha_c)/3 = 55/3 \times 10^{-8}\ ^\circ\mathrm{C}^{-1}, \tag{8a}$$

$$\Delta\alpha_{ij} = (2/3)\Delta\alpha \begin{Bmatrix} 1 & 0 & 0 \\ 0 & -1/2 & 0 \\ 0 & 0 & -1/2 \end{Bmatrix}, \tag{8b}$$

$$\Delta\alpha = (\alpha_a - \alpha_b) = 35 \times 10^{-8}\ ^\circ\mathrm{C}^{-1}. \tag{8c}$$

The overall effect of this on the polycrystal when a temperature change of ΔT is applied is an overall expansion, governed by the average coefficient $\bar{\alpha}$ and incompatible volume conserving distortions within each crystal, deriving from the deviating component $\Delta\alpha_{ij}$. As these strains cannot remain compatible with neighbouring crystals, linear elastic stresses are set up so that the net strain in each crystal remains zero. Hence, by elementary arguments, the elastic stress $\hat{\sigma}_{ij}$ in typical crystal, in relation to $(x, y, z) = (b, a, c)$ is given by

$$\hat{\sigma}_{ij} = \sigma_t \begin{Bmatrix} 1 & 0 & 0 \\ 0 & -1/2 & 0 \\ 0 & 0 & -1/2 \end{Bmatrix}, \tag{9}$$

where $\sigma_t = 2E\Delta\alpha\Delta T/(1+\nu)$. The elastic limit is then given by the von Mises yield condition as $3/2\sigma_t = \sigma_y$. A small amount of plastic strain then allows ΔT to increase to a reverse plasticity limit where the elastic stress varies over a range of twice yield and $\Delta T = \Delta T_S$ where,

$$\sigma_t = 2E\Delta\alpha\Delta T_s/(1+\nu) = 4/3\sigma_y. \tag{10}$$

For $\Delta T > \Delta T_s$, a state of reverse plasticity is set up in each crystal and the polycrystal shows no cyclic strain growth. Each crystal suffers equal and opposite plastic strains

$$\Delta \varepsilon_{ij}^{p} = \pm \begin{Bmatrix} 1 & 0 & 0 \\ 0 & -1/2 & 0 \\ 0 & 0 & -1/2 \end{Bmatrix} \Delta \varepsilon^{p}. \tag{11}$$

The question now arises: what is the growth of strain per cycle if a small external constant stress $\Delta \Sigma_x$ is applied? Anderson and Bishop [1, 3] adopted a form of analysis that closely follows that used for Cottrell Creep. They assumed that equal strain increments occur at each extreme of the cycle, given by replacing Eq. (2) by Eq. (11), but following the same averaging process. Again, the arguments are entirely kinematic and the details of the internal stress are not considered. Their analysis produced the answer

$$\Delta E_x = \left(\frac{\Delta \Sigma_x}{E} \right) \frac{32}{27} \left(\frac{\Delta T - \Delta T_s}{\Delta T_s} \right). \tag{12}$$

This solution, and various adaptations, has been widely used over the intervening years for a variety of other systems where internal thermal expansion strains occur. Greenwood and Johnson [4] adapted this theory for cycling through phase changes, and it is the Appendix to this paper that appears to be the main source for subsequent authors in material science. The Anderson Bishop results are much quoted in the literature (e.g. [5–8, 10–12]) and have been refined in terms of micro-models, see, for example Leblond [6, 7] and Taleb and Sideroff [8]. Recently Greenwood [5] has given a review of subsequent work in this area. Ratchetting in metal matrix composites was identified by Daehn and Gonzalez-Doncel [11] as being a related phenomenon and the functional form of the Anderson Bishop analysis was adopted. Other related work on metal matrix composites is summarised by Clyne and Withers [12]. There are certainly in excess of 100 papers in the literature which uses this result and also use Anderson's extension of the work to creep [2].

It should be emphasized that Anderson and Bishop did not regard their analysis as a detailed realistic micro-model of the polycrystal. The assumption of a von Mises yield condition is certainly appropriate for the overall behaviour of a polycrystal, but not necessarily appropriate for a single crystal. The model is essentially phenomenological—describing in general terms the dependence of the strain on governing quantities but probably not reliable in detail. Hence details of non-compliance of the theory with experimental data has not been regarded as a barrier to its use.

Those readers familiar with thermal loading problem of this nature may well have already wondered if the Anderson Bishop analysis is the complete answer. Ratchetting in structures due to thermal cycling is common. Ponter and Cocks [14, 15] looked at ratchet rates for such problems and derived relationships of a similar form to (12). But the source of ratcheting in the structural cases came from a very different mode of behaviour. The kinematic restrain argument of Anderson and Bishop do not apply but ratcheting arises from changes in residual stress during the cycle,

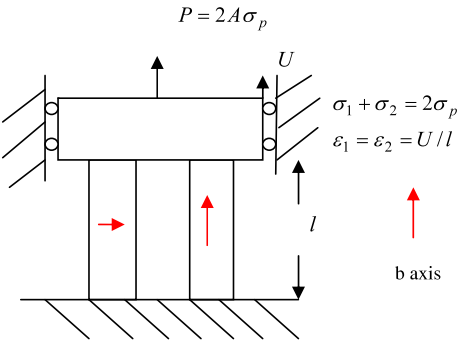

Fig. 4 Simple two bar structure. The bars have equal elastic and plastic properties but unequal coefficients of thermal expansion α_1 and α_2

allowing cyclic strain growth due to transfer of load from one part of the structure to another. It is worth asking the question if both sources of ratchet strain growth is present in this problem, that considered by Anderson and Bishop and the Bree-like ratchetting of structures. A particular situation may easily be considered where the Anderson Bishop strain growth does not apply, a two bar structure, and this is discussed in detail in the next section.

2 A Two Bar Structure

Consider the simple structure shown in Fig. 4 where two differently orientated crystals are constrained to equal strains in one direction. The bars have the same physical dimensions and have equal yield stresses and Young's modulus E but unequal coefficients of thermal expansion α_1 and $\alpha_2 > \alpha_1$ in the direction of stress. It is immediately obvious that the Anderson Bishop analysis method would predict that no ratchetting occurs and their methodology is not applicable.

This type of problem is well known in structural mechanics. Indeed, numerical methods for generating properties of the solution of such problems now forms standard components in the design of high temperature plant and is available for use in the UK Life Assessment Method R5 [16–18]. It is, therefore, worthwhile looking in detail at this simple two element problem to provide a common area between structural mechanics and the Anderson Bishop analysis.

The elastic stresses due to applied load $P = 2A\sigma_p$ and temperature rise ΔT are given by

$$\sigma_1 = \sigma_p - \sigma_t, \qquad \sigma_2 = \sigma_p + \sigma_t, \quad \text{where } \sigma_t = E\Delta\alpha\Delta T/2 \tag{13}$$

and elastic limit is given by

$$\sigma_2 = \sigma_p + \sigma_t = \sigma_y \quad \text{Elastic Limit.} \tag{14}$$

The full analysis for this problem is summarised in Table 1 where the complete solution is shown for conditions of elastic behaviour, shakedown, reverse plasticity and ratchetting. The overall behaviour is summarised in the interaction diagram shown

Table 1 Solutions for two bar structure of Fig. 4

	Elastic $\hat{\sigma}_i$	Constant $\bar{\rho}_i$	Varying ρ_i^r	Total σ_i
(a) Shakedown solution $\sigma_p^s + \sigma_t/2 = \sigma_y$, $\sigma_t \le 2\sigma_y$, $\rho_i^r = 0$				
$T = T_0 + \Delta T$ σ_1	$\sigma_p^s + \sigma_t$	$-\sigma_t/2$	0	$\sigma_p^s + \sigma_t/2 = \sigma_y$
$T = T_0 + \Delta T$ σ_2	$\sigma_p^s - \sigma_t$	$\sigma_t/2$	0	$-\sigma_y \le \sigma_p^s - \sigma_t/2 \le \sigma_y$
$T = T_0$ σ_1	σ_p^s	$-\sigma_t/2$	0	$-\sigma_y \le \sigma_p^s - \sigma_t/2 \le \sigma_y$
$T = T_0$ σ_2	σ_p^s	$\sigma_t/2$	0	$\sigma_p^s + \sigma_t/2 = \sigma_y$
(b) Ratchetting solution $\sigma_p^s + \Delta\sigma_p + \sigma_t/2 \ge \sigma_y$, $\sigma_t \le 2\sigma_y$				
$T = T_0 + \Delta T$ σ_1	$\sigma_p^s + \Delta\sigma_p + \sigma_t$	$-\sigma_t/2$	$-\Delta\sigma_p$	$\sigma_p^s + \sigma_t/2 = \sigma_y$
$T = T_0 + \Delta T$ σ_2	$\sigma_p^s + \Delta\sigma_p - \sigma_t$	$\sigma_t/2$	$+\Delta\sigma_p$	$-\sigma_y \le \sigma_p^s + \Delta\sigma_p - \sigma_t/2 \le \sigma_y$
$T = T_0$ σ_1	$\sigma_p^s + \Delta\sigma_p$	$-\sigma_t/2$	$+\Delta\sigma_p$	$-\sigma_y \le \sigma_p^s + \Delta\sigma_p - \sigma_t/2 \le \sigma_y$
$T = T_0$ σ_2	$\sigma_p^s + \Delta\sigma_p$	$\sigma_t/2$	$-\Delta\sigma_p$	$\sigma_p^s + \sigma_t/2 = \sigma_y$
(c) Reverse plasticity solution $\sigma_p = 0$, $\sigma_t \ge 2\sigma_y$				
$T = T_0 + \Delta T$ σ_1	$+\sigma_t$	$-\sigma_t/2$	$+(\sigma_y - \sigma_t/2)$	$+\sigma_y$
$T = T_0 + \Delta T$ σ_2	$-\sigma_t$	$\sigma_t/2$	$-(\sigma_y - \sigma_t/2)$	$-\sigma_y$
$T = T_0$ σ_1	0	$-\sigma_t/2$	$-(\sigma_y - \sigma_t/2)$	$-\sigma_y$
$T = T_0$ σ_2	0	$\sigma_t/2$	$+(\sigma_y - \sigma_t/2)$	$+\sigma_y$
(d) Ratchetting solution $\sigma_t \ge 2\sigma_y$, $\sigma_p = \Delta\sigma_p$				
$T = T_0 + \Delta T$ σ_1	$\Delta\sigma_p + \sigma_t$	$-\sigma_t/2$	$+(\sigma_y - \sigma_t/2) - \Delta\sigma_p$	$+\sigma_y$
$T = T_0 + \Delta T$ σ_2	$\Delta\sigma_p - \sigma_t$	$\sigma_t/2$	$-(\sigma_y - \sigma_t/2) + \Delta\sigma_p$	$\sigma_y \ge -\sigma_y + 2\Delta\sigma_p \ge -\sigma_y$
$T = T_0$ σ_1	$\Delta\sigma_p$	$-\sigma_t/2$	$-(\sigma_y - \sigma_t/2) + \Delta\sigma_p$	$\sigma_y \ge -\sigma_y + 2\Delta\sigma_p \ge -\sigma_y$
$T = T_0$ σ_2	$\Delta\sigma_p$	$\sigma_t/2$	$+(\sigma_y - \sigma_t/2) - \Delta\sigma_p$	$+\sigma_y$

in Fig. 5. For $\sigma_p + (1/2)\sigma_t \le \sigma_y$either purely elastic behaviour (E) or shakedown (S) occurs. In excess of $\sigma_p + (1/2)\sigma_t = \sigma_y$ratchetting (R) occurs at a rate per cycle give by

$$\Delta\varepsilon^p = 4\Delta\sigma_p/E \tag{15}$$

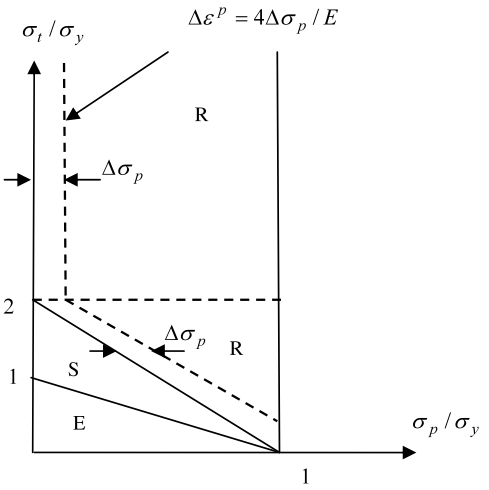

Fig. 5 Interaction diagram for two bar structure, showing the elastic (E), shakedown (S) and ratchetting (R) regions

where $\Delta\sigma_p$ is the increase of σ_p either above the shakedown limit for $\sigma_t \leq 2\sigma_y$ or above zero for $\sigma_t > 2\sigma_y$. The reverse plasticity region is reduced to the axis $\sigma_p = 0$ and $\sigma_t > 2\sigma_y$.

The solution shows that the ratchet strain $\Delta\varepsilon^p$ per cycle is obtained by sequential plastic strain in each of the bars at separate instants during the cycle when the other bar remains within the elastic range. The Anderson Bishop analysis is concerned with behaviour for small σ_p for $\sigma_t > 2\sigma_y$ where they predict a ratchet rate of the general form, in the notation of this example

$$\Delta\varepsilon^p = K(\Delta T - \Delta T_s)\Delta\sigma_p / E \tag{16}$$

where ΔT_s is the temperature difference corresponding to $\sigma_t = 2\sigma_y$. Note the primary difference between (15) and (16). We find, for the polycrystalline problem, the solution consist of a combination of the two modes of behaviour exemplified by Eqs. (15) and (16).

3 Polycrystalline Models

The two bar structure, despite its simplicity, shows all the characteristic modes of behaviour of all such problems, but excludes the precise phenomenon identified by Anderson and Bishop as the cause of ratchetting in alpha-uranium. As a result, the behaviour of a polycrystal may be expected to show both forms of ratcheting. The associated analysis is, therefore, rather more complex and will not be discussed in detail here. Effectively the problem may be solved by combining the arguments of Anderson and Bishop [1, 3] but taking into account the fact that the residual stress within each crystal is not constant but varies. Plastic strains in reverse plasticity will always occur at both ends of the cycle, but the additional plastic strains that contribute to the ratchet mechanism when stress is applied may only occur at one

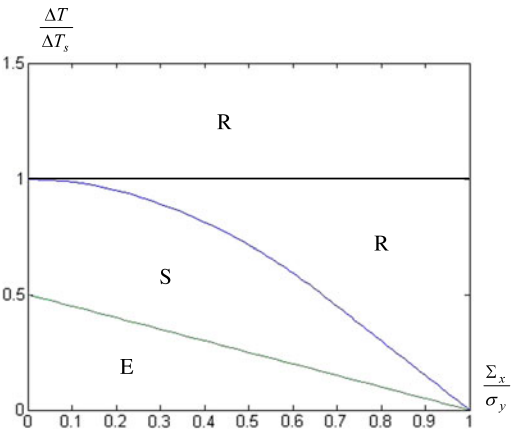

Fig. 6 Interaction diagram for three element model showing the elastic (E), shakedown (S) and ratchetting (R) regions

instant in the cycle. A detailed analysis (Ponter and Cocks [19]) of the structure of the problem shows this to be the case. Two models are considered. The first simplifies the crystal structure by assuming that all crystals have their b direction orientated along each of the axis of a fixed set of axis, a third in each direction. In the following we refer to this as the three element model. This simplification allows a more complete analytic solution than in the fully anisotropic case.

The full interaction diagram, for comparison with Fig. 5, is shown in Fig. 6 for the three element model. There are many similarity, except that the shakedown boundary at $\Delta T/\Delta T_S = 1$, the reverse plasticity limit, meets the $\Sigma_x/\sigma_y = 0$ axis at a right angle. This is associated with a rate of increase of ratchet strain with increases in load beyond shakedown becoming zero. This is unlike the two bar structure, Fig. 5 where this angle is obtuse and the ratchet rate remains constant.

For $\Delta T/\Delta T_S > 1$ both the three element model and the polycrystal model may be evaluated for comparison with Anderson and Bishop. Although Anderson and Bishop did not consider the three element model, the analysis with their assumptions may easily be carried out. A comparison between all the solutions is shown in Fig. 7.

There a number of features of Fig. 7 of immediate interest. The solutions for the three element and the fully isotropic models are very similar. This indicates that analysis of the much simpler three element model provides a close approximation to the more complex case, providing a useful route to future studies using more complex behaviour, such as creep. The other, perhaps surprising, result is that the solution that includes both ratcheting phenomenon gives lower ratchet rates than the Anderson and Bishop analysis, which only includes one. The reason for this is that Anderson and Bishop assumed that a contribution to the ratchet strain occurred throughout the polycrystal at both extremes of the temperature cycle whereas, due to changing residual stress fields, it only occurs at one extreme. Hence Anderson and Bishop in this respect overestimated the ratchet strain but underestimated it by leaving out conventional structural ratcheting. Note that at $\Delta T/\Delta T_S = 1$the ratchet rate is zero, whereas for the two bar structure it has a high value.

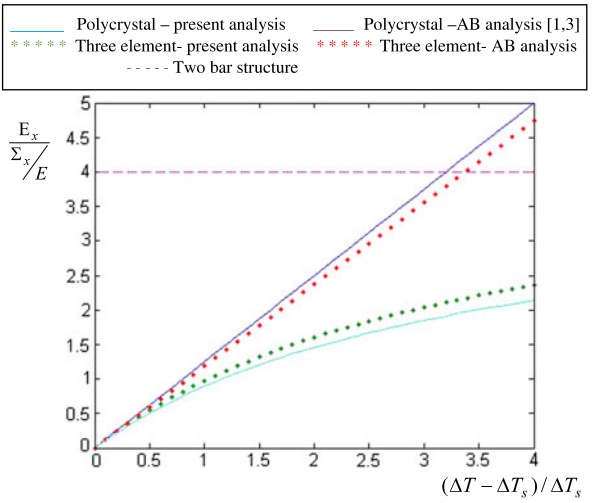

Fig. 7 Comparison of Anderson Bishop and present analysis. *Solid*—polycrystal, *dashed*—three element model

4 Conclusion

The Anderson Bishop [1–3] model for the linear plastic ratchetting of polycrystals with anisotropic crystal thermal expansion properties when subjected to cyclic temperature and Greenwood's [4, 5] adaptation of the model for alloys cycled through a phase change have remained unchallenged since the early 1960's. Neither model was put forward as an exact model of behaviour and various assumptions may be challenged. Crystals were assumed to be isotropic in both their elastic and plastic behaviour and satisfy the von Mises yield condition and associated perfectly plastic flow condition. The total microstrain was assumed to remain the same as a uniform macrostrain, although this has remained an assumption in subsequent work. The material constants are assumed independent of temperature. The models should, perhaps, be sufficient to demonstrate the relationship between the observed superplasticity behaviour and the micromechanical phenomena. Anderson and Bishop [1–3] demonstrated that the phenomenon may be explained through the movement of the yield point around the yield surface, constrained by overall kinematic conditions and the associated flow law. They give a resulting equation (12) where the accumulation of plastic strain for each cycle of temperature increases linearly with applied stress and temperature variation. The purpose of this paper is to show that a separate micromechanics phenomena also makes a contribution, the redistribution of stress through a varying residual stress. This results in plastic ratchet strains, in an individual crystal, occuring only at one extreme of the thermal cycle. Hence, at the two extremes a proportion of the crystals suffer plastic strain growth while the remainder remain elastic. At the opposing end of the cycle the reciprocal set of crystals experience plastic ratchet strains. This behaviour may be demonstrated in a two bar structure. The effect on the resulting prediction is to reduce the ratchet rate significantly compared to the Anderson Bishop analysis as shown in Fig. 7. The new solution shows a lower rate of ratchetting.

The Anderson Bishop solutions were not expected to give close predictions of behaviour and, of course, neither does this new solution Eq. (17), below (Ponter and Cocks [19]). The primary purposes of this paper bring to the notice of those workers in Direct Methods that this neglected ratchet phenomenon exists and remind future workers in that if more detailed micromechanics is attempted of this class of problems then phenomena associated with changing residual stress field exists. In the three cases discussed here, the two bar structure, the three element problem and the polycrystal problem, all the solutions have the same overall form (Ponter and Cocks [19]):

$$\Delta E_x = \left(\frac{\Delta \Sigma_x}{E}\right) \frac{(\Delta T - \Delta T_s)/\Delta T_s}{(a + b(\Delta T - \Delta T_s)/\Delta T_s)} \tag{17}$$

where for:

Two Bar structure: $a = 0, b = 1/4$.
Three Element Model: $a = 27/32, b = 1/4$.
Polycrystal Model: $a = 4/5, b = 0.244$.
The Anderson Bishop model corresponds to $b = 0$.

The analysis does not include the effects of high temperature creep, the subject of Anderson's second report [2]. This problem is more complex and has not been discussed in this paper. Creep strain rates vary very rapidly with temperature and it seems likely that most of such problems will involve both plastic and creep strains within the cycle of temperature, an aspect not considered by Anderson[2], indicating that the creep problem may now be usefully looked at again, following the results of this paper

Acknowledgements The first author first became aware of the Anderson and Bishop solutions when working with Roger Anderson on the modelling of a similar phenomena in the irradiation induced swelling of structural steels [20]. In recent years, following an interest in the thermal properties of metal matrix composites it became clear that the solutions have been extensively applied to problems in material science.

The authors wish to thanks Roger Anderson for assistance in this work. The work for this paper was part support by a Leverhulme Emeritus Fellowship to the first named author, which is gratefully acknowledges.

References

1. Anderson RG, Bishop JFW (1957) United Kingdom Atomic Energy Authority Industrial Group report TN/C681, UK National Archive reference AB 7/7441. Copy is available with the permission of the National Archive for downloading from http://www.le.ac.uk/departments/engineering/people/academic-staff/alan-ponter/papers
2. Anderson RG (1958) United Kingdom Atomic Energy Authority Industrial Group report TN/C681, UK National Archive reference AB 7/ 6213. Copy is available with the permission of the National Archive for downloading from http://www.le.ac.uk/departments/engineering/people/academic-staff/alan-ponter/papers

3. Anderson RG, Bishop JFW (1962) The effect of neutron irradiation and thermal cycling on permanent deformations in uranium under load. In: Proceedings of the institute of metals symposium on uranium and graphite, Institute of Metals, London, paper 3. Copy is available with the permission of the National Archive for downloading from http://www.le.ac.uk/departments/engineering/people/academic-staff/alan-ponter/papers
4. Greenwood GW, Johnson RH (1964) The deformation of metals under stresses during phase transformation. Proc R Soc A 283:403–422
5. Greenwood GW (2010) Generation of internal stress and its effects. Mater Sci Technol 26(4):398–403
6. Leblond JB, Devaux J, Devaux JC (1989) Mathematical modelling of transformation plasticity in steels, I: case of ideal-plastic phases. Int J Plast 5:551–572
7. Leblond JB (1989) Mathematical modelling of transformation plasticity in steels, II: coupling with strain hardening phenomena. Int J Plast 5:573–591
8. Taleb L, Sidoroff F (2003) A micromechanical modeling of the Greenwood–Johnson mechanism in transformation induced plasticity. Int J Plast 19(10):1821–1842
9. Bishop JFW, Hill R (1951) A theory of the plastic distortion of a polycrystalline aggregate under combined stress. Philos Mag 42:1298
10. Hutchinson JM, McCrum NG (1974) Microstress mechanisms for the time dependence of the modulus of crystalline polymers following an imposed change in volume. Nat Phys Sci 270:295–296
11. Daehn GS, Gonzalez-Doncel G (1989) Deformation of whisker-reinforced metal matrix composites under changing temperature conditions. Metall Trans 20A:2355–2368
12. Clyne TW, Withers PJ (1993) An introduction to metal matrix composites. Cambridge University Press, Cambridge, Chap 5
13. Bree J (1967) Elasto-plastic behaviour of thin tubes subjected to internal pressure and intermittent high-heat fluxes with applications to fast reactor fuel elements. J Strain Anal 2(3):226–238
14. Ponter ARS, Cocks ACF (1984) The incremental strain growth of an elastic-plastic body loaded in excess of the shakedown limit. J Appl Mech 51(3):465–469
15. Ponter ARS, Cocks ACF (1984) The incremental strain growth of elastic-plastic bodies subjected to high levels of cyclic thermal loading. J Appl Mech 51(3):470–474
16. Goodall IW, Goodman AM, Chell GC, Ainsworth RA, Williams JA (1991) R5: an assessment procedure for the high temperature response of structures. Report, Nuclear Electric Ltd., Barnwood, Gloucester
17. Chen HF, Ponter ARS, Ainsworth RA (2006) The linear matching method applied to the high temperature life assessment of structures, part 1: assessments involving constant residual stress fields. Int J Press Vessels Piping 83:123–135
18. Chen HF, Ponter ARS, Ainsworth RA (2006) The linear matching method applied to the high temperature life assessment of structures, part 2: assessments beyond shakedown involving changing residual stress fields. Int J Press Vessels Piping 83:136–147
19. Ponter ARS, Cocks ACF (2013) Thermal ratchetting of polycrystalline metals with inhomogeneous thermal properties. Philos Mag, accepted May 2013, available online
20. Anderson RG, Ponter ARS (1972) An estimate of the Cottrell creep of a metal during swelling. In: British nuclear energy society conference on irradiation embrittlement and creep in fuel cladding and core components, London

Recent Development and Application of the Linear Matching Method for Design Limits in Plasticity and Creep: An Overview

Haofeng Chen and Weihang Chen

Abstract Engineering design and integrity assessment of components under the action of cyclic thermal and mechanical loading require the assessment of load histories for which certain types of material failure do not occur. This involves the determination of the shakedown limit, ratchet limits, plastic strain range concerning fatigue crack initiation in a low cycle fatigue assessment, and creep fatigue interaction.

In this paper a state-of-the-art direct method, the Linear Matching Method (LMM), is summarized for the evaluation of these design limits in both plasticity and creep. These have been solved by characterizing the steady cyclic state using a general cyclic minimum theorem. For a prescribed class of kinematically admissible inelastic strain rate histories, the minimum of the functional for these design limits are found by either global minimization process or dual minimization process. The applications of the LMM to three practical problems are outlined to confirm the efficiency and effectiveness of the method and demonstrate that Direct Methods may be applied to a much wider range of circumstances than have hitherto been possible.

Keywords Plasticity · Creep · Direct methods · Cyclic loading · Shakedown · Ratchetting · Creep-fatigue interaction

1 Introduction

Imperfections in structures can arise in the initial production process, or during the heat-treatment of the component, particularly during welding processes. These defects or flaws are unavoidable within structure components, and they do not generally lead to an immediate failure. Failure modes occurring from these structures are different from industry to industry, but mostly such failures result from the application of cyclic loading with high temperature. In general, the lifetimes of these components, operating at elevated temperatures, depend on the nature of plastic

H. Chen (✉) · W. Chen
Department of Mechanical and Aerospace Engineering, University of Strathclyde, Glasgow G1 1XJ, UK
e-mail: haofeng.chen@strath.ac.uk

K. Spiliopoulos, D. Weichert (eds.), *Direct Methods for Limit States in Structures and Materials*, DOI 10.1007/978-94-007-6827-7_13,

and creep deformation they experience. The first failure mode is mainly concerned with the excessive plastic deformations associated with the phenomenon of plastic collapse, shakedown and ratchetting, while the second is concerned with the creep fatigue interaction. The ability to accurately model these behaviours of component subjected to cyclic and variable loading conditions would provide a means of assessing the remaining life of the structural components. Thus, the elastic-plastic-creep response of a structure needs to be well understood when using it as a design condition.

The determination of these design limits has attracted the attentions of many researchers. The phenomena of shakedown and ratchetting associated with the steady cyclic response have been researched and modeled extensively by plasticity theorists, materials scientists, mathematicians and engineers. Since closed form solutions of these design limits are very limited due to the complexity of the problem, the numerical approaches play a key role for the assessment of these design limits in plasticity.

One approach is to simulate the detailed elastic-plastic response of the structure for a specified cyclic load history, most commonly by the incremental Finite Element Analysis (FEA) [1]. However, this method requires significant computer time for complex structures, due to the reason of its investigation of any load cycle. A relatively new cyclic analysis method, Direct Cyclic Analysis (DCA) [2], has been developed to avoid excessive numerical expense associated with the incremental FEA. It has been recently incorporated into ABAQUS to evaluate the stabilized cyclic behaviour directly. However, both the incremental FEA and DCA do not predict shakedown or ratchet limits directly. It can only be used to show whether elastic shakedown, plastic shakedown or ratchetting occurs [3].

To define the shakedown and ratchet limits, alternative approach has been developed. It involves the application of numerical methods [4–9] for addressing the structural response in structures subjected to both severe mechanical and thermal loads. The assessments, provided from these new methods, have the potential of providing results that combine the accuracy of non-linear FEA simulation methods [10, 11] with the efficiency of rules-based methods [12, 13]. These are direct methods based upon a programming technique. Direct methods were incorporated into finite element analysis in order to evaluate the shakedown limit. The material model is considered to be elastic perfectly plastic, and the load domain including all the possible load paths eliminates the necessity to know the detailed load history. Such direct methods include; the mathematical programming methods [14–16], the Generalized Local Stress Strain (GLOSS) r-node method [17], the Elastic Compensation Method (ECM) [18], and the Linear Matching Method (LMM) [7, 19, 20]. Among these direct methods, the LMM is counted to be the method most amenable to practical engineering applications involving complicated thermomechanical load history. The LMM has been extensively applied to a range of problems [8, 19], through various adaptations, extended to the calculation required for the UK assessment procedure R5 [21] for the high temperature response of structures. The LMM describes non-linear inelastic material behaviour by linear solutions where the material coefficients vary both spatially and in time, which makes the method

particularly flexible. The LMM has been regarded as an efficient and effective upper bound programming method for which, in many circumstances, strict convergence proofs may be constructed. In the past two years, the LMM has been further developed to account for the lower bound shakedown and ratchets limits, and investigate more complicated cyclic problems. Moreover, the extensions of LMM have resulted in the application of the method to high temperature creep behavior including the effect of elastic follow-up [20], i.e. the evaluation of local creep damage due to the relaxation of stress during creep dwell times.

There are four objectives leading to using the basics of these methods in this study where limit in plasticity and creep are designed. The first objective is to obtain a LMM approach used for more general purposes. This LMM must be able to address to a wider class of problems and prospective procedures for lower and upper bound design limits. The second objective is to assess the cyclic response under creep fatigue conditions by presenting a new numerical procedure. The third is the examination and the improvement of convergence problems existing in the iterative approach and the last objective is to validate the efficiency and effectiveness of LMM while designing the limits in plasticity and creep. This validation is performed on three typical practical problems. The first problem is; a defective pipeline subjected to cyclic thermal loading and constant operating pressure. In the second problem the effects of drilling holes on the ratchet limit and crack tip plastic strain range for a central cracked plate subjected to constant tensile loading and cyclic bending moment are investigated, and in the last one the cyclic structural responses of a cruciform weldment under creep fatigue interaction is being addressed.

In the following sections, a general cyclic minimum theorem for perfect plasticity and the application of the LMM for a particular class of problems for the design limits in plasticity and creep will be described. This is followed by the discussion of convergence and the application of three practical examples with numerical verifications of the proposed methods.

2 Cyclic Behaviour

2.1 General Cyclic Problem

Consider a body with volume V and surface S, where the material is isotropic, elastic-plastic and satisfies the von Mises yield condition. A cyclic history of temperature $\lambda\theta(x,t)$ occurs within volume V. A cyclic load history $\lambda P(x,t)$ is applied over part of S, namely S_T. Here λ denotes a scalar load parameter. On the remainder of S, namely S_u, zero displacements are maintained. Both load and temperature histories have the same cycle time Δt and, in the following, we are concerned with the behaviour of the body in a typical cycle $0 \le t \le \Delta t$ in a cycle state. For the problem defined above the stresses and strain rates will asymptote to a cyclic state where

$$\sigma_{ij}(t) = \sigma_{ij}(t + \Delta t), \qquad \dot{\varepsilon}_{ij}(t) = \dot{\varepsilon}_{ij}(t + \Delta t). \tag{1}$$

This arbitrary asymptotic cyclic history may be expressed in terms of three components, the elastic solution, a transient solution accumulated up to the beginning of the cycle and a residual solution that represents the remaining changes within the cycle. The linear elastic stress solution is denoted by $\lambda\hat{\sigma}_{ij}$. The general form of the stress solution is given by

$$\sigma_{ij}(x,t) = \lambda\hat{\sigma}_{ij}(x,t) + \bar{\rho}_{ij}(x) + \rho^r_{ij}(x,t) \tag{2}$$

where $\bar{\rho}_{ij}$ denotes a constant residual stress field in equilibrium with zero surface traction on S_T and corresponds to the residual state of stress at the beginning and end of the cycle. The history ρ^r_{ij} is the change in the residual stress during the cycle and satisfies;

$$\rho^r_{ij}(x,0) = \rho^r_{ij}(x,\Delta t). \tag{3}$$

It is worth noting that the arguments in this section do not explicitly call on the properties of perfect plasticity and are therefore common to all cyclic states associated with inelastic material behaviour.

2.2 Description of Design Limits in Plasticity and Creep Under Cyclic Loading

2.2.1 Design Limits in Plasticity

One well-known illustration defining the plasticity limit of the structure under cyclic load history is Bree interaction diagram [22, 23]. Bree [22, 23] developed theoretical solutions for a simplified 2-dimensional model of a nuclear reactor fuel can. In his model, constant pressure stress and cyclic temperature gradient was applied across the can wall during start-up and shutdown. These theoretical solutions were illustrated on Bree interaction diagram in order to provide different modes of material behaviour for different cyclic loading conditions. These diagrams with various cyclic loading combinations are helping the designers especially in their early stages of design.

Figure 1 is the Bree diagram [22, 23], illustrating the responses for the case of a fuel can subject to cyclic through-wall thermal stress and a constant internal pressure. The ordinate and abscissa give normalised values of pressure and thermal stress respectively, where the stresses have been normalised against the yield stress of the material. The distinct feature on the interaction diagram is the separation of the different modes of material behaviour. In this particular analysis, the diagram is divided into four design regions, namely:

Pure Elastic Region In this region, it was found that the load level is sufficiently small; the response is purely elastic, no permanent strains are induced, and the structure returns to its original configuration after each load application.

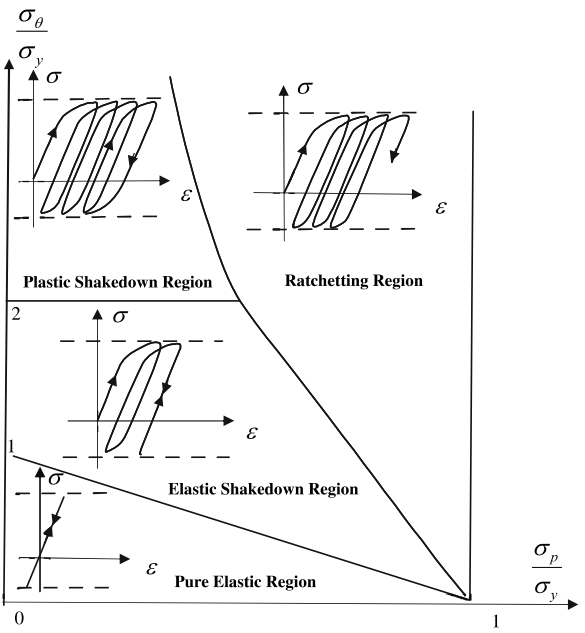

Fig. 1 Bree diagram for pressurized tube and thermal loading [22, 23]

Elastic Shakedown Region In this region, the stresses are exceeding the yield stress at the first few load cycles, which give rise to constant residual stress in the structure such that in subsequent load cycles only elastic deformation occurs. The constant residual stress field has caused the redistribution of the stresses within the structure. This effectively has the effect of pulling the stress fields, the sum of the elastic and residual stresses in to the yield surface.

Reverse Plasticity/Plastic Shakedown Region The transition to this region occurs when the effective elastic stresses exceed twice the yield stress. This was made possible with the accommodation of the time-varying residual stress field, causing the stress distribution at the outer fibre of the plate, to exceed twice the yield stress. When the structure exhibits reverse plasticity over each cycle, the positive plastic strain in the first half of the load cycle followed by equal magnitude negative strain in the second half, such that there is no accumulation of plastic strain during load cycle. And the failure mechanism for plastic shakedown is low-cycle fatigue.

Ratchetting Region This region is best characterized by the breakdown of the elastic, shakedown and reverse-plasticity conditions. In each cycle, plastic strains accumulate over a significant volume of the plate, leading to structural failure from the unlimited accumulation of plastic deformation and eventually incremental plastic collapse.

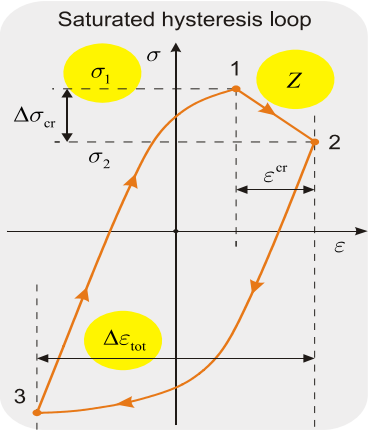

Fig. 2 The Hysteresis cycle which provides the information for fatigue and creep damage

2.2.2 Design Limits in Creep Under Cyclic Loading

In the presence of creep, the response of the structure to cyclic loading changes significantly. Interaction of plasticity and creep is the key feature of creep-fatigue mechanism under cyclic loading condition with creep. Assessments must be carried out to ensure avoidance of creep-fatigue failure by, creep rupture and cyclically enhanced creep. The term cyclically enhance creep refers to the threat of gross section creep failure due to the accumulation of creep strains arising from the cyclic loading. The life design limit under creep fatigue interaction can be defined by construction of stress strain hysteresis loops since this hysteresis loop provides the information of life damage due to fatigue and creep, and this information also is the key to an R5 V2/3 assessment. Figure 2 is the construction of the hysteresis cycle; it provides the total strain range, $\Delta\varepsilon_{tot}$ from which the fatigue damage is calculated, and the start of dwell stress, σ_1 and creep strain, ε^{cr} from which the creep damage is calculated.

3 Minimization Processes of the Linear Matching Method

The strategy of locating each of above critical limits consists of defining an appropriate class of kinematically admissible strain rate histories $\dot{\varepsilon}^c_{ij}$ then solving a corresponding minimizing process for $I(\dot{\varepsilon}^c_{ij}, \lambda)$ by considering the incremental form;

$$I\left(\dot{\varepsilon}^c_{ij}, \lambda\right) = \sum_{n=1}^{N} I^n, \tag{4a}$$

$$I^n\left(\Delta\varepsilon^n_{ij}, \lambda\right) = \int_V \left\{\sigma^n_{ij}\Delta\varepsilon^n_{ij} - \left(\lambda\hat{\sigma}_{ij}(t_n) + \rho_{ij}(t_n) + \bar{\rho}_{ij}\right)\Delta\varepsilon^n_{ij}\right\} dV, \tag{4b}$$

$$\rho_{ij}(t_n) = \bar{\rho}^0_{ij} + \sum_{l=1}^{n} \Delta\rho_{ij}(t_l), \tag{4c}$$

where $\dot{\varepsilon}_{ij}^{c}$ is replaced by a sequence of increments of strain $\Delta\varepsilon_{ij}^{n}$ occurring at a sequence of N times t_n, $n = 1$ to N, during the cycle. The incremental minimization of $I^n(\Delta\varepsilon_{ij}^{n}, \lambda)$ assumes that the prior history of the residual stress is known and compatibility of the total elastic and plastic strain in the increment is used. $\bar{\rho}_{ij}^{0}$ is the constant element of the changing residual stress $\rho_{ij}(t_n)$ and represents as,

$$\bar{\rho}_{ijM}^{0} = \sum_{n=1}^{N} \Delta\rho_{ij}{}_{1}^{n} + \sum_{n=1}^{N} \Delta\rho_{ij}{}_{2}^{n} + \cdots + \sum_{n=1}^{N} \Delta\rho_{ij}{}_{M-1}^{n} \tag{5}$$

where M represents the total number of cycles. In this section, the linear matching processes for minimization of $I(\dot{\varepsilon}_{ij}^{c}, \lambda)$ are summarized for both the shakedown and ratchet limits.

3.1 Global Minimization for Shakedown Limit

The global minimization of $I(\dot{\varepsilon}_{ij}^{c}, \lambda)$makes use of the compatibility from the sum of the increments of plastic strain over the cycle. When a set of increments $\Delta\varepsilon_{ij}^{nk}$ at kth iteration are assumed known, a linear material can be defined so that linear shear modulus $\bar{\mu}^{nk}$ ensures that the resulting deviatoric stress is at yield, i.e.

$$\frac{2}{3}\bar{\mu}^{nk}\bar{\varepsilon}\left(\Delta\varepsilon_{ij}^{nk}\right) = \sigma_0 \tag{6}$$

where $\bar{\varepsilon}$ denotes the von Mises effective strain.

For shakedown problems, the changing component of residual stress vanishes, i.e. $\rho_{ij}^{r} = 0$. Hence, the cyclic stress history for shakedown problem is given by

$$\sigma_{ij}(x,t) = \lambda\hat{\sigma}_{ij}(x,t) + \bar{\rho}_{ij}(x). \tag{7}$$

A set of linear incremental relationships are then defined by

$$\Delta\varepsilon_{ij}^{n(k+1)\prime} = \frac{1}{2\bar{\mu}^{nk}}\left[\lambda\hat{\sigma}_{ij}'(t_n) + \bar{\rho}_{ij}^{k+1\prime}\right], \qquad \Delta\varepsilon_{kk}^{n(k+1)} = 0 \tag{8}$$

where the upper 'dash' refers to deviatoric components. Summing over the cycle produces a relationship between the compatible strain $\Delta\varepsilon_{ij}^{(k+1)} = \sum_n \Delta\varepsilon_{ij}^{n(k+1)}$ and the constant residual stress $\bar{\rho}_{ij}^{k+1}$with an initial stress state;

$$\Delta\varepsilon_{ij}^{(k+1)\prime} = \frac{1}{2\bar{\mu}^{k}}\left(\sigma_{ij}^{initial\,\prime} + \bar{\rho}_{ij}^{k+1\prime}\right), \qquad \Delta\varepsilon_{kk}^{(k+1)} = 0 \tag{9a}$$

where

$$\frac{1}{\bar{\mu}^{k}} = \sum_{n}\frac{1}{\bar{\mu}^{nk}} \quad \text{and} \quad \sigma_{ij}^{initial} = \bar{\mu}^{k}\sum_{n}\frac{\lambda\hat{\sigma}_{ij}(t_n)}{\bar{\mu}^{nk}}. \tag{9b}$$

The solution of the continuum problem corresponding to Eqs. (9a), (9b) has the property that $I(\Delta\varepsilon_{ij}^{(k+1)}, \lambda) \le I(\Delta\varepsilon_{ij}^{k}, \lambda)$, which is proved by [6].

3.2 Dual Minimization Process for Ratchet Analysis

We consider a structure subjected to a general cyclic load condition, which can be decomposed into cyclic and constant components, i.e. $\hat{\sigma}_{ij}(x,t) = \hat{\sigma}_{ij}^{\Delta}(x,t) + \lambda\hat{\sigma}_{ij}^{\overline{F}}(x)$. The calculation of the ratchet limit includes dual minimization processes, the first an incremental minimization for the evaluation of a cyclic history of residual stresses and plastic strain range in a stable cycle and the second a global minimization for the ratchet limit due to an extra constant load. By decoupling the evaluation of the changing residual stress and the constant residual stress in Eqs. (4a)–(4c), the entire numerical procedure of ratchet analysis includes two steps [24]. The first step is to calculate the history of the changing residual stress associated with the applied cyclic load $\hat{\sigma}_{ij}^{\Delta}(x,t)$ and the corresponding plastic strain ranges for the low cycle fatigue assessment. The second step is to locate the ratchet limit due to the extra constant load $\lambda\hat{\sigma}_{ij}^{\overline{F}}(x)$ as a conventional shakedown analysis where a constant residual stress is evaluated by global minimization (Sect. 3.1) and the elastic stress history is augmented by the changes in residual stress calculated in the first step.

The global minimization process for step 2 of ratchet analysis is as same as the global minimization for shakedown limit in Sect. 3.1. Next a distinct minimization process—incremental minimization is summarized for step 1 of ratchet analysis to evaluate the changing residual stress ρ_{ij}^{r} and the associated plastic strain range corresponding to the cyclic component of the elastic stress $\hat{\sigma}_{ij}^{\Delta}$.

3.2.1 Incremental Minimization for the Varying Residual Stress Field and Plastic Strain Range

The incremental minimization of $I^n(\Delta\varepsilon_{ij}^n, \lambda)$ assumes the prior history of the residual stress is known and compatibility of the total elastic and plastic strain in the increment is used. With an initial estimate of $\Delta\varepsilon_{ij}^n = \Delta\varepsilon_{ij}^{nk}$, a linear modulus is defined by linear matching $\sigma_0 = 2/3\bar{\mu}^{nk}\bar{\varepsilon}(\Delta\varepsilon_{ij}^{nk})$, where the von Mises yield stress σ_0 could be either constant or temperature-dependent.

An incremental linear equation is then defined;

$$\Delta\varepsilon_{ij}^{Tn(k+1)\prime} = \frac{1}{2\mu}\Delta\rho_{ij}^{n(k+1)\prime} + \Delta\varepsilon_{ij}^{n(k+1)\prime}, \tag{10a}$$

$$\Delta\varepsilon_{kk}^{Tn(k+1)} = \frac{1}{3K}\Delta\rho_{kk}^{n(k+1)}, \tag{10b}$$

$$\Delta\varepsilon_{ij}^{n(k+1)\prime} = \frac{1}{2\bar{\mu}^{nk}}\left\{\hat{\sigma}_{ij}^{\Delta}(t_n) + \rho_{ij}(t_{n-1}) + \Delta\rho_{ij}^{n(k+1)}\right\}', \tag{10c}$$

where the prior history of the residual stress is known, i.e.

$$\rho_{ij}(t_{n-1}) = \rho_{ij}(t_0) + \Delta\rho_{ij}^1 + \Delta\rho_{ij}^2 + \cdots + \Delta\rho_{ij}^{n-1}, \qquad \rho_{ij}(t_0) = \bar{\rho}_{ij}^0. \tag{11}$$

The entire iterative procedure requires a number of cycles, where each cycle contains N iterations associated with N load instances. The first iteration is to evaluate

the changing residual stress $\Delta\rho_{ij}^{1}$ associated with the elastic solution $\hat{\sigma}_{ij}^{\Delta}(t_1)$ at the first load instance. Define $\Delta\rho_{ij}{}_{m}^{n}$ as the evaluated changing residual stress for nth load instance at mth cycle of iterations, where $n = 1, 2, \ldots, N$ and $m = 1, 2, \ldots, M$. At each iteration, the above changing residual stress $\Delta\rho_{ij}{}_{m}^{n}$ is calculated. When the convergence occurs at the Mth cycle of iterations, the summation of changing residual stresses at N time points must approach to zero ($\sum_{n=1}^{N}\Delta\rho_{ij}{}_{M}^{n} = 0$) due to the stable cyclic response. Hence the constant residual stress $\rho_{ij}(t_0) = \bar{\rho}_{ij}^{0}$ over the cycle can also be determined by

$$\bar{\rho}_{ij}^{0} = \sum_{n=1}^{N}\Delta\rho_{ij}{}_{1}^{n} + \sum_{n=1}^{N}\Delta\rho_{ij}{}_{2}^{n} + \cdots + \sum_{n=1}^{N}\Delta\rho_{ij}{}_{M}^{n}. \tag{12}$$

The corresponding plastic strain magnitude occurring at time t_n is calculated by

$$\Delta\varepsilon_{ij}^{P}(t_n) = \frac{1}{2\bar{\mu}^{n}}\left(\hat{\sigma}_{ij}^{\Delta\prime}(t_n) + \rho_{ij}'(t_n)\right) \tag{13}$$

where $\bar{\mu}^{n}$ is the iterative shear modulus and $\rho_{ij}(t_n)$ is the converged accumulated residual stress at the time instant t_n, i.e.

$$\rho_{ij}(t_n) = \bar{\rho}_{ij}^{0} + \sum_{k=1}^{n}\Delta\rho_{ij}{}_{M}^{k}. \tag{14}$$

4 Evaluation of Upper and Lower Bound Limits

4.1 Upper Bound Shakedown and Ratchet Limit

Combining $0 \le I(\Delta\varepsilon_{ij}^{(k+1)}, \lambda) \le I(\Delta\varepsilon_{ij}^{k}, \lambda)$ and Eqs. (4a)–(4c), with ρ_{ij} and $\bar{\rho}_{ij}$ eliminated Based upon the Koiter's theorem [25] the upper bound shakedown limit is given as,

$$I\left(\Delta\varepsilon_{ij}, \lambda^{S}\right) = \int_{V}\sum_{n=1}^{N}\left\{\sigma_{ij}^{n}\Delta\varepsilon_{ij}^{n} - \lambda^{S}\hat{\sigma}_{ij}(t_n)\Delta\varepsilon_{ij}^{n}\right\}dV \ge 0, \tag{15a}$$

i.e.

$$\lambda^{S} \le \frac{\int_{V}(\sum_{n=1}^{N}\sigma_{ij}^{n}\Delta\varepsilon_{ij}^{n})dV}{\int_{V}(\sum_{n=1}^{N}\hat{\sigma}_{ij}(t_n)\Delta\varepsilon_{ij}^{n})dV} = \frac{\int_{V}(\sigma_y\sum_{n=1}^{N}\bar{\varepsilon}(\Delta\varepsilon_{ij}^{n}))dV}{\int_{V}(\sum_{n=1}^{N}\hat{\sigma}_{ij}(t_n)\Delta\varepsilon_{ij}^{n})dV} = \lambda_{UB}^{S}. \tag{15b}$$

Equation (15b) provides a monotonically reducing sequence of upper bound to the shakedown limit, i.e. $\lambda_{UB}^{S(k+1)} \le \lambda_{UB}^{S(k)}$. It is worth noting that a limit load can be calculated by Eq. (15b) as a special case of the shakedown analysis, where the cyclic load condition reduces to monotonic load condition, i.e. $N = 1$.

For the upper bound ratchet limit, the numerical technique can be accommodated within the existing methods of shakedown analysis where the linear elastic solution is augmented by the changing residual stress field, i.e.

$$\hat{\sigma}_{ij} = \lambda \hat{\sigma}_{ij}^{\bar{F}} + \hat{\sigma}_{ij}^{\Delta}(x,t) + \rho_{ij}(x,t) \tag{16}$$

where the history of the residual stress field $\rho_{ij}(t_n)$ associated with the cyclic component of the load history has been calculated by an incremental minimization process (Sect. 3.2.1).

For the von Mises yield condition and the associated flow rule, an upper bound ratchet limit multiplier can be obtained by

$$\lambda_{UB}^{R} = \frac{\int_V \sum_{n=1}^{N} \sigma_y \bar{\varepsilon}(\Delta\varepsilon_{ij}^n) dV - \int_V \sum_{n=1}^{N} (\hat{\sigma}_{ij}^{\Delta}(t_n) + \rho_{ij}(t_n)) \Delta\varepsilon_{ij}^n dV}{\int_V \hat{\sigma}_{ij}^{\bar{F}} (\sum_{n=1}^{N} \Delta\varepsilon_{ij}^n) dV} \tag{17}$$

which gives the capacity of the body subjected to a predefined cyclic load history $\hat{\sigma}_{ij}^{\Delta}(t_n)$ to withstand an additional constant load $\hat{\sigma}_{ij}^{\bar{F}}$ before ratchetting takes place.

4.2 Lower Bound Shakedown and Ratchet Limit

Both the constant residual stress $\bar{\rho}_{ij}(x)$ and varying residual stress $\rho_{ij}^{r}(x,t)$ in Eq. (2) for a stabilised load cycle have been calculated by incremental and global minimization processes. Hence, based upon the lower bound theorem [26], a lower bound of shakedown or ratchet limit can be constructed in the same upper bound procedure by maximizing the lower bound load parameter λ_{LB} under the condition where for any potentially active load/temperature path, the stabilised cyclic stresses in Eq. (2) nowhere violate the yield condition.

As the upper bound iterative process provides a sequence of residual stress fields, a sequence of lower bound at each iteration can be calculated by scaling the elastic solution so that the cyclic stress everywhere satisfies yield. The lower bound of shakedown limit multiplier can be described as:

$$\lambda_{LB}^{s} = \max \lambda_{LB} \tag{18a}$$

$$\text{s.t. } f\left(\lambda_{LB}\hat{\sigma}_{ij}(x,t) + \bar{\rho}_{ij}(x)\right) \le 0. \tag{18b}$$

The lower bound of ratchet limit multiplier can be written as:

$$\lambda_{LB}^{R} = \max \lambda_{LB} \tag{19a}$$

$$\text{s.t. } f\left(\lambda_{LB}\hat{\sigma}_{ij}^{\bar{F}} + \hat{\sigma}_{ij}^{\Delta}(x,t) + \rho_{ij}(x,t) + \bar{\rho}_{ij}(x)\right) \le 0. \tag{19b}$$

5 Numerical Procedures for the Creep Strain and Flow Stress

In the incremental minimization process (Sect. 3.2.1) where the plastic strain amplitudes are evaluated, σ_0 (Eq. (6)) is adopted as the material yield stress. However, when the accumulated creep strain is calculated during the dwell period at the

creep load time instance, σ_0 in Eq. (6) needs to be replaced by the creep flow stress $\sigma_0 = \bar{\sigma}_c$. The creep flow stress is an implicit function of creep strain $\Delta\bar{\varepsilon}^c$ and residual stress $\Delta\bar{\rho}^c$ during the creep dwell period. The detailed numerical procedures for the evaluation of creep strain and flow stress are described in [27, 28] and these processes are summarized as follows:

We assume a time hardening creep constitutive relation:

$$\dot{\bar{\varepsilon}}^c = B\bar{\sigma}^{n^*} t^{m^*} \tag{20}$$

where $\dot{\bar{\varepsilon}}^c$ is the effective creep strain rate, $\bar{\sigma}$ is the effective von-Mises stress, t is the dwell time, and B, m^* and n^* are the creep constants of the material. When $m^* = 0$, the time hardening constitutive equation becomes the Norton's law.

During the relaxation process we assume, at each point in space that an elastic follow up factor Z exists:

$$\dot{\bar{\varepsilon}}^c = -\frac{Z}{\bar{E}}\dot{\bar{\sigma}} \tag{21}$$

where $\bar{E} = 3E/2(1+v)$, E is the Young's modulus and $\dot{\bar{\sigma}} = \dot{\bar{\sigma}}(\sigma_{ij})$.

Combining Eqs. (20) and (21) and integrating over the dwell time, we obtain

$$\frac{B\bar{E}\Delta t^{m^*+1}}{Z(m^*+1)} = \frac{1}{n^*-1}\left\{\frac{1}{(\bar{\sigma}_c)^{n^*-1}} - \frac{1}{(\bar{\sigma}_s)^{n^*-1}}\right\} \tag{22}$$

where $\bar{\sigma}_s$ is the effective value of the start of dwell stress, $\bar{\sigma}_c$ is the effective value of the creep flow stress, and $\bar{\sigma}_c = \bar{\sigma}(\sigma_{sij} + \Delta\rho_{Cij})$. Integrating Eq. (21) gives the effective creep strain during the dwell period Δt as,

$$\Delta\bar{\varepsilon} = -\frac{Z}{\bar{E}}(\bar{\sigma}_c - \bar{\sigma}_s). \tag{23}$$

Combining Eqs. (22) and (23) and eliminating $Z/\bar{E}$ gives

$$\Delta\bar{\varepsilon}^c = \frac{B(n^*-1)\Delta t^{m^*+1}(\bar{\sigma}_s - \bar{\sigma}_c)}{(\frac{1}{\bar{\sigma}_c^{n^*-1}} - \frac{1}{\bar{\sigma}_s^{n^*-1}})(m^*+1)}. \tag{24}$$

For the pure creep where $\bar{\sigma}_s = \bar{\sigma}_c$, the creep strain becomes:

$$\Delta\bar{\varepsilon}^c = \frac{B\bar{\sigma}_s^{n^*}\Delta t^{m^*+1}}{m^*+1}. \tag{25}$$

The creep strain rate $\dot{\bar{\varepsilon}}^F$ at the end of dwell time Δt is calculated by Eqs. (22) and (24):

$$\dot{\bar{\varepsilon}}^F = B(\bar{\sigma}_c)^{n^*}\Delta t^{m^*} = \frac{\Delta\bar{\varepsilon}^c}{\Delta t}\frac{(m^*+1)}{(n^*-1)}\frac{\bar{\sigma}_c^{n^*}}{(\bar{\sigma}_s - \bar{\sigma}_c)}\left(\frac{1}{\bar{\sigma}_c^{n^*-1}} - \frac{1}{\bar{\sigma}_s^{n^*-1}}\right). \tag{26}$$

For the pure creep where $\bar{\sigma}_s = \bar{\sigma}_c$, the creep strain rate $\dot{\bar{\varepsilon}}^F$ becomes:

$$\dot{\bar{\varepsilon}}^F = B(\bar{\sigma}_s)^{n^*}\Delta t^{m^*}. \tag{27}$$

Hence in the iterative process, we begin with current estimated $\bar{\sigma}_c^i, \bar{\sigma}_s^i$ and use Eqs. (24), (26) or (27) to compute a new value of the creep stress $\bar{\sigma}_c = \bar{\sigma}_c^f$ from Eq. (28) to replace $\sigma_0(t_n)$ in the linear matching condition Eq. (6).

$$\bar{\sigma}_c = \left(\frac{\bar{\dot{\varepsilon}}^F}{B \Delta t^{m^*}} \right)^{\frac{1}{n^*}}. \tag{28}$$

6 Convergence Considerations

The necessary condition for convergence and the exact proof for upper bounds are provided by [5, 6]. According to this study, in order to get convergent minimum upper bound limits three conditions must be fulfilled as follows: (1) The material yield surface must be convex; (2) The class of strain rates and the associated strain increments guarantee that the minimum upper bound is limited with this class; (3) The class of selected compatible strain distributions must be adequately extensive to guarantee a satisfactory upper bound.

The first two conditions can be easily satisfied by an appropriate choice of a class of linear materials. Condition (3) is vital to the implementation of the LMM within a finite element scheme. Within the LMM, the equilibrium of the residual stress field ρ_{ij} relies on the class of displacement field Δu_i from which $\Delta \varepsilon_{ij}$ is derived, i.e. ρ_{ij} is in equilibrium if and only if $\int_V \rho_{ij} \Delta \varepsilon_{ij} dV = 0$. Hence, for a given finite element mesh, the process will converge to the least upper bound associated with the FE mesh and within this class of displacement field Δu_i. However, during the FE implementation, the volume integration is not exact but usually depends upon the Gaussian integration to give an exact integral. Hence a point-wise condition is used to replace above equilibrium condition;

$$\sum_{el} \sum_{k} w_k \rho_{ij}^k \Delta \varepsilon_{ij}^k = 0 \tag{29}$$

where w_k are the Gaussian weighting factors at the Gauss integration points.

According to the lower and upper bound theorems, the LMM ensures that the maximum lower bound will be less than the least upper bound. However, unlike the strict convergence of the upper bound, the magnitude of lower bound may not always increase monotonically with iterations. But upon convergence, the maximum lower bound will equal to the least upper bound, where by equilibrium condition (Eq. (29)) the matching condition is applied at Gauss points.

Due to the point-wise condition of equilibrium (Eq. (29)), whereas the deviation from convergence at a few Gauss points has little effect on the upper bound which is determined by volume integrals, the convergence of the upper bound in terms of a particular number of significant figures may allow some deviation from convergence locally. Hence the convergence of lower bound may be affected significantly as it is determined by single Gauss point. Generally the upper bound converges (monotonically) more quickly than the lower bound and the rate of convergence for lower bound depends upon the characteristic of the problem and also the adopted FE

model, such as the complexity of the geometry and boundary conditions, the mesh arrangement, etc. For some cases where the lower bound converges very slowly, the convergence is usually judged entirely in terms of the upper bound. Further investigation of the convergence of the LMM iterative algorithms has been carried out and a separate paper is being prepared for this context.

7 Examples of Applications

In this section, three practical examples of the LMM for differing applications are provided to confirm the efficiency and effectiveness of the method; the behaviour of a defective pipeline subjected to cyclic thermal loading and constant operating pressure, the effects of drilling holes on the ratchet limit and crack tip plastic strain range for a centre cracked plate subjected to constant tensile loading and cyclic bending moment, and the cyclic structural responses of a cruciform weldment under creep fatigue interaction.

7.1 Defective Pipelines Subjected to Cyclic Thermal Loading and Constant Operating Pressure

Figure 3 gives a finite element model of a defective pipeline with four types of slot, where the symmetry boundary conditions are applied to the half section of the model. Such pipes are subjected to particular severe thermal loading, resulting in the possibility of ratchetting or premature failure due to low cycle fatigue.

Figure 4 presents the calculated shakedown and ratchet limit interaction curve for a pipeline with these four types of slots, which clearly shows the effect of part-through slot on the shakedown and ratchet limits. It is observed that any part-through slot significantly reduces the reverse plasticity limit of the pipeline due to the stress concentration caused by the existence of the slot. It is also identified that at different levels of cyclic thermal loading the ratchet limit boundary decreases sharply for a defective pipeline with axial and large area slot and it remains almost constant for small and circumferential slot, compared with a defect-free pipeline. Figure 4 further shows that for the cases of axial and large area slots, the ratchet limit ends at cyclic thermal loading points $\Delta\theta = 4.1\Delta\theta_0$ and $\Delta\theta = 5.5\Delta\theta_0$, respectively, which indicates that when the cyclic thermal loading $\Delta\theta$ beyond these cyclic thermal loading limits ($4.1\Delta\theta$ for axial slot and $5.5\Delta\theta$ for large area slot), any amount of constant internal pressure will result in ratchetting.

A full discussion of the solutions including plastic strain range concerning the fatigue crack initiation and verifications with ABAQUS detailed step-by-step analysis are given by [29]. This example demonstrates that, for these practical industrial problems, the method is capable of providing solutions that are much more illuminating than conventional analysis.

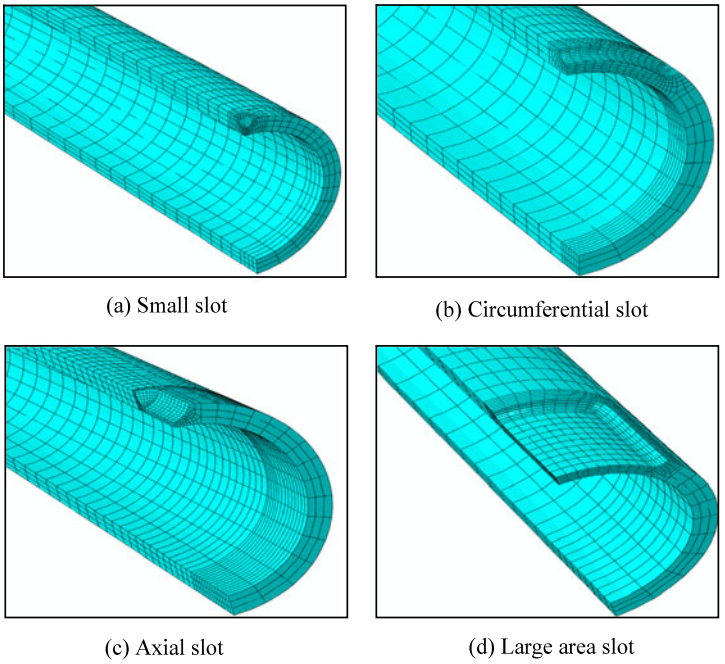

Fig. 3 The finite element mesh for a pipeline with part-through slot: (**a**) small slot; (**b**) circumferential slot; (**c**) axial slot and (**d**) large area slot

Fig. 4 Shakedown and ratchet limit interaction curve for defect-free and defective pipelines

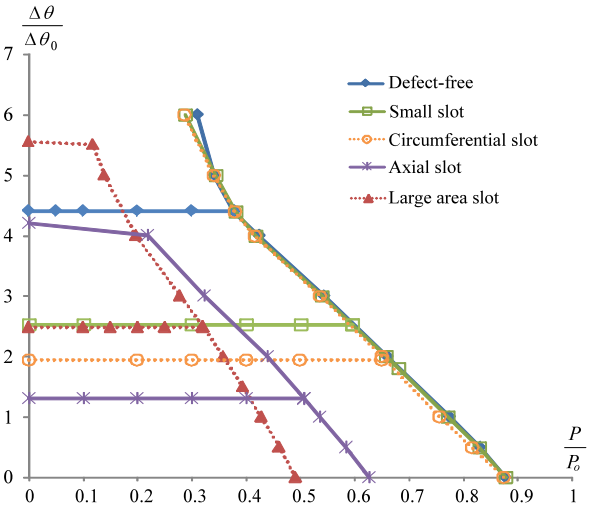

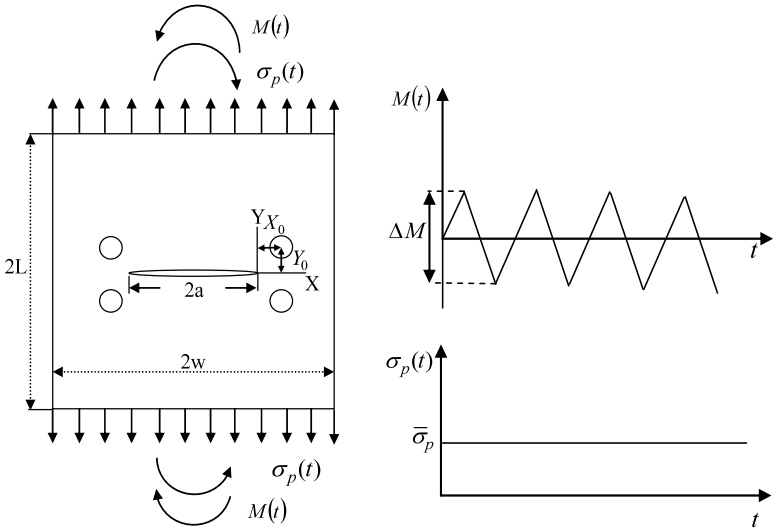

Fig. 5 Centre cracked plate with symmetric holes subjected to reversed bending moment range ΔM and constant tension $\bar{\sigma}_p$

7.2 Centre Cracked Plate with Circular Holes

The second example concerns the effect of circular holes in a centre cracked plate subjected to cyclic bending moment and constant tensile loading on the ratchet limit and crack tip plastic strain range. Drilling holes in front of the crack tip is an effective way to arrest crack growth. However the optimum location and size of the holes need to be researched to produce the smallest crack tip plastic strain range, i.e. the best fatigue crack growth life, and to have the least reduction in ratchet limit.

The geometrical shape and cyclic loading history of the centre cracked plate with symmetric drilled holes are shown in Fig. 5, where the half-crack length a is 500 mm and the ratios W/a and L/a are both 2. The hole locations (X_0, Y_0) are referred to a co-ordinate system X, Y, the origin of which is located at the crack tip. The centre cracked plate is subjected to cyclic reversed bending moment with range ΔM and constant uniaxial tension $\bar{\sigma}_p$. By applying symmetry conditions, a FE half symmetry model was adopted (Fig. 6).

Figure 7 presents the calculated lower and upper ratchet limit and limit load interaction diagram for the hole location at $X/a = -1$, $Y/a = 0.3$ and the diameter of hole $D = 100$ mm, where the applied constant pressure in X-axis is normalized with respect to the reference uniaxial tension $\bar{\sigma}_{po} = 100$ MPa, while the amplitude of the reversed bending moment in Y-axis is normalized using the reference bending moment range $\Delta M_0 = 100$ N mm. It can be seen that the ratchet limit and the limit load curves do not coincide, which means that an increase in the loads beyond the ratchet limit will not automatically cause plastic collapse. Any combination of loads which lies between these two boundaries will result in ratchetting.

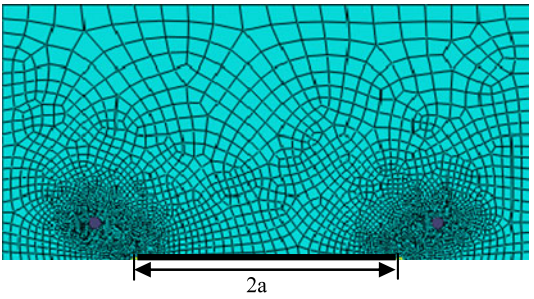

Fig. 6 FE half symmetry model for centre cracked plate with symmetric holes

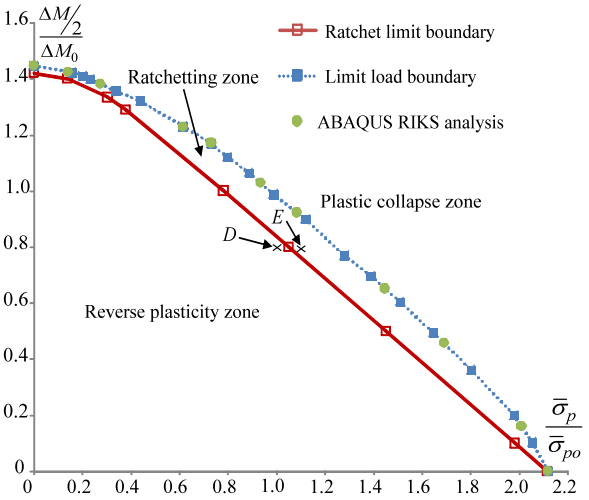

Fig. 7 Ratchet limit and limit load interaction curve with hole location at $\frac{X}{a} = -0.1$, $\frac{Y}{a} = 0.3$ ($D = 100$ mm)

As shown in Fig. 7, the accuracy of the lower and upper bound limit load boundary obtained by the LMM has been verified by ABAQUS RIKS analysis. For the verification of LMM lower and upper bound ratchet limit boundary the cyclic load points D ($\Delta M = 1.6\Delta M_0, \bar{\sigma}_p = \bar{\sigma}_{p0}$), and E ($\Delta M = 1.6\Delta M_0, \bar{\sigma}_p = 1.1\bar{\sigma}_{p0}$), which are just below and above the calculated upper bound ratchet limit boundary (Fig. 7), respectively, are chosen for the step-by-step analysis in ABAQUS.

Figure 8 shows the plastic strain history at the crack tip for the cyclic loading D and E calculated by ABAQUS step-by-step analysis. The calculated plastic strain for the load case D settles to a stable cycle after about 5 load cycles showing a reverse plasticity mechanism, and the load case E shows a strong ratchetting mechanism, with the plastic strain increasing at every cycle. This directly confirms the accuracy of the predicted LMM lower and upper bound ratchet limits.

Optimization studies were performed further involving holes with different diameters drilled at different locations. The study shown that the most significant decrease in crack tip plastic strain range with least reduction in the ratchet limit is identified for the hole size $D = 150$ mm at the optimum location $X_0/a = -0.1$, $Y_0/a = 0.3$, which gives a 72 % reduction in the plastic strain range and does not reduce the ratchet limit.

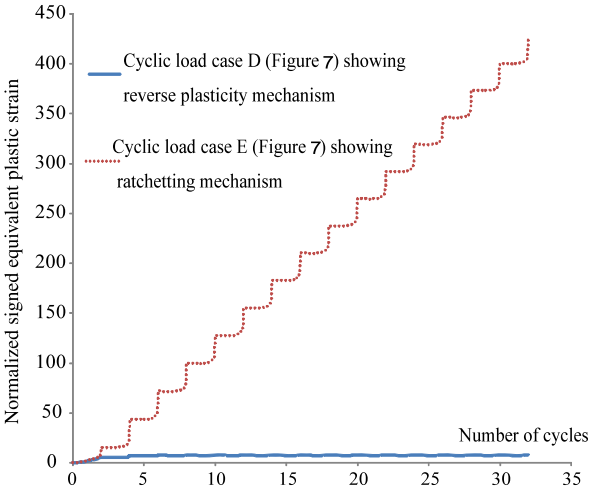

Fig. 8 ABAQUS verification of the ratchet limit for the cyclic bending moment case using detailed step by step analysis

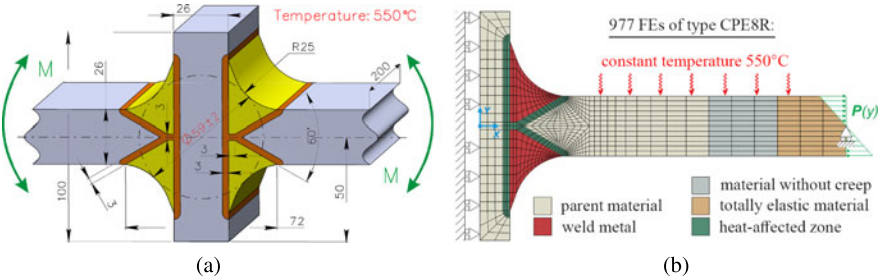

Fig. 9 Geometrical and analysis parameters of the cruciform weld specimens: (**a**) dimensions and applied loading; (**b**) FE-mesh with designation of different materials, boundary conditions and mechanical loading

A full discussion of the solutions is given by [30]. This example demonstrates that the method is capable of providing accurate solutions to the crack structures.

7.3 Creep-Fatigue Analysis of a Cruciform Weldment

The LMM has been extended recently to directly evaluate steady-state cyclic response of components with creep fatigue interaction taking into consideration, which is able to generate both the closed and non-closed hysteresis loops, providing details of creep strain and plastic strain range for creep and fatigue damage assessments. This example shows a practical application of this method on a cruciform weldment subjected to cyclic bending moment under creep condition.

Figure 9 describes the geometry of the weldment specimen and the applied 2D symmetric FE model of the specimen assuming a plane strain condition.

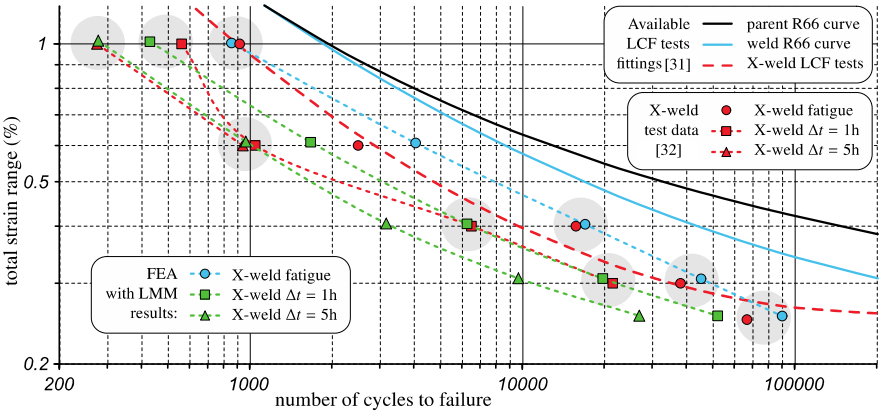

Fig. 10 Results of creep-fatigue assessment in application to cruciform weldment and comparison with experiments [31, 32]

A Ramberg-Osgood formulation was adopted to simulate cyclic stress strain relationship, and a time hardening creep constitutive model was used to characterise creep behaviour. In this creep fatigue damage assessment, the LMM was adopted to evaluate a steady-state cyclic behaviour and to construct a saturated hysteresis loop. Then obtained total strain range during the cycle was used to assess fatigue damage combining R6 fatigue endurance curves [31]. The evaluated creep strain and stress relaxation data were adopted to evaluate creep damage considering time fraction rule and using the experimental creep rupture data. The final lifetime of the cruciform weldment was then obtained based on the calculated fatigue and creep damage under creep-fatigue interaction conditions.

The detailed results of cruciform weldment creep fatigue assessment by the LMM and comparisons with experimental solutions [32] are presented in Fig. 10. Visual comparison of the observed and predicted in Fig. 10 for 3 variants of dwell period Δt shows that 9 of the 11 simulations accurately predict the experimental results. Therefore, it can be used for the formulation of an analytic assessment model suitable for the fast estimation of lifetime for a variety of loading conditions. The low computational effort required by the LMM compared to other computational techniques makes it possible and relatively easy to extrapolate numerical predictions for loading conditions not captured by the available experiments.

A full discussion of the solutions and validations with experimental results are given by Gorash and Chen [33]. This example demonstrates that, for such complex industrial problems, the LMM is capable of providing lifetime related solutions that are much more illuminating than conventional analysis.

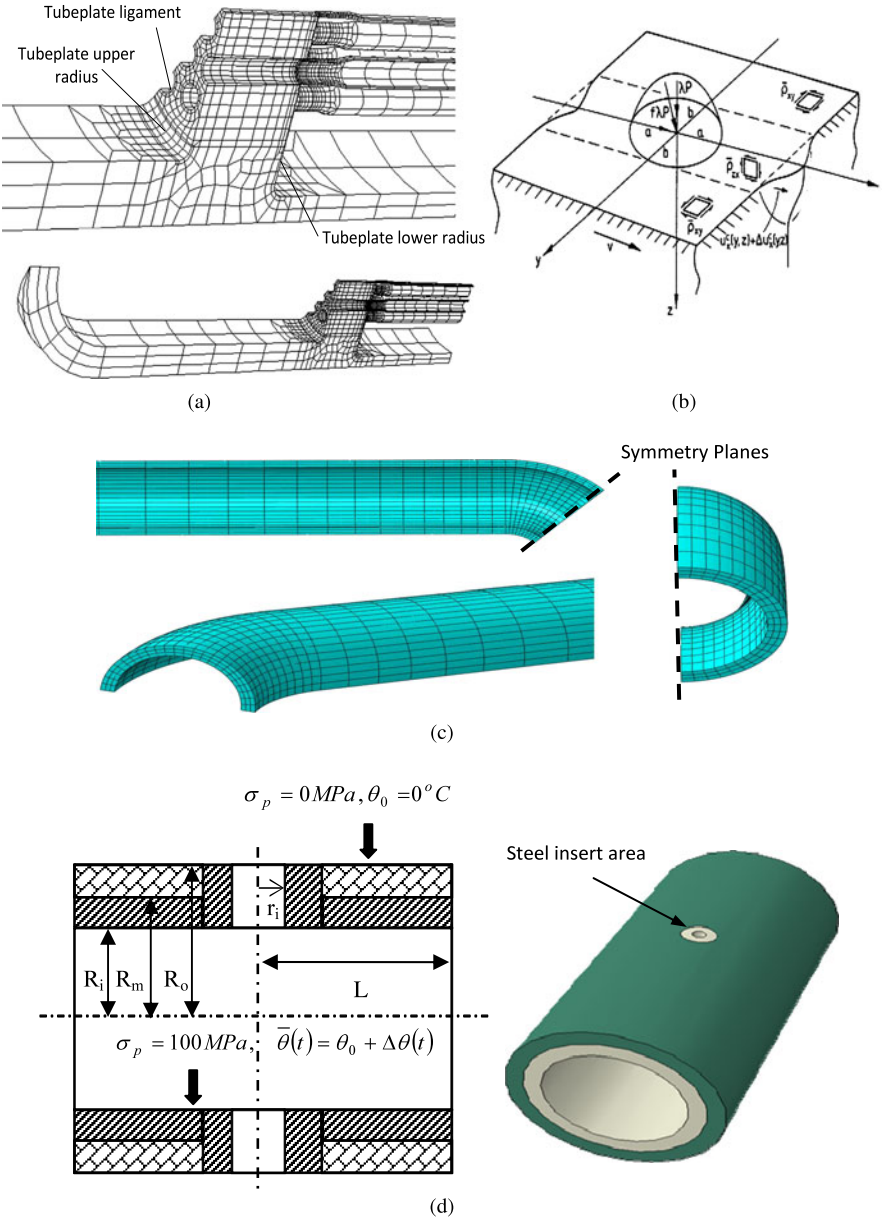

Fig. 11 Other applications (**a**) a heat exchanger tube plane (**b**) rolling contact problem (**c**) 90 pipe bends (**d**) composite cylinder with a crosshole

8 Other Applications

The stable and accurate results of the mentioned LMM on shakedown and ratchet analysis have been confirmed in many industrial applications, including the problem of a heat exchanger tube plate subjected to severe cyclic thermal loading and constant operating pressure (Fig. 11(a)) [8], the application to rolling contact problem (Fig. 11(b)) [34], shakedown and limit analysis of 90 pipe bends under internal pressure, cyclic in-plane bending and cyclic thermal loading (Fig. 11(c)) [35], and the shakedown analysis of a composite cylinder with a cross hole (Fig. 11(d)) [36] and etc.

9 Conclusions

This study focuses on the performance of an elastic plastic body subjected to cyclic loading. The design limits in plasticity and creep including shakedown limit, ratchet limit, cyclic response under creep-fatigue interaction and plastic strain range regarding the fatigue crack initiation have been addressed in this study. The analysis is performed by describing the steady cyclic state employing a general cyclic minimum theorem. In order to estimate the class of kinematically allowable strain rate histories, the Linear Matching Method is used for obtaining the minimum of the functional for these design limits. Three practical examples of the LMM are provided to confirm the efficiency and effectiveness of the method and demonstrate that the LMM may be applied to a much wider range of circumstances than have hitherto been possible.

Acknowledgements The author gratefully acknowledges the support of the Engineering and Physical Sciences Research Council (EP/G038880/1) of the United Kingdom, and the University of Strathclyde during the course of this work. The author would also like to thank Prof Alan Ponter of the Department of Engineering, Leicester University, for his advice and discussion on the theoretical development of the LMM.

References

1. ABAQUS (2007) User's manual. Version 6.7
2. Nguyen-Tajan TMI, Pommier B, Maitournam H, Houari M, Verger L, Du ZZ et al (2003) Determination of the stabilized response of a structure undergoing cyclic thermal–mechanical loads by a direct cyclic method. In: ABAQUS users' conference proceedings
3. Carter P (2005) Analysis of cyclic creep and rupture, part 2: calculation of cyclic reference stresses and ratcheting interaction diagrams. Int J Press Vessels Piping 1(82):27–33
4. Ponter ARS, Carter KF (1997) Limit state solutions, based upon linear elastic solutions with a spatially varying elastic modulus. Comput Methods Appl Mech Eng 140:237–258
5. Ponter ARS, Engelhardt M (2000) Shakedown limits for a general yield condition: Implementation and application for a von-Mises yield condition. Eur J Mech Appl Solids 19:423–445
6. Ponter ARS, Chen HF (2001) A minimum theorem for cyclic load in excess of shakedown, with application to the evaluation of a ratchet limit. Eur J Mech Appl Solids 20:539–553

7. Chen HF, Ponter ARS (2001) A methodfor the evaluation of a ratchet limit and the amplitude ofplastic strain for bodies subjected to cyclic loading. Eur J Mech Appl Solids 20:555–571
8. Chen HF, Ponter ARS (2005) Interity assessment of a 3D tube plate using the linear matching method, creep relaxation and reverse plasticity. J Press Vessel Technol 82:85–104
9. Chen HF, Ponter ARS (2003) Methods for the evaluation of creep relaxation and the amplitude of strains for bodies reverse-plastic strains for bodies reverse-plastic subjected to cyclic loading. In: Pressure vessels and piping, transaction of the ASME, Cleveland, OH, July 2003
10. ANSYS Inc. Southpointe, 275 Technology Drive, Canonsburg, PA 15317. www.ansys.com
11. Hibbit, Karlson and Sorensen Inc (1997) ABAQUSIStandard user's manual, version 6.1, vols 1, 2 & 3. USA
12. ASME (1990) Boiler and pressure vessel code. Code case: nuclear components, case N-47-29, class I components in elevated temperature service. Sect 11, division I
13. AFCEN (1985) Design and construction rules for mechanical components of FBR nuclear islands. RCC-MR, AFCEN, Paris
14. Liu YH, Carvelli V, Maier G (1997) Integrity assessment of defective pressurized pipelines by direct simplified methods. Int J Press Vessels Piping 74:49–57
15. Vu DK, Yan AM, Nguyen DH (2004) A primal–dual algorithm for shakedown analysis of structures. Comput Methods Appl Mech Eng 193:4663–4674
16. Staat M, Heitzer M (2001) LISA a European project for FEM-based limit and shakedown analysis. Nucl Eng Des 206:151–166
17. Seshadri R (2005) Inelastic evaluation of mechanical and structural components using the generalized local stress strain method of analysis. Nucl Eng Des 153:203–287
18. Mackenzie D, Boyle JT, Hamilton R, Shi J (1996) Elastic compensation method in shell-based design by analysis. In: Proceedings of the 1996 ASME pressure vessels and piping conference, vol 338, pp 203–208
19. Chen HF, Ponter ARS, Ainsworth RA (2006) The linear matching method applied to the high temperature life integrity of structures, part 1: assessments involving constant residual stress fields. Int J Press Vessels Piping 83(2):123–135
20. Chen HF, Ponter ARS, Ainsworth RA (2006) The linear matching method applied to the high temperature life integrity of structures, part 2: assessments beyond shakedown involving changing residual stress fields. Int J Press Vessels Piping 83(2):136–147
21. Ainsworth RA (ed) (2003) R5: assessment procedure for the high temperature response of structures. British Energy Generation Ltd, London, p 3
22. Bree J (1967) Elastic-plastic behaviour of thin tubes subjected to internal pressure and intermittent high-heat fluxes with application to fast-nuclear-reactor fuel elements. J Strain Anal 2:226–238
23. Bree J (1989) Plastic deformation of a closed tube due to interaction of pressure stresses and cyclic thermal stresses. Int J Mech Sci 31(11–12):865–892
24. Chen HF, Ponter ARS (2010) A direct method on the evaluation of ratchet limit. J Press Vessel Technol 132:041202
25. Koiter WT (1960) General theorems for elastic plastic soloids. In: Sneddon JN, Hill R (eds) Progress in solid mechanics, vol 1. North Holland, Amsterdam, pp 167–221
26. Melan E (1936) Theorie statisch unbestimmter Systeme aus ideal-plastischem Bastoff. Sitzungsber Akad Wiss Wien, Abtiia 145:195–218
27. Chen HF, Ponter ARS (2006) Linear matching method on the evaluation of plastic and creep behaviours for bodies subjected to cyclic thermal and mechanical loading. Int J Numer Methods Eng 68:13–32
28. Chen H, Chen W (2012) A direct method on the evaluation of cyclic behaviour with creep effect. In: Proceedings of the ASME 2012 pressure vessels & piping division conference, Toronto, ON, Canada, 15–19 July 2012
29. Chen H, Chen W, Li T, Ure J (2011) On ratchet, shakedown and limit analyses of defective pipeline. J Press Vessel Technol
30. Chen H, Chen W, Li T, Ure J (2011) Effect of circular holes on the ratchet limit and crack tip plastic strain range in a centre cracked plate. Int J Fract Mech 78:2310–2324

31. Bate SK, Hayes JP, Hooton DG, Smith NG (2005) Further analyses to validate the R5 volume 2/3 procedure for the assessment of austenitic weldments. Report for British Energy Generation Ltd No SA/EIG/11890/R002, Serco Assurance, Warrington, UK
32. Bretherton I, Knowles G, Hayes JP, Bate SK, Austin CJ (2004) Final report on the fatigue and creep fatigue behaviour of welded cruciform joints. Report for British Energy Generation Ltd No RJCB/RD01186/R01, Serco Assurance, Warrington, UK
33. Gorash Y, Chen HF (2012) Creep fatigue life assessment of cruciform weldments using the linear matching method. Int J Press Vessels Piping 104:1–13
34. Chen H, Ponter ARS (2005) The linear matching method for shakedown and limit analysis applied to rolling and sliding point contact. Road Mater Pavement Des 6:9–30
35. Chen H, Ure J, Li T, Chen W (2011) Shakedown and limit analysis of 90° pipe bends under internal pressure, cyclic in-plane bending and cyclic thermal loading. Int J Press Vessels Piping 88:213–222
36. Chen H, Chen W, Li T, Ure J (2011) Shakedown analysis of composite cylinders with cross hole. J Press Vessel Technol 133:031206